SMART HYDROGELS IN TISSUE ENGINEERING AND REGENERATIVE MEDICINE

EDITED BY: Xing Wang, Yanyu Yang, Yi Shi and Fei Jia
PUBLISHED IN: Frontiers in Chemistry

frontiers Research Topics

ISSN 1664-8714
ISBN 978-2-88963-765-2
DOI 10.3389/978-2-88963-765-2

About Frontiers

Frontiers is more than just an open-access publisher of scholarly articles: it is a pioneering approach to the world of academia, radically improving the way scholarly research is managed. The grand vision of Frontiers is a world where all people have an equal opportunity to seek, share and generate knowledge. Frontiers provides immediate and permanent online open access to all its publications, but this alone is not enough to realize our grand goals.

Frontiers Journal Series

The Frontiers Journal Series is a multi-tier and interdisciplinary set of open-access, online journals, promising a paradigm shift from the current review, selection and dissemination processes in academic publishing. All Frontiers journals are driven by researchers for researchers; therefore, they constitute a service to the scholarly community. At the same time, the Frontiers Journal Series operates on a revolutionary invention, the tiered publishing system, initially addressing specific communities of scholars, and gradually climbing up to broader public understanding, thus serving the interests of the lay society, too.

Dedication to Quality

Each Frontiers article is a landmark of the highest quality, thanks to genuinely collaborative interactions between authors and review editors, who include some of the world's best academicians. Research must be certified by peers before entering a stream of knowledge that may eventually reach the public - and shape society; therefore, Frontiers only applies the most rigorous and unbiased reviews.
Frontiers revolutionizes research publishing by freely delivering the most outstanding research, evaluated with no bias from both the academic and social point of view. By applying the most advanced information technologies, Frontiers is catapulting scholarly publishing into a new generation.

What are Frontiers Research Topics?

Frontiers Research Topics are very popular trademarks of the Frontiers Journals Series: they are collections of at least ten articles, all centered on a particular subject. With their unique mix of varied contributions from Original Research to Review Articles, Frontiers Research Topics unify the most influential researchers, the latest key findings and historical advances in a hot research area! Find out more on how to host your own Frontiers Research Topic or contribute to one as an author by contacting the Frontiers Editorial Office: researchtopics@frontiersin.org

SMART HYDROGELS IN TISSUE ENGINEERING AND REGENERATIVE MEDICINE

Topic Editors:
Xing Wang, Institute of Chemistry (CAS), China
Yanyu Yang, Zhengzhou University, China
Yi Shi, Sun Yat-sen University, China
Fei Jia, Massachusetts Institute of Technology, United States

Citation: Wang, X., Yang, Y., Shi, Y., Jia, F., eds. (2020). Smart Hydrogels in Tissue Engineering and Regenerative Medicine. Lausanne: Frontiers Media SA.
doi: 10.3389/978-2-88963-765-2

Table of Contents

frontiers in Chemistry

EDITORIAL
published: 15 April 2020
doi: 10.3389/fchem.2020.00245

Editorial: Smart Hydrogels in Tissue Engineering and Regenerative Medicine

Xing Wang[1,2]*, *Yanyu Yang*[3], *Yi Shi*[4] *and Fei Jia*[5]

[1] Beijing National Laboratory for Molecular Sciences, Institute of Chemistry, Chinese Academy of Sciences, Beijing, China, [2] University of Chinese Academy of Sciences, Beijing, China, [3] College of Materials Science and Engineering, Zhengzhou University, Zhengzhou, China, [4] Sun Yat-sen University, Guangzhou, China, [5] Massachusetts Institute of Technology, Cambridge, MA, United States

Keywords: hydrogel, tissue engineering, regeneration medicine, stimuli responsive, high performance

Editorial on the Research Topic

Smart Hydrogels in Tissue Engineering and Regenerative Medicine

Tissue engineering, consisting of scaffolds, cells, favorable growth factors, and biomechanical stimulation, has been a most promising therapeutic strategy for tissue reconstruction and regenerative medicine. In general, an ideal tissue-engineered scaffold should be porous, non-toxic, with a matched biodegradable rate, high mechanics, and diffused nutrients and metabolite properties, which can effectively benefit the cell growth, proliferation, and migration, as well as the tissue vascularization process to promote tissue generation. Hydrogels, occurring abundantly with characteristics such as high-water absorption, biodegradation, adjustable porosity, and biocompatibility like that of the natural extracellular matrix (ECM), have been recognized as one of the most suitable scaffold biomaterials for tissue engineering and regenerative medicine. In addition, these scaffold-oriented hydrogels can also be utilized as idea carriers for embedding living cells, transporting tissue cells and growth factors, controlling degradation profiles and releasing stimulatory growth into the specific tissues at different time scales. Due to this, many researchers have been greatly interested in hydrogels with hierarchical structures to mimic the complex interaction of cells with their microenvironment at multiple length scales.

In this Research Topic, we have brought together 9 articles written by 60 authors containing 3 reviews and 6 original research articles. Review articles presented several up-to-date aspects of smart hydrogels in biomedical applications, such as the promoted tissue engineering (Liu et al.), improved transcatheter arterial chemoembolization (Chen Y.-P. et al.), and localized cancer therapy (Fan et al.) by means of their flexibly structural fabrications and functional organizations. As for the original research papers, many researchers were also focused on controllable hydrogel within a wide range of biomedical fields. For example, Bao et al. had prepared a self-assembled nanogel in solutions with a precise design of hierarchical structures using the feasible UV triggers for the potential drug carriers. Also, Hu et al. reported an injectable and compatible hyaluronic acid-based composite hydrogel with pH sensitive behaviors, which exhibited the low toxicity and acceptable mechanical property for liver cancer therapy and scaffolds for biomedical fields. In addition, Shi et al. reported a thermogelling system comprising poly(ω-pentadecalactone) (PPDL), poly(ethylene glycol) (PEG), and poly(propylene glycol) (PPG). The thermogels showed excellent thermal stability, fast response to temperature change, remarkable self-healing property and good biocompatibility, which showed high potential as a drug reservoir for a sustainable release profile of anti-tumor DOX payloads, and exhibited significant inhibition on the growth of tumor (Shi et al.). The other original research papers are covering important aspects of various

OPEN ACCESS

Edited and reviewed by:
Pellegrino Musto,
Italian National Research Council, Italy

***Correspondence:**
Xing Wang
wangxing@iccas.ac.cn

Specialty section:
This article was submitted to Polymer Chemistry, a section of the journal Frontiers in Chemistry

Received: *24 February 2020*
Accepted: *16 March 2020*
Published: *15 April 2020*

Citation:
Wang X, Yang Y, Shi Y and Jia F (2020) Editorial: Smart Hydrogels in Tissue Engineering and Regenerative Medicine. Front. Chem. 8:245. doi: 10.3389/fchem.2020.00245

hydrogels on tissue repair and regeneration, such as bone, hyaline cartilage, and osteoarthritis treatments. Zhang et al. demonstrated a controlled aspirin-sustained release system based on the uniform tetra-PEG hydrogels, which exerted favorable effects on the periodontal ligament stem cells-mediated bone regeneration, providing a new way of thinking about bone regenerative therapy. Wang et al. prepared a kartogenin-grafted PLGA-PEG-PLGA thermogel for achieving the cartilage regeneration and inhibiting the joint inflammation of arthritic knees in a rabbit model for osteoarthritis treatment. Chen Y.-R. et al. had synthesized a low-molecular-weight heparin-functionalized chitosan-chondroitin sulfate hydrogel, which could control the TGF-β3 release and promote the *in vitro* neocartilage formation for construction of tissue-engineered cartilage.

Therefore, the grand aim of this Research Topic is to underpin the importance of preparation, modification, and application of the various hydrogels for tissue engineering and regenerative medicine, which has been achieved by presenting a promising avenue in various fields and postulating real-world respective potentials. Collectively, owing to the intricate nature of emotions, studies aiming at its connection with the high performance of hydrogels are necessarily complex and multifocal. We sincerely hope that you will enjoy reading all the papers in this special edition.

AUTHOR CONTRIBUTIONS

All authors listed have made a substantial, direct and intellectual contribution to the work, and approved it for publication.

FUNDING

This work was supported by the National Natural Science Foundation of China (51973226 and 51803188).

ACKNOWLEDGMENTS

We thank all authors for their contribution to this Research Topic and we would also like to acknowledge the work of the reviewers whose constructive comments contributed to improve the quality of the articles.

Conflict of Interest: The authors declare that the research was conducted in the absence of any commercial or financial relationships that could be construed as a potential conflict of interest.

frontiers in Chemistry

REVIEW
published: 05 June 2019
doi: 10.3389/fchem.2019.00408

Recent Advances on Polymeric Beads or Hydrogels as Embolization Agents for Improved Transcatheter Arterial Chemoembolization (TACE)

Yun-Ping Chen[1], *Jiang-Ling Zhang*[1], *Yanhong Zou*[2] *and Yun-Long Wu*[2]*

[1] *Department of Oncology, The 910 Hospital of PLA, Quanzhou, China,* [2] *Fujian Provincial Key Laboratory of Innovative Drug Target Research, School of Pharmaceutical Sciences, Xiamen University, Xiamen, China*

Transcatheter arterial chemoembolization (TACE), aiming to block the hepatic artery for inhibiting tumor blood supply, became a popular therapy for hepatocellular carcinoma (HCC) patients. Traditional TACE formulation of anticancer drug emulsion in ethiodized oil (i.e., Lipiodol®) and gelatin sponge (i.e., Gelfoam®) had drawbacks on patient tolerance and resulted in undesired systemic toxicity, which were both significantly improved by polymeric beads, microparticles, or hydrogels by taking advantage of the elegant design of biocompatible or biodegradable polymers, especially amphiphilic polymers or polymers with both hydrophilic and hydrophobic chains, which could self-assemble into proposed microspheres or hydrogels. In this review, we aimed to summarize recent advances on polymeric embolization beads or hydrogels as TACE agents, with emphasis on their material basis of polymer architectures, which are important but have not yet been comprehensively summarized.

Keywords: hydrogel, polymeric beads, drug delivery, TACE, cancer therapy

OPEN ACCESS

Edited by:
Xing Wang,
Institute of Chemistry (CAS), China

Reviewed by:
Benhui Hu,
Nanjing Medical University, China
Huaqiong Li,
Chinese Academy of Sciences, China

***Correspondence:**
Yun-Long Wu
wuyl@xmu.edu.cn

Specialty section:
This article was submitted to Polymer Chemistry, a section of the journal Frontiers in Chemistry

Received: *04 May 2019*
Accepted: *20 May 2019*
Published: *05 June 2019*

Citation:
Chen Y-P, Zhang J-L, Zou Y and Wu Y-L (2019) Recent Advances on Polymeric Beads or Hydrogels as Embolization Agents for Improved Transcatheter Arterial Chemoembolization (TACE). Front. Chem. 7:408. doi: 10.3389/fchem.2019.00408

INTRODUCTION

Transcatheter arterial chemoembolization (TACE), which aimed to block the hepatic artery to inhibit the blood supply of solid tumor and to achieve localized chemotherapy, has now been popularly applied for liver cancer patients who were at a middle or late stage and were not suitable for surgical resection (Schwartz and Weintraub, 2008; Hyun et al., 2018). TACE was firstly proposed by Yamada et al. (1983), who showed that the interruption or reduction of hepatic artery blood supply during chemotherapy process was found to induce tumor necrosis or shrinkage without adverse reaction (Tsurusaki and Murakami, 2015). Since then, TACE has been widely applied in clinical practice, because this localized direct injection of chemotherapeutic drugs could lead to more than a 200 times local drug concentration increase and could achieve a fast curative effect, as well as a minimal side reaction (Varela et al., 2007).

The success of TACE was heavily reliant on the design of embolization reagents (Aliberti et al., 2017). Ideal embolization reagents should be able to (1) quickly and effectively block the blood supply upon intra-arterial injection; (2) release the embedded anticancer drugs for localized chemotherapy; (3) degrade after treatment for preventing thrombus; (4) potentially impair the angiogenesis. Initially, Lipiodol® (ethiodized oil, in form of iodinated fatty acid esters of seed oil) was utilized to emulsify the anticancer drugs due to its lipophilic feature for intra-arterial chemotherapy, which was followed by Gelfoam® (gelatin sponge) embolization and was

recognized as conventional TACE. However, the manual fabrication of Gelfoam®,as well as its heterogeneous feature, led to the embolization effect of <3 days. Even worse, the injection time interval between Lipiodol® and Gelfoam® might lead to diffusion, systematic toxicity, and impaired patient tolerance of anticancer drugs, indicating the urgent need for better embolization agent designs.

Recently, polymers, especially amphiphilic polymers or polymers with both hydrophilic and hydrophobic chains which could self-assemble into microspheres, beads, or hydrogels (Hu et al., 2017a,b; Wu et al., 2017; Cai et al., 2018; Cheng et al., 2018b; Javanbakht and Namazi, 2018; Luo et al., 2018, 2019; Liu et al., 2019; Xu et al., 2019), have been successfully designed as a new generation of TACE embolization reagents, due to their ability to increase chemotherapeutic treatment efficiency and patient tolerance in comparison with traditional TACE by the formulation of Lipiodol® and Gelfoam® (Chen et al., 2016, 2018; Cai et al., 2017; Ding and Li, 2017; Fan et al., 2017a,b; Li and Loh, 2017; Li et al., 2017; Liu et al., 2017; Morimoto et al., 2017; Xiang et al., 2017; Yang et al., 2017; Zheng et al., 2017; Chan et al., 2018; Cheng et al., 2018a, 2019; Gao et al., 2018). In this report, we aim to summarize the current design of new generation embolization beads or hydrogels as illustrated in **Figure 1**, with emphasis on their material basis of polymer architectures, which are important but have not yet been comprehensively reviewed.

POLYMER BASED BEADS OR MICROPARTICLES AS TACE REAGENTS

Polymeric microspheres or beads with an ability to encapsulate chemotherapeutic reagents were developed as drug-eluting beads (DEB) and served as a significant advance. In comparison with traditional TACE formulation of Lipiodol® and Gelfoam®, DEB with drug encapsulation in polymeric beads could effectively prevent the systematic diffusion of chemotherapeutics, especially at its first injection with high concentrations, and slowly release the embedded drug in a controllable manner to improve patience tolerance. As the first commercial DEB, DC Bead® was fabricated by free radical polymerization of poly(vinyl alcohol) (PVA) with modification of N-acryloyl-aminoacetaldehyde (NAAADA), 2-acrylamido-2-methylpropane sulphonate sodium salt (AMPS), and cellulose acetate butyrate. DC Bead® with sulfonate groups was able to encapsulate chemotherapeutic Doxorubicin (DOX), Irinotecan, Topotecan, or Epirubicin with H^+ ions, by electron attraction. It was worth mentioning that a clinical study was conducted in 104 hepatocellular carcinoma (HCC) patients receiving treatments of DC Bead® as DEB-TACE reagents by Bruix group (Burrel et al., 2012). The results showed that patients with DEB-TAC treatments could obviously receive a high dose of DOX without considering the undesired systematic circulation of injected drugs in comparison with conventional TACE formulation. This improvement might be beneficial for localized drug concentration increase and for overcoming drug resistance, indicating the great advantages on the safety of DEB-TACE. Furthermore, Gupta et al. (2011) demonstrated that chemotherapeutic DOX loaded superabsorbent microparticles could effectively increase the DOX intention concentration and increase the therapeutic effect in a liver tumor rabbit model. More importantly, Seki et al. (2011) explored the therapy procedure of 135 patients receiving TACE treatments with chemotherapeutic epirubicin-embedded superabsorbent polymer microparticles. The clinical results revealed that over 90% of patients receiving these treatments were not found to have hepatic artery damage and their 1- or 2- year survival rates were around 70 or 60%, respectively, indicating the practical value of drug eluting polymeric beads for patients with non-resected HCC.

Due to the non-bioresorbable nature of DC beads, many researchers have developed bioresorbable DEB by using a biocompatible and biodegradable polymer, to achieve long-term delivery of chemotherapeutics without considering the removal of the device after use. As a typical case, Golzarian's group designed a series of biodegradable DEB with a size of 300–700 μm by using chitosan and carboxylmethyl cellulose (Weng et al., 2011). Thanks to the carboxyl groups in these microspheres, DOX could be effectively loaded in DEB by electron interactions, with an efficiency of up to 0.3–0.7 mg DOX/sphere. Furthermore, this DEB exhibited a lysozyme dependent polymer degradation, which demonstrated a promising safe DOX carrier for transcatheter embolization application.

Recent endeavors also revealed that poly(lactic-*co*-glycolic acid) (PLGA), hydrophobic as well as biocompatible macromolecules, approved by the food and drug administration (FDA), could also serve as potential TACE reagents due to the high biodegradability. As a typical example, Choi et al. (2015) developed DOX embedded PLGA microspheres by the emulsion approach. Furthermore, they further trapped hyaluronic acid-ceramide (HACE) into the PLGA microspheres (MS) during the emulsion process (as shown in **Figure 2A**), to render TACE reagents with active liver cancer cell targeting ability (Lee et al., 2018). It was worth mentioning that intra-arterial injection of this tumor targeting DOX/HACE MS, with size of 13–44 μm, could significantly inhibit liver tumor growth in a McA-RH7777 liver cancer cell implanted rat tumor model, in comparison with the microspheres without targeting ability (as shown in **Figure 2B**).

It was worth mentioning that current commercial biodegradable microspheres still had their limitations. For example, Embocept®, a starch based microspheres with size of <100 μm, was only suitable for vessel embolization for a short time (<1 h) due to size limitation, which was not efficient for tumor necrosis (Yamasaki et al., 2012). Another case of Occlusin 500®, poly(lactide-*co*-glycolide) (PLGA)/collagen core/shell microspheres with size of 150–210 μm, required long degradation time (several months) with undesired inflammatory reactions (Owen et al., 2012). Ideal biodegradable microspheres should: (1) be able to induce vessel blockage for several hours to a few days, which is sufficient for tumor necrosis induction; (2) be able to degrade with non-harmful product and quick elimination; (3) be of uniform size ranging between 100 and 1,000 μm for board vessel embolization; (4) be easy in drug loading and be made of soft polymeric materials for micro-catheter injection

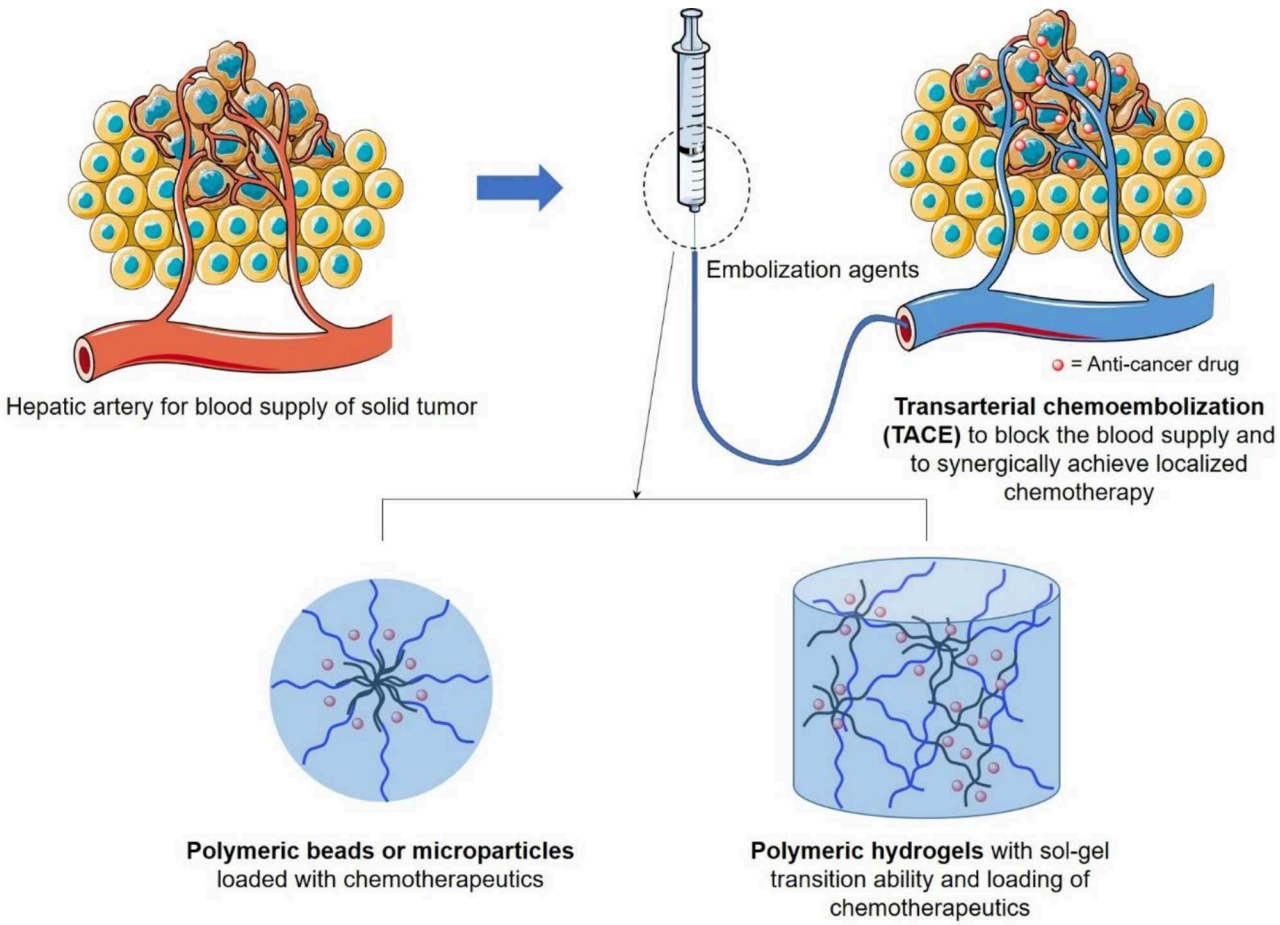

FIGURE 1 | Schematic illustration of design of transarterial chemoembolization (TACE) agents, in terms of polymeric beads or hydrogels, to occulate the blood supply of liver tumor and to synergically achieve localized chemotherapy to reduce its side effects on surrounding healthy tissues.

(Hidaka et al., 2011). To achieve this design, Louguet et al. (2014) synthesized biodegradable polymeric microspheres with a size of 300–500 μm, which was made of amphiphilic poly(ethylene glycol) methacrylate (PEGMA) and biodegradable PEG-PLGA. These PEGMA/PEG-PLGA microspheres could be degraded in a few days with minimal toxicity effects induced by degradation products in fibroblast L929 cells and with a mild inflammatory reaction in an *in vivo* animal model, which showed promising application as safe biodegradable microspheres for TACE utilization.

AMPHIPHILIC POLYMER AS CROSS-LINKER OF MICROBEADS

To achieve a better embolization effect, material scientists tried to further conjugate microbeads into a polymeric mesh, using amphiphilic polymers. As a typical example, Arya et al. (2017) designed biopolymer chitosan-glutaraldehyde (chitosan-GA) microbeads with surface modification, i.e., having sulfated α-cyclodextrin (α-CD) as host molecules on the microbead surfaces, by taking the advantages of electronic attraction between cationic chitosan-GA microbeads and anionic sulfated α-CD (**Figure 3**, upper panel). Furthermore, the reaction between hydrophilic chitosan and hydrophobic n-dodecyl aldehyde rendered amphiphilic chitosan derivatives, whose hydrophobic segments could form an inclusion complex with α-CD due to its hydrophobic inner cavity nature. The experimental results showed that the addition of these amphiphilic chitosan derivatives with α-CD/chitosan-GA microbeads could lead to the bridging occurrence between microbeads and further formation of a polymeric mesh outside the microbeads (**Figure 3**, lower panel). Potentially, these amphiphilic macromolecule based microspheres with cluster formation ability could be utilized for reliable embolization and blood supply blockage.

COMPOSITE MICROBEADS MADE OF MAGNETIC NANOPARTICLES AND POLYMER MATRIX

It was also worth mentioning that the materials or polymeric basis of artery embolization agents were important, but it was not

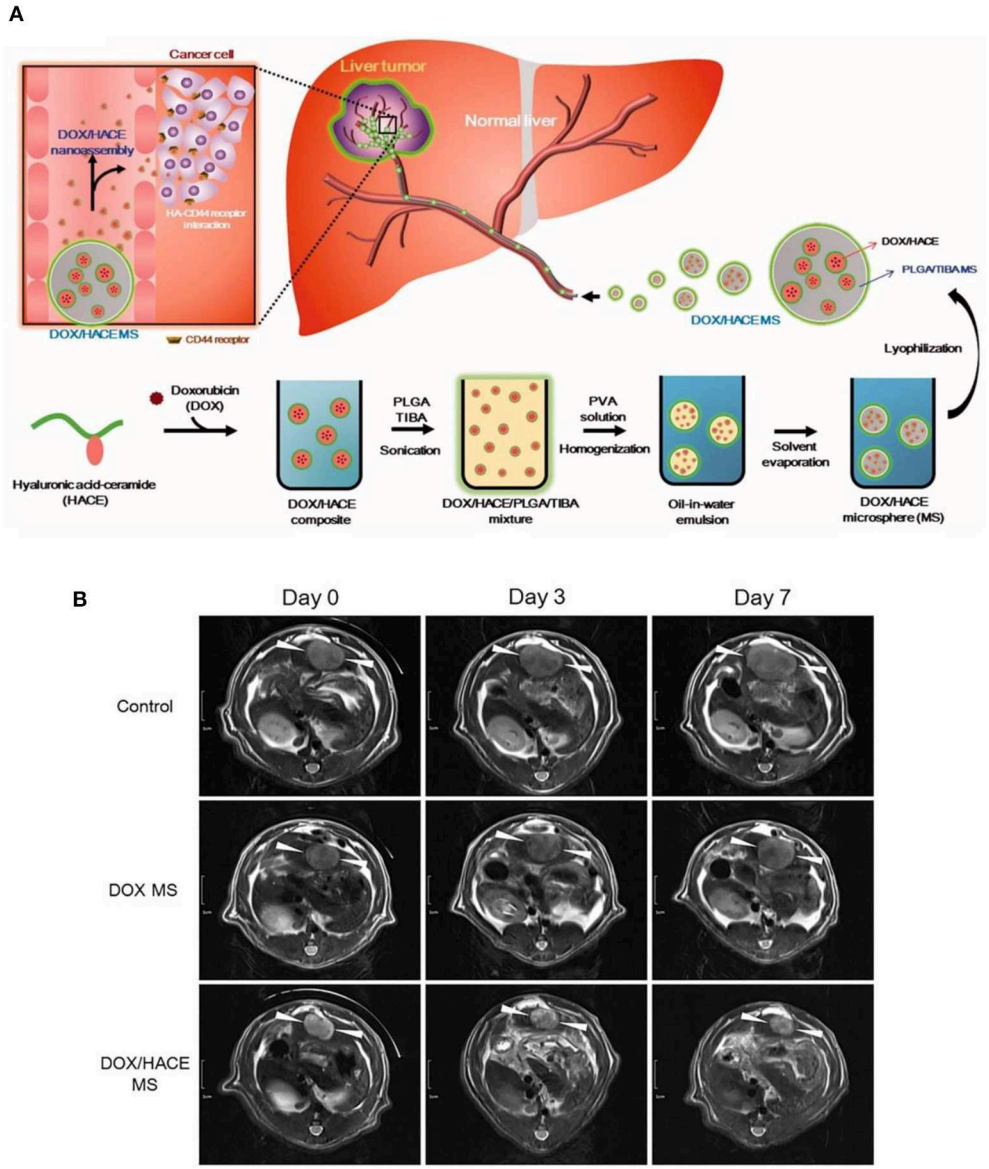

FIGURE 2 | (A) Schematic illustration of tumor targeting HACE modified DOX/PLGA microsphere fabrication and treatment process as TACE reagent. **(B)** DOX/HACE MS (HACE modified DOX/PLGA microsphere) treatment could significantly decrease tumor size in McA-RH7777 tumor-implanted rat model, in comparison with control or DOX MS (DOX/PLGA microsphere) treatments. The tumor was recorded by magnetic resonance imaging. Scale bar is 1 cm. [Reproduced with permission from Lee et al. (2018), Copyright 2018 Taylor & Francis].

the only criteria for embolization design. For example, the size, homogeneity, and specific delivery of microbeads also served as key factors affecting the artery embolization efficiency. Typically, microspheres with size of 40–100 μm were suitable for hepatic artery end branch blockage; microspheres with a size of around 300 μm were utilized for tumor proximal vascular occlusion; while microspheres with size of 500–900 μm were applied for uterine arteries blockage for fibroid treatments; indicating that the size of embolization agents depended on the diameter of the target vessel (Maluccio et al., 2008). Furthermore, particles with undesired homogeneity might attribute to end organ damage or un-predictable distribution of microspheres, indicating the importance of controling the narrow size distribution or geometry of embolization agents (Stampfl et al., 2007). Last but not least, non-specific distribution of embolization agents after intra-arterial injection might induce undesired damage of healthy tissue (Hagit et al., 2010; Pouponneau et al., 2014).

In order to overcome this problem, Nosrati et al. (2018) embedded magnetic iron oxide nanoparticles in a poly(lactic-*co*-glycolic acid) (PLGA) microsphere matrix using droplet microfluidics technology (as shown in **Figure 4A**), to

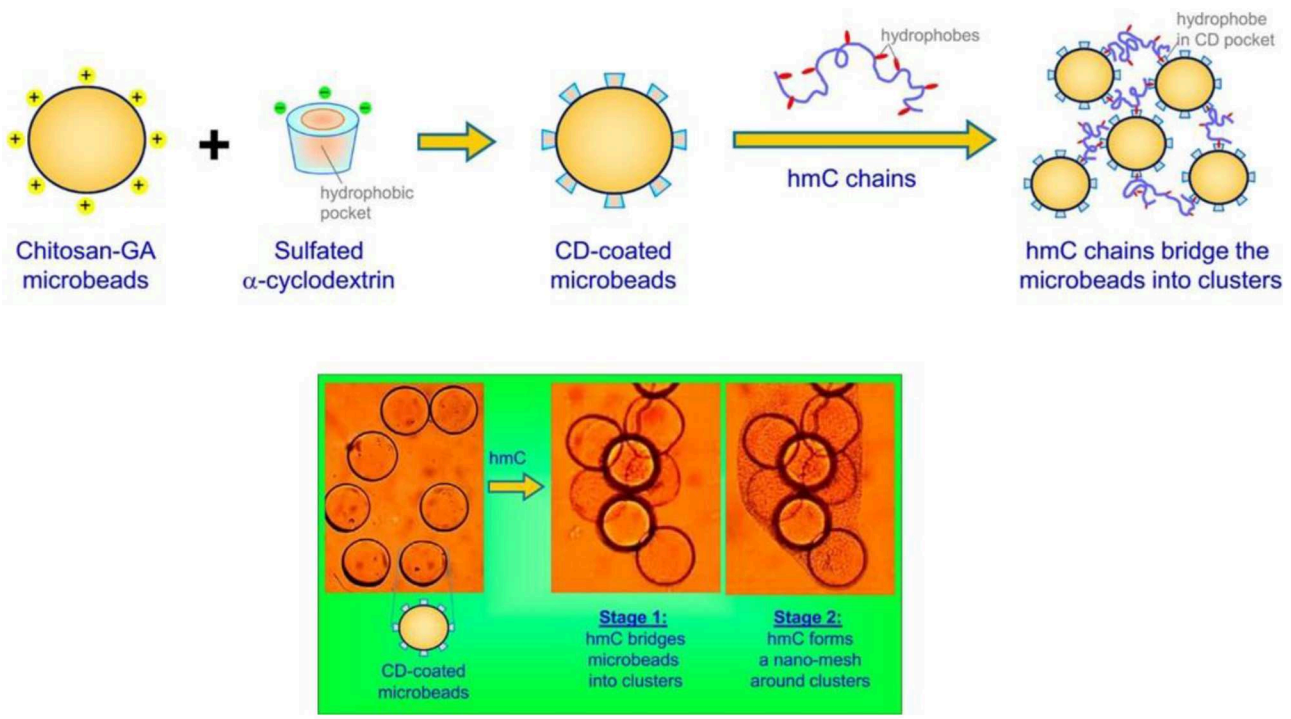

FIGURE 3 | Schematic illustration of using amphiphilic hydrophobically modified chitosan (hmC) as cross-linking reagents for chitosan-glutaraldehyde (chitosan-GA) microbeads with surfaced modification of sulfated α-cyclodextrin (α-CD), as well as the self-assembly between hydrophobic chain of hmC and α-CD cavity, which could lead to formation of polymeric mesh outside microbeads for clotting applications. [Reproduced with permission from Arya et al. (2017), Copyright 2017 American Chemical Society].

fabricate homogeneous magnetic microbeads in a size range of 130–700 μm (as shown in **Figure 4B**). This gave potential to precisely monitor and control the accumulation of microbeads at disease vessel sites. Similarly, Liang et al. (2017) fabricated PLGA based magnetic microspheres (PLGA-MMs) by emulsion of PLGA polymer matrix and iron oxide nanoparticles. More interestingly, upon exposure to alternating magnetic field, these PLGA-MMs could not only act as embolization agents to block the blood supply in the VX2 liver tumor model of rabbit, but could also elevate the synergetic local temperature for magnetic ablation of liver tumors, as shown in **Figure 4C**. Last but not least, Hagit et al. (2010) synthesized composite microparticles using the copolymerization of hydrophobic 2-methacryloyloxyethyl (2,3,5-triiodobenzoate) (MAOETIB) and hydrophilic glycidyl methacrylate (GMA) as a core and a γ-Fe_2O_3 thin layer for shell coating, which were successfully explored as magnetic resonance imaging (MRI) as well as computed tomography (CT) contrast reagents to visualize the embolization procedure in a real-time pace. In short, composite microbeads, made of magnetic nanoparticles and polymeric matrix microspheres, demonstrated great advantages for targeted accumulation of embolization microbeads, thus might induce more desirable tumor ablation effects upon application of alternating magnetic field.

POLYMER BASED HYDROGELS AS TACE REAGENTS

Due to the size limitation, microspheres or DEB were not suitable for large aneurysms, indicating the importance of developing more flexible embolic reagents. As a potential candidate, injectable polymeric hydrogel, with the ability to retain liquid status before injection but to form a solid hydrogel at the desired disease site, was favored and successfully applied to treat hemorrhage, cerebral aneurysms, or used as vessel sealants. For example, Golzarian's group had developed an *in situ* forming porous chemical crosslinking hydrogel made of carboxylmethyl chitosan and cellulose, with biocompatibility to endothelial cells, hemocompatibility, and bio-degradability in lysozyme solution (Weng et al., 2013). More importantly, the hydrogel precursor solution was injected, via a 5-F catheter, into an aneurysm sac and it successfully formed the solid hydrogel to fill the sac site and to prevent endoleakage. Further microcatheter injection of this hydrogel into rabbit kidney induced immediate renal artery occlusion and less injection volume in comparison with bead formulation (1–2 mL hydrogel vs. 5.5–7 mL microsphere), indicating the advantage of using hydrogels as embolization agents.

Besides to chemical crosslinking hydrogel, physical crosslinking hydrogels with stimulus responsive phase changes

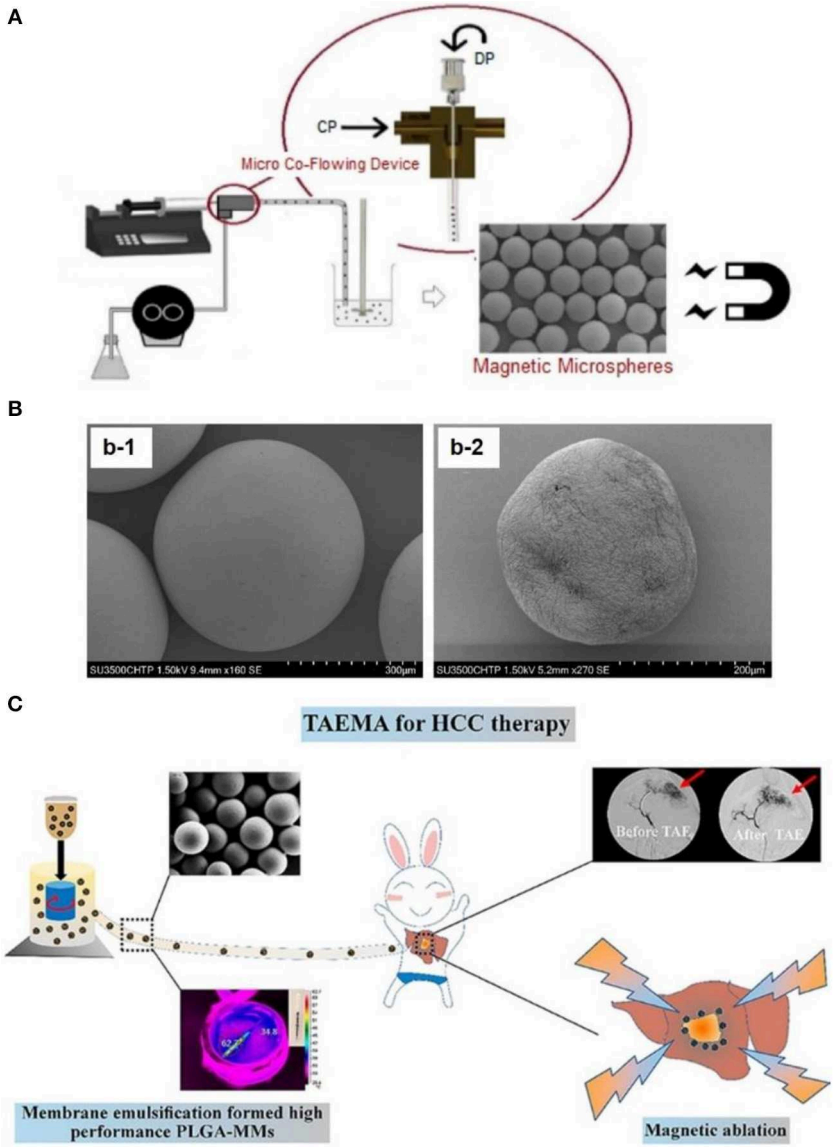

FIGURE 4 | (A) Schematic illustration of fabricating magnetic microbeads by using micro-fluid technique, to fabricate magnetic nanoparticle embedded PLGA microparticles. **(B)** Scanning electron microscopy observation of magnetic microparticles embedding (b-1) 50 wt% magnetic iron oxide nanoparticles and (b-2) 60 wt% magnetic iron oxide nanoparticles. [Reproduced with permission from Nosrati et al. (2018), Copyright 2018 American Chemical Society]. **(C)** Fabrication of magnetic PLGA-MMs (PLGA-magnetic microspheres) by emulsion of PLGA polymer and iron oxide magnetic nanoparticles, which was utilized as liver arterial embolization agent in VX2 liver tumor of rabbit. PLGA-MMs could block the local blood supply and induce local temperature increase upon exposure to alternating magnetic field, which could cause synergetic magnetic ablation of tumor. [Reproduced with permission from Liang et al. (2017), Copyright 2017 American Chemical Society].

were also popular design as TACE reagents. As a typical example, Nguyen et al. (2016) synthesized an amphiphilic anionic PCLA-PUSSM copolymer made of poly(ethylene glycol) (PEG), poly(ε-caprolactone-*co*-lactide) (PCLA), and poly(urethane sulfide sulfamethazine) (PUSSM), as illustrated in **Figure 5A**. The PCLA-PUSSM copolymer solution remained liquid status at pH 8.5 and experienced fast phase change and solid status hydrogel formation upon pH decrease. By taking this unique pH responsive phase change process, this PCL-PUSSM hydrogel could be intra-arterially injected into hepatic tumor of VX2 rabbit model, and achieved embolization as well as controllable release of embedded DOX in a sustainable manner, as shown in **Figure 5B**. Animal model evaluation revealed that this PCLA-PUSSM hydrogel could effectively perform the chemoembolization effect and release DOX in a sustained manner to inhibit the tumor growth, as shown in **Figure 5C**.

Similarly, Lym et al. (2016) designed a pH-responsive PCL-PEG-SM copolymer by free radical polymerization of PEG, poly(ε-caprolactone) (PCL), and sulfamethazine (SM). More interestingly, the aqueous solution of PCL-PEG-SM copolymer

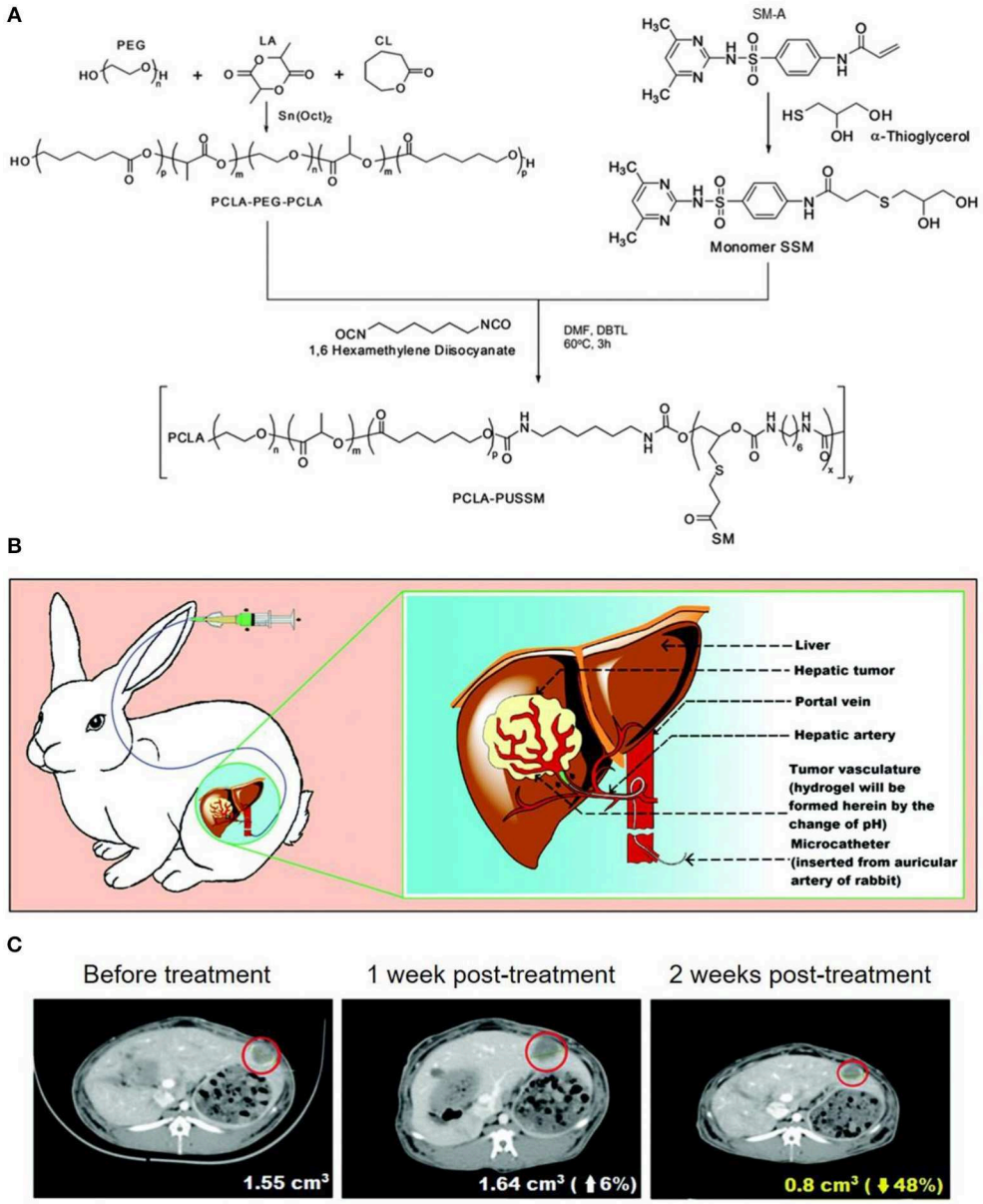

FIGURE 5 | (A) Synthesis of amphiphilic anionic PCLA-PUSSM copolymer with pH-dependent hydrogel formation ability. **(B)** Illustration for the microcatheter mediated intraarterial injection of PCLA-PUSSM hydrogel in rabbit HCC model. **(C)** CT observations revealed the shrinkage of tumor size when using PCLA-PUSSM hydrogel as TACE agent. [Reproduced with permission from Nguyen et al. (2016), Copyright 2016 Royal Society of Chemistry].

experienced a sol-to-gel transition from pH 8.0 to pH 7.4 at 37°C, and could achieve a sustained release of DOX for up to 4 weeks. It was also worth mentioning that the embolic formulation of PCL-PEG-SM copolymer solution at pH 8.0 could be intra-arterially administrated in rabbit VX2 liver tumor model.

In short, injectable hydrogel with environment responsive ability had been successfully applied in TACE procedure for hepatocellular cancer (HCC) treatment in an animal model, and it exhibited the ability to stably maintain high drug concentration at the tumor site. Hence, the design of biocompatible and biodegradable polymeric hydrogels might serve as a practical TACE agents, which could be further combined with a wide spectrum of chemotherapeutics or X-ray contrast agents to show improved performance compared to traditional Lipiodol® or Gelfoam® formulation.

CONCLUSIONS AND PERSPECTIVES

In conclusion, this review showed the recent progress of polymeric TACE agents, in terms of polymeric beads or microparticles, polymeric meshes by crosslinking beads,

polymeric hydrogels, with great potential for treating patients with unresectable HCC. More importantly, the design of these polymeric TAC agents, especially polymer backbone materials, degradability, size, or geometry, was important for safe and efficient tumor blood supply blockage, as well as localized and sustained release of chemotherapeutics to achieve better liver cancer therapy.

It was also worth mentioning that, in addition to the above mentioned formulations of microbeads or microspheres, cross-linked microspheres, and hydrogels, Lipiodol oil embedded PEO-PPO-PEO/PEG (poly(ethylene oxide)-poly(propylene oxide)-poly(ethylene oxide)/poly(ethylene glycol) composite capsules containing paclitaxel (PTX) (Bae et al., 2007), poly(ethylene glycol) PEG liposomes containing 5-fluorouracil

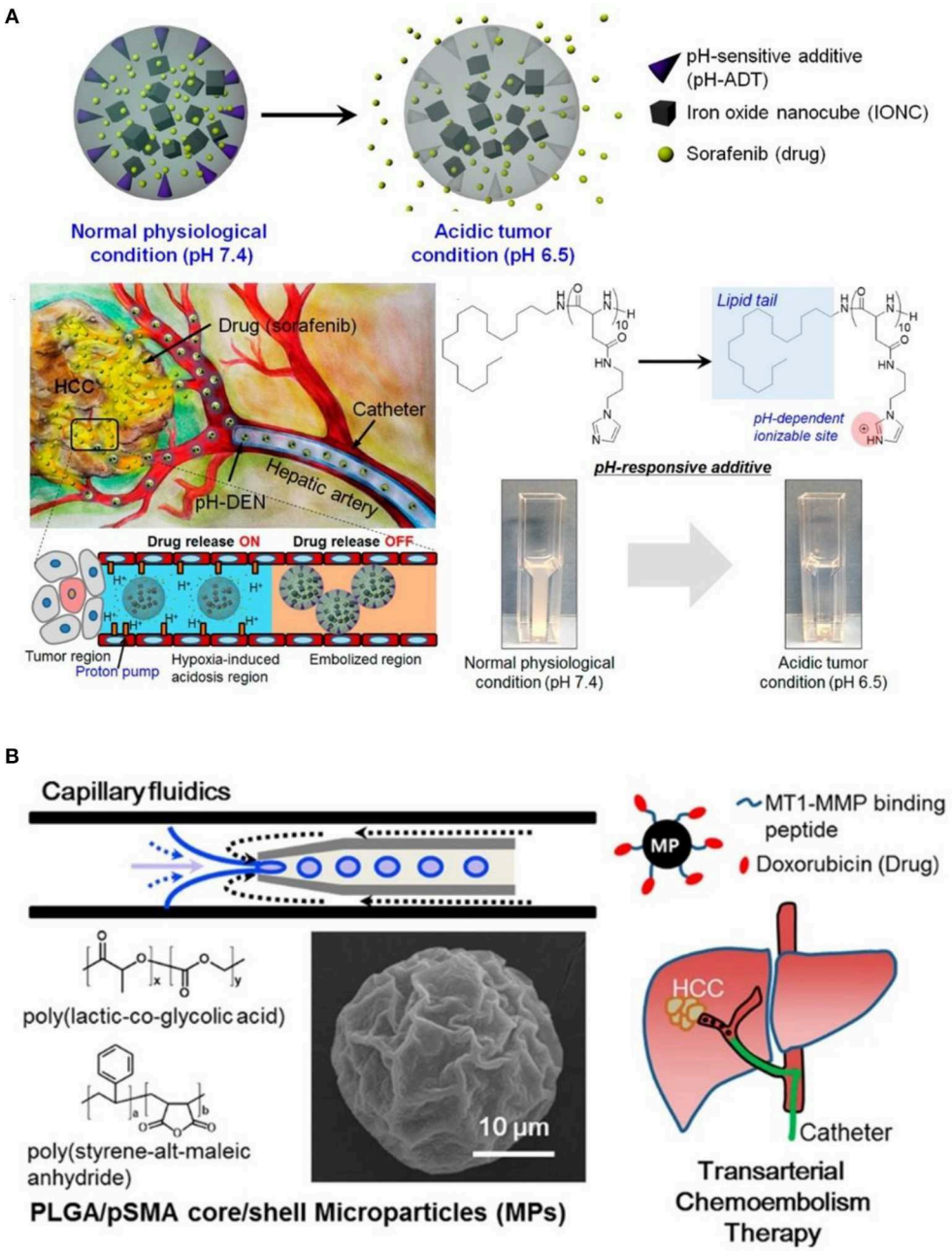

FIGURE 6 | (A) Illustration of environment sensitive drug-eluting composite particles, as well as their low pH responsive chemotherapeutics release in hepatic vessels. [Reproduced with permission from Park et al. (2016), Copyright 2016 American Chemical Society]. **(B)** Synthesis of tumor targeting PLGA/pSMA microspheres with conjugation of MT1-MMP binding peptide and chemotherapeutic doxorubicin, for more precise transarterial chemoembolism therapy. [Reproduced with permission from Davaa et al. (2017), Copyright 2017 American Chemical Society].

(5-FU) (Pohlen et al., 2011), methoxy-poly (ethylene glycol)-*block*-poly(ε-caprolactone) (mPEG-*b*-PCL) micelles carrying doxorubicin (DOX), as well as radio-active rhenium-188 for combined radiotherapy and chemotherapy, were also actively applied for hepatic artery embolization and cancer therapy (Shih et al., 2015). This demonstrates the wide applications of polymeric materials for TACE applications. Furthermore, besides to polymeric embolization agents, injectable precursor of polar lipid phytantriol at cubic liquid crystalline phase (Han et al., 2010), and drug eluting composite containing pH sensitive lipid-peptides conjugation (octadecylamine–poly (API-$_L$-Asp)$_{10}$) as shown in **Figure 6A** (Park et al., 2016), could also be designed for vascular embolization, and to achieve localized drug sustained release. This could also be further combined with polymeric embolization agents for enhanced therapeutic effect. Last but not least, functional peptide could also be conjugated to polymeric microparticles for targeted delivery of embolization beads. As a typical example, Davaa et al. (2017) linked matrix metalloproteinase responsive peptide (MT1-MMP binding peptide) to poly(lactic-*co*-glycolic acid/poly-(styrene-alt-maleic anhydride) (PLGA/pSMA) microspheres, which exhibited enhanced accumulation in MT1-MMP overexpressing Hep3B cells, as shown in **Figure 6B**. More interestingly, these peptide conjugated microspheres could accumulate in hepatic vessels for up to 24 h without undesired diffusion to lung, and they significantly inhibited the tumor growth in a Hep3B xenografted mice model. Hence, we can expect great potential for the design of functional polymeric materials with nationally designed stimulus-responsive crosslinking segments or biodegradable groups, for embolizing tumor blood supply in a fast and controllable manner, as well as ensuring biodegradability in order to be safely removed after use. This might significantly broaden the choice of TACE agents for more successful and precise HCC therapy.

AUTHOR CONTRIBUTIONS

Y-LW and Y-PC initiated the project. Y-PC, J-LZ, YZ, and Y-LW searched the data base, wrote, and finalized the manuscript.

FUNDING

This project is supported by the National Natural Science Foundation of China (81773661), and the Fundamental Research Funds for the Central Universities (20720170066).

REFERENCES

Aliberti, C., Carandina, R., Lonardi, S., Dadduzio, V., Vitale, A., Gringeri, E., et al. (2017). Transarterial chemoembolization with small drug-eluting beads in patients with hepatocellular carcinoma: experience from a cohort of 421 patients at an Italian center. *J. Vasc. Interv. Radiol.* 28, 1495–1502. doi: 10.1016/j.jvir.2017.07.020

Arya, C., Saez Cabesas, C. A., Huang, H., and Raghavan, S. R. (2017). Clustering of cyclodextrin-functionalized microbeads by an amphiphilic biopolymer: real-time observation of structures resembling blood clots. *ACS Appl. Mater. Interfaces* 9, 37238–37245. doi: 10.1021/acsami.7b05435

Bae, K. H., Lee, Y., and Park, T. G. (2007). Oil-encapsulating PEO-PPO-PEO/PEG shell cross-linked nanocapsules for target-specific delivery of paclitaxel. *Biomacromolecules* 8, 650–656. doi: 10.1021/bm0608939

Burrel, M., Reig, M., Forner, A., Barrufet, M., de Lope, C. R., Tremosini, S., et al. (2012). Survival of Patients with hepatocellular carcinoma treated by transarterial chemoembolisation (TACE) using drug eluting beads: implications for clinical practice and trial design. *J. Hepatol.* 56, 1330–1335. doi: 10.1016/j.jhep.2012.01.008

Cai, P., Leow, W. R., Wang, X., Wu, Y.-L., and Chen, X. (2017). Programmable nano–bio interfaces for functional biointegrated devices. *Adv. Mater.* 29:1605529. doi: 10.1002/adma.201605529

Cai, P., Zhang, X., Wang, M., Wu, Y.-L., and Chen, X. (2018). Combinatorial nano-bio interfaces. *ACS Nano* 12, 5078–5084. doi: 10.1021/acsnano.8b03285

Chan, B., Cheng, H., Liow, S., Dou, Q., Wu, Y.-L., Loh, X., et al. (2018). Poly(carbonate urethane)-based thermogels with enhanced drug release efficacy for chemotherapeutic applications. *Polymers* 10:89. doi: 10.3390/polym10010089

Chen, X., Chen, Z., Hu, B., Cai, P., Wang, S., Xiao, S., et al. (2018). Synergistic lysosomal activatable polymeric nanoprobe encapsulating pH sensitive imidazole derivative for tumor diagnosis. *Small* 14:1703164. doi: 10.1002/smll.201703164

Chen, X., Qiu, Y.-K., Owh, C., Loh, X. J., and Wu, Y.-L. (2016). Supramolecular cyclodextrin nanocarriers for chemo- and gene therapy towards the effective treatment of drug resistant cancers. *Nanoscale* 8, 18876–18881. doi: 10.1039/C6NR08055C

Cheng, H., Fan, X., Wang, X., Ye, E., Loh, X. J., Li, Z., et al. (2018a). Hierarchically self-assembled supramolecular host-guest delivery system for drug resistant cancer therapy. *Biomacromolecules* 19, 1926–1938. doi: 10.1021/acs.biomac.7b01693

Cheng, H., Fan, X., Wu, C., Wang, X., Wang, L.-J., Loh, X. J., et al. (2019). Cyclodextrin-based star-like amphiphilic cationic polymer as a potential pharmaceutical carrier in macrophages. *Macromol. Rapid Comm.* 40:1800207. doi: 10.1002/marc.201800207

Cheng, H., Wu, Z., Wu, C., Wang, X., Liow, S. S., Li, Z., et al. (2018b). Overcoming STC2 mediated drug resistance through drug and gene co-delivery by PHB-PDMAEMA cationic polyester in liver cancer cells. *Mater. Sci. Eng. C* 83, 210–217. doi: 10.1016/j.msec.2017.08.075

Choi, J. W., Park, J. H., Baek, S. Y., Kim, D. D., Kim, H. C., and Cho, H. J. (2015). Doxorubicin-loaded poly(lactic-co-glycolic acid) microspheres prepared using the solid-in-oil-in-water method for the transarterial chemoembolization of a liver tumor. *Colloids Surf. B* 132, 305–312. doi: 10.1016/j.colsurfb.2015.05.037

Davaa, E., Lee, J. H., Jenjob, R., and Yang, S. G. (2017). MT1-MMP responsive doxorubicin conjugated poly(lactic-*co*-glycolic acid)/poly(styrene-alt-maleic anhydride) core/shell microparticles for intrahepatic arterial chemotherapy of hepatic cancer. *ACS Appl. Mater. Interfaces* 9, 71–79. doi: 10.1021/acsami.6b08994

Ding, C., and Li, Z. (2017). A review of drug release mechanisms from nanocarrier systems. *Mater. Sci. Eng. C* 76, 1440–1453. doi: 10.1016/j.msec.2017.03.130

Fan, X., Cheng, H., Wang, X., Ye, E., Xian, J. L., Wu, Y. L., et al. (2017a). Thermoresponsive supramolecular chemotherapy by "V"-shaped armed β-cyclodextrin star polymer to overcome drug resistance. *Adv. Healthc. Mater.* 7:1701143. doi: 10.1002/adhm.201701143

Fan, X., Wang, X., Cao, M., Wang, C., Hu, Z., Wu, Y.-L., et al. (2017b). "Y"-shape armed amphiphilic star-like copolymers: design, synthesis and dual-responsive unimolecular micelle formation for controlled drug delivery. *Polym. Chem.* 8, 5611–5620. doi: 10.1039/C7PY00999B

Gao, Y., Xu, H. J., and Cheng, Q. F. (2018). Multiple synergistic toughening graphene nanocomposites through cadmium ions and cellulose nanocrystals. *Adv. Mater. Interfaces* 5:1800145. doi: 10.1002/admi.201800145

Gupta, S., Wright, K. C., Ensor, J., Van Pelt, C. S., Dixon, K. A., and Kundra, V. (2011). Hepatic arterial embolization with doxorubicin-loaded superabsorbent

polymer microspheres in a rabbit liver tumor model. *Cardiovasc. Interv. Radiol.* 34, 1021–1030. doi: 10.1007/s00270-011-0154-6

Hagit, A., Soenke, B., Johannes, B., and Shlomo, M. (2010). Synthesis and characterization of dual modality (CT/MRI) core-shell microparticles for embolization purposes. *Biomacromolecules* 11, 1600–1607. doi: 10.1021/bm100251s

Han, K., Pan, X., Chen, M. W., Wang, R. C., Xu, Y. H., Feng, M., et al. (2010). Phytantriol-based inverted type bicontinuous cubic phase for vascular embolization and drug sustained release. *Eur. J. Pharm. Sci.* 41, 692–699. doi: 10.1016/j.ejps.2010.09.012

Hidaka, K., Moine, L., Collin, G., Labarre, D., Grossiord, J. L., Huang, N., et al. (2011). Elasticity and viscoelasticity of embolization microspheres. *J. Mech. Behav. Biomed. Mater.* 4, 2161–2167. doi: 10.1016/j.jmbbm.2011.08.001

Hu, B., Leow, W. R., Amini, S., Nai, B., Zhang, X., Liu, Z., et al. (2017a). Orientational coupling locally orchestrates a cell migration pattern for re-epithelialization. *Adv. Mater.* 29:1700145. doi: 10.1002/adma.201700145

Hu, B., Leow, W. R., Cai, P., Li, Y. Q., Wu, Y. L., and Chen, X. (2017b). Nanomechanical force mapping of restricted cell-to-cell collisions oscillating between contraction and relaxation. *ACS Nano* 11, 12302–12310. doi: 10.1021/acsnano.7b06063

Hyun, D., Cho, S. K., Shin, S. W., Park, K. B., Lee, S. Y., Park, H. S., et al. (2018). Combined transarterial chemoembolization and radiofrequency ablation for small treatment-naive hepatocellular carcinoma infeasible for ultrasound-guided radiofrequency ablation: long-term outcomes. *Acta Radiol.* 59, 773–781. doi: 10.1177/0284185117735349

Javanbakht, S., and Namazi, H. (2018). Doxorubicin loaded carboxymethyl cellulose/graphene quantum dot nanocomposite hydrogel films as a potential anticancer drug delivery system. *Mater. Sci. Eng. C* 87, 50–59. doi: 10.1016/j.msec.2018.02.010

Lee, S. Y., Choi, J. W., Lee, J. Y., Kim, D. D., Kim, H. C., and Cho, H. J. (2018). Hyaluronic acid/doxorubicin nanoassembly-releasing microspheres for the transarterial chemoembolization of a liver tumor. *Drug Deliv.* 25, 1472–1483. doi: 10.1080/10717544.2018.1480673

Li, Z., Liu, X., Chen, X., Chua, M. X., and Wu, Y.-L. (2017). Targeted delivery of Bcl-2 conversion gene by MPEG-PCL-PEI-FA cationic copolymer to combat therapeutic resistant cancer. *Mater. Sci. Eng. C* 76, 66–72. doi: 10.1016/j.msec.2017.02.163

Li, Z., and Loh, X. J. (2017). Recent advances of using polyhydroxyalkanoate-based nanovehicles as therapeutic delivery carriers. *Wiley Interdiscip. Rev. Nanomed. Nanobiotechnol.* 9:e1429. doi: 10.1002/wnan.1429

Liang, Y. J., Yu, H., Feng, G. D., Zhuang, L. L., Xi, W., Ma, M., et al. (2017). High-performance poly(lactic-*co*-glycolic acid)-magnetic microspheres prepared by rotating membrane emulsification for transcatheter arterial embolization and magnetic ablation in VX2 liver tumors. *ACS Appl. Mater. Interfaces* 9, 43478–43489. doi: 10.1021/acsami.7b14330

Liu, X., Chen, X., Chua, M. X., Li, Z., Loh, X. J., and Wu, Y.-L. (2017). Injectable supramolecular hydrogels as delivery agents of Bcl-2 conversion gene for the effective shrinkage of therapeutic resistance tumors. *Adv. Healthc. Mater.* 6:1700159. doi: 10.1002/adhm.201700159

Liu, X., Li, Z., Loh, X. J., Chen, K., Li, Z., and Wu, Y.-L. (2019). Targeted and sustained corelease of chemotherapeutics and gene by injectable supramolecular hydrogel for drug-resistant cancer therapy. *Macromol. Rapid Comm.* 40:1800117. doi: 10.1002/marc.201800117

Louguet, S., Verret, V., Bedouet, L., Servais, E., Pascale, F., Wassef, M., et al. (2014). Poly(ethylene glycol) methacrylate hydrolyzable microspheres for transient vascular embolization. *Acta Biomater.* 10, 1194–1205. doi: 10.1016/j.actbio.2013.11.028

Luo, Z., Jiang, L., Ding, C. Z., Hu, B. H., Loh, X. J., Li, Z. B., et al. (2018). Surfactant free delivery of docetaxel by poly[(R)-3-hydroxybutyrate-(R)-3-hydroxyhexanoate]-based polymeric micelles for effective melanoma treatments. *Adv. Healthc. Mater.* 7:1801221. doi: 10.1002/adhm.201801221

Luo, Z., Xu, Y., Ye, E., Li, Z., and Wu, Y.-L. (2019). Recent progress in macromolecule-anchored hybrid gold nanomaterials for biomedical applications. *Macromol. Rapid Comm.* 40:1800029. doi: 10.1002/marc.201800029

Lym, J. S., Nguyen, Q. V., Ahn, D. W., Huynh, C. T., Jae, H. J., Kim, Y. I., et al. (2016). Sulfamethazine-based pH-sensitive hydrogels with potential application for transcatheter arterial chemoembolization therapy. *Acta Biomater.* 41, 253–263. doi: 10.1016/j.actbio.2016.05.018

Maluccio, M. A., Covey, A. M., Ben Porat, L., Schubert, J., Brody, L. A., Sofocleous, C. T., et al. (2008). Transcatheter arterial embolization with only particles for the treatment of unresectable hepatocellular carcinoma. *J. Vasc. Interv. Radiol.* 19, 862–869. doi: 10.1016/j.jvir.2008.02.013

Morimoto, M., Kobayashi, S., Moriya, S., Ueno, M., Tezuka, S., Irie, K., et al. (2017). Short-term efficacy of transarterial chemoembolization with epirubicin-loaded superabsorbent polymer microspheres for hepatocellular carcinoma: comparison with conventional transarterial chemoembolization. *Abdom. Radiol.* 42, 612–619. doi: 10.1007/s00261-016-0900-y

Nguyen, Q. V., Lym, J. S., Huynh, C. T., Kim, B. S., Jae, H. J., Kim, Y. I., et al. (2016). A novel sulfamethazine-based pH-sensitive copolymer for injectable radiopaque embolic hydrogels with potential application in hepatocellular carcinoma therapy. *Polym. Chem.* 7, 5805–5818. doi: 10.1039/c6py01141a

Nosrati, Z., Li, N., Michaud, F., Ranamukhaarachchi, S., Karagiozov, S., Soulez, G., et al. (2018). Development of a coflowing device for the size-controlled preparation of magnetic-polymeric microspheres as embolization agents in magnetic resonance navigation technology. *ACS Biomater. Sci. Eng.* 4, 1092–1102. doi: 10.1021/acsbiomaterials.7b00839

Owen, R. J., Nation, P. N., Polakowski, R., Biliske, J. A., Tiege, P. B., and Griffith, I. J. (2012). A preclinical study of the safety and efficacy of occlusin (TM) 500 artificial embolization device in sheep. *Cardiovasc. Interv. Radiol.* 35, 636–644. doi: 10.1007/s00270-011-0218-7

Park, W., Chen, J., Cho, S., Park, S. J., Larson, A. C., Na, K., et al. (2016). Acidic pH-triggered drug-eluting nanocomposites for magnetic resonance imaging-monitored intra-arterial drug delivery to hepatocellular carcinoma. *ACS Appl. Mater. Interfaces* 8, 12711–12719. doi: 10.1021/acsami.6b03505

Pohlen, U., Reszka, R., Buhr, H. J., and Berger, G. (2011). Hepatic arterial infusion in the treatment of liver metastases with PEG liposomes in combination with degradable starch microspheres (DSM) increases tumor 5-FU concentration. An animal study in CC-531 liver tumor-bearing rats. *Anticancer Res.* 31, 147–152. doi: 10.1288/00005537-198504000-00018

Pouponneau, P., Bringout, G., and Martel, S. (2014). Therapeutic magnetic microcarriers guided by magnetic resonance navigation for enhanced liver chemoembilization: a design review. *Ann. Biomed. Eng.* 42, 929–939. doi: 10.1007/s10439-014-0972-1

Schwartz, M., and Weintraub, J. (2008). Combined transarterial chemoembolization and radiofrequency ablation for hepatocellular carcinoma. *Nat. Clin. Pract. Oncol.* 5, 630–631. doi: 10.1038/ncponc1216

Seki, A., Hori, S., Kobayashi, K., and Narumiya, S. (2011). Transcatheter arterial chemoembolization with epirubicin-loaded superabsorbent polymer microspheres for 135 hepatocellular carcinoma patients: single-center experience. *Cardiovasc. Interv. Radiol.* 34, 557–565. doi: 10.1007/s00270-010-9975-y

Shih, Y. H., Peng, C. L., Chiang, P. F., Lin, W. J., Luo, T. Y., and Shieh, M. J. (2015). Therapeutic and scintigraphic applications of polymeric micelles: combination of chemotherapy and radiotherapy in hepatocellular carcinoma. *Int. J. Nanomed.* 10, 7443–7454. doi: 10.2147/Ijn.S91008

Stampfl, S., Stampfl, U., Rehnitz, C., Schnabel, P., Satzl, S., Christoph, P., et al. (2007). Experimental evaluation of early and long-term effects of microparticle embolization in two different mini-pig models. Part II: Liver. *Cardiovasc. Interv. Radiol.* 30, 462–468. doi: 10.1007/s00270-005-0350-3

Tsurusaki, M., and Murakami, T. (2015). Surgical and locoregional therapy of HCC: TACE. *Liver Cancer* 4, 165–175. doi: 10.1159/000367739

Varela, M., Real, M. I., Burrel, M., Forner, A., Sala, M., Brunet, M., et al. (2007). Chemoembolization of hepatocellular carcinoma with drug eluting beads: efficacy and doxorubicin pharmacokinetics. *J. Hepatol.* 46, 474–481. doi: 10.1016/j.jhep.2006.10.020

Weng, L., Le, H. C., Lin, J., and Golzarian, J. (2011). Doxorubicin loading and eluting characteristics of bioresorbable hydrogel microspheres: *in vitro* study. *Int. J. Pharm.* 409, 185–193. doi: 10.1016/j.ijpharm.2011.02.058

Weng, L., Rostambeigi, N., Zantek, N. D., Rostamzadeh, P., Bravo, M., Carey, J., et al. (2013). An *in situ* forming biodegradable hydrogel-based embolic agent for interventional therapies. *Acta Biomater.* 9, 8182–8191. doi: 10.1016/j.actbio.2013.06.020

Wu, Y.-L., Engl, W., Hu, B., Cai, P., Leow, W. R., Tan, N. S., et al. (2017). Nanomechanically visualizing drug–cell interaction at the early stage of chemotherapy. *ACS Nano* 11, 6996–7005. doi: 10.1021/acsnano.7b02376

Xiang, Y., Oo, N. N. L., Lee, J. P., Li, Z., and Loh, X. J. (2017). Recent development of synthetic nonviral systems for sustained gene delivery. *Drug Discovery Today* 22, 1318–1335. doi: 10.1016/j.drudis.2017.04.001

Xu, C., Wu, Y.-L., Li, Z., and Loh, X. J. (2019). Cyclodextrin-based sustained gene release systems: a supramolecular solution towards clinical applications. *Mater. Chem. Front.* 3, 181–192. doi: 10.1039/C8QM00570B

Yamada, R., Sato, M., Kawabata, M., Nakatsuka, H., Nakamura, K., and Takashima, S. (1983). Hepatic artery embolization in 120 patients with unresectable hepatoma. *Radiology* 148, 397–401. doi: 10.1148/radiology.148.2.630672

Yamasaki, T., Saeki, I., Harima, Y., Zaitsu, J., Maeda, M., Tanimoto, H., et al. (2012). Effect of transcatheter arterial infusion chemotherapy using iodized oil and degradable starch microspheres for hepatocellular carcinoma. *J. Gastroenterol.* 47, 715–722. doi: 10.1007/s00535-012-0537-8

Yang, D. P., Oo, M., Deen, G. R., Li, Z., and Loh, X. J. (2017). Nano-star-shaped polymers for drug delivery applications. *Macromol. Rapid Comm.* 38:1700410. doi: 10.1002/marc.201700410

Zheng, C., Gao, H., Yang, D.-P., Liu, M., Cheng, H., Wu, Y.-L., et al. (2017). PCL-based thermo-gelling polymers for *in vivo* delivery of chemotherapeutics to tumors. *Mater. Sci. Eng. C* 74, 110–116. doi: 10.1016/j.msec.2017.02.005

Conflict of Interest Statement: The authors declare that the research was conducted in the absence of any commercial or financial relationships that could be construed as a potential conflict of interest.

frontiers in Chemistry

ORIGINAL RESEARCH
published: 03 July 2019
doi: 10.3389/fchem.2019.00477

An Injectable Hyaluronic Acid-Based Composite Hydrogel by DA Click Chemistry With pH Sensitive Nanoparticle for Biomedical Application

Xiaohong Hu[1*†], *Ziyu Gao*[1†], *Huaping Tan*[2], *Huiming Wang*[1], *Xincheng Mao*[1] and *Juan Pang*[1]

[1] School of Material Engineering, Jinling Institute of Technology, Nanjing, China, [2] Biomaterials for Organogenesis Laboratory, School of Materials Science and Engineering, Nanjing University of Science and Technology, Nanjing, China

Hydrogels with multifunctional properties attracted intensively attention in the field of tissue engineering because of their excellent performance. Also, object-oriented design had been supposed to an effective and efficient method for material design as cell scaffold in the field of tissue engineering. Therefore, a scaffold-oriented injectable composite hydrogel was constructed by two components. One was pH-sensitive bifunctional nanoparticles for growth factor delivery to improve biofunctionability of hydrogel scaffold. The other was Diels-alder click crosslinked hyaluronic acid hydrogel as matrix. pH dependent release behavior of nanoparticle component was confirmed by results. And, its bioactivity was verified by *in vitro* cell culture evaluation. In consideration of high-efficiency and effectiveness, low toxicity, controllability and reversibility, dynamic covalent and reversible Diels-alder click chemistry was used to design a HA hydrogel with two kinds of crosslinking points. The properties of hydrogel like gelation time and swelling ratio were influenced by pH value and polymer concentration. Composite hydrogel was formed by *in situ* polymerization, which exhibited acceptable mechanical property as a scaffold for biomedical field. Lastly, *in vitro* evaluation from results of viability, DNA content and cell morphology confirmed that hydrogels could maintain cell activity and support cell growth. Compared with pure hydrogel, composite hydrogel possessed better properties.

Keywords: hydrogel, Diels-alder click chemistry, pH-sensitive nanoparticle, cell scaffold, growth factor delivery

OPEN ACCESS

Edited by:
Xing Wang,
Institute of Chemistry (CAS), China

Reviewed by:
Qingchen Cao,
Institute of Chemistry (CAS), China
Li Ziyi,
Sun Yat-sen University, China
Yun-Long Wu,
Xiamen University, China

***Correspondence:**
Xiaohong Hu
huxiaohong07@163.com

[†]These authors have contributed equally to this work as co-first authors

Specialty section:
This article was submitted to Polymer Chemistry, a section of the journal Frontiers in Chemistry

Received: *23 April 2019*
Accepted: *20 June 2019*
Published: *03 July 2019*

Citation:
Hu X, Gao Z, Tan H, Wang H, Mao X and Pang J (2019) An Injectable Hyaluronic Acid-Based Composite Hydrogel by DA Click Chemistry With pH Sensitive Nanoparticle for Biomedical Application. Front. Chem. 7:477. doi: 10.3389/fchem.2019.00477

INTRODUCTION

Hydrogel, a water-swollen polymer network, is widely used in fields of biomedical fields due to their physiological-like aqueous environment (Bai et al., 2017; Celie et al., 2019; Massaro et al., 2019; Song et al., 2019; Zhao et al., 2019). Among its applications, scaffold-oriented hydrogel for biomedical application has an extra request of biofunctionability besides general characteristic of low toxicty and aqueous environment (Fu et al., 2012; Yu et al., 2013; Fan et al., 2015; Oh et al., 2016; Williams et al., 2017; Thanusha et al., 2018; Wang C. Z. et al., 2018; Zhu et al., 2018; Celie et al., 2019; Massaro et al., 2019; Song et al., 2019; Zhao et al., 2019). In consideration of natural component of extracellular matrix (ECM), hyaluronic acid (HA), as one of main component of ECM, is an optimal material to fabricate hydrogel for tissue engineering (Yu et al., 2013; Williams et al., 2017; Wang C. Z. et al., 2018; Zhu et al., 2018; Massaro et al., 2019). However, HA itself cannot

form hydrogel naturally in solution due to absence of reactive groups or physical interactions. In early years, chemical crosslinkers were used to form HA hydrogels. But the toxicity of chemical crosslinker cannot satisfy the request of biocompatibility for cell scaffold, especially for that *in situ* formation scaffold. Recently, many efforts had been made to introduce function groups to HA main chain, which can be further crosslinked by their reaction though click chemistry, Michael addition and shift base reaction etc. (Yu et al., 2013; Bai et al., 2017). Although these attempts had been made great progress for HA hydrogel as cell scaffold, they could not be satisfied all requests as scaffold for all kinds of cells. Therefore, HA hydrogels with specific functions for specific cells and environment are also needed. Recently, as for crosslinking reaction, diels-alder clickchemistry has showed favorite characteristics for cell scaffold fabrication due to its low toxicity, high efficiency, moderate reaction condition, and reversible characteristic (Franc et al., 2009; Yu et al., 2013; Bai et al., 2017; Banerjee et al., 2017). Herein, HA hydrogel with self-healing property was designed through Diels-alder click chemistry as a cell scaffold to support cell growth.

Besides scaffold matrix properties, bioactive factors play important roles on cell proliferation and function expression (Akuta et al., 2015; Azevedo et al., 2015; Psarra et al., 2015; Muraoka et al., 2018). However, bioactive protein is liable to loss its function due to the transformation of secondary structure, which was induced by external stimuli. Therefore, one objective of our research is to realize the effective and efficient delivery of growth factor into cells, simultaneously maintaining the bioactivity of growth factor. Since heparin is a verified negative polysaccharide to protect the bioactivity of growth factor, it has been used in a great number of scaffold or carriers for growth factor protection (Psarra et al., 2015; Wu et al., 2015; Song et al., 2018). Another challenge is how to realize the precise delivery to cells. Stimulus from difference between intracellular and extracellular environment including pH value, enzyme, biotin-avidin interaction have been applied to carrier design and preparation for growth factor delivery. In view of mild acid condition of intracellular environment (pH 5.5–6.0), low pH responsive nanoparticle would be considered to be an effective carrier for growth factor delivery. Herein, a dual-structural pH sensitive nanocarrier for growth factor delivery was designed using pH-sensitive acetalated β-cyclodextrin (Ac-β-CD) as main body for pH response property and heparin nanogel as interpenetrating component for growth factor protection. The bioactivity of released growth factor was evaluated by *in vitro* cell behavior indicator like cell viability, DNA content and cell morphology. In the further step, the nanocarrier was incorporated with HA hydrogel to form composite hydrogel as cell scaffold, which was *in vitro* evaluated by 1-week cell growth.

EXPERIMENT

Material

4-(4,6-dimethoxy triazine)-4-methyl morpholine hydrochloride (DMTMM), furylmethylamine, adipicdihydrazide (ADH), maleimide modified PEG (mal-PEG-mal), 2-morpholinoethane sulfonic acid (MES), heparin (HEP), and 3-aminopropyl methacrylate (AMA) were purchased from Aladdin. Dimethyl sulfoxide (DMSO), dichloromethane (DCM), sodium periodate, ammonium persulfate (APS), N,N,N',N'-tetramethylethylenediamine (TEMED), and gelatin were purchased from Shanghai Chemical Industries Co. Ltd (China). Hyaluronate acid (HA, Mw = 1,000 kDa) was obtained from Shandong Furuida Co., China. Trypsin, Dulbecco's modified Eagle's medium (DMEM) and 3-(4, 5-dimethyl) thiazol-2,5-dimethyl tetrazolium bromide (MTT) were obtained from Sigma. Fetal bovine serum (FBS) was purchased from Sijiqing biotech. Co., China. PicoGreen dsDNA Assay Kit was bought from Thermo Fisher Scientific. Ac-β-CD was synthesized previously. All other reagents and solvents were of analytical grade and used as received.

Synthesis and Characterization of Polysaccharide Derivatives

Synthesized processes of polysaccharide derivatives were shown in **Scheme 1**. HEP-AMA and HA-furan were synthesized by amidation between polysaccharides and functional chemical containing amine groups (furylmethylamine or AMA). Briefly, about 0.5 g HA or HEP was first dissolved in 150 mL 100 mM MES buffer solution. Seven hundred milligram of DMTMM were successively added into the solution to activate carboxyl groups for 30 min under magnetic stirring. After activation, 1.5 mmol functional chemical (furylmethylamine or AMA) was dropped or added to reaction system, which was continued to react for 24 h under dark at room temperature. Then the final solution was dialyzed with dialysis bag of 10 kDa cut-off molecular weight for 3 days to remove unreacted chemicals and byproduct of small molecule weight. Finally, polysaccharide derivative (HEP-AMA or HA-furan) was obtained by freeze drying at −60°C at a pressure of 7–8 Pa.

HA-furan-ADH was also obtained by amidation. Briefly, after 700 mg of DMTMM were used to activate carboxyl groups of 150 mL 3.3 mg/mL HA-furan buffer solution containing 100 mM MES for 30 min under magnetic stirring, 1.5 mmol ADH was added to react with HA-furan at room temperature for 24 h. Then HA-furan-ADH was finally obtained after the solution was dialyzed and freeze-dried according to above-mentioned conditions.

HA-furan-CHO was synthesized by oxidation of sodium periodate. Briefly, 5 mL 0.5 mol/L sodium periodate was dropped into 100 mL 5 mg/mL HA-furan solution to oxide HA. After the reaction continued for 2 h, 1 mL ethylene glycol was added to end the reaction. Then HA-furan-CHO was finally obtained after the solution was dialyzed and freeze-dried according to above-mentioned conditions.

These derivatives were characterized by ^{1}H nuclear magnetic resonance (^{1}H NMR, Bruker, AV500) using D_2O as solvent. Grafting ratio of functional molecules for polysaccharides derivatives was calculated by ^{1}H NMR spectra except grafting ratio of aldehyde group, which was qualified by the t-butyl carbazate assay.

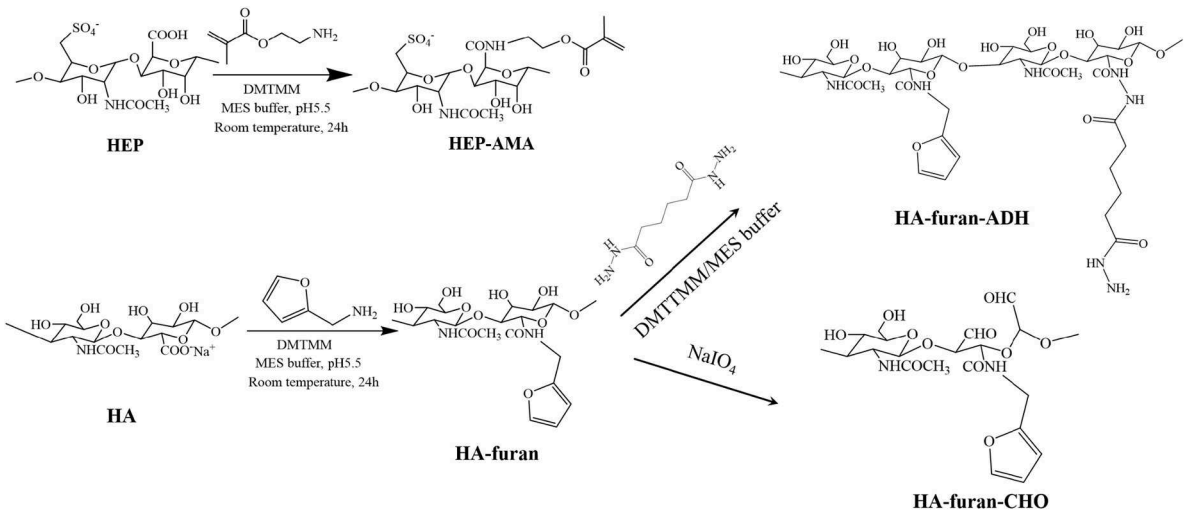

SCHEME 1 | Scheme of synthesis for polysaccharide derivatives.

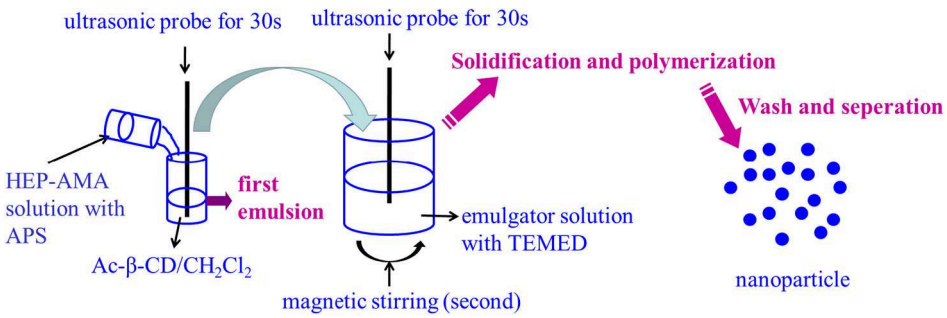

SCHEME 2 | Scheme illustration to show the formation of nanoparticle.

Preparation and Characterization of pH-Sensitive Bifunctional Nanoparticle

pH-sensitive bifunctional nanoparticles were also fabricated by double emulsion method using previous synthesized pH-sensitive Ac-β-CD as a main material (Chen et al., 2017, 2018; Wang X. et al., 2018). The process of preparation was shown in **Scheme 2**. Briefly, 200 μL 40% HEP-AMA solution containing 50 mM APS was first emulsified into 1 mL of 10% w/v Ac-β-CD/DCM solution, which was further emulsified into 5 mL of 3% w/v gelatin aqueous solution containing 50 mM TEMED. Either first or second emulsion was formed under the help of sonication dispersion method, which was carried out by ultrasonic probe with 1 kW for 30 s per step. The obtained emulsion was immediately added into 20 mL of 1% w/v gelatin solution to evaporate DCM under magnetic stirring. At the same time, HEP-AMA was crosslinked by radical polymerization to form nanogel structure. Finally, nanoparticles were collected by centrifugation (14,000 rpm, 10 min) after 10 h. The collected nanoparticles were washed several times by basic water (pH 8.0, adjusted by NH_3) and lyophilized to obtain dry nanoparticle powder. The pH sensitive nanoparticles were resuspended into basic water (pH 8.0, adjusted by NH_3) to form diluted nanoparticle suspension (lower than 100 μg/mL) by ultrasonic probe for 1 min and further characterized by dynamic light scattering (DLS, nano ZS). In morphology investigation, 50 μL of resuspended nanoparticles was dried on silica layer for scanning electron microscope (SEM, S8100), and another 50 μL was dried on copper mesh for transmission electron microscope (TEM, Tecnai 12) at 200 kV.

In vitro Evaluation of VEGF Delivery Property and Bioactivity Performance

VEGF165 was loaded into nanoparticle through absorbance. Briefly, nanoparticle was dispersed in VEGF165 solution. After the mixture was vibrated for 24 h at 4°C to load VEGF165, nanoparticle was centrifuged to remove unloaded growth factor. The loaded amount was calculated by the difference of VEGF165 concentration between before and after growth factor loading, which was determined by ELISA kit. For VEGF165 release assay, 120 mg VEGF165 encapsulated nanoparticle was dispersed in 4 mL PBS under vibration at 37°C. At appropriate intervals, 500 μL released solution was withdrawn after centrifuged and qualified by ELISA kit. Simultaneously, 500 μL fresh solution was supplemented into released solution.VEGF165 concentration of each interval was obtained by referring to the standard curve.

The cumulative released VEGF165 was calculated by VEGF165 amount of each interval.

The released VEGF165 was co-cultured with HUVEC cells for its bioactivity evaluation. Briefly, VEGF165 was released in DMEM medium with 30 mg/mL for 12 h. The released medium was collected for further use. HUVEC cells were incubated in a humidified atmosphere of 95% air and 5% CO_2 at 37°C. The used cells were detached using 0.25% trypsin in PBS for the experiment. Then 100 μL (or 1 mL) of the released medium were added into each well of 96-well (or 12-well) culture plate, into which the 100 μL (or 1 mL) cell suspension with cell density of $2*10^4$ cell/mL was subsequently added. Cell viability (MTT assay), DNA content and cell morphology were characterized as a function of cultural time. For MTT assay, 20 μL MTT was supplemented into each well and successively cultured for another 4 h. Then the absorbance of 200 μL MTT/DMSO solution at 560 nm was recorded by a microplate reader (Infinite M200 PRO).For DNA assay, detached cells of each well (12-well culture plate) was digested by 500 μL 10 mg/mL papain solution at 65°C overnight, which was qualified by Quant-iT^{TM} PicoGreen® dsDNA kit. Finally, cells were observed by fluorescence microscope (IX73).

Hydrogel Formation and Characterization

HA-furan-ADH and HA-furan-CHO were dissolved in water, respectively, to obtain two kind solutions with certain concentration from 2 to 10% w/v. The above-mentioned solutions with same concentration were mixed with equal volume, into which equimolar mal-PEG-mal with furan group on HA derivative was added and stirred. Gelation time was obtained by observation method, which was defined as the interval between mixing and loss of fluidity for mixture. The preparation process for composite nanoparticle was shown in **Scheme 3**. Briefly, nanoparticle was dispersed in HA-furan-CHO solution with final concentration of 10 mg/mL in advance. Composite hydrogel was then fabricated by the same method for pure hydrogel preparation. Composite hydrogel was characterized by rheological measurement in a parallel platemode using a strain-controlled rheometer (MCR102). The self-healing property was recorded by digital photos. Firstly, the formed hydrogel was cut into two parts completely. Secondly, two separated part was put together with complete interface touch for 24 h. Finally, the self-healed hydrogel was recorded by digital photos.

In vitro Cell Growth in Composite Hydrogel

HUVEC cells was incorporated *in situ* into composite hydrogel during hydrogel formation. Briefly, detached HUVEC cells were added to 10% HA-furan-ADH solution to form cell/precursor suspension with cell density of $2*10^6$ cell/mL. The cell/precursor suspension was mixed with another 10% w/v precursor/nanoparticle suspension with 10 mg/mL nanoparticle to form composite hydrogel with cells. Into the above-mentioned solution, mal-PEG-mal was added and mixed. Each cell encapsulated hydrogel carrier with final volume of 200 μL was put in each well of 24-well culture plate and incubated in a humidified atmosphere of 95% air and 5% CO_2 at 37°C. Cytoviability (MTT assay), DNA content and cell morphology (microscope images) were characterized as a function of cultural time. For MTT assay, 100 μL MTT was supplemented into each well and successively cultured for another 4 h. Then hydrogel was dissolved by 1 mL DMSO, the absorbance of 200 μL above solution at 560 nm was recorded by a microplate reader (Infinite M200 PRO). For DNA assay, each gel with cells was digested by 500 μL 10 mg/mL papain solution at 65°C overnight, which was qualified by Quant-iT^{TM} PicoGreen® dsDNA kit. Finally, cells in hydrogel film were observed by fluorescence microscope (IX73).

Statistical Analysis

Data were analyzed using the *t*-test for differences. The software of origin was used to calculate these differences for *p* value. Results were reported as means ± standard deviation, at least 3 replicates (from different samples) formed by above-mentioned method were analyzed in all experiments. The sample size for hydrogel is about 200 mg. The significant level was set at $p < 0.05$.

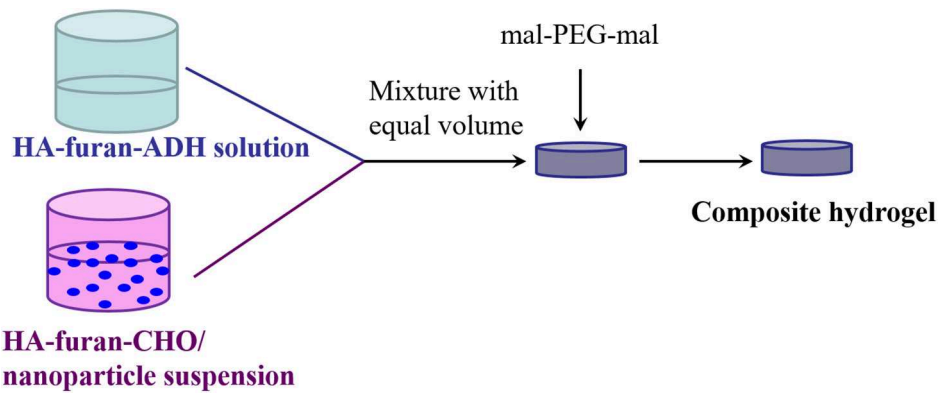

SCHEME 3 | Scheme illustration to show the formation of composite hydrogel.

RESULT AND DISCUSSION

pH-Sensitive Bifunctional Nanoparticle Formation

In order to obtain crosslinkable heparin derivative, HEP-AMA was first synthesized and characterized by ^{1}H NMR spectrum in **Figure 1**. The details of chemical shift are listed as follows: the chemical shift at 1.6 ppm is attributed to the protons of methyl group of AMA at 8 position, the chemical shifts from 3.0 to 4.2 ppm are attributed to the protons of pyranose ring and -CH_2-O from 1 to 6 position, the chemical shifts at 5.6 ppm and 6.2 are attributed to the protons of C=CH_2 of AMA at 7 position. The chemical shift at 7 position confirmed successful grafting of AMA onto HEP main chain.

pH-sensitive bifunctional nanoparticle was prepared by double emulsion method combined with *in situ* polymerization (**Scheme 2**). Final nanoparticle exhibited homogeneous sphere morphology, which was confirmed by SEM image (**Figure 2A**) and TEM image (**Figure 2B**). Furthermore, different brightness and obvious boundary was found in the TEM image, which indicated different phase structure. The dark structure might be ascribed to pH sensitive Ac-β-CD, while the light structure might be attributed to HEP nanogel. Simultaneously, slight

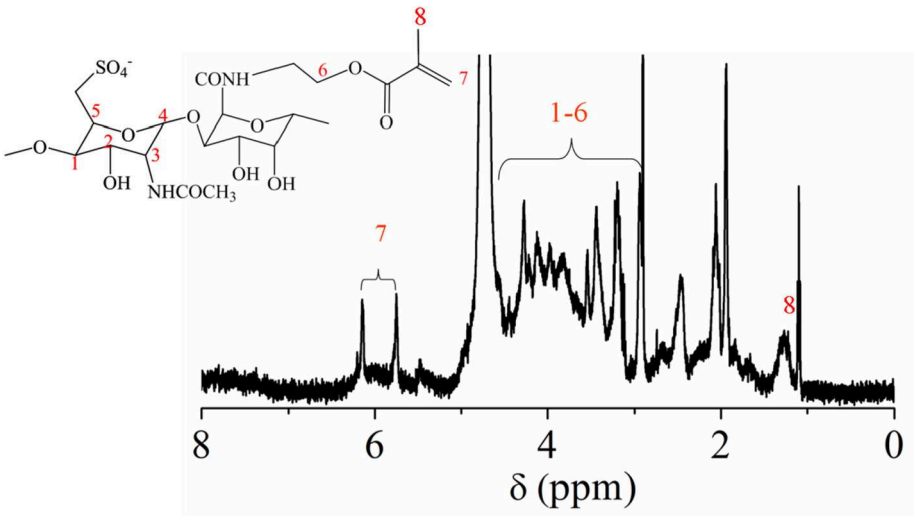

FIGURE 1 | ^{1}H NMR spectrum of HEP-AMA.

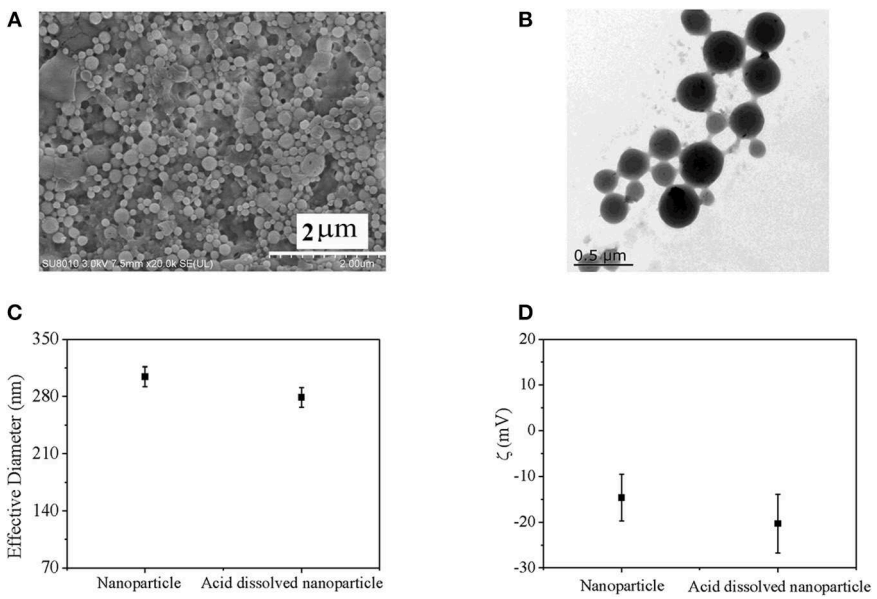

FIGURE 2 | (A) SEM image of nanoparticle; **(B)** TEM image of nanoparticle; **(C)** Effective diameter; and **(D)** zeta potential of nanoparticles determined by DLS.

adhesive structure was also found in the TEM image, which might be due to slight crosslinking of nanogel during the process of *in situ* polymerization and conglutination in drying process of HEP nanogel. These results indicated that nanogel had been successfully synthesized during the preparation of nanoparticle. Moreover, effective diameters and zeta potentials of prepared nanoparticles in PBS and in acid were recorded by DLS method, which was shown in **Figures 2C,D**. Effective diameter of nanoparticle in PBS was 304 ± 12 nm, which was larger than that in acid solution of 279 ± 12 nm. However, the difference between them had no significant difference. Since pH sensitive property of the bifunctional nanoparticle come from Ac-β-CD dissolution in acid solution due to degradation of Ac-β-CD, which was confirmed by transparency variation of nanoparticle suspension, only HEP nanogel existed in acid solution (Chen et al., 2017, 2018; Wang X. et al., 2018). Since nanogel was formed *in situ* during the fabrication of Ac-β-CD nanoparticle, they had similar diameter, which was also confirmed by the TEM image (**Figure 2B**). The zeta potential for nanoparticle in acid solution was larger than that in PBS due to contribution of negative heparin in acid environment. However, no significant difference was found between them. The nanoparticle possessed similar chemical component with nanogel so that they had similar zeta potential except slight influence of pH value.

In vitro Evaluation for the Bifunctional Nanoparticle

The growth factor encapsulated capacity and its release behavior *in vitro* for the bifunctional nanoparticle were investigated in **Figures 3A,B**. The equilibrium encapsulated growth factor in nanoparticles increased with the initial growth factor's concentration especially when the concentration is lower than 120 ng/mL (**Figure 3A**). The maximum growth factor encapsulated capacity was about 1.9 ng/mg nanoparticles, which condition was also used for further release behavior investigation. In PBS (pH 7.4), about 65% could be released in 24 h from nanoparticle, about 50% growth factor was burst released in the first 2 h and remaining 15% growth factor was linearly released from nanoparticles in the following 22 h. In mild acid medium (pH 5.5), nearly all the growth factor dispersed homogeneously in the medium after 1 h due to degradation of Ac-β-CD nanoparticle. But it was not sure whether growth factor had been diffused into medium or still incorporated with homogeneous dispersed heparin nanogel.

The bioactivity of released growth factor was evaluated by *in vitro* cell behavior using cells without growth factor as a control. Cell viability of the growth factor group increased with culture time just as the control group (**Figure 4A**). Furthermore, cell viability of the growth factor group was significantly higher than

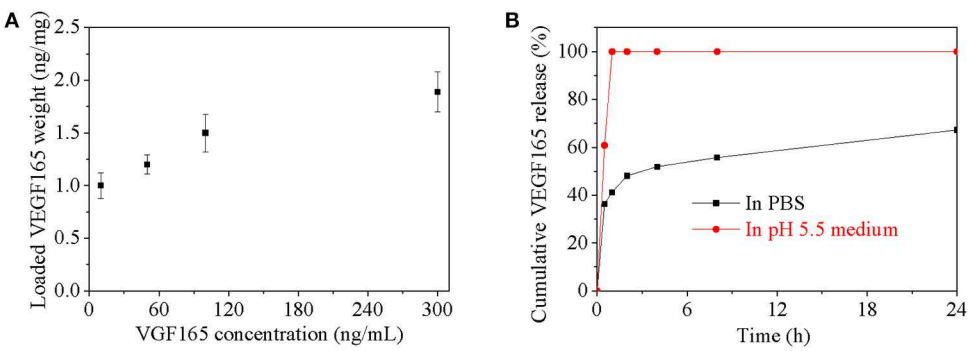

FIGURE 3 | (A) Loaded VEGF165 weight in every microgram nanoparticle as a function of VEGF165 concentration; **(B)** Cumulative VEGF165 release in PBS with pH value of 7.4.

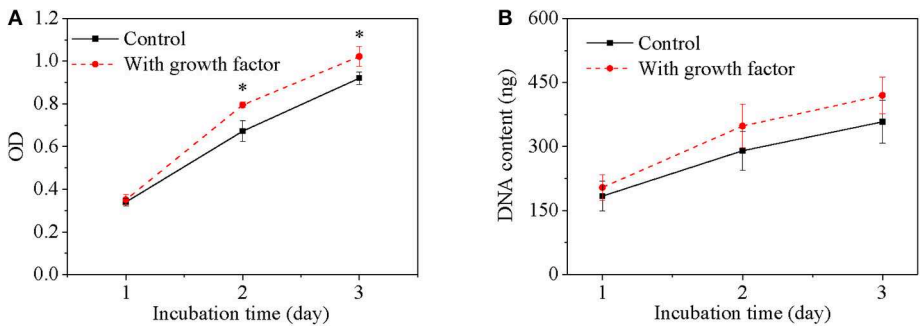

FIGURE 4 | Cell viability **(A)** and DNA content **(B)** of cells as a function of culture time. Cell density is 20,000/mL. Two hundred microliter for MTT assay of 96-well TCPs and 2 mL for DNA assay of 6-well TCPs. *$p < 0.05$.

the control group especially after cell had been cultured for 2 days. Since DNA content of each cell is constant, DNA content reflects cell number. DNA content of cells for the two groups increased with culture time, while DNA content of cells for the growth factor group was higher than that for the control group (**Figure 4B**). However, the increase had no significant difference according to statistical analysis. The space of 2D cell culture for cell growth is limited to a constant value, which may restrict cell proliferation if the space could not accommodate more cells.

Moreover, cell morphology was shown in **Figure 5**. Cell on TCPs exhibited round-like polygon shape regardless culture time and existence of growth factor (**Figures 5A–F**). It was also found that the number of cells for the growth factor group is larger than that of the control group, which was consistent with results of cell viability and DNA content. Therefore, the released growth factor could promote cell growth from the above-mentioned results, which indicated released growth factor could maintain its bioactivity.

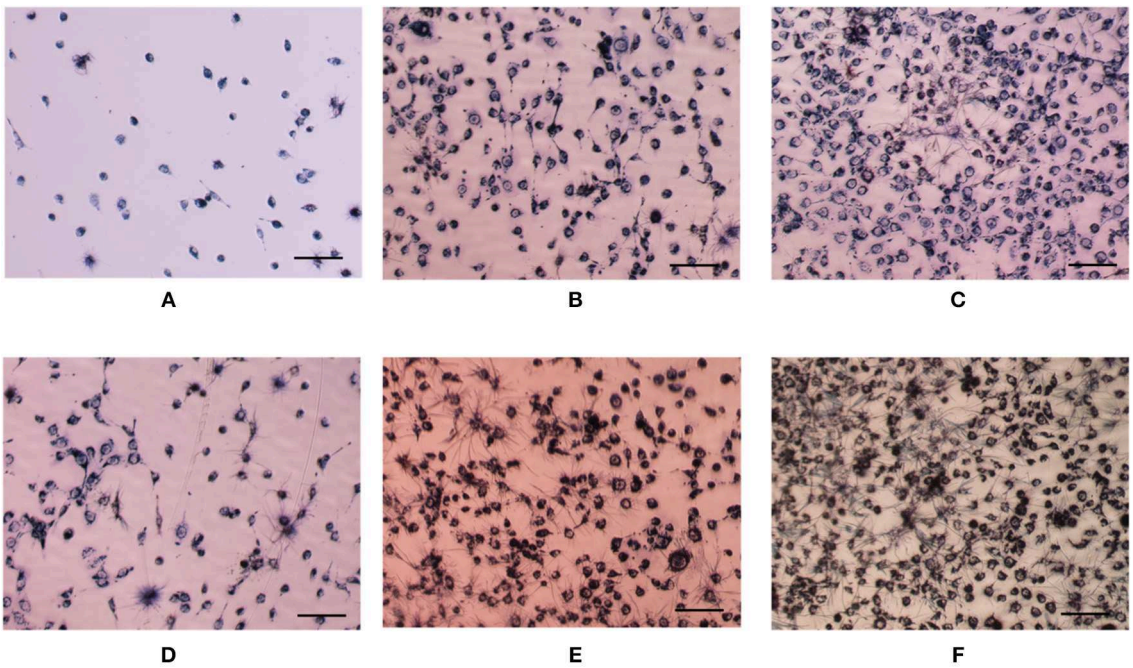

FIGURE 5 | Optical images of HUVEC cells with **(D–F)** or without **(A–C)** growth factor after cultured 1 day **(A,D)**, 2 days **(B,E)**, and 3 days **(C,F)**. Cell seeding density is 4,000/well. Cells were stained by MTT. The scale is 100 μm.

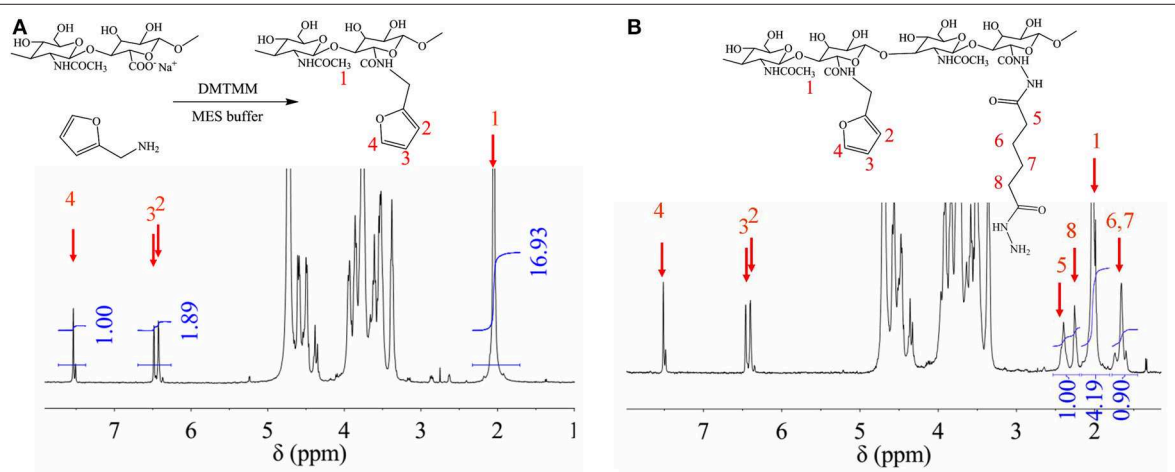

FIGURE 6 | ^{1}H NMR of HA-furan **(A)**, and HA-furan-ADH **(B)**.

Fabrication and Characterization of Injectable Composite Hydrogel

HA-furan and HA-furan-ADH were synthesized and characterized by ^{1}H NMR spectrum in **Figures 6A,B**. Since they are both HA derivatives, chemical shifts from 3.0 to 4.2 ppm in both **Figures 6A,B** are attributed to the protons of pyranose ring. Other chemical shifts for HA-furan (**Figure 6A**) are listed as follows: the chemical shift at 1.9 ppm is attributed to the protons of CH_3-O at 1 position, and the chemical shifts at 6.4, 6.5, and 7.5 ppm are attributed to the protons of furan ring at 2–4 position. The chemical shift at 2–4 position confirmed successful grafting of furan onto HA main chain. Since the H number of 2–4 position in each molecule and CH_3-O group every two pyranose rings are fixed, their relative area ratio could be used to calculate the substitute degree of furan group on HA, which was 17%. Besides **Figure 6A** mentioned, chemical shifts at 1.7, 2.2, and 2.4 ppm for HA-furan-ADH (**Figure 6B**) are attributed to -CH_2 groups at 5–8 position, which confirmed successful grafting of ADH onto HA-furan chain. Similarly, the substitute degree of ADH was calculated to be 17%. In addition, HA-furan-CHO was confirmed and quantified by t-butyl carbazate assay. The substitute degree of CHO was calculated to be 21%.

In the hydrogel system, two kinds of crosslinking points were formed to strengthen polymer network, as shown in **Figure 7A**. One was acyl hydrazone bond formed by CHO and ADH, which was a dynamic covalent and sensitive to pH value. The other was formed by reversible diels-alder click chemistry between furan groups and maleimide groups. Also, properties of hydrogel were related with the double crosslinked network, which was discussed as follows. Gelation time and swelling ratio as a function of polymer concentration as well as pH value were investigated, which was shown in **Figures 7B,C**. Gelation time decreased rapidly along with polymer concentration, and swelling ratio decreased slightly with increase of polymer concentration (**Figure 7B**). Just as our previous research discussed, enlarged crosslinking point in definite volume increased percentage of

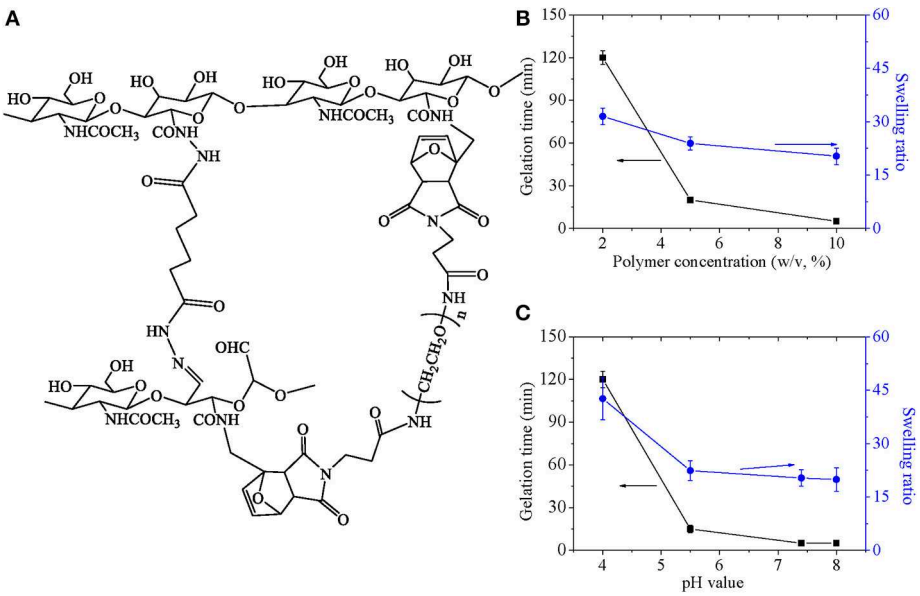

FIGURE 7 | (A) The mechanisms for the formation of the hydrazine bond and for the Diels-Adler reaction. Gelation time and swelling ratio as a function of **(B)** polymer concentration and **(C)** pH value.

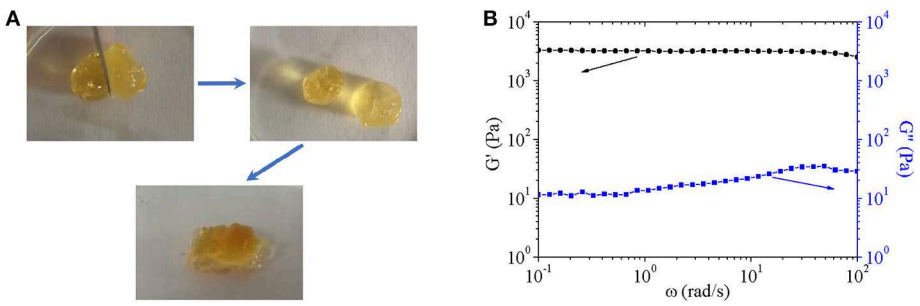

FIGURE 8 | (A) Digital images to show self-healing properties of hydrogel. The process included (1) cutting the formed hydrogel; (2) separating two part of above-mentioned hydrogel completely; (3) putting together of two separated part with complete interface touch for 24 h. **(B)** Storage modulus and loss modulus of composite hydrogel.

reaction between functional groups and accelerate reaction speed, which influenced gelation time and swelling ratio. Gelation time and swelling ratio decreased significantly with decrease of pH value until pH5.5 (**Figure 7C**). Since acyl hydrazone bond was formed at high pH value medium and broken at low pH value medium with critical point of pH 4.0, it was easily understood that gelation time prolonged due to lack of one kind of crosslinkings in low pH value and swelling ratio enlarged due to less crosslink points. In summary, adjustable gelation time ensured the injectable property for composite hydrogel.

Furthermore, the self-healing property was confirmed by **Figure 8A**. Just as above discussed, the hydrogel was crosslinked by dynamic covalent and reversible Diels-alder click chemistry, which endowed hydrogel flexible and reversible crosslinking points. The characteristic gave self-healing property to hydrogel.

Finally, composite hydrogel was characterized by gelation time and swelling ratio, which possessed similar properties to pure hydrogel. Additionally, viscoelastic behaviors of composite hydrogels were shown in **Figure 8B**. Storage moduli of hydrogel was around 3×10^3 Pa, which was 100–300 times higher than loss moduli of 100–300 Pa over the frequency range of 10^{-1}-10^2 rad/s. The result indicated that composite hydrogels had typical characteristics of elastomers. With increasing angular frequency, storage moduli showed little decrease and loss moduli increased gently with no sign of breakage as far as the measured angular frequency range was concerned. The mechanical property ensured its potential application as a scaffold.

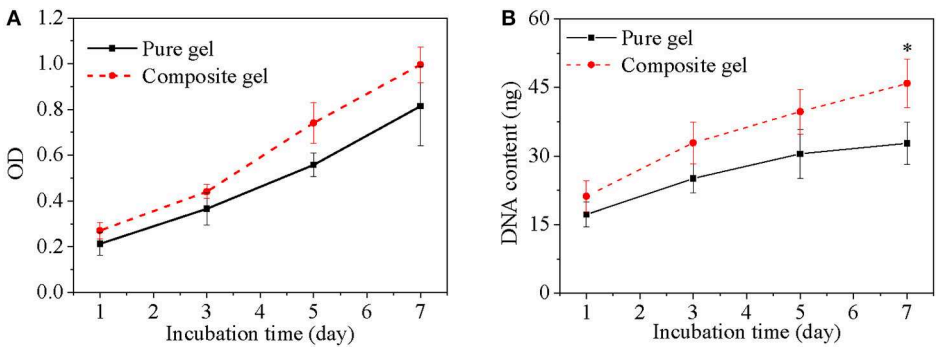

FIGURE 9 | Cell viability **(A)** and DNA content **(B)** of cells in different gels as a function of culture time. cell density is 400,000/gel. *$p < 0.05$.

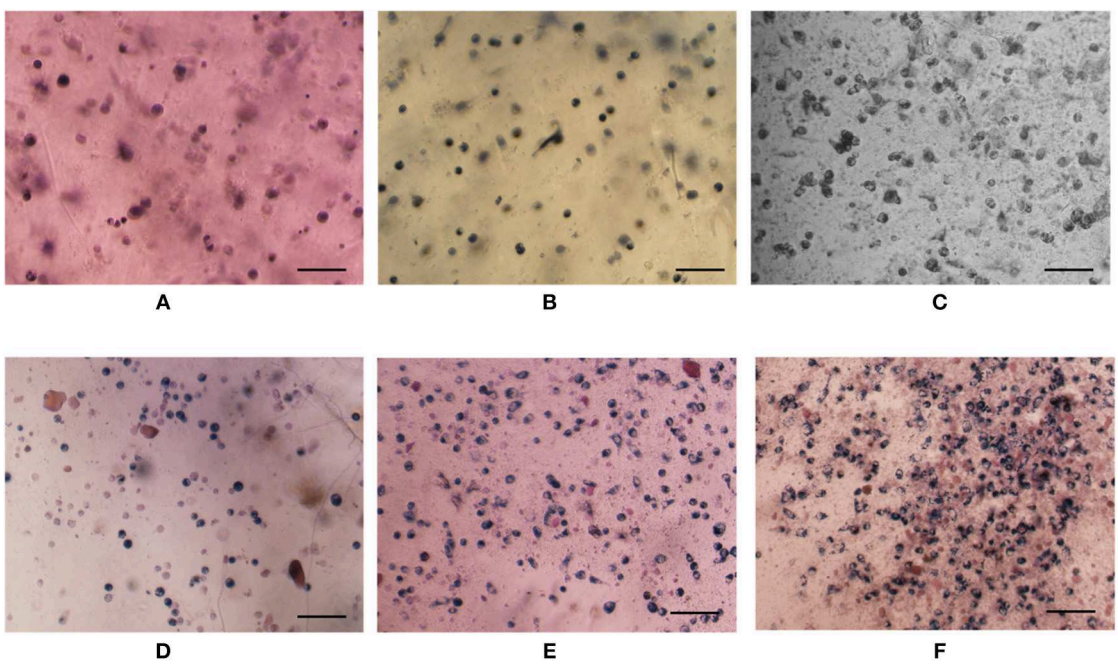

FIGURE 10 | Optical images of cells in gels without **(A–C)** or with **(D–F)** growth factor encapsulated nanoparticle after cultured 1 day **(A,D)**, 3 days **(B,E)**, and 5 days **(C,F)**. Cell seeding density is 400,000/gel. Cells were stained by MTT. The scale is 100 μm.

Moreover, the degradation of both pure hydrogel and composite hydrogel was about 3 weeks. No significant difference for degradation time was found between hydrogel and composite hydrogel.

In vitro Evaluation for Composite Hydrogel

Cell was incorporated into composite hydrogel to evaluate its biomedical application using pure hydrogel without nanoparticle as a control. Cell viability both in either pure hydrogel and in composite hydrogel increased obviously along with culture time and the increase have statistically significant difference (**Figure 9A**), which indicated that either pure hydrogel or composite hydrogel can support cell growth. Moreover, cell viability in composite hydrogel was higher than that in pure hydrogel especially after cells were cultured for 3 days (**Figure 9A**). Especially, for 5 and 7 days, the difference between composite hydrogel and pure hydrogel has obvious statistical significance. Higher cell viability in composite hydrogel was ascribed to encapsulated growth factor. Similarly, DNA content of either pure hydrogel or composite hydrogel increased significantly along with culture time. While DNA content of composite hydrogel was higher than that of pure hydrogel especially after cells were cultured for 3 days (**Figure 9B**). Just as above discussed, DNA content reflects cell number. Hence hydrogels could support cell proliferation and composite hydrogel could accelerate cell proliferation more. Furthermore, cells in hydrogels exhibited round morphology, which was recorded by microscope in **Figure 10**. At day 1, some round cells homogenous dispersed in hydrogels (**Figures 10A,D**); at day 3, homogenous dispersed cells increased (**Figures 10B,E**); at day 5, cells increased further (**Figures 10C,F**). Overally, cell number in composite hydrogel (**Figures 10D–F**) was obvious larger than that in pure hydrogel (**Figures 10A–C**). Therefore, these results were consistent and confirmed that hydrogels could maintain cell activity and support cell growth, and composite hydrogel possessed better properties.

CONCLUSION

pH-sensitive bifunctional nanoparticle was successfully prepared by combined W/O/W technique and *in situ* polymerization. Final nanoparticle exhibited homogeneous sphere morphology and biphase structure. pH sensitive property of the nanoparticle was confirmed by effective diameter change from 314 nm in PBS to 299 nm in acid solution as well as zeta potential change. The growth factor encapsulated capacity in the nanoparticle was influenced by initial growth factor concentration with maximum encapsulated amount of 1.9 ng/mg nanoparticle. Their release behaviors were dependent on pH value of released medium. Detailedly, about 60% could be released in 24 h in PBS; but nearly all the growth factor dispersed homogeneously in pH 5.5 medium after 1 h. *In vitro* investigation including cell viability, DNA content and cell morphology revealed that the released growth factor could increase cell viability and promote cell growth. In further step, HA-furan, HA-furan-ADH, and HA-furan-CHO were successfully synthesized with furan substitute degree of 17%, ADH substitute degree of 17%, CHO substitute degree of 21%. Hydrogel was crosslinked by dynamic covalent and reversible diels-alder click chemistry, which endowed hydrogel flexible and adjustable properties including self-healing property. Gelation time and swelling ratio were influenced by pH value and polymer concentration. Higher polymer concentration or higher pH value resulted in shorter gelation time and smaller swelling ratio. After nanoparticle was incorporated into hydrogel, composite hydrogel exhibited acceptable mechanical property as a scaffold for biomedical field with storage moduli of 3×10^3 Pa and loss moduli of 100–300 Pa. *In vitro* evaluation from viability, DNA content and cell morphology results confirmed that hydrogels could maintain cell activity and support cell growth, and further composite hydrogel possessed better properties.

DATA AVAILABILITY

The raw data supporting the conclusions of this manuscript will be made available by the authors, without undue reservation, to any qualified researcher.

AUTHOR CONTRIBUTIONS

XH provided an idea, designed the whole research, and write the manuscript. ZG synthesized and characterized materials, give evaluations for the injectable composite hydrogel. HT helped to perform *in vitro* evaluation. HW prepared nanoparticle and helped to culture cells. XM helped to synthesize and characterize materials. JP helped to characterize materials.

FUNDING

This study is financially supported by Natural Science Foundation of Jiangsu Province (BK20171113), Natural Science Foundation of China (21702082), Qing Lan Project, Six talent peaks project in Jiangsu Province (JY-071), Excellent scientific and technological innovation team of Jinling institute of Technology.

REFERENCES

Akuta, T., Kikuchi-Ueda, T., Imaizumi, K., Oshikane, H., Nakaki, T., Okada, Y., et al. (2015). Expression of bioactive soluble human stem cell factor (SCF) from recombinant *Escherichia coli* by coproduction of thioredoxin and efficient purification using arginine in affinity chromatography. *Protein Expr. Purif.* 105, 1–7. doi: 10.1016/j.pep.2014.09.015

Azevedo, M. M., Tsigkou, O., Nair, R., Jones, J. R., Jell, G., Stevens, M., et al. (2015). Hypoxia inducible factor-stabilizing bioactive glasses for directing mesenchymal stem cell behavior. *Tissue Eng. Part A* 21, 382–389. doi: 10.1089/ten.tea.2014.0083

Bai, X., Lu, S., Cao, Z., Ni, B., Wang, X., Ning, P., et al. (2017). Dual crosslinked chondroitin sulfate injectable hydrogel formed via continuous Diels-Alder (DA) click chemistry for bone repair. *Carbohydr. Polym.* 166, 123–130. doi: 10.1016/j.carbpol.2017.02.062

Banerjee, S. L., and Singha, N., K. (2017). A new class of dual responsive self-healable hydrogels based on a core crosslinked ionic block copolymer micelle prepared via RAFT polymerization and Diels-Alder "click" chemistry. *Soft Matter* 13, 9024–9035. doi: 10.1039/C7SM01906H

Celie, K. B., Toyoda, Y., Dong, X., Morrison, K. A., Zhang, P., Asanbe, O., et al. (2019). Microstructured hydrogel scaffolds containing differential density interfaces promote rapid cellular invasion and vascularization. *Acta Biomater.* 91, 144–158. doi: 10.1016/j.actbio.2019.04.027

Chen, P., Wang, X., and Hu, X., H. (2018). A new route to fabricate multifunctional and multistage composite nanoparticle. *Int. J. Polym. Sci.* 2018:3035629. doi: 10.1155/2018/3035629

Chen, S. N., Hu, X. H., Gong, X., Gao, Z. G., Wang, X., and Chen, P. (2017). Synthesis and preparation of biocompatible and pH-responsive cyclodextrin-based nanoparticle. *J. Nanoparticle Res.* 19:109. doi: 10.1007/s11051-017-3819-5

Fan, M., Ma, Y., Mao, J., Zhang, Z., and Tan, H. (2015). Cytocompatible *in situ* forming chitosan/hyaluronan hydrogels via a metal-free click chemistry for soft tissue engineering. *Acta Biomater.* 20, 60–68. doi: 10.1016/j.actbio.2015.03.033

Franc, G., and Kakkar, A., K. (2009). Diels-Alder "click" chemistry in designing dendritic macromolecules. *Chemistry* 15, 5630–5639. doi: 10.1002/chem.200900252

Fu, S., Ni, P., Wang, B., Chu, B., Zheng, L., Luo, F., et al. (2012). Injectable and thermo-sensitive PEG-PCL-PEG copolymer/collagen/n-HA hydrogel composite for guided bone regeneration. *Biomaterials* 33, 4801–4809. doi: 10.1016/j.biomaterials.2012.03.040

Massaro, M., Buscemi, G., Arista, L., Biddeci, G., Cavallaro, G., D'Anna, F., et al. (2019). Multifunctional carrier based on halloysite/laponite hybrid hydrogel for kartogenin delivery. *ACS Med. Chem. Lett.* 10, 419–424. doi: 10.1021/acsmedchemlett.8b00465

Muraoka, K., Le, W., Behn, A. W., and Yao, J. (2018). The effect of growth differentiation factor 8 (Myostatin) on bone marrow-derived stem cell-coated bioactive sutures in a rabbit tendon repair model. *Hand.* doi: 10.1177/1558944718792708. [Epub ahead of print].

Oh, S. H., An, D. B., Kim, T. H., and Lee, J., H. (2016). Wide-range stiffness gradient PVA/HA hydrogel to investigate stem cell differentiation behavior. *Acta Biomater.* 35, 23–31. doi: 10.1016/j.actbio.2016.02.016

Psarra, E., Foster, E., Konig, U., You, J., Ueda, Y., Eichhorn, K. J., et al. (2015). Growth factor-bearing polymer brushes–versatile bioactive substrates influencing cell response. *Biomacromolecules* 16, 3530–3542. doi: 10.1021/acs.biomac.5b00967

Song, H., Zhang, Y., Cheng, P., Chen, X., Luo, Y., and Xu, W. (2019). A rapidly self-assembling soft-brush DNA hydrogel based on RCA products. *Chem. Commun.* 55, 5375–5378. doi: 10.1039/C9CC01022J

Song, L., Liang, X., Yang, S., Wang, N., He, T., Wang, Y., et al. (2018). Novel polyethyleneimine-R8-heparin nanogel for high-efficiency gene delivery *in vitro* and *in vivo*. *Drug Deliv.* 25, 122–131. doi: 10.1080/10717544.2017.1417512

Thanusha, A. V., Dinda, A. K., and Koul, V. (2018). Evaluation of nano hydrogel composite based on gelatin/HA/CS suffused with Asiatic acid/ZnO and CuO nanoparticles for second degree burns. *Mater. Sci. Eng. C Mater. Biol. Appl.* 89, 378–386. doi: 10.1016/j.msec.2018.03.034

Wang, C. Z., Eswaramoorthy, R., Lin, T. H., Chen, C. H., Fu, Y. C., Wang, C. K., et al. (2018). Enhancement of chondrogenesis of adipose-derived stem cells in HA-PNIPAAm-CL hydrogel for cartilage regeneration in rabbits. *Sci. Rep.* 8:10526. doi: 10.1038/s41598-018-28893-x

Wang, X., Zhang, L., Wang, H. M., and Hu, X., H. (2018). A magnetic and pH-sensitive composite nanoparticle for drug delivery. *J. Nanomater.* 2018:1506342. doi: 10.1155/2018/1506342

Williams, D. L., Wirostko, B. M., Gum, G., and Mann, B., K. (2017). Topical cross-linked HA-based hydrogel accelerates closure of corneal epithelial defects and repair of stromal ulceration in companion animals. *Invest. Ophthalmol. Vis. Sci.* 58, 4616–4622. doi: 10.1167/iovs,.16-20848

Wu, W., Yao, W., Wang, X., Xie, C., Zhang, J., and Jiang, X. (2015). Bioreducible heparin-based nanogel drug delivery system. *Biomaterials* 39, 260–268. doi: 10.1016/j.biomaterials.2014.11.005

Yu, F., Cao, X., Zeng, L., Zhang, Q., and Chen, X. (2013). An interpenetrating HA/G/CS biomimic hydrogel via Diels-Alder click chemistry for cartilage tissue engineering. *Carbohydr. Polym.* 97, 188–195. doi: 10.1016/j.carbpol.2013.04.046

Zhao, Q., Zhao, Y., Lu, Z., and Tang, Y. (2019). Amino acid-modified conjugated oligomer self-assembly hydrogel for efficient capture and specific killing of antibiotic-resistant bacteria. *ACS Appl. Mater. Interfaces.* 11, 16320–16327. doi: 10.1021/acsami.9b02643

Zhu, Q., Jiang, M., Liu, Q., Yan, S., Feng, L., Lan, Y., et al. (2018). Enhanced healing activity of burn wound infection by a dextran-HA hydrogel enriched with sanguinarine. *Biomater. Sci.* 6, 2472–2486. doi: 10.1039/C8BM00478A

Conflict of Interest Statement: The authors declare that the research was conducted in the absence of any commercial or financial relationships that could be construed as a potential conflict of interest.

frontiers in Chemistry

REVIEW
published: 11 October 2019
doi: 10.3389/fchem.2019.00675

Injectable Hydrogels for Localized Cancer Therapy

Dao-yang Fan, Yun Tian and Zhong-jun Liu**

Department of Orthopedics, Peking University Third Hospital, Beijing, China

Traditional intravenous chemotherapy is relative to many systemic side effects, including myelosuppression, liver or kidney dysfunction, and neurotoxicity. As an alternative method, the injectable hydrogel can efficiently avoid these problems by releasing drugs topically at the tumor site. With advantages of localized drug toxicity in the tumor site, proper injectable hydrogel as the drug delivery system has become a research hotspot. Based on different types and stages of cancer, a variety of hydrogel drug delivery systems were developed, including thermosensitive, pH-sensitive, photosensitive, and dual-sensitive hydrogel. In this review, the latest developments of these hydrogels and related drug delivery systems were summarized. In summary, our increasing knowledge of injectable hydrogel for localized cancer therapy ensures us that it is a more durable and effective approach than traditional chemotherapy. Smart release system reacting to different stimuli at different time according to the micro-environment changes in the tumor site is a promising tendency for further studies.

Keywords: smart hydrogels, injectable, localized chemotherapy, stimuli responsive, drug delivery

OPEN ACCESS

Edited by:
Xing Wang,
Institute of Chemistry (CAS), China

Reviewed by:
Daifeng Li,
Stanford Bio-X, Stanford University, United States
Xiangjie Su,
Utrecht University, Netherlands
Sophie Sun,
Chinese Academy of Sciences, China

****Correspondence:***
Yun Tian
tiany@bjmu.edu.cn
Zhong-jun Liu
zjliu@bjmu.edu.cn

Specialty section:
This article was submitted to Polymer Chemistry, a section of the journal Frontiers in Chemistry

Received: *19 August 2019*
Accepted: *25 September 2019*
Published: *11 October 2019*

Citation:
Fan D, Tian Y and Liu Z (2019) Injectable Hydrogels for Localized Cancer Therapy. Front. Chem. 7:675. doi: 10.3389/fchem.2019.00675

INTRODUCTION

With the deterioration of the environment, the incidence of cancer is increasing year by year. In 2018, there were 18.1 million new cancer cases worldwide (9.5 million males and 8.6 million females), and the death toll was 9.6 million (5.4 million males and 4.2 million females) (Bray et al., 2018). The global cancer burden is further aggravated. One in five men and one in six women worldwide will develop cancer, and 1 in 8 men and 1 in 11 women will die for cancer (Bray et al., 2018; Sivaram et al., 2018).

Different strategies and methods are applied for cancer patients according to their different diagnose and stage. Possible therapies include chemotherapy, radiation, surgery, immunotherapy, targeted therapy, and gene therapy (Wang et al., 2013; Roy and Trinchieri, 2017; Bykov et al., 2018; Senft et al., 2018). Among those options, chemotherapy plays a pivotal role in tumor control and prevention of recurrence. The anti-tumor activity of chemotherapeutic drugs kill tumor cells with its drug toxicity (Zhou et al., 2017). Without selective or targeted killing, normal tissues could be harmed by chemical drugs along with tumor cells (Andreyev et al., 2014).

With the development of hydrogel, traditional chemotherapy drugs are booming a new life. Drugs are injected within the hydrogel directly into the tumor or adjacent to it (Elias et al., 2015; Ma et al., 2015; Pan et al., 2018). Drugs could be localized in a crosslinked 3D network of hydrophilic polymer chains (Wang et al., 2013, 2017; Bu et al., 2017). In this way, drug toxicity is limited within a localized area where tumor cells lie. Meanwhile, localized hydrogel reveals the ability for continuous efficient drug delivery in the tumor site (Yang Y. Y. et al., 2016; Yang et al., 2018). To enhance this character, a variety of systems have been developed with different composition, including polyphosphazene (PPZ), polyethylene glycol (PEG), and Polylactate glycolic acid PLGA (Bu et al., 2017; Ahmad et al., 2018; Cheng et al., 2018; Gajendiran et al., 2019).

Most of the hydrogel is insoluble in water but excellent in water absorption capacity (from 10% to thousands of times their dry weight) (Bin Imran et al., 2014; Murgia et al., 2018) (**Figure 1**). The soft, moist surface, and affinity with the tissue greatly reduce the stimulation of the human body. Most materials that make hydrogels are non-toxic (Zhang et al., 2015; Batista et al., 2019; Gajendiran et al., 2019). According to the response to external stimuli, hydrogels can be divided into ordinary hydrogels and smart hydrogels (Gu et al., 2017). Original hydrogels are not sensitive to environmental changes (Castelletto et al., 2019; Kerdsirichairat et al., 2019; Luo et al., 2019). While smart hydrogels could be affected by pH, temperature, and photoelectricity. It results in changeable gel volume and traits for smart hydrogels (Deepa et al., 2012; Chen and Liu, 2016; Chen X. et al., 2016; Milcovich et al., 2017; Chen et al., 2019). These hydrogels are currently widely used in tissue engineering, drug delivery, and other fields (Bae et al., 2013; Del Bufalo et al., 2016; Casey et al., 2017; Castelletto et al., 2019).

THERMOSENSITIVE HYDROGELS

Temperature-sensitive hydrogels are hydrogels that change in volume as the ambient temperature changes (Klouda, 2015; Chen et al., 2018). The gel always has a certain proportion of hydrophobic and hydrophilic groups. Temperature changes can affect the hydrophobic interaction of these groups. The hydrogen bonding between the macromolecular chains causes the gel structure to change, and volume changes occur (Fan et al., 2015). The temperature at which the volume changes is referred as lower critical solution temperature (LCST) (Sapino et al., 2019). Under this temperature, the gel swells in aqueous solution. Once the temperature rises to LCST, the gel shrinks (Lei et al., 2012; Wang et al., 2015). Its unique properties can be used as a drug carrier, which is injected into the body after being combined with a drug at a low temperature (Le et al., 2018). Forming a colloidal state with the help of body temperature makes it a drug sustained-release system, which simplifies not only medical treatment but also patients' suffering (Wang et al., 2015, 2016; Yang Y. et al., 2016). Main thermosensitive injectable hydrogels include chitosan/glycerophosphate (C/GP), hyaluronic acid (HA), PLGA based hydrogel, PEG-based hydrogel, PECE, and PECT (Guo et al., 2012; Klouda, 2015; Huang et al., 2016; Le et al., 2018; Sapino et al., 2019). Their characters and drug delivery systems were summarized in **Table 1**.

In one study (Huang et al., 2016), injectable thermosensitive doxorubicin (DOX) delivery system was developed with PECT hydrogel. Instead of hydrogel based on free DOX diffusion, which suffered from rapid drug clearance and poor drug penetration in tumor tissue, self-polymerized drug-loaded nanoparticles were encapsulated into PECT hydrogel (Huang et al., 2016). After *in vivo* injection, PECT gel exhibited a transition phase between sol and gel. The viscosity increased abruptly once the

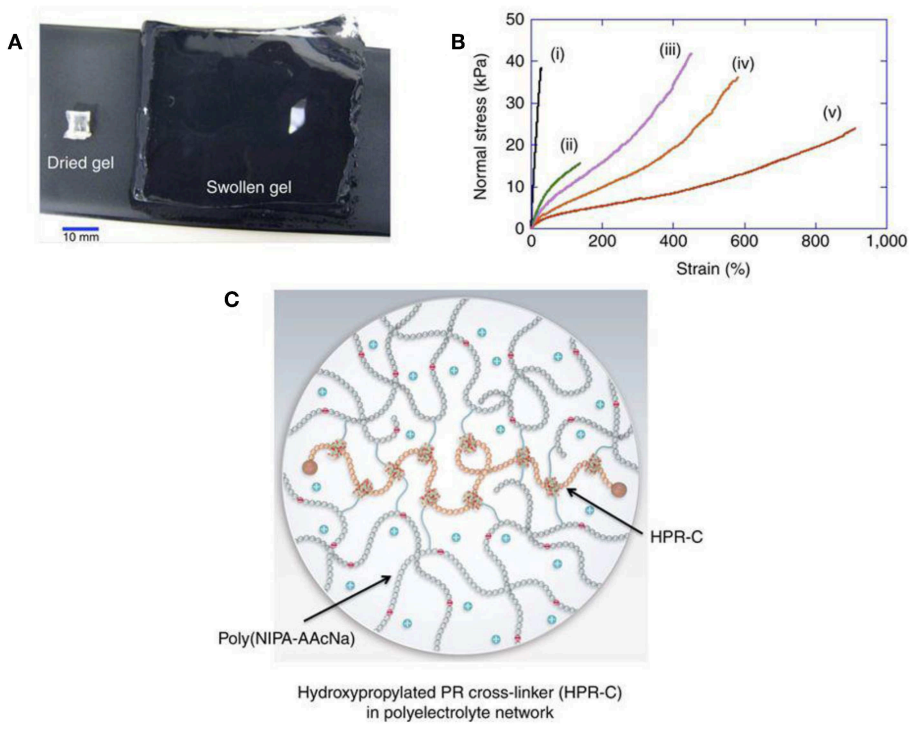

FIGURE 1 | Hydrogel forms crosslinked 3D network and shows excellent water absorption capacity. **(A)** Hydrogel swelling from 129 mg (dry gel) to 80,000 mg (water-swollen gel). **(B)** Stress-strain curves of different hydrogels (i–v). **(C)** Schematic of swollen hydrogel (Bin Imran et al., 2014). Reproduced, with permission, from Bin Imran et al. (2014).

TABLE 1 | Main thermosensitive injectable hydrogel and drug delivery system.

Hydrogel	Drug	Cell line (*in vitro*)	Cancer (*in vivo*)	Characteristics and applications	References
Chitosan/ glycerophosphate (CS/GP)	Indocyanine green (ICG)	Hepatocellular carcinoma (HCC)	–	Hydrogel loaded with ICG is a feasible agent for fluorescence imaging and drug delivery. It forms *in situ* compact gel and has a good ability for filling vessels	Salis et al., 2015
CS/GP	DOXorubicin (DOX)	H22 and SMMC 7721 (hepatoma)	Hepatoma	This *in situ* gelling thermosensitive hydrogel is capable of drug delivery to tumor tissue constantly and efficiently	Ren et al., 2016
Hyaluronic acid (HA) and Pluronic F127 (PF127)	DOXorubicin (DOX) and Docetaxel (DOC)	CT-26 (colorectal carcinoma)	Colorectal carcinoma	Thermosensitive hydrogels loaded with DOX and DOX has a good potential for dual drug delivery, which efficiently enhanced cancer management with minimal side effects	Sheu et al., 2016
PLGA-PEG-PLGA	PLK1shRNA/PEI-Lys and DOX	Saos-2 and MG63 (osteosarcoma)	Osteosarcoma	Localized hydrogel with RNA and DOX co-loaded is promising for efficient clinical management of osteosarcoma	Ma et al., 2014
PLGA	Paclitaxel (PTX)	M234-p (mammary tumor)	mammary tumor	Four times the efficacy of existing commercial drugs	Pesoa et al., 2018
POR–PEG–PCL	fluorescence tag	HepG2 (hepatoma)	hepatoma	Good safety and biocompatibility *in vitro* and *in vivo*	Dong et al., 2016
PCL-PTSUO-PEG	TNP/DOX/ZnPC	5637 (bladder cancer cells)	Bladder carcinoma	Double insurance from TNP/ZnPC and TNP/DOX loaded in hydrogel for the management of bladder carcinoma	Huang et al., 2018
PEG–PCL–PEG, PECE	PTX	4T1 (breast cancer)	Breast cancer	Great antitumor effect and wound healing promotion.	Lei et al., 2012
PECT	PTX	MCF-7	Breast cancer	High concentration in tumor tissue for 21 days	Lin et al., 2016

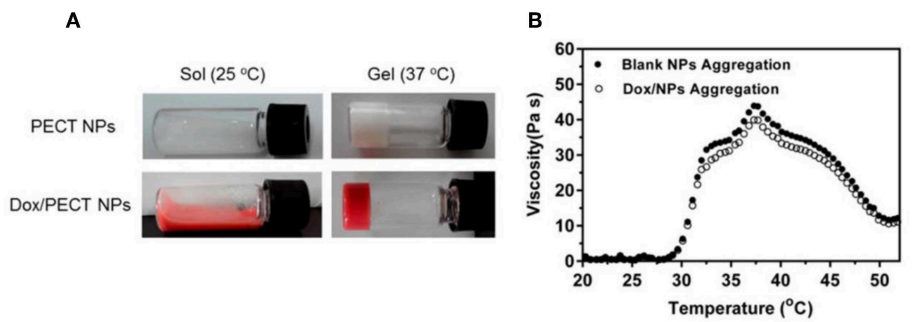

FIGURE 2 | The thermosensitive property of hydrogel. **(A)** State of the thermosensitive hydrogel at different temperatures (25°C, 37°C). **(B)** Hydrogel viscosity increase of aqueous solution as a function of temperature. Source: Reproduced, with permission, from Huang et al. (2016).

temperature is higher than 28°C. With the highest viscosity at 37°C, the hydrogel turned to gel from sol (**Figure 2**). Loaded nanoparticles were dissociated from hydrogel and diffused within tumor tissue by EPR effect. Intracellular chemical drug release limited its toxic effects and enhanced its anti-tumor effectiveness. Contrasted with intravenous drug injections (*I.V.*), a thermosensitive hydrogel with nanomedicine loaded is an efficient drug delivery system, which enabled continuous drug release around tumor tissues (Huang et al., 2016).

Two or more elements loaded in one thermosensitive hydrogel has emerged as a promising drug delivery system for its superior anti-tumor efficacy. Polo-like kinase 1 (PLK1) gene is recognized as a key regulator of tumor cell meiosis and mitosis (Ma et al., 2014). RNA interference-based on PLK1shRNA can specifically reduce the function of the target gene in the tumor. A strategy of DOX and PLK1shRNA/PEI-Lys co-delivery hydrogel was developed for the treatment of osteosarcoma (Ma et al., 2014). In this method, PLK1shRNA/PEI-Lys in the hydrogel can greatly enhance the anti-tumor effect of DOX. With the synergistic effect from PLK1shRNA/PEI-Lys and DOX, significant osteosarcoma apoptosis was caused by the co-loaded hydrogel (**Figure 3**) (Ma et al., 2014).

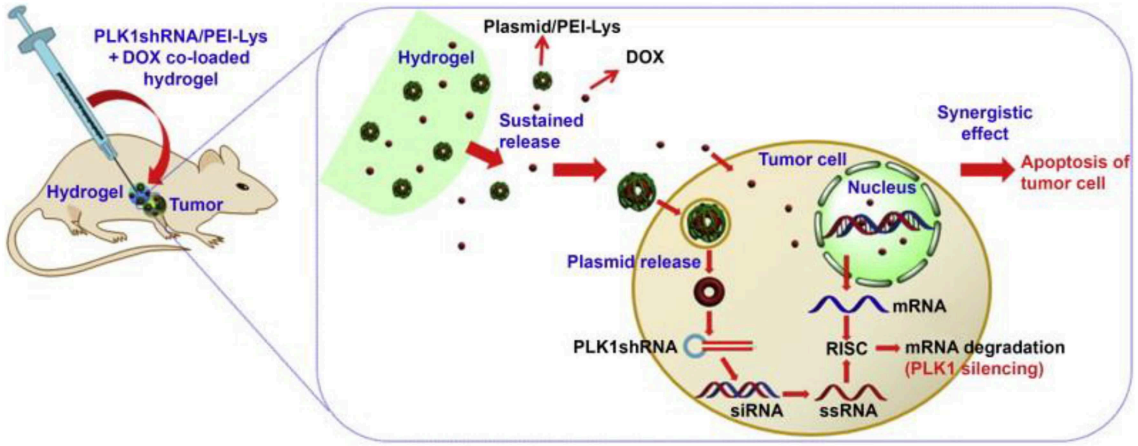

FIGURE 3 | Schematic for synergism of PLK1shRNA/PEI-Lys and DOX from the hydrogel promotes tumor apoptosis on osteosarcoma in nude mice. Reproduced, with permission, from Ma et al. (2014).

TABLE 2 | pH-sensitive hydrogels and drug delivery system.

Hydrogel	Drug	Cell line (*in vitro*)	Cancer (*in vivo*)	Characteristics and applications	References
Acrylic Acid and PEGDA	Salicylic Acid (SA)	3t3 fibroblast cells	–	Sa based pH sensitive hydrogel reveals good pH sensibility and great biocompatibility	Demirdirek and Uhrich, 2017
CS and GP	DOX	Mcf-7 cells (breast cancer)	Breast cancer	With an LCST of 39°C, the gel reveals DOX when pH =5.5	Fathi et al., 2019
Chitosan Dihydrocaffeic Acid (CS-DA) and Oxidized Pullulan (OP)	DOX and Amoxicillin	Hct116 cells (colon tumor cells) and e. Coli	Colon tumor and infection	DOX and amoxicillin co-loaded hydrogel response to pH decrease. The hydrogel is an ideal system for mucosa-localized tumor and infection management	Liang et al., 2019
GC-PF127	DOX	H22 (breast cancer)	Breast cancer	Response to small pH change, hydrogel release DOX-loaded micelles with tumor-targeted	Liu et al., 2017
CEC-PEGDA	DOX	Hepg2 (liver cancer) and l929	Liver carcinoma	Good cytocompatibility and anti-tumor effect. The pH-responsive hydrogel is a promising delivery system for liver cancer treatment	Qu et al., 2017
PEGMA and AAC	5-FU	Hepg2 (liver cancer) and LO2	Liver carcinoma	Controlled and targeted drug delivery for liver carcinoma	Yue et al., 2019
CS/HA/GP	DOX	Hela (cervical cancer)	Cervical cancer	Good pH sensitivity for the localized management of cervical cancer	Zhang et al., 2018

PH-SENSITIVE HYDROGELS

Glycolysis of tumor cells can cause acidification in the environment next to tumor tissues, resulting in lower pH value in the extracellular matrix than normal tissues (Kenney et al., 2018; Hu et al., 2019). A pH-sensitive hydrogel is a polymer gel in which the volume of the hydrogel changes depending on the pH of the external environment and the ionic strength (Liao et al., 2017; Liu et al., 2019). Such gels contain a large number of readily hydrolyzable or protonated acids, base groups such as carboxyl groups and amino groups (Lym et al., 2016). The dissociation of these groups is affected by the external pH. When the external pH changes, the degree of dissociation of these groups changes correspondingly, causing the internal and external ion concentration to change (Norouzi et al., 2016). In addition, the dissociation of these groups will destroy the corresponding hydrogen in the gel. The bond reduces the cross-linking point of the gel network, causing a change in the structure of the gel network and the degree of swelling of the hydrogel (Qu et al., 2017; Oroojalian et al., 2018). With this property, the rate of diffusion and release of the drug in the gel can be conveniently adjusted and controlled (Samanta et al., 2015).

A variety of elements for pH-sensitive hydrogel were explored in the past decades. Their characters and drug delivery systems were summarized in **Table 2**. One of the choices is based on chitosan-grafted-dihydrocaffeic acid (CS-DA) and oxidized pullulan (OP) (Liang et al., 2019). With classical drug for anti-tumor therapy, DOX-loaded hydrogel was tested to explore its

reactions for the pH changes in the tumor environment. With glycolysis in the tumor site, a decrease of pH triggered the drug release (Liang et al., 2019). Compared with the morphology of hydrogel at pH 7.4, significant disintegration of hydrogel resulted in larger pore size at pH 5.5 (**Figure 4**) (Liang et al., 2019). After 60 h at pH 5.5, more than 80% of DOX was released from the hydrogel. The hydrogel was co-cultured with Hct116 cells (colon tumor cells) to test its anti-tumor effect (Liang et al., 2019). DOX is continuously stable released from hydrogel at pH 5.5 and 7.4. In both conditions, DOX can be effectively released for more than 3 days (Liang et al., 2019).

In recent years, aspirin has been found to inhibit carbon monoxide synthase, inhibit nitrite-mediated DNA damage, reduce surviving, inhibit nuclear transcription factors, proteasomes, and calcium-activated neutral proteasome genes by inhibiting cyclooxygenase (Lu et al., 2008; Choi et al., 2013). The expression and other mechanisms play an anti-tumor effect. After loading aspirin into the hemicellulose hydrogel, it was found that 85% of the drug could be released continuously for 5–6 h under pH 7.4 (Choi et al., 2013). Sun et al. successfully prepared a series of acrylic acid and acrylamide copolymer grafted hemicellulose hydrogels by free radical polymerization (Sun et al., 2013). The combination of aspirin and the drug showed that the release rate of the drug in the simulated gastric juice was slower, and the release rate in the simulated intestinal fluid was significantly faster than that of the simulated gastric juice. When the release time was 12 h, the cumulative release rate reached 90%, which shows excellent sustained release properties (Sun et al., 2013).

In addition, Wang et al. first inserted dexamethasone phosphate into molecularly imprinted polymer nanospheres and loaded the polymer onto a pH-sensitive hydrogel, making it a biosensor that inhibits inflammation (Wang et al., 2010). Since the inflammatory reaction can lead to an acidic environment, this pH-sensitive hydrogel can rapidly release the drug at pH 6.0∼7.4 to inhibit the inflammation (Wang et al., 2010). This different method is resistant to pH-sensitive hydrogels. The application of oncology drugs has brought new ideas.

PHOTOSENSITIVE HYDROGELS

The mechanism of a light-sensitive hydrogel is divided into two types according to the properties of the photosensitive material (Chang et al., 2019). One is to directly add the photosensitive molecular material to the temperature-sensitive gel, and convert the light energy into heat energy to make the temperature inside the gel reach the phase transition temperature. In this way, hydrogel produces photosensitivity. Another kind of chromophore is introduced into the gel structure (Norouzi et al., 2016). The physicochemical properties of the chromophore are changed when subjected to light stimulation. By changing the network structure, hydrogel macroscopically exhibits photosensitivity. Usually, a structure such as azobenzene, spiropyran, o-naphthoquinone, anthracene, nitrophenyl, and coumarin is introduced into the gel (Tam et al., 2017). Among them, ruthenium, nitrophenyl, and coumarin compounds mainly take advantage of photo-cleavage photosensitive groups, which are bonded to the hydrophobic end through an aryl methyl bond (Norouzi et al., 2016; Tam et al., 2017). Under ultraviolet light or near-infrared light, the ester group is broken. The photosensitive reaction is caused. The hydrophobic end is converted to a hydrophilic end, causing the gel to dissociate. The azobenzene compound is controlled by the conversion of the cis-trans structure. Their characters and drug delivery systems were summarized in **Table 3**.

One of the applications for photosensitive hydrogels is the platform for cell culture and 3D tumor micro-environment studies. With advantages of its photosensitive character, cell detachment on the surface of hydrogel was done layer-by-layer to form a 3D cell culture medium (**Figure 5**) (Wang et al., 2014). Photoinitiated copolymerization of P (OEGMA-co-VDT-co-SPAA) (POVSP) hydrogels happened with UV irradiation. The compressive strengths of hydrogels were up to 5.1 MPa, which is strong enough for cell culture (Wang et al., 2014). It is revealed that photosensitive hydrogel is suitable for 3D cell culture model, which is vital for the study of the mechanism for tumor development.

To achieve the same purpose, a photocleavable terpolymer hydrogel was developed as the basic technique for 3D bio-printing. This hydrogel is capable of self-shaping directly to the UV irradiation. It is designable by using selective illumination to UV light with the specific area covered with darkness (**Figure 6**) (Liao et al., 2015). The printable hydrogel is an inspiring design for controlled drug delivery with district distribution. It is a key technique for the realization of 4D drug delivery with both dimensions of time and space. With drugs loaded in the 3D space of hydrogels, dynamic drug release can be realized. In this process, different drug could be controlled to be released in different time with purpose (Xu et al., 2015; Chen Y. et al., 2016; Kim et al., 2017; Guo et al., 2018). This is the typical way of 4D drug delivery with additional dimensions of time.

DUAL-SENSITIVE HYDROGELS

With the increasing requirements for the precision of controlled release of drugs, multi-sensitive hydrogels have received more and more attention (Bardajee et al., 2017). In particular, co-sensitive hydrogels for temperature and pH is widely researched. Temperature and pH are two important factors in physiological, biological, and chemical systems (Bardajee et al., 2017; Fathi et al., 2019). The temperature-pH double-sensitive hydrogel consists of a temperature-sensitive and pH-sensitive two-part hydrophilic polymer network (Lym et al., 2016). Usually formed with two or more monomers or polymers, which respond to temperature and pH, respectively.

The combination of temperature and pH sensitivity is crucial for the management of locoregional tumor recurrence (Mackiewicz et al., 2019). A novel pH-sensitive thermosensitive hydrogel loaded with modified doxorubicin-based prodrug nanoparticles (PDNPs), which is more efficient for tumor management than free DOX (Liu et al., 2019). Good biocompatibility and anti-tumor activity were verified by

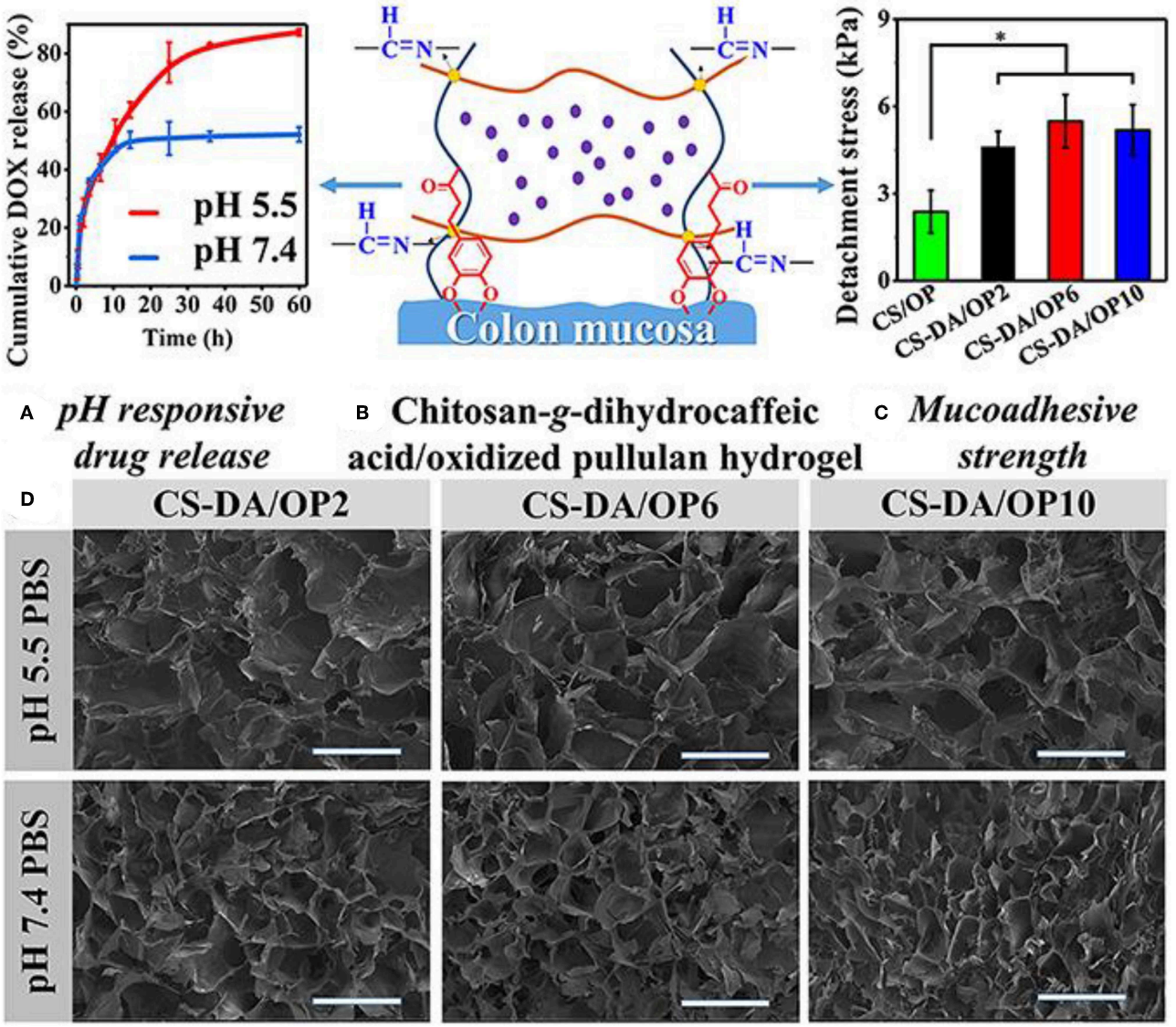

FIGURE 4 | Characters of the pH-sensitive hydrogel. **(A)** pH-responsive drug release. **(B)** Schematic for pH-sensitive hydrogel. **(C)** Mucoadhesive strength of different elements. **(D)** SEM images of the pH-sensitive hydrogel after swelling in PBS with different pH values. *$P < 0.05$. Reproduced, with permission, from Liang et al. (2019).

TABLE 3 | Photosensitive hydrogels and drug delivery system.

Hydrogel	Drug	Cell line (*in vitro*)	Cancer (*in vivo*)	Characteristics and applications	References
Hyaluronic Acid (HA)	Matrix metalloproteinase (MMP)	MDA-MB-231 cells (breast cancer)	–	Biomimetic 3D cell culture model for cancer researches.	Tam et al., 2017
DNA Polyacrylamide Conjugate (DPC)	DNA and DOX	CEM (lymphocytic leukemia)	Lymphocytic leukemia	Controlled release with DNA crosslinked inside the photo-responsive hydrogel	Kang et al., 2011
Hyperbranched polyprodrug (PPM)	PPM	A549 cells (lung cancer)	Lung Cancer	DOX and amoxicillin co-loaded hydrogel response to pH decrease. The hydrogel is an ideal system for mucosa-localized tumor and infection management	Guo et al., 2018

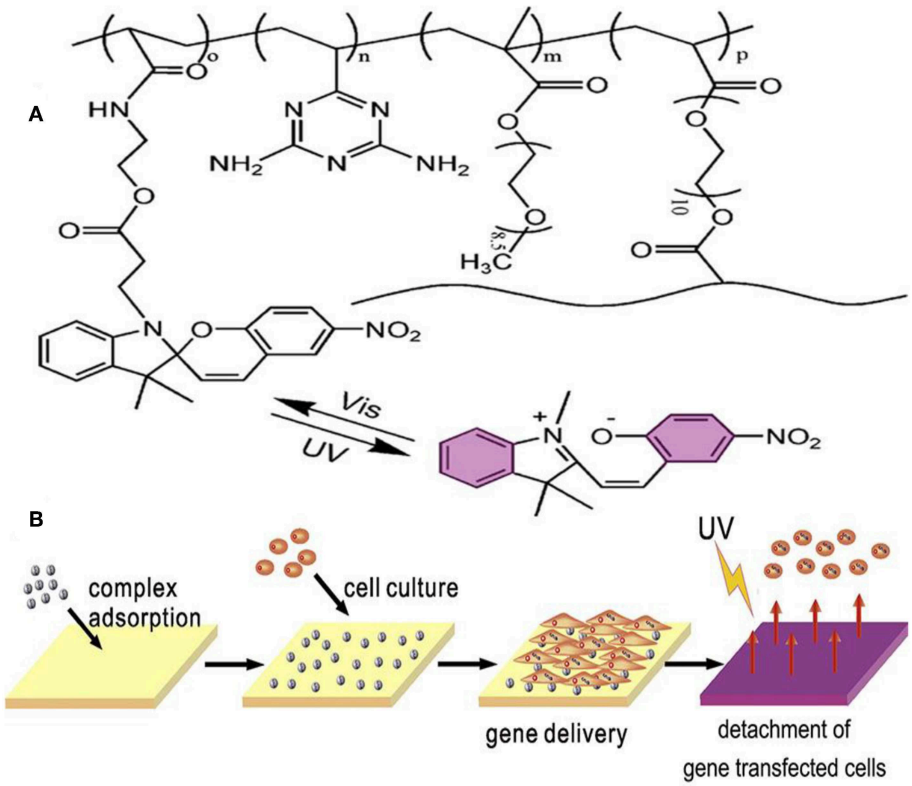

FIGURE 5 | Schematic structure and mechanism of the photosensitive hydrogel. **(A)** Schematic molecular structure of hydrogel. **(B)** UV irradiation triggers the detachment of cells from the surface of the hydrogel. Reproduced, with permission, from Wang et al. (2014).

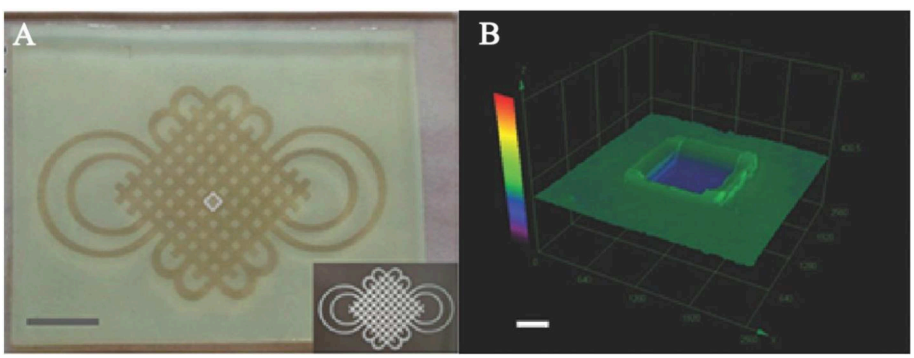

FIGURE 6 | Photoactive self-shaping hydrogel spontaneous swelling caused by UV irradiation. **(A)** Hydrogel shaped by selected UV irradiation to form a designed pattern. **(B)** 3D image of a square unit for the design of UV irradiation. Reproduced, with permission, from Liao et al. (2015).

in vitro uptake and cell toxicity. For *in vivo* experiment, 4T1 cells with luciferase-tagged expression were implanted into mice. Management by temperature and pH co-sensitive hydrogel was remarkable (**Figure 7**) (Liu et al., 2019). It is a promising strategy for preventing the locoregional recurrence of the tumor.

Co-sensitive hydrogel with dual photoluminescence was developed with PL and PNIPAM (Zhao et al., 2016). This hydrogel contains a core which was made up of a red-emission complex and a blue-emission d-TPE. This nanoparticle is sensitive to the change of temperature and pH (Zhao et al., 2016). This hydrogel is stimulated by both temperature and pH and is more adaptable to the complex environment of human body fluids. In addition, the application of two or more materials, through their interaction, not only can improve the mechanical strength of the hydrogel, but also improve the precision of controlled release. With this character, the stimuli-responsive hydrogel has a wide application in medical imaging, cancer diagnosis, and advanced antitumor drug delivery (Zhao et al., 2016).

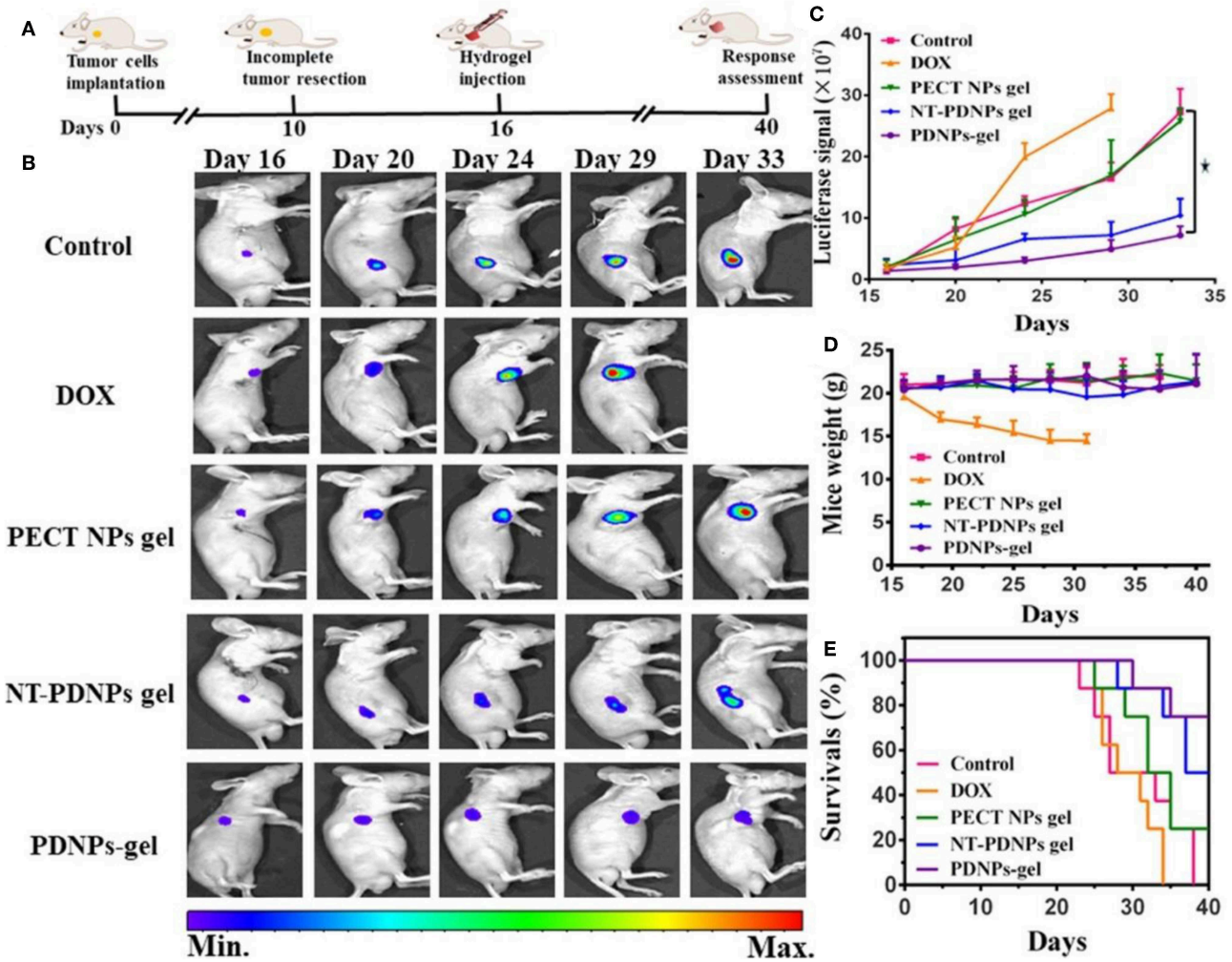

FIGURE 7 | *In vivo* luciferase-tagged tumor model with the management of hydrogel. **(A)** Experiment process. **(B)** Bioluminescence images of mice treated with different formulations, **(C)** Quantified bioluminescence for tumors in mice. **(D)** Mice weight changes. **(E)** Survival rates of mice treated with different methods. Reproduced, with permission, from Liu et al. (2019).

CONCLUSIONS

The unique character of hydrogel makes it an efficient functional medium for drug delivery (Zhang et al., 2018; Fathi et al., 2019; Mackiewicz et al., 2019). Given the limits from chemical drug toxicity for normal tissue and organs, localized drug delivery system by hydrogel has been a crucial method for cancer management. Related studies mainly focused on the delivery function and the methods of stimuli-response (Lym et al., 2016; Bardajee et al., 2017; Wei et al., 2017; Fathi et al., 2019). The smart hydrogel was developed with accurate responses to tiny changes in temperature, pH, and light. For now, drugs can be easily delivered to cancer tissue at the right time point. In the future, co-loaded drugs, including DNA, RNA, protein, and related products, would be a key point. The constantly accurate drug delivery system can realize anti-tumor drugs release followed by tissue repair factors. In this way, demission of time and space for drug delivery would be mixed in one hydrogel, making it a 4D functional hydrogel. It can make hydrogel a perfect choice for local chemotherapy and cancer management.

AUTHOR CONTRIBUTIONS

All authors listed have made a substantial, direct and intellectual contribution to the work, and approved it for publication.

ACKNOWLEDGMENTS

The financial support from Ministry of Science and Technology of China (2016YFB1101501) is gratefully acknowledged.

REFERENCES

Ahmad, R., Kaus, N. H. M., and Hamid, S. (2018). Synthesis and characterization of PLGA-PEG thymoquinone nanoparticles and its cytotoxicity effects in tamoxifen-resistant breast cancer cells. *Adv. Exp. Med. Biol.* 1, 1–18. doi: 10.1007/5584_2018_302

Andreyev, J., Ross, P., Donnellan, C., Lennan, E., Leonard, P., Waters, C., et al. (2014). Guidance on the management of diarrhoea during cancer chemotherapy. *Lancet Oncol.* 15, e447–e460. doi: 10.1016/S1470-2045(14)70006-3

Bae, W. K., Park, M. S., Lee, J. H., Hwang, J. E., Shim, H. J., Cho, S. H., et al. (2013). Docetaxel-loaded thermoresponsive conjugated linoleic acid-incorporated poloxamer hydrogel for the suppression of peritoneal metastasis of gastric cancer. *Biomaterials* 34, 1433–1441. doi: 10.1016/j.biomaterials.2012.10.077

Bardajee, G. R., Hooshyar, Z., Farsi, M., Mobini, A., and Sang, G. (2017). Synthesis of a novel thermo/pH sensitive nanogel based on salep modified graphene oxide for drug release. *Mater. Sci. Eng. C Mater. Biol. Appl.* 72, 558–565. doi: 10.1016/j.msec.2016.11.109

Batista, R. A., Espitia, P. J. P., Quintans, J. S. S., Freitas, M. M., Cerqueira, M. A., Teixeira, J. A., et al. (2019). Hydrogel as an alternative structure for food packaging systems. *Carbohydr. Polym.* 205, 106–116. doi: 10.1016/j.carbpol.2018.10.006

Bin Imran, A., Esaki, K., Gotoh, H., Seki, T., Ito, K., Sakai, Y., et al. (2014). Extremely stretchable thermosensitive hydrogels by introducing slide-ring polyrotaxane cross-linkers and ionic groups into the polymer network. *Nat. Commun.* 5:5124. doi: 10.1038/ncomms6124

Bray, F., Ferlay, J., Soerjomataram, I., Siegel, R. L., Torre, L. A., and Jemal, A. (2018). Global cancer statistics 2018: GLOBOCAN estimates of incidence and mortality worldwide for 36 cancers in 185 countries. *CA Cancer J. Clin.* 68, 394–424. doi: 10.3322/caac.21492

Bu, Y., Shen, H., Yang, F., Yang, Y., Wang, X., and Wu, D. (2017). Construction of tough, *in situ* forming double-network hydrogels with good biocompatibility. *ACS Appl. Mater. Interfaces* 9, 2205–2212. doi: 10.1021/acsami.6b15364

Bykov, V. J. N., Eriksson, S. E., Bianchi, J., and Wiman, K. G. (2018). Targeting mutant p53 for efficient cancer therapy. *Nat. Rev. Cancer* 18, 89–102. doi: 10.1038/nrc.2017.109

Casey, J., Yue, X., Nguyen, T. D., Acun, A., Zellmer, V. R., Zhang, S., et al. (2017). 3D hydrogel-based microwell arrays as a tumor microenvironment model to study breast cancer growth. *Biomed. Mater.* 12:025009. doi: 10.1088/1748-605X/aa5d5c

Castelletto, V., Edwards-Gayle, C. J. C., Greco, F., Hamley, I. W., Seitsonen, J., and Ruokolainen, J. (2019). Self-assembly, tunable hydrogel properties and selective anti- cancer activity of a carnosine-derived lipidated peptide. *ACS Appl. Mater. Interfaces* 11, 33573–33580. doi: 10.1021/acsami.9b09065

Chang, G., Zhang, H., Li, S., Huang, F., Shen, Y., and Xie, A. (2019). Effective photodynamic therapy of polymer hydrogel on tumor cells prepared using methylene blue sensitized mesoporous titania nanocrystal. *Mater. Sci. Eng. C Mater. Biol. Appl.* 99, 1392–1398. doi: 10.1016/j.msec.2019.02.056

Chen, C. H., Kuo, C. Y., Chen, S. H., Mao, S. H., Chang, C. Y., Shalumon, K. T., et al. (2018). Thermosensitive injectable hydrogel for simultaneous intraperitoneal delivery of doxorubicin and prevention of peritoneal adhesion. *Int. J. Mol. Sci.* 19:E1373. doi: 10.3390/ijms19051373

Chen, X., and Liu, Z. (2016). A pH-responsive hydrogel based on a tumor-targeting mesoporous silica nanocomposite for sustained cancer labeling and therapy. *Macromol. Rapid Commun.* 37, 1533–1539. doi: 10.1002/marc.201600261

Chen, X., Liu, Z., Parker, S. G., Zhang, X., Gooding, J. J., Ru, Y., et al. (2016). Light-induced hydrogel based on tumor-targeting mesoporous silica nanoparticles as a theranostic platform for sustained cancer treatment. *ACS Appl. Mater. Interfaces* 8, 15857–15863. doi: 10.1021/acsami.6b02562

Chen, Y., Hao, Y., Huang, Y., Wu, W., Liu, X., Li, Y., et al. (2019). An injectable, near-infrared light-responsive click cross-linked azobenzene hydrogel for breast cancer chemotherapy. *J. Biomed. Nanotechnol.* 15, 1923–1936. doi: 10.1166/jbn.2019.2821

Chen, Y., Zhang, F., Fu, Q., Liu, Y., Wang, Z., and Qi, N. (2016). *In vitro* proliferation and osteogenic differentiation of human dental pulp stem cells in injectable thermo-sensitive chitosan/beta-glycerophosphate/hydroxyapatite hydrogel. *J. Biomater. Appl.* 31, 317–327. doi: 10.1177/0885328216661566

Cheng, C., Meng, Y., Zhang, Z., Li, Y., and Zhang, Q. (2018). Tumoral acidic pH-responsive cis-diaminodichloroplatinum-incorporated Cy5.5-PEG- g-A-HA nanoparticles for targeting delivery of CDDP against cervical cancer. *ACS Appl. Mater. Interfaces* 10, 26882–26892. doi: 10.1021/acsami.8b07425

Choi, B. H., Chakraborty, G., Baek, K., and Yoon, H. S. (2013). Aspirin-induced Bcl-2 translocation and its phosphorylation in the nucleus trigger apoptosis in breast cancer cells. *Exp. Mol. Med.* 45:e47. doi: 10.1038/emm.2013.91

Deepa, G., Thulasidasan, A. K., Anto, R. J., Pillai, J. J., and Kumar, G. S. (2012). Cross-linked acrylic hydrogel for the controlled delivery of hydrophobic drugs in cancer therapy. *Int. J. Nanomed.* 7, 4077–4088. doi: 10.2147/IJN.S30149

Del Bufalo, F., Manzo, T., Hoyos, V., Yagyu, S., Caruana, I., Jacot, J., et al. (2016). 3D modeling of human cancer: a PEG-fibrin hydrogel system to study the role of tumor microenvironment and recapitulate the *in vivo* effect of oncolytic adenovirus. *Biomaterials* 84, 76–85. doi: 10.1016/j.biomaterials.2016.01.030

Demirdirek, B., and Uhrich, K. E. (2017). Novel salicylic acid-based chemically crosslinked pH-sensitive hydrogels as potential drug delivery systems. *Int. J. Pharm.* 528, 406–415. doi: 10.1016/j.ijpharm.2017.05.047

Dong, X., Wei, C., Lu, L., Liu, T., and Lv, F. (2016). Fluorescent nanogel based on four-arm PEG-PCL copolymer with porphyrin core for bioimaging. *Mater. Sci. Eng. C Mater. Biol. Appl.* 61, 214–219. doi: 10.1016/j.msec.2015.12.037

Elias, P. Z., Liu, G. W., Wei, H., Jensen, M. C., Horner, P. J., and Pun, S. H. (2015). A functionalized, injectable hydrogel for localized drug delivery with tunable thermosensitivity: synthesis and characterization of physical and toxicological properties. *J. Control. Release* 208, 76–84. doi: 10.1016/j.jconrel.2015.03.003

Fan, R., Tong, A., Li, X., Gao, X., Mei, L., Zhou, L., et al. (2015). Enhanced antitumor effects by docetaxel/LL37-loaded thermosensitive hydrogel nanoparticles in peritoneal carcinomatosis of colorectal cancer. *Int. J. Nanomed.* 10, 7291–7305. doi: 10.2147/IJN.S89066

Fathi, M., Alami-Milani, M., Geranmayeh, M. H., Barar, J., Erfan-Niya, H., and Omidi, Y. (2019). Dual thermo-and pH-sensitive injectable hydrogels of chitosan/(poly(N-isopropylacrylamide-co-itaconic acid)) for doxorubicin delivery in breast cancer. *Int. J. Biol. Macromol.* 128, 957–964. doi: 10.1016/j.ijbiomac.2019.01.122

Gajendiran, M., Jo, H., Kim, K., and Balasubramanian, S. (2019). Green synthesis of multifunctional PEG-carboxylate pi back-bonded gold nanoconjugates for breast cancer treatment. *Int. J. Nanomed.* 14, 819–834. doi: 10.2147/IJN.S190946

Gu, D., O'Connor, A. J., G, G. H. Q., and Ladewig, K. (2017). Hydrogels with smart systems for delivery of hydrophobic drugs. *Expert Opin. Drug Deliv.* 14, 879–895. doi: 10.1080/17425247.2017.1245290

Guo, D., Xu, S., Huang, Y., Jiang, H., Yasen, W., Wang, N., et al. (2018). Platinum(IV) complex-based two-in-one polyprodrug for a combinatorial chemo-photodynamic therapy. *Biomaterials* 177, 67–77. doi: 10.1016/j.biomaterials.2018.05.052

Guo, D. D., Hong, S. H., Jiang, H. L., Kim, J. H., Minai-Tehrani, A., Kim, J. E., et al. (2012). Synergistic effects of Akt1 shRNA and paclitaxel-incorporated conjugated linoleic acid-coupled poloxamer thermosensitive hydrogel on breast cancer. *Biomaterials* 33, 2272–2281. doi: 10.1016/j.biomaterials.2011.12.011

Hu, S. W., Wang, J., Zhang, T. T., Li, X. L., Chen, H. Y., and Xu, J. J. (2019). Targeted transmembrane delivery of Ca(2+) via FA-nanogel for synergistically enhanced chemotherapy. *ACS Appl. Mater. Interfaces* 11, 16412–16420. doi: 10.1021/acsami.9b04967

Huang, P., Song, H., Zhang, Y., Liu, J., Zhang, J., Wang, W., et al. (2016). Bridging the gap between macroscale drug delivery systems and nanomedicines: a nanoparticle-assembled thermosensitive hydrogel for peritumoral chemotherapy. *ACS Appl. Mater. Interfaces* 8, 29323–29333. doi: 10.1021/acsami.6b10416

Huang, Z., Xiao, H., Lu, X., Yan, W., and Ji, Z. (2018). Enhanced photo/chemo combination efficiency against bladder tumor by encapsulation of DOX and ZnPC into *in situ*-formed thermosensitive polymer hydrogel. *Int. J. Nanomed.* 13, 7623–7631. doi: 10.2147/IJN.S179226

Kang, H., Liu, H., Zhang, X., Yan, J., Zhu, Z., Peng, L., et al. (2011). Photoresponsive DNA-cross-linked hydrogels for controllable release and cancer therapy. *Langmuir* 27, 399–408. doi: 10.1021/la1037553

Kenney, R. M., Boyce, M. W., Whitman, N. A., Kromhout, B. P., and Lockett, M. R. (2018). A pH-sensing optode for mapping spatiotemporal

gradients in 3D paper-based cell cultures. *Anal. Chem.* 90, 2376–2383. doi: 10.1021/acs.analchem.7b05015

Kerdsirichairat, T., Narang, A. K., Thompson, E., Kim, S. H., Rao, A., Ding, K., et al. (2019). Hydrogel spacer for borderline resectable and locally advanced pancreatic cancer: a feasibility human study. *Gastroenterology* 157, 933–935. doi: 10.1053/j.gastro.2019.07.012

Kim, Y. M., Potta, T., Park, K. H., and Song, S. C. (2017). Temperature responsive chemical crosslinkable UV pretreated hydrogel for application to injectable tissue regeneration system via differentiations of encapsulated hMSCs. *Biomaterials* 112, 248–256. doi: 10.1016/j.biomaterials.2016.10.025

Klouda, L. (2015). Thermoresponsive hydrogels in biomedical applications: a seven-year update. *Eur. J. Pharm. Biopharm.* 97(Pt B), 338–349. doi: 10.1016/j.ejpb.2015.05.017

Le, P. N., Huynh, C. K., and Tran, N. Q. (2018). Advances in thermosensitive polymer-grafted platforms for biomedical applications. *Mater. Sci. Eng. C Mater. Biol. Appl.* 92, 1016–1030. doi: 10.1016/j.msec.2018.02.006

Lei, N., Gong, C., Qian, Z., Luo, F., Wang, C., Wang, H., et al. (2012). Therapeutic application of injectable thermosensitive hydrogel in preventing local breast cancer recurrence and improving incision wound healing in a mouse model. *Nanoscale* 4, 5686–5693. doi: 10.1039/c2nr30731f

Liang, Y., Zhao, X., Ma, P. X., Guo, B., Du, Y., and Han, X. (2019). pH-responsive injectable hydrogels with mucosal adhesiveness based on chitosan-grafted-dihydrocaffeic acid and oxidized pullulan for localized drug delivery. *J. Colloid Interface Sci.* 536, 224–234. doi: 10.1016/j.jcis.2018.10.056

Liao, W. C., Lilienthal, S., Kahn, J. S., Riutin, M., Sohn, Y. S., Nechushtai, R., et al. (2017). pH- and ligand-induced release of loads from DNA-acrylamide hydrogel microcapsules. *Chem. Sci.* 8, 3362–3373. doi: 10.1039/C6SC04770J

Liao, Y., An, N., Wang, N., Zhang, Y., Song, J., Zhou, J., et al. (2015). Photoactive self-shaping hydrogels as noncontact 3D macro/microscopic photoprinting platforms. *Macromol. Rapid Commun.* 36, 2129–2136. doi: 10.1002/marc.201500390

Lin, Z., Xu, S., Gao, W., Hu, H., Chen, M., Wang, Y., et al. (2016). A comparative investigation between paclitaxel nanoparticle- and nanocrystal-loaded thermosensitive PECT hydrogels for peri-tumoural administration. *Nanoscale* 8, 18782–18791. doi: 10.1039/C6NR05498F

Liu, H., Shi, X., Wu, D., Kahsay Khshen, F., Deng, L., Dong, A., et al. (2019). Injectable, biodegradable, thermosensitive nanoparticles-aggregated hydrogel with tumor-specific targeting, penetration, and release for efficient postsurgical prevention of tumor recurrence. *ACS Appl. Mater. Interfaces* 11, 19700–19711. doi: 10.1021/acsami.9b01987

Liu, Z., Xu, G., Wang, C., Li, C., and Yao, P. (2017). Shear-responsive injectable supramolecular hydrogel releasing doxorubicin loaded micelles with pH-sensitivity for local tumor chemotherapy. *Int. J. Pharm.* 530, 53–62. doi: 10.1016/j.ijpharm.2017.07.063

Lu, M., Strohecker, A., Chen, F., Kwan, T., Bosman, J., Jordan, V. C., et al. (2008). Aspirin sensitizes cancer cells to TRAIL-induced apoptosis by reducing survivin levels. *Clin. Cancer Res.* 14, 3168–3176. doi: 10.1158/1078-0432.CCR-07-4362

Luo, Y., Wei, X., Wan, Y., Lin, X., Wang, Z., and Huang, P. (2019). 3D printing of hydrogel scaffolds for future application in photothermal therapy of breast cancer and tissue repair. *Acta Biomater.* 92, 37–47. doi: 10.1016/j.actbio.2019.05.039

Lym, J. S., Nguyen, Q. V., Ahn da, W., Huynh, C. T., Jae, H. J., Kim, Y. I., et al. (2016). Sulfamethazine-based pH-sensitive hydrogels with potential application for transcatheter arterial chemoembolization therapy. *Acta Biomater.* 41, 253–263. doi: 10.1016/j.actbio.2016.05.018

Ma, H., He, C., Cheng, Y., Li, D., Gong, Y., Liu, J., et al. (2014). PLK1shRNA and doxorubicin co-loaded thermosensitive PLGA-PEG-PLGA hydrogels for osteosarcoma treatment. *Biomaterials* 35, 8723–8734. doi: 10.1016/j.biomaterials.2014.06.045

Ma, H., He, C., Cheng, Y., Yang, Z., Zang, J., Liu, J., et al. (2015). Localized co-delivery of doxorubicin, cisplatin, and methotrexate by thermosensitive hydrogels for enhanced osteosarcoma treatment. *ACS Appl. Mater. Interfaces* 7, 27040–27048. doi: 10.1021/acsami.5b09112

Mackiewicz, M., Romanski, J., Drabczyk, K., Waleka, E., Stojek, Z., and Karbarz, M. (2019). Degradable, thermo-, pH- and redox-sensitive hydrogel microcapsules for burst and sustained release of drugs. *Int. J. Pharm.* 569:118589. doi: 10.1016/j.ijpharm.2019.118589

Milcovich, G., Lettieri, S., Antunes, F. E., Medronho, B., Fonseca, A. C., Coelho, J. F. J., et al. (2017). Recent advances in smart biotechnology: hydrogels and nanocarriers for tailored bioactive molecules depot. *Adv. Colloid Interface Sci.* 249, 163–180. doi: 10.1016/j.cis.2017.05.009

Murgia, X., Loretz, B., Hartwig, O., Hittinger, M., and Lehr, C. M. (2018). The role of mucus on drug transport and its potential to affect therapeutic outcomes. *Adv. Drug Deliv. Rev.* 124, 82–97. doi: 10.1016/j.addr.2017.10.009

Norouzi, M., Nazari, B., and Miller, D. W. (2016). Injectable hydrogel-based drug delivery systems for local cancer therapy. *Drug Discov. Today* 21, 1835–1849. doi: 10.1016/j.drudis.2016.07.006

Oroojalian, F., Babaei, M., Taghdisi, S. M., Abnous, K., Ramezani, M., and Alibolandi, M. (2018). Encapsulation of thermo-responsive gel in pH-sensitive polymersomes as dual-responsive smart carriers for controlled release of doxorubicin. *J. Control. Release* 288, 45–61. doi: 10.1016/j.jconrel.2018.08.039

Pan, A., Wang, Z., Chen, B., Dai, W., Zhang, H., He, B., et al. (2018). Localized co-delivery of collagenase and trastuzumab by thermosensitive hydrogels for enhanced antitumor efficacy in human breast xenograft. *Drug Deliv.* 25, 1495–1503. doi: 10.1080/10717544.2018.1474971

Pesoa, J. I., Rico, M. J., Rozados, V. R., Scharovsky, O. G., Luna, J. A., and Mengatto, L. N. (2018). Paclitaxel delivery system based on poly(lactide-co-glycolide) microparticles and chitosan thermo-sensitive gel for mammary adenocarcinoma treatment. *J. Pharm. Pharmacol.* 70, 1494–1502. doi: 10.1111/jphp.13006

Qu, J., Zhao, X., Ma, P. X., and Guo, B. (2017). pH-responsive self-healing injectable hydrogel based on N-carboxyethyl chitosan for hepatocellular carcinoma therapy. *Acta Biomater.* 58, 168–180. doi: 10.1016/j.actbio.2017.06.001

Ren, S., Dai, Y., Li, C., Qiu, Z., Wang, X., Tian, F., et al. (2016). Pharmacokinetics and pharmacodynamics evaluation of a thermosensitive chitosan based hydrogel containing liposomal doxorubicin. *Eur. J. Pharm. Sci.* 92, 137–145. doi: 10.1016/j.ejps.2016.07.002

Roy, S., and Trinchieri, G. (2017). Microbiota: a key orchestrator of cancer therapy. *Nat. Rev. Cancer* 17, 271–285. doi: 10.1038/nrc.2017.13

Salis, A., Rassu, G., Budai-Szucs, M., Benzoni, I., Csányi, E., Berkó, S., et al. (2015). Development of thermosensitive chitosan/glicerophospate injectable *in situ* gelling solutions for potential application in intraoperative fluorescence imaging and local therapy of hepatocellular carcinoma: a preliminary study. *Expert Opin. Drug Deliv.* 12, 1583–1596. doi: 10.1517/17425247.2015.1042452

Samanta, D., Meiser, J. L., and Zare, R. N. (2015). Polypyrrole nanoparticles for tunable, pH-sensitive and sustained drug release. *Nanoscale* 7, 9497–9504. doi: 10.1039/C5NR02196K

Sapino, S., Chirio, D., Peira, E., Abellán Rubio, E., Brunella, V., Jadhav, S. A., et al. (2019). Ocular drug delivery: a special focus on the thermosensitive approach. *Nanomaterials* 9:884. doi: 10.3390/nano9060884

Senft, D., Qi, J., and Ronai, Z. A. (2018). Ubiquitin ligases in oncogenic transformation and cancer therapy. *Nat. Rev. Cancer* 18, 69–88. doi: 10.1038/nrc.2017.105

Sheu, M. T., Jhan, H. J., Su, C. Y., Chen, L. C., Chang, C. E., Liu, D. Z., et al. (2016). Codelivery of doxorubicin-containing thermosensitive hydrogels incorporated with docetaxel-loaded mixed micelles enhances local cancer therapy. *Colloids Surf. B Biointerfaces* 143, 260–270. doi: 10.1016/j.colsurfb.2016.03.054

Sivaram, S., Majumdar, G., Perin, D., Nessa, A., Broeders, M., Lynge, E., et al. (2018). Population-based cancer screening programmes in low-income and middle-income countries: regional consultation of the International Cancer Screening Network in India. *Lancet Oncol.* 19, e113–e122. doi: 10.1016/S1470-2045(18)30003-2

Sun, X. F., Wang, H. H., Jing, Z. X., and Mohanathas, R. (2013). Hemicellulose-based pH-sensitive and biodegradable hydrogel for controlled drug delivery. *Carbohydr. Polym.* 92, 1357–1366. doi: 10.1016/j.carbpol.2012.10.032

Tam, R. Y., Smith, L. J., and Shoichet, M. S. (2017). Engineering cellular microenvironments with photo- and enzymatically responsive hydrogels: toward biomimetic 3D cell culture models. *Acc. Chem. Res.* 50, 703–713. doi: 10.1021/acs.accounts.6b00543

Wang, C., Javadi, A., Ghaffari, M., and Gong, S. (2010). A pH-sensitive molecularly imprinted nanospheres/hydrogel composite as a coating for implantable biosensors. *Biomaterials* 31, 4944–4951. doi: 10.1016/j.biomaterials.2010.02.073

Wang, N., Zhang, J., Sun, L., Wang, P., and Liu, W. (2014). Gene-modified cell detachment on photoresponsive hydrogels strengthened through hydrogen bonding. *Acta Biomater.* 10, 2529–2538. doi: 10.1016/j.actbio.2014.02.017

Wang, W., Song, H., Zhang, J., Li, P., Li, C., Wang, C., et al. (2015). An injectable, thermosensitive and multicompartment hydrogel for simultaneous encapsulation and independent release of a drug cocktail as an effective combination therapy platform. *J. Control. Release* 203, 57–66. doi: 10.1016/j.jconrel.2015.02.015

Wang, X., Li, D., Yang, F., Shen, H., Li, Z., and Wu, D. (2013). Controlled cross-linking strategy: from hybrid hydrogels to nanoparticle macroscopic aggregates. *Polym. Chem.* 4, 4596–4600. doi: 10.1039/c3py00811h

Wang, X., Wang, J., Wu, W., and Li, H. (2016). Vaginal delivery of carboplatin-loaded thermosensitive hydrogel to prevent local cervical cancer recurrence in mice. *Drug Deliv.* 23, 3544–3551. doi: 10.1080/10717544.2016.1205158

Wang, X., Wang, J., Yang, Y., Yang, F., and Wu, D. (2017). Fabrication of multi-stimuli responsive supramolecular hydrogels based on host-guest inclusion complexation of a tadpole-shaped cyclodextrin derivative with the azobenzene dimer. *Polym. Chem.* 8, 3901–3909. doi: 10.1039/C7PY00698E

Wei, L., Chen, J., Zhao, S., Ding, J., and Chen, X. (2017). Thermo-sensitive polypeptide hydrogel for locally sequential delivery of two-pronged antitumor drugs. *Acta Biomater.* 58, 44–53. doi: 10.1016/j.actbio.2017.05.053

Xu, Y., Li, Z., Li, X., Fan, Z., Liu, Z., Xie, X., et al. (2015). Regulating myogenic differentiation of mesenchymal stem cells using thermosensitive hydrogels. *Acta Biomater.* 26, 23–33. doi: 10.1016/j.actbio.2015.08.010

Yang, Y., Wang, X., Yang, F., Wang, L., and Wu, D. (2018). Highly elastic and ultratough hybrid ionic-covalent hydrogels with tunable structures and mechanics. *Adv. Mater. Weinheim.* 30:e1707071. doi: 10.1002/adma.201707071

Yang, Y., Zhao, H., Jia, Y., Guo, Q., Qu, Y., Su, J., et al. (2016). A novel gene delivery composite system based on biodegradable folate-poly (ester amine) polymer and thermosensitive hydrogel for sustained gene release. *Sci. Rep.* 6:21402. doi: 10.1038/srep21402

Yang, Y. Y., Wang, X., Yang, F., Shen, H., and Wu, D. (2016). A universal soaking strategy to convert composite hydrogels into extremely tough and rapidly recoverable double-network hydrogels. *Adv. Mater.* 28, 7178–7184. doi: 10.1002/adma.201601742

Yue, Z., Che, Y., Jin, Z., Wang, S., Ma, Q., Zhang, Q., et al. (2019). A facile method to fabricate thermo- and pH-sensitive hydrogels with good mechanical performance based on poly(ethylene glycol) methyl ether methacrylate and acrylic acid as a potential drug carriers. *J. Biomater. Sci. Polym. Ed.* 30, 1375–1398. doi: 10.1080/09205063.2019.1634859

Zhang, J., Wang, X., Wang, L., Yang, F., and Wu, D. (2015). Controlled cross-linking strategy for formation of hydrogels, microgels and nanogels. *J. Control. Release* 213:e25. doi: 10.1016/j.jconrel.2015.05.038

Zhang, W., Jin, X., Li, H., Zhang, R. R., and Wu, C. W. (2018). Injectable and body temperature sensitive hydrogels based on chitosan and hyaluronic acid for pH sensitive drug release. *Carbohydr. Polym.* 186, 82–90. doi: 10.1016/j.carbpol.2018.01.008

Zhao, Y., Shi, C., Yang, X., Shen, B., Sun, Y., Chen, Y., et al. (2016). pH- and temperature-sensitive hydrogel nanoparticles with dual photoluminescence for bioprobes. *ACS Nano* 10, 5856–5863. doi: 10.1021/acsnano.6b00770

Zhou, J., Yu, G., and Huang, F. (2017). Supramolecular chemotherapy based on host-guest molecular recognition: a novel strategy in the battle against cancer with a bright future. *Chem. Soc. Rev.* 46, 7021–7053. doi: 10.1039/C6CS00898D

Conflict of Interest: The authors declare that the research was conducted in the absence of any commercial or financial relationships that could be construed as a potential conflict of interest.

frontiers in Chemistry

ORIGINAL RESEARCH
published: 17 October 2019
doi: 10.3389/fchem.2019.00682

A Tetra-PEG Hydrogel Based Aspirin Sustained Release System Exerts Beneficial Effects on Periodontal Ligament Stem Cells Mediated Bone Regeneration

Yunfan Zhang[1†], Ning Ding[2†], Ting Zhang[1], Qiannan Sun[1], Bing Han[1] and Tingting Yu[1*]*

[1] Department of Orthodontics, Peking University School and Hospital of Stomatology & National Engineering Laboratory for Digital and Material Technology of Stomatology & Beijing Key Laboratory of Digital Stomatology, Beijing, China, [2] School of Life Science and Medicine, Dalian University of Technology, Panjin, China

OPEN ACCESS

Edited by:
Xing Wang,
Institute of Chemistry (CAS), China

Reviewed by:
Lesan Yan,
University of Pennsylvania, United States
Yao Liu,
China Medical University, China
Xiaoxing Kou,
Sun Yat-sen University, China

***Correspondence:**
Bing Han
kqbinghan@bjmu.edu.cn
Tingting Yu
tiffanyutt@126.com

[†]*These authors have contributed equally to this work as co-first authors*

Specialty section:
This article was submitted to Polymer Chemistry, a section of the journal Frontiers in Chemistry

Received: *20 August 2019*
Accepted: *01 October 2019*
Published: *17 October 2019*

Citation:
Zhang Y, Ding N, Zhang T, Sun Q, Han B and Yu T (2019) A Tetra-PEG Hydrogel Based Aspirin Sustained Release System Exerts Beneficial Effects on Periodontal Ligament Stem Cells Mediated Bone Regeneration. Front. Chem. 7:682. doi: 10.3389/fchem.2019.00682

Bone defects, massive bone defects in particular, is still an issue clinically. Acetylsalicylic acid (ASA), also known as aspirin, has been proven to be conducive for mesenchymal stem cells osteogenic differentiation, which may be benefited for bone regeneration. In order to achieve a more appealing prognosis of bone defect, here we develop a well-defined tetra-PEG hydrogel sealant with rapid gelation speed, strong tissue adhesion, and high mechanical strength. After *in-situ* encapsulation of aspirin, this drug-loaded tetra-PEG hydrogel possessed a sustained release, anti-inflammation, and osteoinductive properties. *In vitro* experiments showed that the cell proliferation was slightly facilitated, and the osteogenic differentiation was notably augmented when periodontal ligament stem cells (PDLSCs) were co-incubating with the hydrogel materials. Moreover, *in vivo* study manifested that the aspirin sustained release system significantly facilitated the PDLSCs mediated bone defect regeneration. Overall, tetra-PEG hydrogel-based aspirin sustained release system is applicable not only for enhancing the osteogenesis capacity of PDLSC but also providing a new thought of bone regenerative therapy.

Keywords: hydrogel, drug delivery system, periodontal ligament stem cell, bone regeneration, aspirin

INTRODUCTION

Autologous and allogenic bone grafts are currently the most common used therapeutic strategies for treating bone defect (Miller and Chiodo, 2016; Panagopoulos et al., 2017). However, the high cost of the bone harvesting procedures accompanied with donor site inflammation, pain, and hematomas limited its therapeutic usage. In comparison to currently available treatment modalities, mesenchymal stem cells (MSCs) based bone tissue engineering was indicated as an advantageous alternative therapeutic option for bone tissue regeneration (Botelho et al., 2017; Confalonieri et al., 2018), including high-quality regeneration capacity, low risk of autoimmune rejection, and no donor-site harvesting procedure.

Mesenchymal stem cells are existing in multiple tissue types, including the craniofacial, and dental tissues. It has been reported that orofacial tissues derived MSCs obtained superior

proliferation, immunomodulation, and multiple-lineage differentiation abilities when compared with bone marrow derived mesenchymal stem cells (BMMSCs) (Gronthos et al., 2000; Seo et al., 2004; Zhang et al., 2009). Moreover, the neural crest origin of these MSCs makes them attractive for craniofacial regeneration strategies (Zheng et al., 2009; Xuan et al., 2018). Among the dental derived MSCs, periodontal ligament stem cells (PDLSCs) is of particular interest. It was reported that *ex vivo*-expanded PDLSCs was capable of achieving better bone regeneration capacity compared with other types of dental derived MSCs (Moshaverinia et al., 2014), and they could be easily collected in dental clinic from discarded tissue samples.

Mesenchymal stem cells biological behaviors can be affected by various factors, the recipient local microenvironment in which immune cells and cytokines may modulate MSCs mediated bone regeneration capacity (Liu et al., 2011). Acetylsalicylic acid (ASA) is one of the most widely used non-steroidal anti-inflammatory drugs (NSAIDs) that affects multiple biological process. It has been reported that ASA could be used in rodent osteoporosis treatment through activated osteoblasts and inhibited osteoclasts (Yamaza et al., 2008). When treated on MSCs, ASA is capable of elevating BMMSCs-mediated bone regeneration (Liu et al., 2011) and improving stem cells from human exfoliated deciduous teeth (SHED) osteogenic differentiation capacity (Liu et al., 2015). However, as ASA possessed a rapid dissolution profile and short half-life *in vivo* (Bliden et al., 2016), fabricating a suitable scaffold and delivery system to carry and sustain ASA efficacy at the site of bone repair is essential.

Among the biomaterials, hydrogels possess great potential in utilizing as delivery scaffolds for bone regeneration (Tan et al., 2019; Xu et al., 2019). Unlike other sustained release drug delivery systems, nanoparticles, for instance, hydrogels are comprised of a large amount of water within their 3D networks, which are excellent biomimicry for extracellular matrix. As tissue engineering scaffolds, hydrogels compose variable molecules which endue hydrogels diverse mechanical and biological properties (Seliktar, 2012), which have attracted great attentions in applications of drug release matrices, tissue-engineering scaffolds and coating biomaterials. However, most of hydrogels are generally mechanically soft or brittle, significantly limiting their scope of applications. A series of high-tough hydrogels like nanocomposite (NC) hydrogels, sliding-ring (SR) hydrogels, tetra-polyethylene glycol hydrogels (tetra-PEG hydrogels), ionically cross-linked hydrogels, and double-network (DN) hydrogels were well-developed in recent years (Tao et al., 2009; Yang et al., 2016, 2018; Bu et al., 2017). Wherein, tetra-PEG hydrogels were recognized as an ideal homogeneous biomaterial on account of the essentially non-immunogenic, antifouling, and biocompatible properties. In addition, tetra-PEG hydrogels have more advantages on facilely functional modification for construction of more-functional biomaterials in a convenient and practical way. In the present study, we investigated whether tetra-PEG hydrogels loaded with aspirin (PEG-ASA) complex is a suitable scaffold for delivering aspirin locally, and we hypothesized that the PEG-ASA complex might serve as an ideal approach for PDLSCs-mediated bone regeneration. We established the critical sized cranial bone defect on mice and analyzed the capability of the PEG-ASA complex to promote PDLSCs-mediated bone repair. The data may provide a new therapeutic strategy for achieving anti-inflammation and bone regeneration in repairing cranial bone defects.

MATERIALS AND METHODS

Human PDLSCs Isolation and Cultivation

Periodontal ligament tissues were acquired from healthy premolars due to orthodontic treatment. The donors were aged from 18 to 25 years without any history of periodontitis or tooth decay. The protocol of PDLSCs isolation and cultivation was in accordance with previous publication (Seo et al., 2004). P3 cells are used in all experiments. The experiment procedure was approved by the Ethical Guidelines of Peking University (PKUSSIRB-201311103).

In vitro Osteogenic Differentiation Assay

2×10^4 PDLSCs were seeded per well in 12-well plates (Corning Incorporated, USA). The cells were cultured in growth medium (GM) containing α-modified Eagle's medium (Corning Incorporated), 15% fetal bovine serum (FBS, Biological Industries, Israel), and 1% penicillin/streptomycin (Solarbio Life Sciences, China) at 37°C and humidified 5% CO_2. Then growth medium was replaced by osteogenic differentiation medium (ODM) containing α-modified Eagle's medium (Corning Incorporated), 15% FBS (Biological Industries), 1% penicillin/streptomycin (Solarbio Life Sciences), 0.01 μM Dexamethasone sodium phosphate (Sigma-Aldrich, USA), 1.8 mM KH_2PO_4, 0.1 mM L-ascorbic acid phosphate (Sigma-Aldrich), and 2 mM glutamine (Gibco, USA) when the cell confluence reached 70–80%. The ASA (Cat. A2093, Sigma-Aldrich) and hydrogel degradation (HD) was added into medium at the same time to reach a specific concentration (ASA: 0, 50, 100, 200, and 400 μg/mL; HD: 0 μg/mL, 10 μg/mL). The medium was replaced every 2 days. Alizarin red s staining was conducted at day 14 after osteogenesis induction. The cells were fixed by 60% isopropanol. After rehydrated in distilled water, 1% Alizarin red s (Sigma-Aldrich) solution was used to stain. The stain was removed. Cells were rinsed by distilled water 3 times and dried at room temperature. ImageJ (ver. 1.8.0; NIH, USA) were used to quantify the stained areas and shown as a percentage of the total area.

Real-Time PCR

PDLSCs were cultivated in ODM with specific concentration of ASA (0, 50, 100, 200, and 400 μg/mL) and HD (0 μg/mL, 10 μg/mL) for 7 days. The total RNA was extracted following manufacturer's instruction by TRIzol reagent (Cat. 15596026, Invitrogen, USA). RNA concentration was measured by NanoDrop 8000 (Thermal Fisher Scientific, USA). 1 μg total RNA was reverse-transcribed to cDNA by PrimeScript RT Reagent Kit (Cat. RR037A, Takara Bio Inc., Japan). Quantitative PCR (qPCR) was performed by FastStart Universal SYBR Green Master (Cat. 04913914001, Roche, Swiss) on ABI Prism 7500 Real-Time PCR System (Applied Biosystem, USA). The gene expression was normalized by *GAPDH*. The result was analyzed by $2^{(-\Delta\Delta C_T)}$ method. The primers sequences are listed in **Table 1**.

TABLE 1 | Sequences of quantitative polymerase chain reaction primers.

Gene	Forward primer (5′-3′)	Reverse primer (5′-3′)
GAPDH	GGAGCGAGATCCCTCCAAAAT	GGCTGTTGTCATACTTCTCATGG
RUNX2	TGGTTACTGTCATGGCGGGTA	TCTCAGATCGTTGAACCTTGCTA
ALP	AACATCAGGGACATTGACGTG	GTATCTCGGTTTGAAGCTCTTCC
OCN	CACTCCTCGCCCTATTGGC	CCCTCCTGCTTGGACACAAAG

GAPDH, glyceraldehyde-3-phosphate dehydrogenase; RUNX2, runt-related transcription factor 2; ALP, alkaline phosphatase; OCN, osteocalcin.

Synthesis of Tetra-PEG-SG

The tetra-PEG-SG was prepared in two steps. Firstly, the intermediate product tetra-armed poly (ethylene glycol) glutarate acid was prepared as follows: tetra-PEG-OH (0.1 mmol, 10 g), glutaric anhydride (4 mmol, 456 mg), and DMAP (4 mmol, 488 mg) were dissolved in anhydrous CH_2Cl_2 (150 mL). After reaction for 24 h, the solution was washed with brine for three times. The organic layer was collected, dried with $MgSO_4$, and concentrated under vacuum, which was further precipitated twice in excess diethyl ether to give the tetra-armed poly (ethylene glycol) succinic acid. Then the tetra-armed poly (ethylene glycol) succinic acid (0.05 mmol, 5 g), EDCI (2 mmol, 384 mg), and NHS (2 mmol, 230 mg) were dissolved in dry CH_2Cl_2 (100 mL). The system was stirred at 37°C for 24 h and then directly washed with brine (3 × 100 mL). The organic layer was collected and dried with $MgSO_4$ to obtain the white solid under vacuum. The structures of the compounds were confirmed by ^{1}H NMR and ^{13}C NMR measurement in $CDCl_3$. Yield: 62.5%.

Preparing of Tetra-PEG Hydrogel and ASA-Loaded Tetra-PEG Hydrogel

Precursor solution of tetra-PEG-NH_2 (8 wt%) and precursor solution tetra-PEG-SG (8 wt%) were prepared in two different sample bottles. By simultaneously injecting them into the molds using dual syringe, the tetra-PEG hydrogel was obtained at room temperature within 1 min. The ASA-loaded hydrogel was obtained by mixing the tetra-PEG-NH_2 (8 wt%) and tetra-PEG-SG (8 wt%) including the appropriate amount of ASA (100 μg/mL for each experimental sample) into the molds at room temperature with the same methods.

In vitro Release Profile of Aspirin From the Hydrogel

The hydrogel was prepared in a container with the diameter of 10 mm and height of 2 mm, and aspirin was encapsulated inside the hydrogel. Then, the ASA-contained hydrogel was immersed into the PBS and the solutions were collected at the appointed intervals of time. The collected solution at different time were tested using the UV-visible spectroscopy.

Scanning Electron Microscopy (SEM) Observation of the Hydrogel

The hydrogel samples(φ 14 mm × h 2 mm) were lyophilized by SPEX 6770 freeze drier (Labconco, USA). To characterize the internal microstructure of hydrogels, the freeze-dried samples were cut and observed under a scanning electron microscopy (SEM, Hitachi S-4800, Japan).

Cell Viability and Cell Proliferation Assay

Cell Counting Kit-8 (CCK-8, Cat. CK04, Dojindo, Japan) was applied under manufacturer's protocol. PDLSCs were seeded in 48-well plate (Corning Incorporated), 6,000 cells per well. GM was replaced, HD was added 24 h after seeding. Briefly, the cells were incubated with CCK-8 for 2 h, and OD value (450 nm) was detected. 24 h cell viability was defined as OD ratio between treated and untreated groups.

Cell live and dead viability was determined by Live/Dead Viability/Cytotoxicity Kit (Cat. L3224, Invitrogen) according to the manufacturer's instruction. PDLSCs were seeded and incubated in GM for 24 hours, HD was added and incubating for further 24 hours. IX53 fluorescence microscope (Olympus, Japan) was used to observe green (live) and red (dead) cells after staining.

PDLSCs were seeded on φ 20 mm slides (NEST, China), 1 × 10^4 cells per slide. Cell treatments were the same as live and dead assay above. Then, PDLSCs were treated 12 h with 1:200 BrdU antibody (Cat. MA3-071, Invitrogen) after incubating the cells with 1:100 BrdU labeling reagent (Cat. 000103, Thermal Fisher Scientific) for 12 h. Then, irrigated cells were treated by Alexafluoro 568 conjugated secondary antibody for 1 h at room temperature. Finally, the slides were mounted by Vectasheild mounting medium containing DAPI (Vector Laboratories, USA). Zeiss Axio Observer Z1 (Zeiss, Germany) was used to examine the BrdU-positive cells.

Toxicity Assay of Hydrogels *in vivo*

All the *in vivo* studies were approved by Peking University Biomedical Ethics Committee (LA2019074). Aged 8 weeks, female BALB/c nude mice were purchased from Weitonglihua (China). The nude mice were randomly divided into three groups: (1) control group; (2) tetra-PEG hydrogel group; (3) tetra-PEG hydrogel loaded with ASA group (for each group, $n = 6$), the materials were placed subcutaneously on the dorsum of the mice. The mice were euthanized 2 weeks postoperatively, the skin and subcutaneous implants were fixed by 4% neutral-buffered formaldehyde immediately after harvest for 2 days. All the samples were gradually dehydrated and embedded, sections (3 μm) were prepared and stained with hematoxylin and eosin (H&E) to evaluate the toxicity of the hydrogels in nude mice.

Mouse Calvaria Bone Defects and Transplantation Treatment

Hydrogel samples (φ 5 × h 2 mm) were incubated in GM with PDLSCs for 48 h at 37°C, 5% CO_2. The hydrogels were rinsed by PBS before implantation. Female C57BL/6 mice aged 8 weeks were purchased from Weitonglihua (China). Human PDLSCs used in this experiment were cultivated from one donor sample. Φ 5 mm calvaria bone defect was made by stainless-steel trephine. The mice are blindly randomized into 3 groups with the following: (1) control group, defects were not filled; (2) hydrogel-PDLSCs group, defect areas were filled by pretreated hydrogel matrix; (3) hydrogel-ASA-PDLSCs group, defect areas were filled by pretreated hydrogel with ASA loaded on. Then the mice were sacrificed at 8 weeks after operation. The calvaria bone was isolated and fixed with 4% neutral-buffered formaldehyde for 2 days. Then, the specimens were

decalcified, dehydrated, and embedded. Serial sections 4 μm thick were prepared and stained with H&E and Masson to assess new bone formation. Local interferon-γ (IFN-γ) was assessed by immunofluorescence. IFN-γ antibody (Cat. sc-373727, Santa Cruz Biotechnology, USA) and goat-anti-mouse IgG-FITC (Cat. ZF-0312, ZSGB bio, China) was used in this experiment. Laser confocal microscopy (LMS710, Zeiss) was used to observe green and blue fluorescence emitted by FITC and DAPI.

Micro Computed Tomography (Micro-CT) Analysis

Mice calvarial samples were radiographed with a micro-CT system (SkyScan 1174; Burker) at 53 kV and 810 μA. 3D image were reconstructed by using NRecon and CTvox software (Burker). The CTAn (Burker) software was used to analysis the volume of new bone.

Statistics Analysis

All the results are presented as mean and standard deviation (mean ± S.D.) of 3–6 independent experiments. The statistics were analyzed by SPSS software (ver. 13.0; SPSS Inc., USA). Independent unpaired two-tailed Student's *t*-tests were used for comparing between two groups. One-way ANOVA was applied for more than two groups. $p < 0.05$ was considered to be significant.

RESULT

ASA Promotes the Osteogenic Differentiation of PDLSCs *in vitro*

In order to investigate the effect of ASA on osteogenic differentiation of PDLSCs and select an appropriate concentration to encapsulate ASA in the tetra-PEG hydrogel, we set up a series doses of ASA to treat PDLSCs and analyzed its osteogenic potential. ARS staining was performed 14

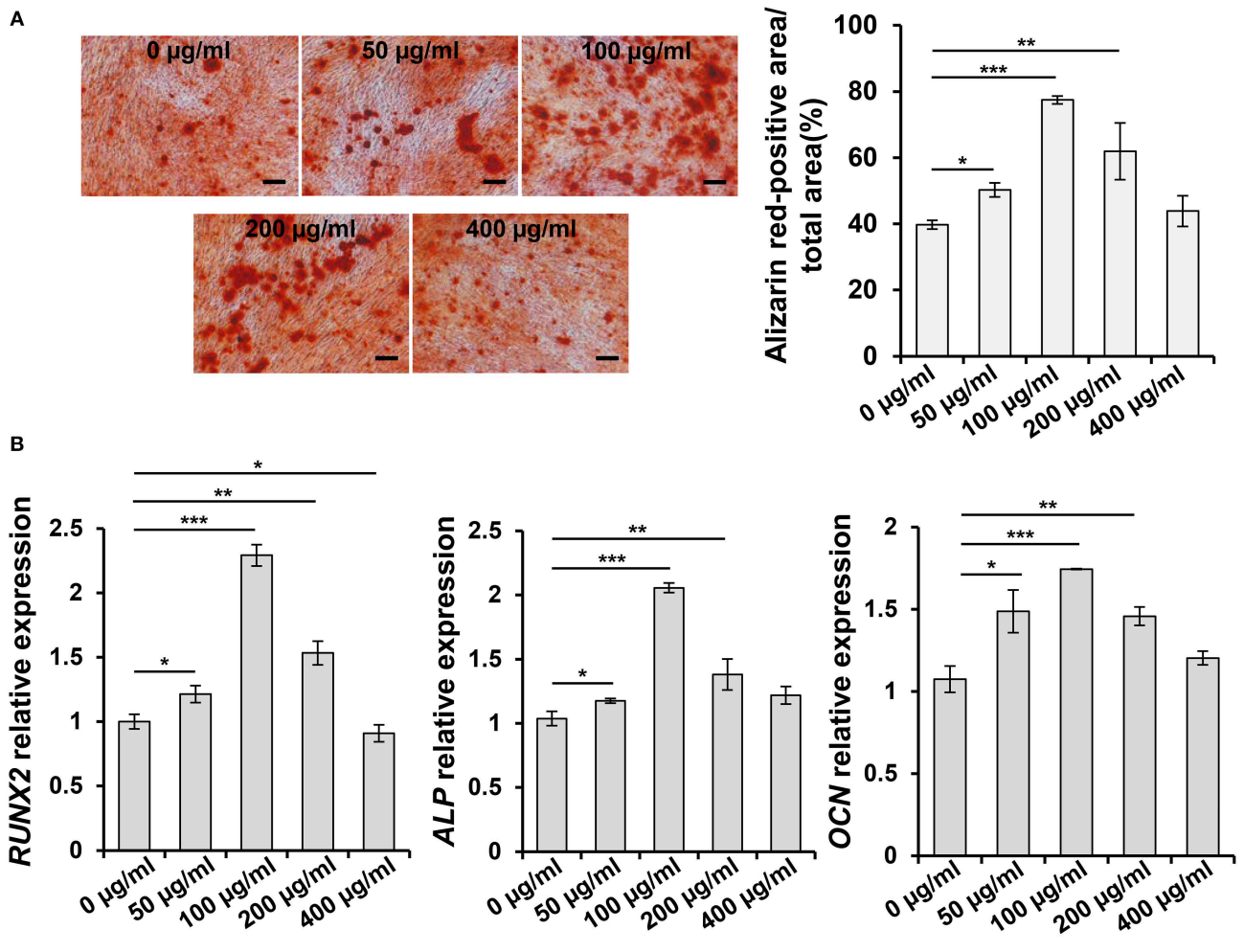

FIGURE 1 | Aspirin promotes the osteogenic differentiation capacity of PDLSCs *in vitro*. **(A)** PDLSCs were treated with gradient concentration of aspirin (0, 50, 100, 200, and 400 μg/ml) for 14 days, the mineralized nodule formation was assessed by alizarin red staining. Scale bar, 200 μm. *$p < 0.05$, **$p < 0.01$, ***$p < 0.001$. **(B)** qPCR analysis showed the *RUNX2*, *ALP*, and *OCN* expression levels after 7 days gradient concentration of aspirin treatment under osteogenic induction condition. *$p < 0.05$, **$p < 0.01$, ***$p < 0.001$.

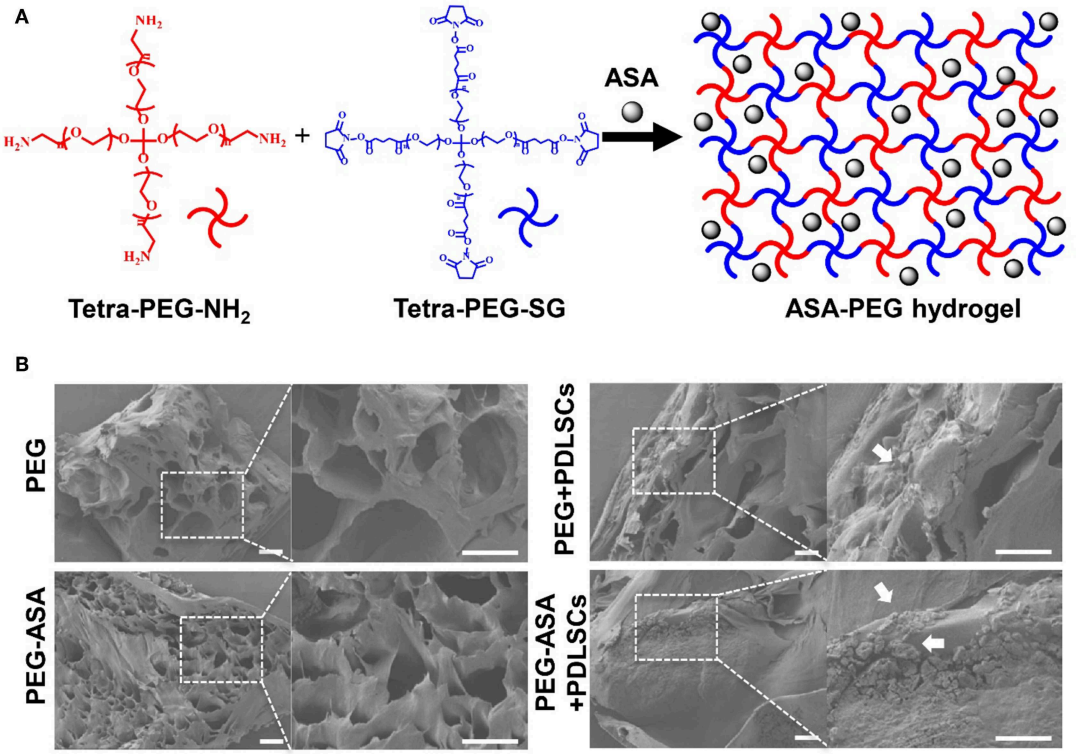

FIGURE 2 | Scheme illustration and characterization of PEG hydrogels. **(A)** Scheme of the synthesis procedure for ASA-PEG hydrogels. **(B)** SEM images of PEG, PEG-ASA, and hydrogels co-cultured with PDLSCs. White arrowheads pointed out the cells. Scale bar, 100 μm.

days post-treatment. The result demonstrated that osteogenic differentiation of PDLSCs was enhanced with the increase of ASA from 0 to 100 μg/mL. However, the augmentation was attenuated with ASA concentration reached 200 and 400 μg/mL, in a dose-dependent manner. The measurement of mineralization areas approved that mineralized nodule formation capacity of PDLSCs peaked when treated with 100 μg/mL ASA (**Figure 1A**). Next, to further confirm the functional effect of ASA, the mRNA levels of osteogenic markers were evaluated 7 days after osteogenic induction as assessed by qPCR. The result demonstrated that there was a significant increase of runt-related transcription factor 2 (*RUNX2*), alkaline phosphatase (*ALP*), and Osteocalcin (*OCN*) at the dose of 100 μg/mL treated group when compared with control group ($p < 0.001$, **Figure 1B**). The mRNA expression profiles were consistent with those obtained from ARS staining. These data suggested that ASA is able to promote PDLSCs' osteogenic differentiation capacity, and 100 μg/mL might be an ideal concentration for ASA to be encapsulated during scaffold construction.

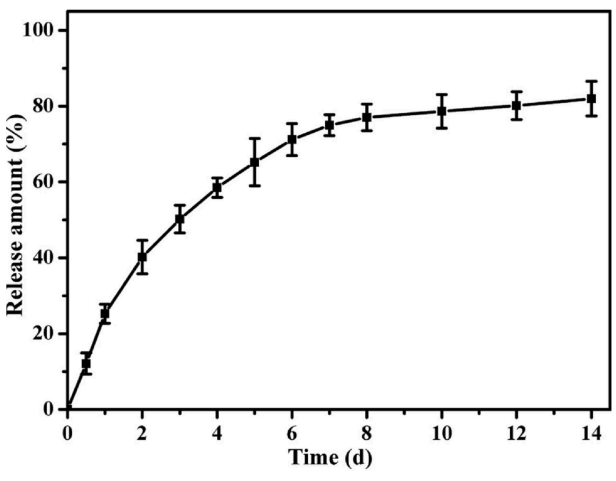

FIGURE 3 | The releasing curves of aspirin from PEG hydrogels.

Synthesis and Characterization of Hydrogels Loaded With ASA

Hydrogel and hydrogel loaded with ASA were fabricated with good accessibility by simply mixing the tetra-PEG-NH_2 solution and the tetra-PEG-SG containing ASA solution (100 μg/mL) at room temperature. The synthesis procedures for PEG hydrogels were shown in **Figure 2A**. By the use of a dual syringe method, the tetra-PEG hydrogels can be formed in any mold with desired shape, exhibiting the injectable materials of *in-situ* free-shapeable properties. The topography and roughness of the hydrogels were investigated by the SEM technique as observed in **Figure 2B**. SEM images showed a varied of inner porous microstructure of the tetra-PEG hydrogels. It reveals that the pores diameters

were ranging from 40 to 80 μm in the lyophilized state, which provided good chance to enable the sustained release of the encapsulated ASA drugs, cell entry and substance exchange intra-extra of the tetra-PEG hydrogels. As our expectation, we encapsulated ASA in PEG hydrogel without changing its appearance characteristics. Images of PEG and PEG-ASA co-cultured with PDLSCs manifested the excellent cell adhesion capacity of the hydrogels.

After the characterizations of hydrogels, we detected the release profile of ASA loaded in tetra-PEG hydrogel *in vitro*. As shown in **Figure 3**, constant and sustained release of ASA was observed up to 14 days. In the first 2 days, cumulative release of ASA quickly reached round 40%. This initial burst release of ASA could afford sufficient stimuli to the defect areas. Then the release rates of ASA approached its plateaus at day 8, and the cumulative release rate of ASA reached 80% at day 14. This result indicated a sustained release profile of ASA loaded within tetra-PEG based hydrogel.

Cell Viability and Proliferation

As we have manufactured a feasible tetra-PEG based hydrogel scaffold loaded with ASA. In order to investigate its biocompatibility, series of cell proliferation, and cytotoxicity assays were set up. Live/dead assay confirmed that in the early stages of the culture (24 h), as it demonstrated in **Figure 4A**, PDLSCs manifest high viability. Quantitatively, PEG-ASA and PEG not only maintained but also improved cell viability vs. control group at 24 h ($p < 0.01$, **Figure 4B**). These results demonstrated hydrogels exerted low cytotoxicity on PDLSCs. To investigate if PEG-ASA and PEG are able to support the

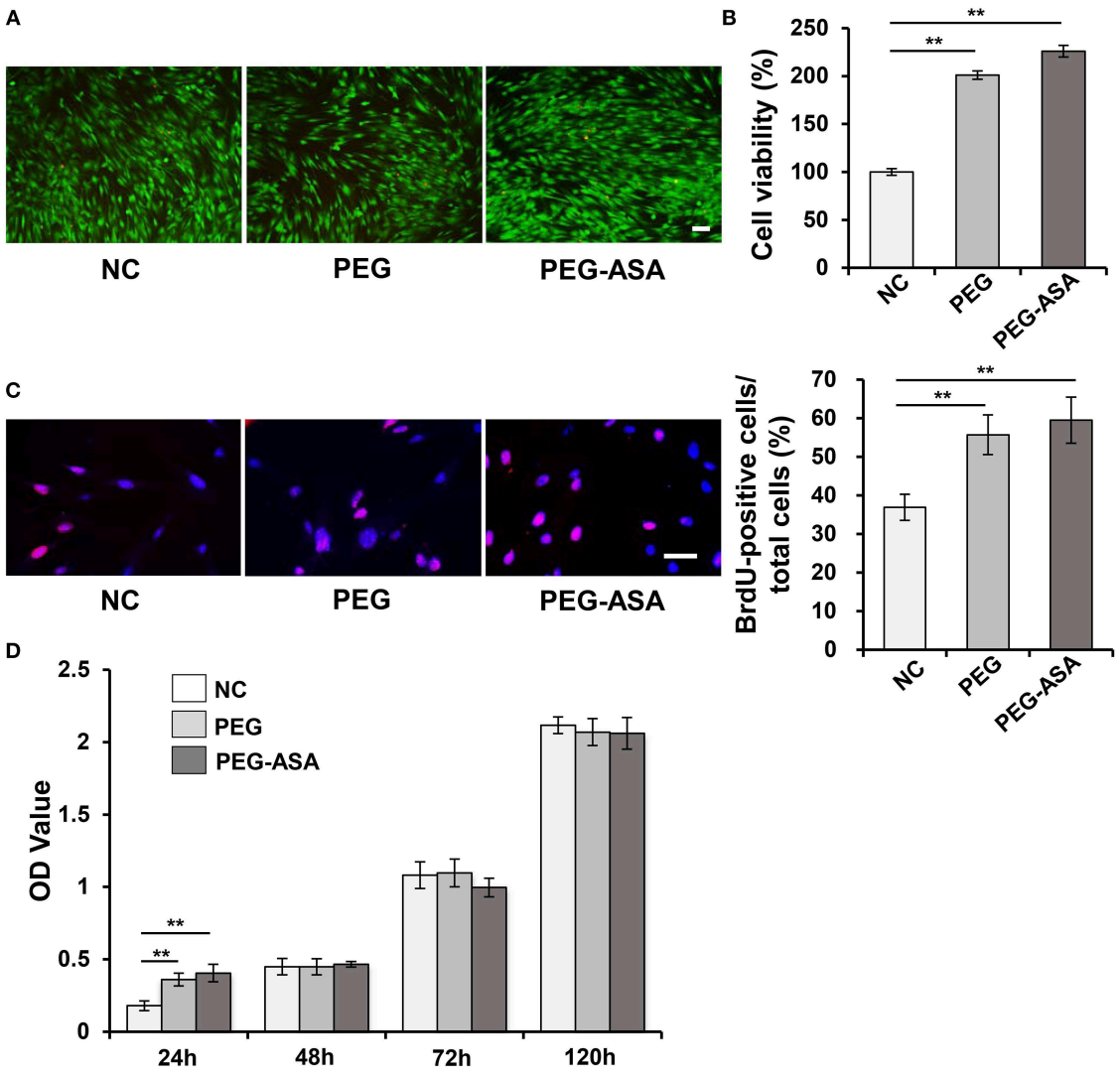

FIGURE 4 | Cytotoxicity of hydrogels *in vitro*. **(A)** Live/dead staining of PDLSCs. Cells in green manifest living PDLSCs, while cells in red manifest dead ones. Scale bar, 100 μm. **(B)** Cell viability was detected by Cell Counting Kit-8 after 24 h cultivation. $^{**}p < 0.01$. **(C)** The proliferating PDLSCs was labeled in red and the percentage of Brdu-positive cells was calculated. Scale bar, 200 μm. $^{**}p < 0.01$. **(D)** Cell proliferation was detected at specific time points (24, 48, 72, 120 h) by using CCK-8. $^{**}p < 0.01$. NC, negative control.

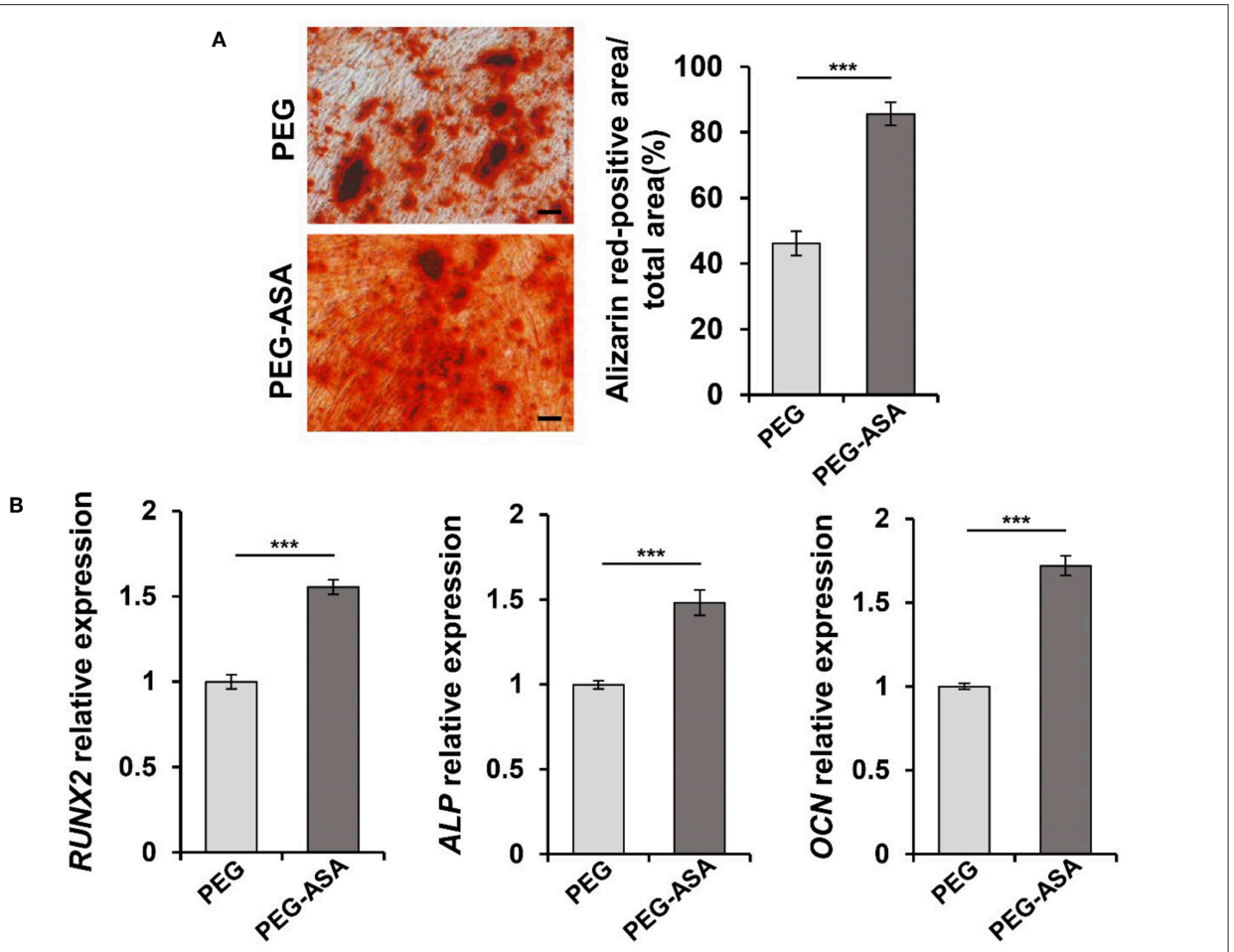

FIGURE 5 | PEG-ASA promote osteogenic differentiation of PDLSCs *in vitro*. **(A)** PDLSCs incubated with hydrogels degradation for 14 days, the mineralized nodule formation was assessed by alizarin red s staining. Scale bar, 200 μm. ***$p < 0.001$. **(B)** qPCR analysis showed the *RUNX2*, *ALP*, and *OCN* expression levels after 7 days hydrogels degradation treatment. ***$p < 0.001$.

proliferation of PDLSCs. The BrdU assay was carried out, the result showed that the percentage of BrdU positive cells were elevated significantly in group PEG-ASA and group PEG after 24 h incubation ($p < 0.01$, **Figure 4C**). In addition, to observe a long-term proliferation profile on PDLSCs, CCK8 assay was conducted and OD value at 450 nm was measured at 48, 72, and 120 h after treatment with PEG and PEG-ASA. Interestingly, no significant difference between groups at these time point (**Figure 4D**) was found. These results indicated that the cell proliferation rate was promoted at early phase (24 h) of co-culturing with PEG and PEG-ASA, and it was not significantly inhibited at later phase (48, 72, and 120 h).

PEG-ASA Promote Osteogenic Differentiation of PDLSCs *in vitro*

In the previous studies, we manifested that PEG-ASA possessed a low cytotoxicity characteristic and was able to sustain the proliferation of PDLSCs. Next, to investigate its osteoinduction ability, ARS staining and qPCR assay were used to examine. As shown in **Figure 5A**, the result indicated that PEG-ASA significantly increased the calcification nodules formation ability of PDLSCs after 14 days osteogenic induction. The expression levels of osteogenesis markers *RUNX2*, *ALP*, and *OCN* was significantly leveled up at day 7 in ASA sustained release system ($p < 0.001$, **Figure 5B**). These data verified our hypothesis that PEG-ASA exhibited osteoinductive ability on PDLSCs *in vitro*.

Toxicity of PEG-ASA Hydrogels *in vivo*

To validate the toxicity and degradation of hydrogels *in vivo*, subcutaneous implant assay on BALB/c nude mice was carried out (**Figure 6A**). Two weeks after surgery, both PEG and PEG-ASA hydrogels were almost absorbed *in vivo* from the general observation (**Figure 6B**). Macroscopically, the surrounding tissues of PEG groups displayed a slight inflammation response with mild local redness and swelling (**Figure 6C**). However, the surrounding tissues located around implanted PEG-ASA displayed no obvious inflammation response, with no significant redness, and exudate (**Figure 6D**). Since the nude mice lack of immune organs, BALB/c mice were used as an ideal animal model for the toxicity evaluation *in vivo*. The hydrogels along

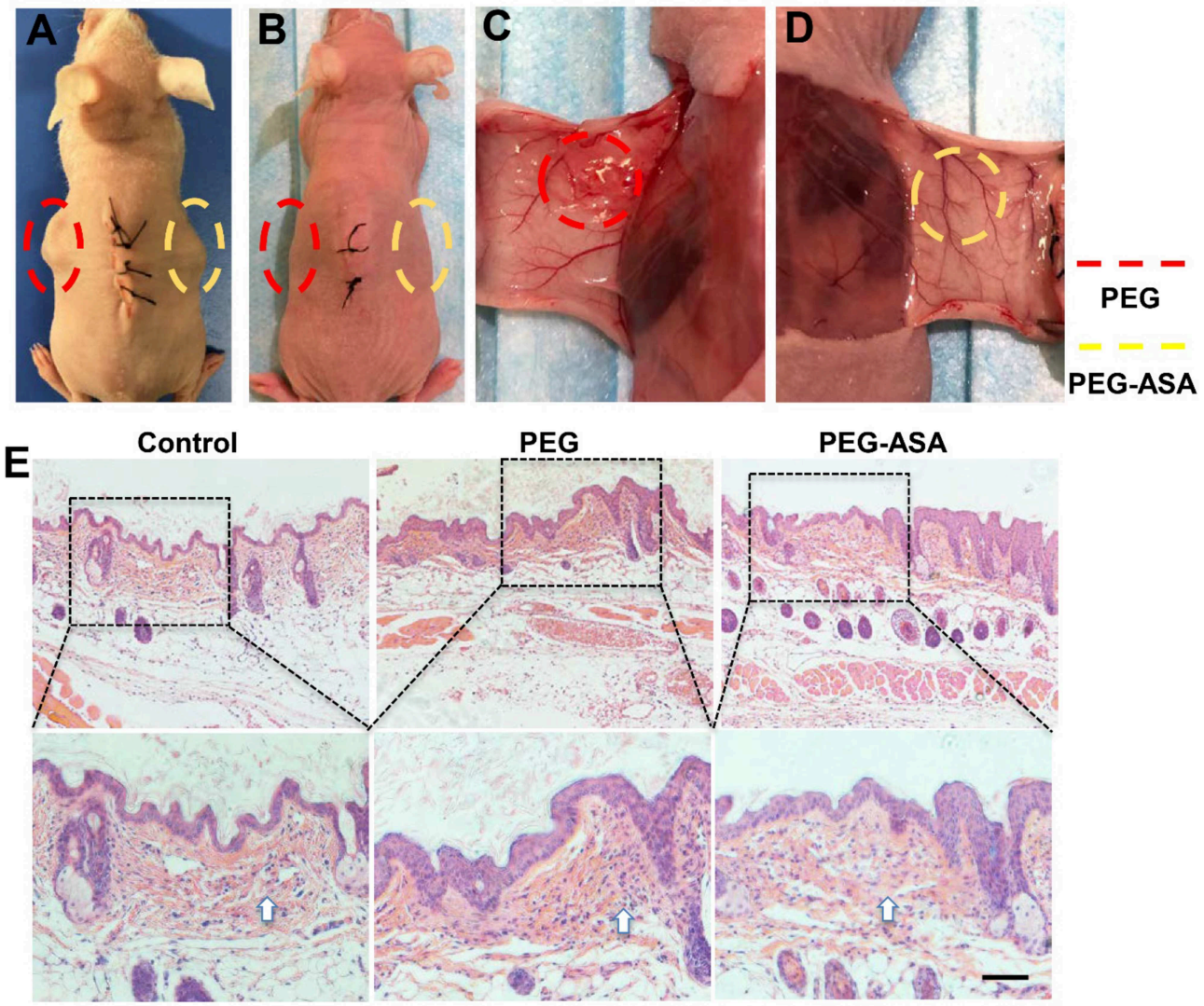

FIGURE 6 | *In vivo* evaluation of the toxicity and degradation of the hydrogels. **(A)** Hydrogels cuboids were placed subcutaneously in BALB/c nude mice. The gross view **(B–D)** and subcutaneous tissue histology **(E)** of implant sites 2 weeks post-surgery. Scale bar, 200 μm. Implant sites of hydrogels were circled by dotted lines. The arrowhead indicated the inflammatory cells.

with surrounding tissues were collected and analyzed using H&E staining. From the histological examination, we observed that both PEG and PEG-ASA were biodegradable in 14 days, with no scaffold structures were found subcutaneously. Moreover, an increase amount of the inflammatory cells was detected located at epithelium tissues in PEG groups compared with no treatment control group (**Figure 6E**). The PEG-ASA displayed an inhibitory effect on aggregation of inflammatory cells which may attribute to the sustained release of aspirin. These results indicated that PEG hydrogel is a biodegradable scaffold and is not able to initiate severe inflammation response *in vivo*. PEG hydrogels loaded with or without ASA can be serve as a biocompatible scaffold for further therapeutic usage.

PEG-ASA Improves PDLSCs-Mediated Bone Regeneration in Calvaria Bone Defect Model

According to the results above, PEG-ASA displayed a remarkable osteoinduction effect on PDLSCs *in vitro*. Thus, we hypothesized that the scaffold may also promote PDLSCs-mediated bone regeneration *in vivo*. Herein, we established the critical sized calvaria bone defect mice model and transplanted PDLSCs with hydrogels to the bone defect region. 8 weeks post-transplantation, Micro-CT images illustrated that PEG-ASA group obtained the newest bone regeneration than PEG alone group (**Figures 7A,C,E,G**). Statistical analysis showed that the area of new bone formation in the PEG and PEG-ASA group

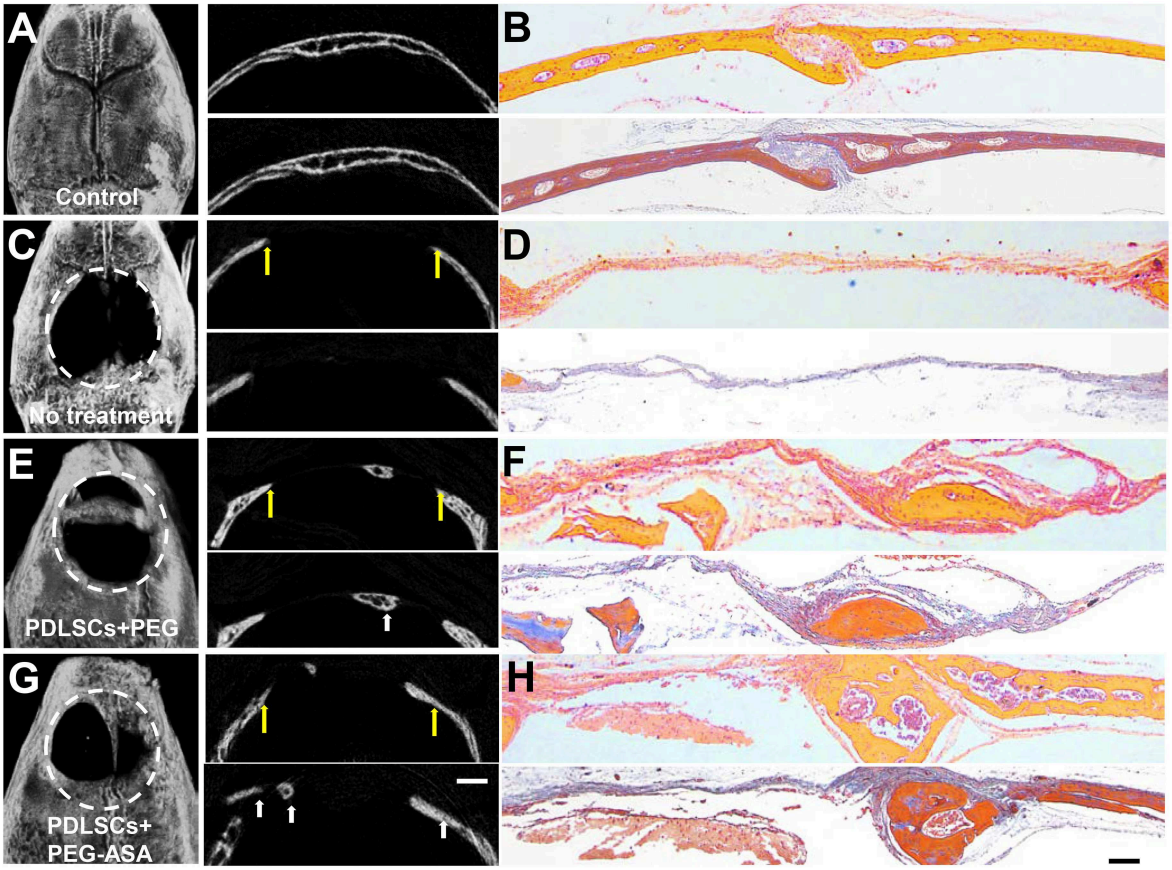

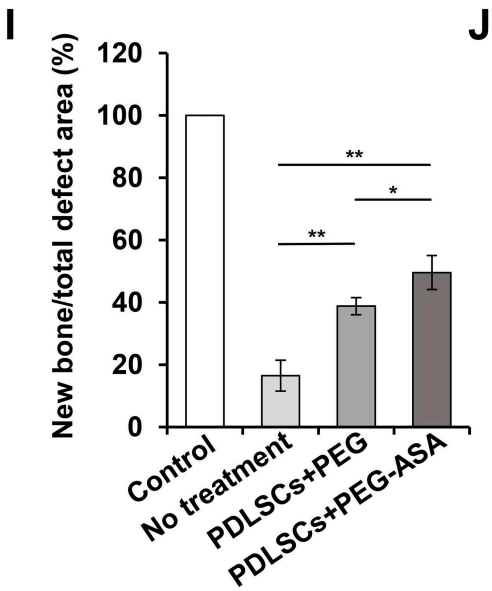

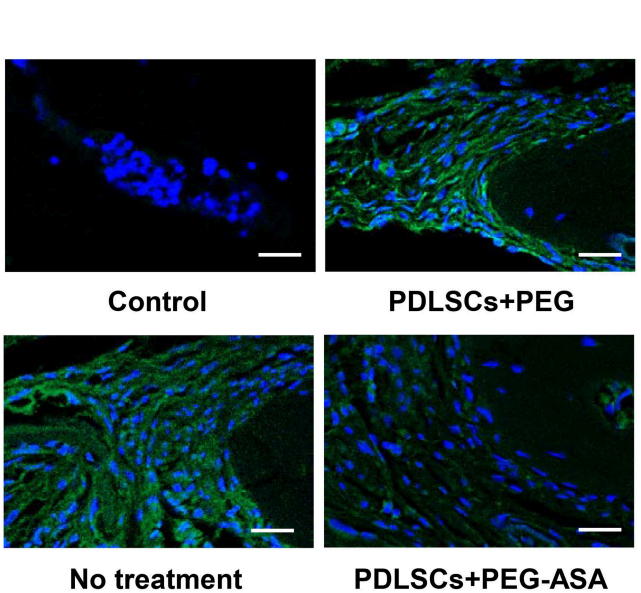

FIGURE 7 | PEG-ASA improved PDLSCs-mediated critical-sized calvaria bone-defect bone formation. **(A)** Microcomputed tomography (micro-CT), **(B)** H&E (upper) and Masson staining (lower) images of unmanipulated wild-type C57BL/6 mice calvaria bone structure. **(C)** Micro-CT, **(D)** H&E (upper), and Masson staining (lower) images of untreated experimentally-induced calvaria bone defects. **(E)** Micro-CT (left), **(F)** H&E (upper), and Masson staining (lower) images of calvaria bone defects after transplantation of PDLSCs and PEG hydrogels. **(G)** Micro-CT (left), **(H)** H&E (upper), and Masson staining (lower) images of calvaria bone defects after transplantation of PDLSCs and PEG-ASA hydrogels. The yellow arrows in **(A,C,E,G)** indicate the margins of bone defects, the white arrows indicate the new bone. White dotted line defines the bone defect area. **(I)** Semiquantitative analysis of bone formation via micro-CT images from the groups described in **(A,C,E,G)**. **(J)** Immunofluorescence staining of IFN-γ positive cells. Scale bar, 1,000 μm (micro-CT), 200 μm (H&E and Masson), 25 μm (immunofluorescence). $^{*}p < 0.05$, $^{**}p < 0.01$.

were much higher than no treatment control group. The PEG-ASA treated group displayed a significant elevation of new bone formation than the PEG group (**Figure 7I**).

To evaluate the amount of bone tissue regeneration, the histological section of the experimental region was made and stained by hematoxylin and eosin (H&E) and Masson's trichrome (**Figures 7B,D,F,H**). The PEG and PEG-ASA groups showed an increased PDLSCs-mediated bone formation compared to the untreated group, and PEG-ASA group displayed the most efficient treatment on mediating new bone formation. Immunofluorescence (**Figure 7J**) reveals relative low local inflammation status which might attribute to ASA laden. These results indicated that PEG-ASA could abate the inflammatory response during bone regeneration, and exerts beneficial effects on directing PDLSCs osteogenesis *in vivo*.

DISCUSSION

Massive bone defects, especially occurred in craniofacial area, make impacts on patients' aesthetics as well as function. Utilizing stem cells, biocompatible scaffolds and growth factors, tissue engineering provides more opportunities for bone tissue reconstruction. In this study, the viability and osteogenesis capability of PDLSCs cultured with tetra-PEG based hydrogel scaffold were measured for the first time. The tetra-PEG hydrogels established here is biocompatible, fully degradable, and capable of sustaining release of drug, which provided a promising scaffold for bone tissue engineering.

It has been reported that host proinflammatory T lymphocytes inhibit MSCs-mediated bone regeneration which induces cell apoptosis (Liu et al., 2011). Gibon et al. revealed that prolonged or aberrant immune activation is deleterious for bone regeneration (Gibon et al., 2017). These findings remained us that the host local immune response during calvaria bone defect repairment might play an important role in control MSCs-mediated bone tissue regeneration. Aspirin (ASA), widely used as analgesic and antipyretic for decades, is able to augment MSCs osteogenic potential through activate telomerase reverse transcriptase (Liu et al., 2015) (TERT) or inhibit tumor necrosis factor-α (TNF-α) and interferon-γ (IFN-γ) pathways (Liu et al., 2011). It is reported that MSCs osteogenesis was improved when exposed to relative low dosage (10–100 μg/mL) of ASA. Nevertheless, ASA shows significantly higher cytotoxicity and lower osteoinductivity when reached higher dosage (Cao et al., 2015; Liu et al., 2015; Yuan et al., 2018). In our study, we demonstrated that 100 μg/mL of ASA is the most efficient concentration for inducing PDLSCs toward osteogenic differentiation. Based on the beneficial effect of aspirin and our current findings, these evidences provide us the basis for fabricating a suitable delivery system for a sustained release of ASA to facilitate bone regeneration.

To achieve high-quality tissue regeneration, biomaterials have been used to control and manipulate the fate of stem cells (Engler et al., 2006; Fitzsimmons et al., 2018). In calvaria bone tissue engineering, the biomaterial plays an essential role to provide suitable microenvironment for supporting MSCs viability, proliferation, and directing the cells toward osteogenic differentiation (Moshaverinia et al., 2014). In our study, the viability of PDLSCs was significantly improved in both PEG and PEG-ASA hydrogels at 24 h, and the proliferation rate of PDLSCs was maintained as control group at 48, 72, and 120 h, which indicated the hydrogels we fabricated obtained a superior biocompatibility to support PDLSCs. Moreover, PEG hydrogel possesses a unique advantage as a drug carrier and contains almost no any harmful organics or crosslinking agents (Payyappilly et al., 2014). In our study, ASA loaded PEG hydrogels displayed a slowly release profile that could promote osteogenic differentiation of PDLSC both *in vivo* and *in vitro*. According to the previous reports, depending on the cell type and animal model, the most suitable concentration of ASA is between 50 and 200 μg/mL (Liu et al., 2011; Cao et al., 2015; Yuan et al., 2018). In our mice calvaria bone defect model, 100 μg/mL ASA were loaded on PEG hydrogels and located in the distinct bone defect area, the inflammation factors were inhibited along with the long-term release of ASA, which provide a suitable microenvironment for PDLSCs-mediated bone regeneration. Our result indicated that the area of new bone formation was largest with PEG-ASA hydrogel compared to PEG alone or the group with no treatment. These data suggest that PEG-ASA is safe and beneficial as a therapeutic method for clinic use.

CONCLUSION

In this study, we fabricated a tetra-PEG hydrogel based aspirin sustained release system and demonstrated that the scaffold possesses an appropriate microenvironment for supporting PDLSCs' viability and proliferation. The *in vivo* study showed that both PEG and PEG-ASA hydrogels were capable of promoting PDLSCs-mediated calvaria bone regeneration in mice, and the effect of the PEG-ASA was more efficient than PEG alone. We anticipated that this finding may provide a new strategy for bone regenerative therapy.

DATA AVAILABILITY STATEMENT

The datasets generated for this study are available on request to the corresponding author.

ETHICS STATEMENT

The studies involving human participants were reviewed and approved by The Ethical Guidelines of Peking University (PKUSSIRB-201311103). The patients/participants provided their written informed consent to participate in this study. The animal study was reviewed and approved by Peking University Biomedical Ethics Committee (LA2019074).

AUTHOR CONTRIBUTIONS

YZ and TY designed the experiments and wrote the manuscript. YZ, ND, TY, TZ, and QS performed the experiments and collected and analyzed the data. ND and BH designed the experiments and revised the manuscript. All co-authors approved the final version of the manuscript for publication.

FUNDING

This work was supported by the National Natural Science Foundation of China (Nos. 51903003, 51972005, 51672009), and Peking University Medicine Fund of Fostering Young Scholars' Scientific & Technological Innovation (BMU2018PYB009), supported by the Fundamental Research Funds for the Central Universities.

REFERENCES

Bliden, K. P., Patrick, J., Pennell, A. T., Tantry, U. S., and Gurbel, P. A. (2016). Drug delivery and therapeutic impact of extended-release acetylsalicylic acid. *Future Cardiol.* 12, 45–58. doi: 10.2217/fca.15.60

Botelho, J., Cavacas, M. A., Machado, V., and Mendes, J. J. (2017). Dental stem cells: recent progresses in tissue engineering and regenerative medicine. *Ann. Med.* 49, 644–651. doi: 10.1080/07853890.2017.1347705

Bu, Y., Shen, H., Yang, F., Yang, Y., Wang, X., and Wu, D. (2017). Construction of tough, *in situ* forming double-network hydrogels with good biocompatibility. *ACS Appl. Mater. Interfaces* 9, 2205–2212. doi: 10.1021/acsami.6b15364

Cao, Y., Xiong, J., Mei, S., Wang, F., Zhao, Z., Wang, S., et al. (2015). Aspirin promotes bone marrow mesenchymal stem cell-based calvarial bone regeneration in mini swine. *Stem Cell Res. Ther.* 6:210. doi: 10.1186/s13287-015-0200-4

Confalonieri, D., Schwab, A., Walles, H., and Ehlicke, F. (2018). Advanced therapy medicinal products: a guide for bone marrow-derived MSC application in bone and cartilage tissue engineering. *Tissue Eng. Part B Rev.* 24, 155–169. doi: 10.1089/ten.teb.2017.0305

Engler, A. J., Sen, S., Sweeney, H. L., and Discher, D. E. (2006). Matrix elasticity directs stem cell lineage specification. *Cell* 126, 677–689. doi: 10.1016/j.cell.2006.06.044

Fitzsimmons, R. E. B., Mazurek, M. S., Soos, A., and Simmons, C. A. (2018). Mesenchymal stromal/stem cells in regenerative medicine and tissue engineering. *Stem Cells Int.* 2018:8031718. doi: 10.1155/2018/8031718

Gibon, E., Lu, L. Y., Nathan, K., and Goodman, S. B. (2017). Inflammation, ageing, and bone regeneration. *J. Orthop. Transl.* 10, 28–35. doi: 10.1016/j.jot.2017.04.002

Gronthos, S., Mankani, M., Brahim, J., Robey, P. G., and Shi, S. (2000). Postnatal human dental pulp stem cells (DPSCs) *in vitro* and *in vivo*. *Proc. Natl. Acad. Sci. U.S.A.* 97, 13625–13630. doi: 10.1073/pnas.240309797

Liu, Y., Chen, C., Liu, S., Liu, D., Xu, X., Chen, X., et al. (2015). Acetylsalicylic acid treatment improves differentiation and immunomodulation of SHED. *J. Dent. Res.* 94, 209–218. doi: 10.1177/0022034514557672

Liu, Y., Wang, L., Kikuiri, T., Akiyama, K., Chen, C., Xu, X., et al. (2011). Mesenchymal stem cell-based tissue regeneration is governed by recipient T lymphocytes via IFN-gamma and TNF-alpha. *Nat. Med.* 17, 1594–1601. doi: 10.1038/nm.2542

Miller, C. P., and Chiodo, C. P. (2016). Autologous Bone Graft in Foot and Ankle Surgery. *Foot Ankle Clin.* 21, 825–837. doi: 10.1016/j.fcl.2016.07.007

Moshaverinia, A., Chen, C., Xu, X., Akiyama, K., Ansari, S., Zadeh, H. H., et al. (2014). Bone regeneration potential of stem cells derived from periodontal ligament or gingival tissue sources encapsulated in RGD-modified alginate scaffold. *Tissue Eng. Part A* 20, 611–621. doi: 10.1089/ten.TEA.2013.0229

Panagopoulos, G. N., Mavrogenis, A. F., Mauffrey, C., Lesensky, J., Angelini, A., Megaloikonomos, P. D., et al. (2017). Intercalary reconstructions after bone tumor resections: a review of treatments. *Eur. J. Orthop. Surg. Traumatol.* 27, 737–746. doi: 10.1007/s00590-017-1985-x

Payyappilly, S., Dhara, S., and Chattopadhyay, S. (2014). Thermoresponsive biodegradable PEG-PCL-PEG based injectable hydrogel for pulsatile insulin delivery. *J. Biomed. Mater. Res. A* 102, 1500–1509. doi: 10.1002/jbm.a.34800

Seliktar, D. (2012). Designing cell-compatible hydrogels for biomedical applications. *Science* 336, 1124–1128. doi: 10.1126/science.1214804

Seo, B. M., Miura, M., Gronthos, S., Bartold, P. M., Batouli, S., Brahim, J., et al. (2004). Investigation of multipotent postnatal stem cells from human periodontal ligament. *Lancet* 364, 149–155. doi: 10.1016/S0140-6736(04)16627-0

Tan, J., Zhang, M., Hai, Z., Wu, C., Lin, J., Kuang, W., et al. (2019). Sustained release of two bioactive factors from supramolecular hydrogel promotes periodontal bone regeneration. *ACS Nano* 13, 5616–5622. doi: 10.1021/acsnano.9b00788

Tao, L., Liu, J., Xu, J., and Davis, T. P. (2009). Bio-reversible polyPEGylation. *Chem. Commun.* 43, 6560–6562. doi: 10.1039/b915512k

Xu, X., Gu, Z., Chen, X., Shi, C., Liu, C., Liu, M., et al. (2019). An injectable and thermosensitive hydrogel: promoting periodontal regeneration by controlled-release of aspirin and erythropoietin. *Acta Biomater.* 86, 235–246. doi: 10.1016/j.actbio.2019.01.001

Xuan, K., Li, B., Guo, H., Sun, W., Kou, X., He, X., et al. (2018). Deciduous autologous tooth stem cells regenerate dental pulp after implantation into injured teeth. *Sci. Transl. Med.* 10:eaaf3227. doi: 10.1126/scitranslmed.aaf3227

Yamaza, T., Miura, Y., Bi, Y., Liu, Y., Akiyama, K., Sonoyama, W., et al. (2008). Pharmacologic stem cell based intervention as a new approach to osteoporosis treatment in rodents. *PLoS ONE* 3:e2615. doi: 10.1371/journal.pone.0002615

Yang, Y., Wang, X., Yang, F., Shen, H., and Wu, D. (2016). A universal soaking strategy to convert composite hydrogels into extremely tough and rapidly recoverable double-network hydrogels. *Adv. Mater. Weinheim.* 28, 7178–7184. doi: 10.1002/adma.201601742

Yang, Y., Wang, X., Yang, F., Wang, L., and Wu, D. (2018). Highly elastic and ultratough hybrid ionic-covalent hydrogels with tunable structures and mechanics. *Adv. Mater. Weinheim.* 30:e1707071. doi: 10.1002/adma.201707071

Yuan, M., Zhan, Y., Hu, W., Li, Y., Xie, X., Miao, N., et al. (2018). Aspirin promotes osteogenic differentiation of human dental pulp stem cells. *Int. J. Mol. Med.* 42, 1967–1976. doi: 10.3892/ijmm.2018.3801

Zhang, Q., Shi, S., Liu, Y., Uyanne, J., Shi, Y., Shi, S., et al. (2009). Mesenchymal stem cells derived from human gingiva are capable of immunomodulatory functions and ameliorate inflammation-related tissue destruction in experimental colitis. *J. Immunol.* 183, 7787–7798. doi: 10.4049/jimmunol.0902318

Zheng, Y., Liu, Y., Zhang, C. M., Zhang, H. Y., Li, W. H., Shi, S., et al. (2009). Stem cells from deciduous tooth repair mandibular defect in swine. *J. Dent. Res.* 88, 249–254. doi: 10.1177/0022034509333804

Conflict of Interest: The authors declare that the research was conducted in the absence of any commercial or financial relationships that could be construed as a potential conflict of interest.

frontiers in Chemistry

ORIGINAL RESEARCH
published: 18 October 2019
doi: 10.3389/fchem.2019.00683

Self-Healable, Fast Responsive Poly(ω-Pentadecalactone) Thermogelling System for Effective Liver Cancer Therapy

Huihui Shi[1†], Hong Chi[2†], Zheng Luo[3], Lu Jiang[4], Xian Jun Loh[4], Chaobin He[1] and Zibiao Li[4*]*

*[1] Department of Materials Science and Engineering, National University of Singapore, Singapore, Singapore, [2] Shandong Provincial Key Laboratory of Molecular Engineering, School of Chemistry and Pharmaceutical Engineering, Qilu University of Technology (Shandong Academy of Sciences), Jinan, China, [3] Fujian Provincial Key Laboratory of Innovative Drug Target Research and State Key Laboratory of Cellular Stress Biology, School of Pharmaceutical Sciences, Xiamen University, Xiamen, China, [4] Institute of Materials Research and Engineering, A*STAR (Agency for Science, Technology and Research), Singapore, Singapore*

OPEN ACCESS

Edited by:
Xing Wang,
Institute of Chemistry (CAS), China

Reviewed by:
Jia Hong Pan,
North China Electric Power University, China
Dai-Xu Wei,
Northwest University, China
Yuan Ping,
Zhejiang University, China

***Correspondence:**
Chaobin He
msehc@nus.edu.sg
Zibiao Li
lizb@imre.a-star.edu.sg

[†] These authors have contributed equally to this work

Specialty section:
This article was submitted to Polymer Chemistry, a section of the journal Frontiers in Chemistry

Received: *17 August 2019*
Accepted: *01 October 2019*
Published: *18 October 2019*

Citation:
Shi H, Chi H, Luo Z, Jiang L, Loh XJ, He C and Li Z (2019) Self-Healable, Fast Responsive Poly(ω-Pentadecalactone) Thermogelling System for Effective Liver Cancer Therapy. Front. Chem. 7:683. doi: 10.3389/fchem.2019.00683

A polyurethane based thermogelling system comprising poly(ω-pentadecalactone) (PPDL), poly(ethylene glycol) (PEG), and poly(propylene glycol) (PPG), termed as PDEP, was synthesized. The incorporation of PPDL lowers critical micelle concentration (CMC) as well as critical gelation concentration (CGC) of the novel copolymers compared to commercial Pluronic® F127. The thermogels showed excellent thermal stability at high temperature up to 80°C, fast response to temperature change in a time frame of less than second, as well as remarkable self-healing properties after being broken at high strain. *In vitro* drug release studies using docetaxel (DTX) and cell uptake studies using doxorubicin (DOX) show high potential of the hydrogel as drug reservoir for sustainable release profile of payloads, while the *in vivo* anti-tumor evaluation using mice model of hepatocellular carcinoma further demonstrated the significant inhibition on the growth of tumor. Together with its excellent biocompatibility in different organs, the novel PDPE thermogelling copolymers reported in this work could potentially be utilized as *in situ*-forming hydrogels for liver cancer therapy.

Keywords: hydrogel, drug formulation, polymer synthesis, cancer therapy, self-healable, temperature responsive hydrogel, biodegradable (co)polymers

INTRODUCTION

Thermoresponsive hydrogels, also known as thermogels, are an important class of physically crosslinked hydrogels whose aqueous polymer solution undergoes reversible sol-gel transition upon temperature change depending on the delicate balance between hydrophilicity and hydrophobicity (Liow et al., 2016). Especially, considerable attention has been drawn to thermogel systems with gelation temperature range of 10–40°C for biomedical applications such as minimally invasive drug delivery, injectable tissue engineering, wound healing, 3D cell culture and prevention of post-surgical adhesion (Moon et al., 2012).

Pluronic, a triblock copolymer of PEG and PPG, is a well-known thermogelling system which has been approved by Food and Drug Administration (FDA) for decades and attractive for

in situ drug delivery and wound healing due to its excellent biocompatibility and tunable transition temperature (Wu et al., 2016a). However, Pluronic gels have been reported to demonstrate poor mechanical properties and be prone to erosion, usually persisting for <1 day *in vivo*. Meanwhile, they are not biodegradable and generally require high critical gelation concentration (CGC), which may result in side effects from accumulation (Yu et al., 2009). These disadvantages limited the potential application of Pluronic systems, and thus, much efforts have been devoted to the modification of Pluronic copolymers. Jeong et al. coupled Pluronic® F127 with diphenylalanine which could form coordination bonds with metal ions Zn^{2+}, and obtained thermogels with modulus increasing from 15–21 to 24–28 kPa and durability of gel against water-erosion prolonging from 24 to 60 h at 37°C (Kim et al., 2017). Park et al. modified triblock PEG-PPG-PEG copolymers with D-lactide or L-lactide oligomers on both sides. The hydrogels formed from the two-component copolymer solution not only exhibited sol-gel transition between 10 and 40°C, but much lower CGC value, greatly enhanced mechanical strength and improved stability in aqueous environment due to the stereocomplex formation between D-lactide and L-lactide oligomers (Chung et al., 2008). Besides, incorporation of another hydrophobic block via step growth polymerization to drive the self-assemble of amphiphilic block copolymers by hydrophobic interactions has been a popular strategy nowadays to give polyurethane based Pluronic derivates with enhanced mechanical properties and decreased CGC values. Biodegradable polyesters including poly(lactic acid) (PLA) (Loh et al., 2008; Wu et al., 2016c), polycaprolactone (PCL) (Li et al., 2012; Zheng et al., 2017; Liu et al., 2019), and polyhydroxyalkanoate (PHA) (Li Z. et al., 2008; Wu et al., 2016b; Wee et al., 2017; Zhu et al., 2018; Jiang et al., 2019) are mostly selected as the third segment to produce desired thermogelling copolymers, while some cases based on polycarbonates (Loh et al., 2012a; Chan et al., 2018) are also reported.

Cancer is a leading cause of death worldwide, among which liver cancer ranks as the sixth most common type of cancer and contributes to the second largest percentage of cancer mortality (McGlynn et al., 2015). Chemotherapy is one of the most important means in cancer treatment nowadays, killing cancer cells by using cytotoxic drugs such as docetaxel (DTX) and doxorubicin (DOX) (Norouzi et al., 2016; Li et al., 2017; Yang D. P. et al., 2017). A major drawback of traditional chemotherapy is the non-specificity, which often results in low drug efficacy and damages to normal cells and tissues. Alternatively, localized chemotherapy based on various drug delivery system such as hydrogels (Xing et al., 2016), nanoparticles (Sun et al., 2014), micelles (Amjad et al., 2017), and liposomes (Eloy et al., 2016) have been widely investigated in recent years. Thermogels are regarded as one of the most promising candidates as they can simply be administrated via subcutaneous injection and form gels *in situ* quickly at physiological temperature which could increase the solubility and stability of drugs *in vivo* and serve as a sustaining drug delivery depot to targeted tumor site (Liow et al., 2016).

In this work, we design a novel polyurethane based thermogelling copolymer by copolymerizing poly(ω-pentadecalactone) (PPDL), which has been reported to possess good biocompatibility as well as excellent mechanical properties (Xiao et al., 2018), with PEG and PPG. The molecular properties, micellar properties and gel properties of the synthesized copolymers were investigated. Furthermore, the potential of the developed thermogels as anti-tumor drug delivery carrier were further explored through a series of *in vitro* and *in vivo* biological experiments.

EXPERIMENTAL SECTION

Materials

Poly(ethylene glycol) (PEG, $M_n = 2{,}000$), poly(propylene glycol) (PPG, $M_n = 2{,}050$), dibutyltin dilaurate (DBT) (95%), 1,6-hexamethylene diisocyanate (HDI) (98%), ω-pentadecalactone (98%), ethylene glycol (99.8%), dibutyltin oxide (DBTO) (98%), 1,6-diphenyl-1,3,5-hexatriene (DPH), Pluronic® F127 ($PEG_{100}PPG_{70}PEG_{100}$ triblock polymer), phosphate buffered saline (PBS), docetaxel (DTX), and doxorubicin (DOX) were purchased from Sigma-Aldrich (Singapore). Organic solvents including anhydrous toluene, diethyl ether, isopropanol (IPA), tetrahydrofuran (THF) and ethanol were of ACS grade and obtained from commercial sources. Dulbecco's modified Eagle's medium (DMEM), penicillin, streptomycin sulfate and fetal bovine serum (FBS) were purchased from Life Technology Co., Ltd. (Waltham, MA, USA). Thiazolyl blue tetrazolium bromide (MTT), hematoxylin and eosin staining kit were purchased from Yeasen Biotechnology Co., Ltd. (Shanghai, China). Dialysis tubing (MWCO 3,500 *D*a) was purchased from Spectrum Laboratories (USA). PEG, PPG, ω-pentadecalactone and ethylene glycol were dried under vacuum overnight before use. PBS buffer (0.01 M, pH = 7.4) were prepared by dissolving PBS powder in deionized water. Other materials were used as received.

Synthesis of Poly(ω-Pentadecalactone) Diol (PPDL-Diol)

PPDL-diol was synthesized by the ring opening polymerization of ω-pentadecalactone (Kratz et al., 2009). Twenty gram ω-pentadecalactone (83.2 mmol) was heated to 130°C and then 0.17 g ethylene glycol (2.7 mmol) and 0.07 g DBTO (0.28 mmol) were added under argon atmosphere as initiator and catalyst, respectively. The reaction mixture was dissolved in THF after stirring for 21 days and precipitated in a 5-fold excess of an ethanol/water mixture (50/50 vol%). The resultant PPDL diol was washed with ethanol and vacuum dried at room temperature with a yield of 85% and an average molecular weight of $M_n = 6{,}310\ g{\cdot}mol^{-1}$.

Synthesis of Poly(PPDL/PEG/PPG Urethane) (PDEP) Copolymers

A series of poly(PPDL/PEG/PPG urethane)s were synthesized through a process similar to Chan's study (Chan et al., 2018). The molar ratio of segments PEG and PPG was fixed at 2:1 and the feed weight percentage of PPDL content was set at

2, 5, and 8 wt%, respectively. The resultant copolymers were denoted as *n*PDEP copolymers, where *n* represents for the feed weight percentage of PPDL component, PD for PPDL, E for PEG, and P for PPG. Typically, 10 g starting materials in total, including 6.53 g of PEG (M_n = 2,000, 3.3 mmol), 3.27 g of PPG (M_n = 2,050, 1.6 mmol), and 0.2 g of PPDL-diol (M_n = 6,310, 3.2×10^{-5} mol) were charged into a 250 mL round bottom flask. Dissolve reactants with 100 mL of anhydrous toluene and remove most of the solvent by rotary evaporation with about 10 mL of toluene left. The mixture was stirred and heated up to 110°C under argon atmosphere and then 1.25 mL of HDI (7.8 mmol) and two drops of DBT was injected into the flask as chain extender and catalyst, respectively. The mixture turned viscous gradually and extra 20 mL of anhydrous toluene was added each time when it was hard for the magneton to rotate. After 24 h reaction, products were precipitated from diethyl ether, re-dissolving in IPA and followed by dialysis in deionized water for 72 h. The final pure 2PDEP was obtained by freeze dry. 5PDEP and 8PDEP were prepared through this method, too. Copolymer yields were 70–75%.

Molecular Characterization

^{1}H nuclear magnetic resonance (NMR) and ^{13}C NMR spectra were conducted on JEOL 500 MHz NMR spectrometer (Tokyo, Japan) at room temperature. Deuterated chloroform ($CDCl_3$) was used as solvent for all the samples and chemical shifts were referenced to the solvent peaks at 7.3 and 77 ppm, respectively. Fourier transform infrared (FT-IR) spectra of the copolymer films dissolved in the chloroform coated on KBr tablets were conducted on Spectrum 2000 Perkin Elmer FT-IR spectrophotometer at room temperature. FT-IR spectra were obtained by signal averaging 32 scans at resolution of 4 cm^{-1}.

Thermal Analysis

Thermogravimetric analysis (TGA) was performed on TA Instruments TGA Q500 analyzer (USA) with a heating rate of 20°C·min^{-1} from room temperature to 800°C under a dynamic nitrogen stream (flow rate = 60 mL·min^{-1}). Differential scanning calorimetry (DSC) thermal analysis was performed on photo differential scanning calorimeter (PDSC, Q100, TA Instruments, USA) and indium was used for calibration. The sample was equilibrated at −80°C for 5 min and heated up to 200°C at the rate of 20°C·min^{-1}, then equilibrated at 200°C for 2 min and cooled down to −80°C at the rate of −20°C·min^{-1}. Measurement was conducted twice and data from the second run were used for analysis in case of thermal history in the first run.

Critical Micelle Concentration (CMC) Determination

Aqueous copolymer solution (10 mg·mL^{-1}) was prepared and gradient diluted to obtain samples with a series of concentration. Twenty microliter DPH methanol solution (0.6 mmol·L^{-1}) was added into every 1 mL aqueous copolymer solution and incubated equilibrated at 4°C overnight. UV-vis spectra of the copolymer/DPH solution in the range of 320–460 nm were measured by UV-Vis spectrophotometer (UV-2501 PC, Shimadzu, Japan) at 25°C. Difference in absorbance at 378 and 400 nm (A_{378}-A_{400}) vs. the logarithmic concentration was plotted to determine the CMC value.

Particle Size Analysis

Dynamic light scattering (DLS) measurements were conducted on Zetasizer Nano ZS (Malvern Instruments, Southborough, MA) at 633 nm laser light and 173° scattering angle. Particle size and size distribution were characterized by intensity. Aqueous copolymer solutions (1 mg·mL^{-1}) were passed through a 0.45 μm pore-sized syringe filter before measurements. Reversibility of micelle was evaluated by reversible transition test at 25 and 70°C for 5 cycles, with 15 min equilibration time between each measurement run.

Sol-gel Transition Phase Diagram Determination

Two milliliter aqueous copolymer solution of a given concentration ranging from 6 to 20 wt% were prepared in 4 mL vials and placed at 4°C for 24 h to achieve full dissolution. The samples were equilibrated in water bath with designated temperature for 5 min ranging from 4 to 80°C at interval of 2°C. Critical gelation temperature were defined by the formation of firm gels which kept intact when inverted the vials for a while.

Rheological Studies

The rheological measurements of the thermogels were conducted on TA Instruments Discovery DHR-3 hybrid rheometer (New Castle, DE, USA) fitted with a flat-plate geometry (SST ST 40 mm diameter) and a temperature-controlled peltier base plate. Storage modulus (G') and loss modulus (G") were measured under different types of oscillatory tests. Amplitude sweeps (strain of 0.01–100% and frequency of 1 Hz) and frequency sweeps (frequency of 0.1–100 Hz and strain of 1%) were both performed at 37°C. Temperature ramps were performed between 25 and 37°C and temperature sweeps were performed from 4 to 80°C at a heating rate of 5°C·min^{-1}, both with strain fixed at 1% and frequency fixed at 1 Hz. Self-healing properties of the thermogels were evaluated by amplitude sweep test at two predetermined strain for 10 cycles, 300 s at low strain and 120 s at high strain, with temperature fixed at 37°C and frequency fixed at 1 Hz.

In vitro DTX Release From PDEP Thermogel

One milligram docetaxel was dissolved in an acetone solution together with 10 mg polymer material, dispersed in a phosphate buffer solution, and self-assembled in water to form micelles. The acetone was removed by dialysis, and the micelle solution was added to a polymer-containing PBS solution (2 mL) under low temperature conditions, stirred at a low temperature until thoroughly mixed, and then gelatinized at 37°C. Transfer it to a 15 ml tube, add 10 ml of PBS solution pre-warmed to 37°C, place in a shaker, release the drug at 100 rpm, collect 500 μl of solution per day, and re-add the same volume of fresh PBS solution. The collected solution was detected by high performance liquid chromatography (HPLC) with a mobile phase of 50% acetonitrile and a detection wavelength of 227 nm.

Cytotoxicity Analysis

Hepatoma cells HepG2 cells (American type culture collection, ATCC) were cultured in high glucose medium containing double antibody and 10% fetal bovine serum at 37°C, 5% CO_2 (MacDiarmid et al., 2009). Cytotoxicity analysis was performed using the classical MTT method. HepG2 cells in good growth state were seeded in 96-well plates at a density of 5,000 cells per well, and cultured at 37°C, 5% CO_2 for 24 h. The cells were treated with different samples (PDEP group with the concentration of PDEP from 0 to 1,000 $\mu g \cdot mL^{-1}$, DTX group with the concentration of DTX from 0 to 50 $\mu g \cdot mL^{-1}$ and DTX/PDEP groups with the concentration of DTX from 0 to 50 $\mu g \cdot mL^{-1}$ and the concentration of PDEP from 0 to 250 $\mu g \cdot mL^{-1}$), and after 24 h, the configured MTT solution was added and incubated for 4 h. The results were detected by a microplate reader.

Cell Uptake Analysis

HepG2 cells were placed in a 24-well plate containing glass slides at a density of 20,000 cells per well, and cultured at 37°C, 5% CO_2 for 24 h, and the prepared sample solution (DOX group with the concentration of DOX at 1 $\mu g \cdot mL^{-1}$ and DOX/PDEP groups with the concentration of DOX at 1 $\mu g \cdot mL^{-1}$ and the concentration of PDEP at 5 $\mu g \cdot mL^{-1}$) was added for 2, 6, and 12 h, respectively. After that, the samples were washed away with PBS and fixed with 4% paraformaldehyde for 15 min, then mounted with a DAPI containing sealer and photographed with a confocal microscope Zeiss LSM5.

In vivo Antitumor Effect

All animal experiments were carried out in accordance with the Animal Care Guidelines of Xiamen University under Protocol Number: XMULAC20190033. HepG2 cells in good condition were inoculated to the dorsal side of Balb/c nude mice at a density of 4 million cells per tumor. After the tumor has grown to the appropriate size, the mice are treated with PBS, 2PDEP (12 wt%), 5PDEP (14 wt%), 8PDEP (20 wt%), DTX (1 $mg \cdot ml^{-1}$), DTX (1 $mg \cdot ml^{-1}$)/2PDEP (12 wt%), DTX (1 $mg \cdot ml^{-1}$)/5PDEP (14 wt%), and DTX (1 $mg \cdot ml^{-1}$)/8PDEP (20 wt%) with three nude mice randomly divided into each group. The PBS group and DTX group were given twice a drug (5 $mg \cdot kg^{-1}$) every 2 weeks, and the hydrogel groups were given drug (5 $mg \cdot kg^{-1}$) once a week. The size of the tumor was recorded with a vernier caliper every other day, and the body weight was weighed. The tumor volume was calculated according to the formula of $1/2 \times \text{length} \times \text{width}^2$. After 2 weeks, the mice were sacrificed and the relevant tumor tissues were collected for the next step analysis.

H&E Staining Analysis

The collected tissues and organs were subjected to gradient dehydration for 24 and 12 h with high glucose solutions of 15 and 30%, respectively, and frozen sections were cut at a thickness of 6 μm, followed by staining with hematoxylin and eosin staining for observation and analysis.

Statistical Analysis

All charts and data processing were processed using origin 8 analysis software, the experimental data were expressed as mean and variance, and the significance analysis was analyzed using GraphPad 5.0.

RESULTS AND DISCUSSION

Synthesis and Characterization of PDEP Copolymers

As shown in **Scheme 1**, PPDL-diol was first prepared via ring opening polymerization of ω-pentadecalactone at the presence of initiator ethylene glycol and catalyst DBTO. Then a series of random multiblock PDEP copolymers with different amounts of PPDL incorporated were synthesized via co-condensation of the macrodiols of PPDL, PEG, and PPG using an aliphatic diisocyanate HDI as coupling reagent in the presence of catalyst DBT linker.

The chemical structure of the ω-pentadecalactone, PPDL-diol and PDEP copolymers were verified by ^{1}H NMR and ^{13}C NMR spectroscopy. According to **Figures 1A**,**B**, the specific peaks of PPDL-diol are almost consistent with its monomers except the signals at 4.3 ppm that belong to the methylene of ethylene glycol. And by comparing their integration values, the polymerization degree is estimated to be 26 and the average molecular weight of PPDL-diol is ∼6,310 $g \cdot mol^{-1}$.

Figure 1C and **Figure S1** show the typical ^{1}H NMR spectrum of PDEP in $CDCl_3$ with all proton signals belonging to PEG, PPG, and PPDL segments confirmed (Jiang, 2011; Li et al., 2012). In details, the signals corresponding to methyl protons of PPG are presented at 1.1 ppm while the signals corresponding to protons attached to backbone carbons in PPG are observed at 3.4 and 3.5 ppm. The signals at 3.6 ppm are assigned to methylene protons in repeated unites of PEG segments while the signals at 1.2 ppm are attributed to methylene protons in repeated unites of PPDL segments. The compositions of each component in the PDEP copolymers could be calculated from the integration ratio of distinguishable proton signals at 1.2, 3.4, and 3.6 ppm, and the results are shown in **Table 1**.

^{13}C spectrum of 2PDEP is shown in **Figure 1D**. The signals at 17.3, 73.4, and 75.4 ppm are ascribed to methyl, methylene and methine carbon of PPG segments, respectively, and the signals at 70.6 ppm are attributed to methylene carbon of the PEG segments (Li et al., 2012). The signals at 174.0 and 34.5 ppm are attributed to the carbonyl carbon and methylene carbon alpha to the carbonyl group of PPDL segments, respectively, while the signals corresponding to the rest methylene carbon could be found between 25 and 30 ppm (Jiang, 2011). Meanwhile, the spectrum also presents signals generated from the HDI junction unit at 26.4, 30.0, 41.0, and 156.5 ppm, indicating that the polycondensation reaction was successful (Li et al., 2012).

FT-IR spectra of a series of PDEP copolymers and macrodiols of PEG, PPG and PPDL further confirm the successful synthesis of copolymers (**Figure 2A**). The FT-IR spectrum of PPDL-diol is typical of the stretching vibration of C=O in ester group whose absorption band is strong and sharp at 1,730 cm^{-1} (Pilate

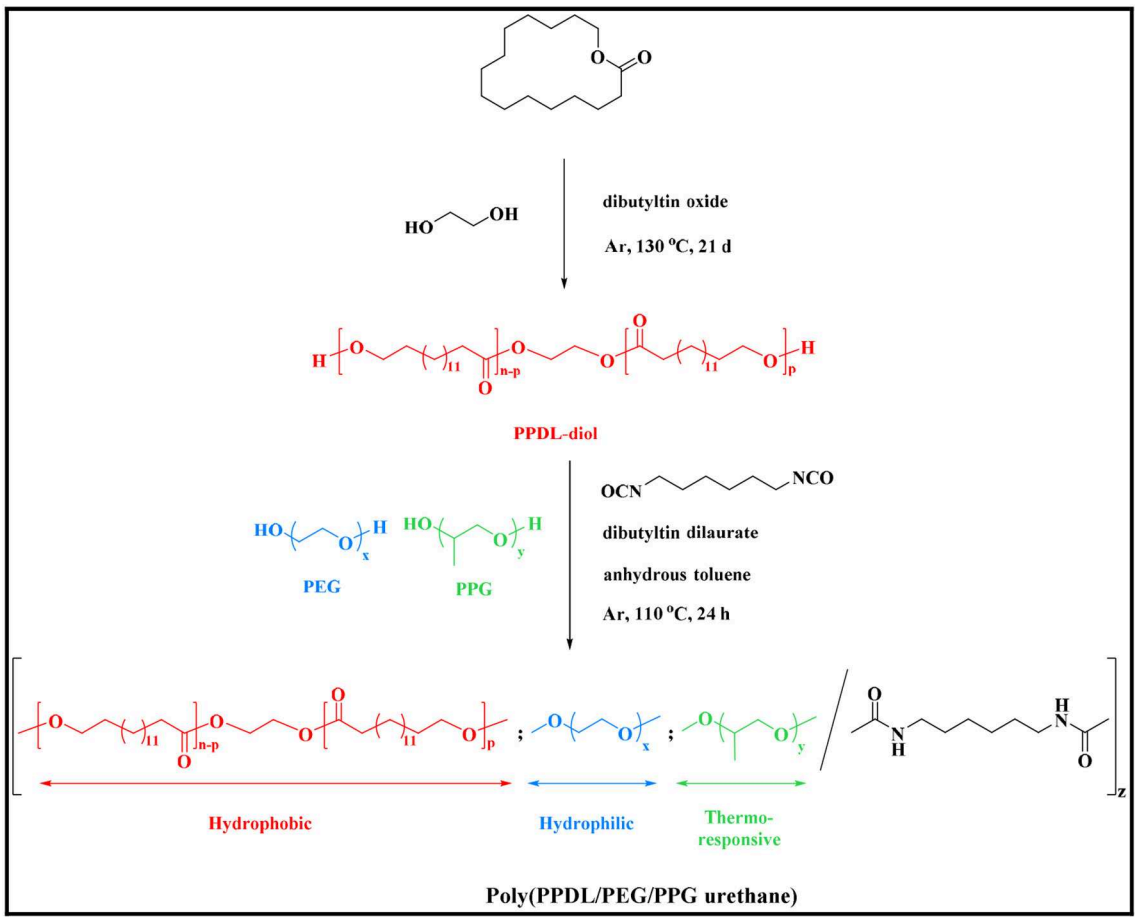

SCHEME 1 | Synthetic routes of PDEP copolymers.

et al., 2018). Both PEG and PPG precursors present an intensive absorption band at 1,102 cm^{-1} due to the stretching vibration of C-O-C in the repeated unites (Loh et al., 2007). Absorption band for stretching vibration of saturated C-H in three macrodiols are exhibited at 2,875 and 2,918 cm^{-1}. All these characteristic absorption bands are clearly observed in the FT-IR spectra of PDEP copolymers, confirming the presence of PPDL, PEG, and PPG segments. Additionally, the characteristic absorption band of HDI between 2,260 cm^{-1} and 2,280 cm^{-1} attributed to the stretching vibration of NCO disappears while a new small absorption band corresponding to the deformation vibration of N-H appears at 1,534 cm^{-1} in the FT-IR spectra of copolymers (Pilate et al., 2018), which gives evidence of the successful reaction between hydroxy groups in polymer precursors and isocyanate groups in HDI.

The thermal analysis of PDEP copolymers are conducted as well to understand the influence of the incorporation of PPDL and confirm the suitability of temperature for biomedical applications. The TGA curves shown in **Figure 2B** represent similar profile with F127 (Qin et al., 2013), but better thermal stability measured by decomposition temperature. Compared to commercial Pluronic® F127 which starts to lose weight at around 220°C, all the synthesized copolymers are thermally stable below 300°C. Defined as the onset temperature at 5% weight loss, the decomposition temperature (T_d) for 2PDEP, 5PDEP, and 8PDEP is 335.48, 313.98, and 304.59°C, respectively. The incorporation of the urethane linkages and the hydrophobic PPDL segments enhances the rigidity of the backbone as well as the intermolecular forces, contributing to the improvement in thermal performance for the copolymers together (Wang et al., 2015). But meanwhile, the addition of PPDL might compromise the regularity of the polymer chains to some extent, which counteracts the positive effects and makes the T_d of the copolymers decline with the increasing amount of PPDL (Yang S. et al., 2017).

As for the DSC results of PDEP copolymers, two melting peaks in heating curves (**Figure 2C**) and two crystallization peaks in cooling curves (**Figure 2D**) are observed for all copolymers, which might be attributed to the presence of two different types of crystalline domains rich in PPDL and PEG segments, respectively (Araneda et al., 2012). Meanwhile, the copolymers exhibit a single glass transition in heating curves, suggesting that the PPDL segments are likely to be thermodynamically miscible with PEG and PPG segments (Yeo et al., 2018). The crystalline temperature

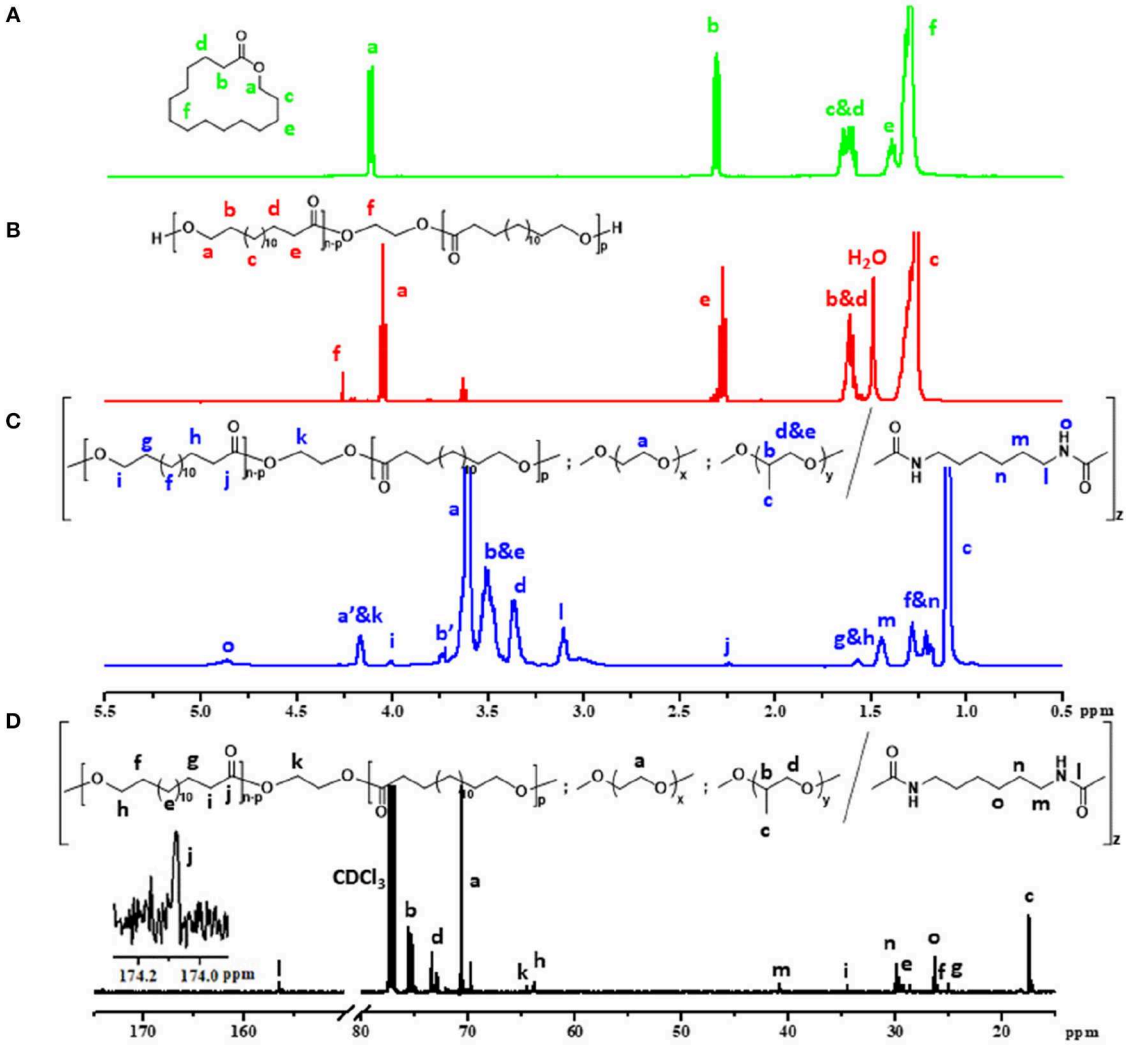

FIGURE 1 | Five hundred megahertz ^{1}H NMR spectrum of **(A)** ω-pentadecalactone, **(B)** PPDL-diol, **(C)** 2PDEP (a', b' represent protons on terminal unit of PEG and PPG segments which reacted with HMDI) and **(D)** ^{13}C NMR spectrum of 2PDEP in $CDCl_3$.

(T_c), melting temperature (T_m) and glass transition temperature (T_g) of the copolymers are tabulated in **Table 1**. Compared with the value of T_c and T_m for PEG (35 and 53°C) and PPDL (85 and 90°C) in reference to literature (Martino et al., 2012; Kuru and Aksoy, 2014), T_c and T_m of the copolymers are both lowered as copolymerization depresses the regularity of polymer chains and reduces the crystallinity (Li B. et al., 2008). However, the influence of PPDL content on T_c, T_m, and T_g are not evident, probably because the PPDL content is too low and close to make a difference.

Micellar Properties of Aqueous Copolymer Solutions

The PDEP copolymers are amphiphilic and able to form micelles in aqueous solution above the critical micelle concentration (CMC). The CMC values for these copolymers were determined by dye solubilization method at 25°C. The absorption coefficient of hydrophobic dye DPH in a hydrophobic environment is higher than that in a hydrophilic environment. When micelles are formed with increasing copolymer concentration, DPH molecules are incline to entering the hydrophobic core of the micelles and thus the absorbances of the aqueous copolymer solutions at 344, 358, and 378 nm increased (**Figure 3A**, **Figures S2A,C**) (Alexandridis et al., 1994). The point where the absorbance values display a sharp increase is defined as the CMC at which micelle formation occurs. As shown in **Figure 3B** and **Figures S2B,D**, the difference of absorbance at 378 nm and 400 nm (A_{378}-A_{400}) is plotted vs. the logarithmic concentration of the copolymers to determine the CMC values, which are tabulated in **Table 1**. In view that the CMC value for commercial Pluronic® F127 with similar mass fraction of PEG and PPG is reported to be 2.5×10^{-3} g·mL^{-1} at 25°C by literature (Perry et al., 2011), the incorporation of hydrophobic PPDL segments makes a remarkable decrease of the CMC values for

TABLE 1 | Molecular characteristics and properties of PDEP copolymers.

Copolymer	Feed ratio/g			Composition in copolymer/wt%[a]			Copolymer characteristics	Thermal properties			
	PPDL	PEG	PPG	PPDL	PEG	PPG	CMC[b] (g·mL^{-1})	T_d/°C[c]	T_c/°C[d]	T_m/°C[d]	T_g/°C[d]
2PDEP	0.2	6.53	3.27	2.9	68.3	28.8	7.24×10^{-4}	335.48	30.57/−2.63	86.83/41.43	−57.12
5PDEP	0.5	6.33	3.17	5.0	67.1	27.9	7.85×10^{-4}	313.98	30.12/−0.83	86.27/37.71	−58.26
8PDEP	0.8	6.13	3.07	9.5	63.8	26.7	7.10×10^{-4}	304.59	31.04/2.46	86.34/36.82	−58.58

[a] *Calculated from ^{1}H NMR spectroscopy results.*
[b] *Determined by the dye solubilization technique at 25°C.*
[c] *Obtained from TGA analysis.*
[d] *Obtained from DSC analysis.*

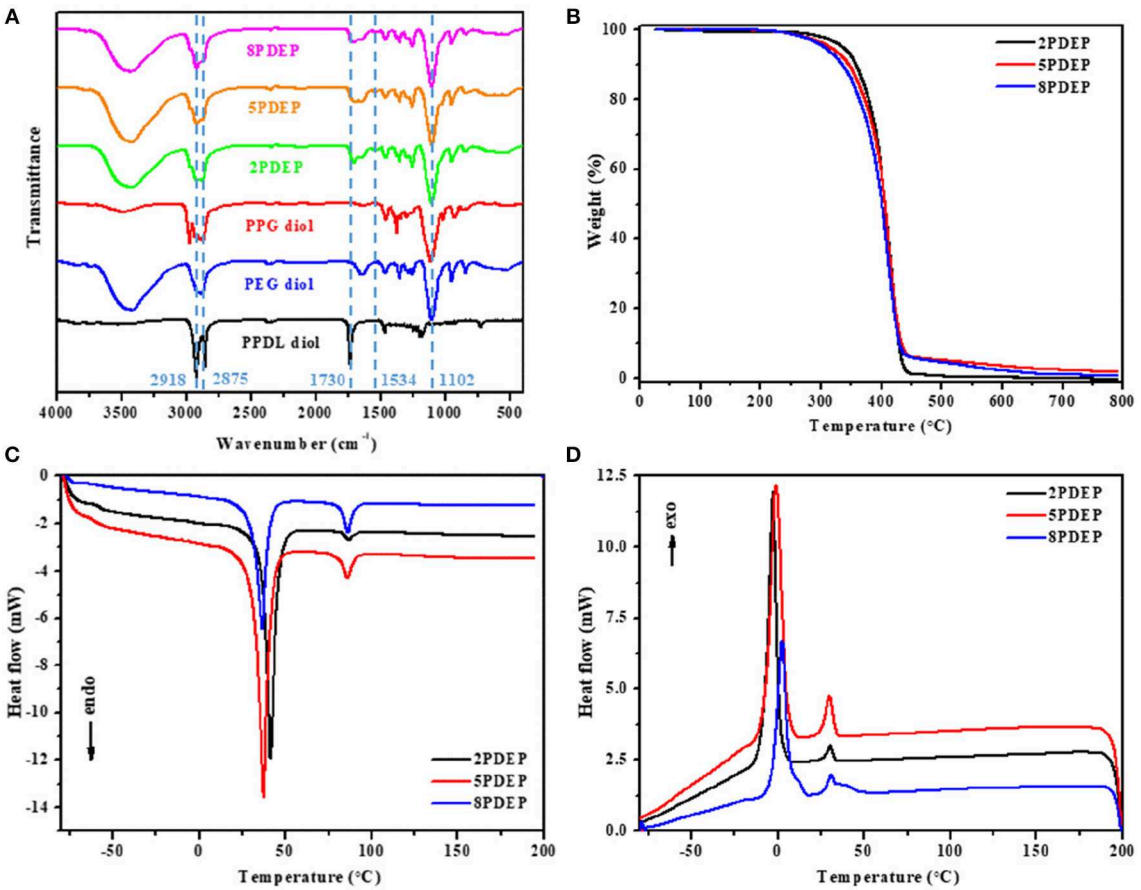

FIGURE 2 | (A) FT-IR spectra of PDEP copolymers and macrodiols, **(B)** TGA curves of PDEP copolymers, **(C)** DSC heating curves of PDEP copolymers and **(D)** DSC cooling curves of PDEP copolymers.

PDEP copolymers to around 7×10^{-4} g·mL^{-1} as a result of the enhanced hydrophobic interaction as well as driving force for self-assembly to achieve a state of minimum free energy. Nonetheless, the CMC values for the copolymers show no significant change with the increasing of the PPDL content, which might be ascribed to the relatively close PPDL content and the wide molecular distribution.

The micelles formed from PDEP copolymers are typically composed of a hydrophobic core and hydrophilic corona (Nakashima and Bahadur, 2006). The presence of PPG segments, well-known for exhibiting hydrophilicity at lower temperature and hydrophobicity at higher temperature, endows the copolymer micelles with thermal sensitivity (Shinohara et al., 2014). To investigate this property, the hydrodynamic diameter distribution by intensity for 2PDEP micelles in aqueous solutions (1 mg·mL^{-1}) were investigated by DLS at two different temperatures (25 and 70°C). As shown in **Figure 3C**, at lower temperature, there are double peaks with partially overlap, one peak value of which is at around 60 nm and the other is at around 340 nm. The corresponding mean

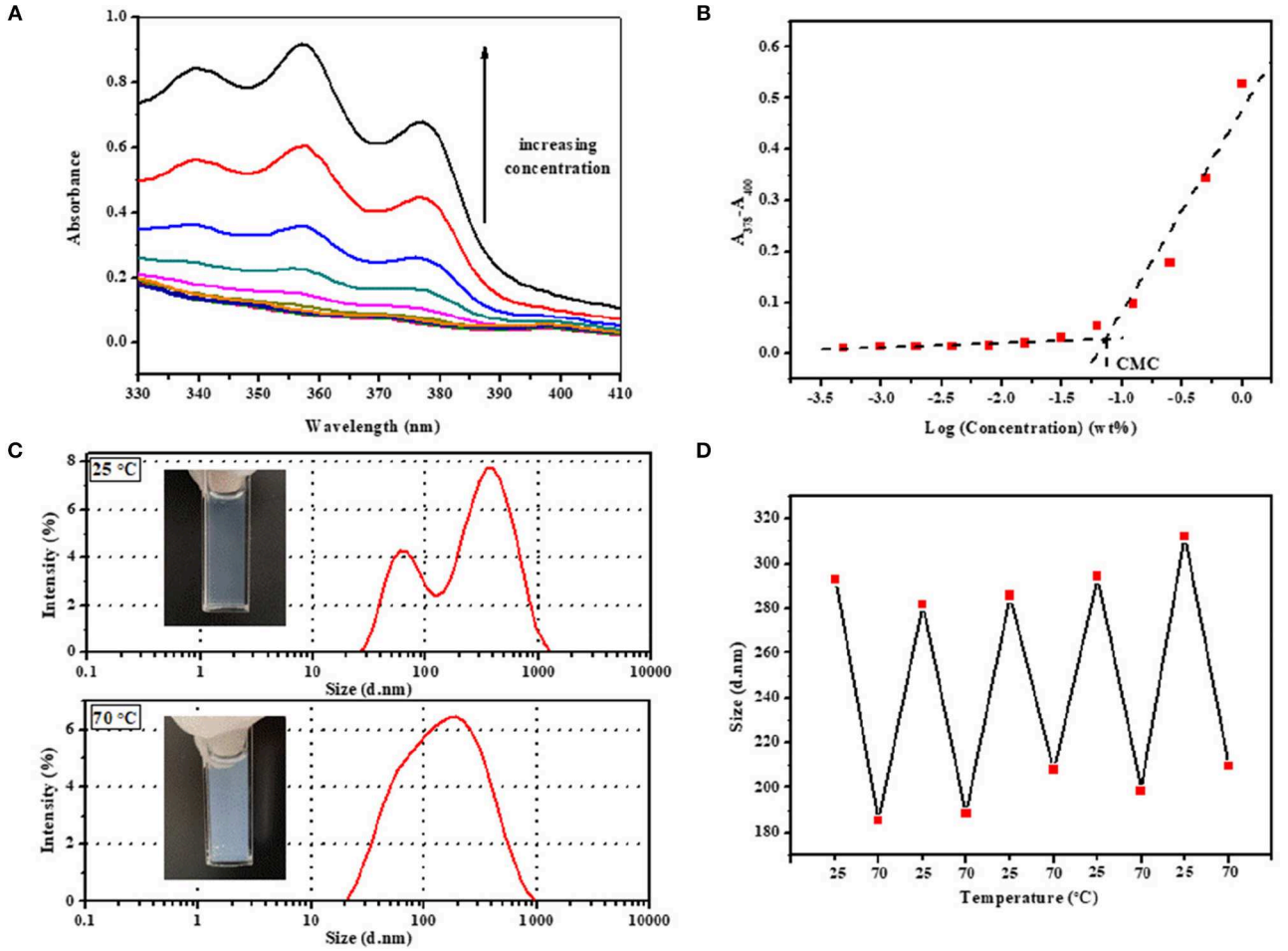

FIGURE 3 | (A) UV–vis spectra of aqueous copolymer solution with concentration ranging from 0.005 to 10 mg·mL^{-1} at 25°C and **(B)** CMC determination for 2PDEP. **(C)** Real images and hydrodynamic diameter distribution by intensity of micelles at 25 and 70°C and **(D)** reversible transition in mean hydrodynamic diameter distribution of micelles between 25 and 70°C for 2PDEP aqueous solution with concentration of 1 mg·mL^{-1}.

diameter and PDI of the micelles are 293.1 nm and 0.512, respectively. According to literature, hydrodynamic micelle diameter for commercial Pluronic® F127 at 25°C has been observed as 30 nm or so with a single peak in size distribution (Desai et al., 2001). Thus, this result indicates that the incorporation of hydrophobic PPDL segments might lead to an increase in micelle size as well as aggregation of micelles to provide a favorable hydrophilic and hydrophobic balance. At higher temperature, the size distribution curve tended to be unimodal with the peak value at around 190 nm. The corresponding mean diameter and PDI of the micelles are 185.6 and 0.306, respectively. With elevated temperature, the PPG chains become more hydrophobic and tend to pack more tightly into the micelle core, resulting in smaller micelles, but meanwhile, the percentage of micellar aggregates increase since the PPG units are more liable to dehydrate and collapse with each other, supported by the significantly decreases in the optical transmittance of the copolymer solution from 25 to 70°C. The integration of these two effect makes the double peaks come closer and brings out one merged peak with an overall decrease in mean diameter by intensity eventually.

The reversibility of the hydrodynamic micelle size change triggered by temperature was characterized by DLS too. The transition of 2PDEP aqueous solution were conducted between 25 and 70°C for five cycles with 15 min for equilibrium before measurement each time. As shown in **Figure 3D**, the mean hydrodynamic diameter by intensity of the micelles decreases from 293 ± 10 nm at 25°C to much smaller value of 198 ± 10 nm at 70°C, exhibiting good reversibility upon temperature change due to the reversible hydrophilicity and hydrophobicity transition of PPG segments.

Thermo-Responsive Sol-gel Transition and Gel Properties

Similar to thermogelling systems we have reported previously (Loh et al., 2012b; Wu et al., 2016c; Wee et al., 2017), PDEP copolymers in aqueous solutions render an increasing tendency to successively form micelles, micellar aggregates, and gels with temperature and copolymer concentration going up as a

result of enhancing intra- and inter-micellar interactions. To investigate the gel formation ability of PDEP copolymers in aqueous, the tube inverting method was employed to determine their phase diagrams which underwent a monotonic increase of temperature from 4 to 80°C at interval of 2°C. Instead of typical sol-gel-sol transition with increasing temperature for

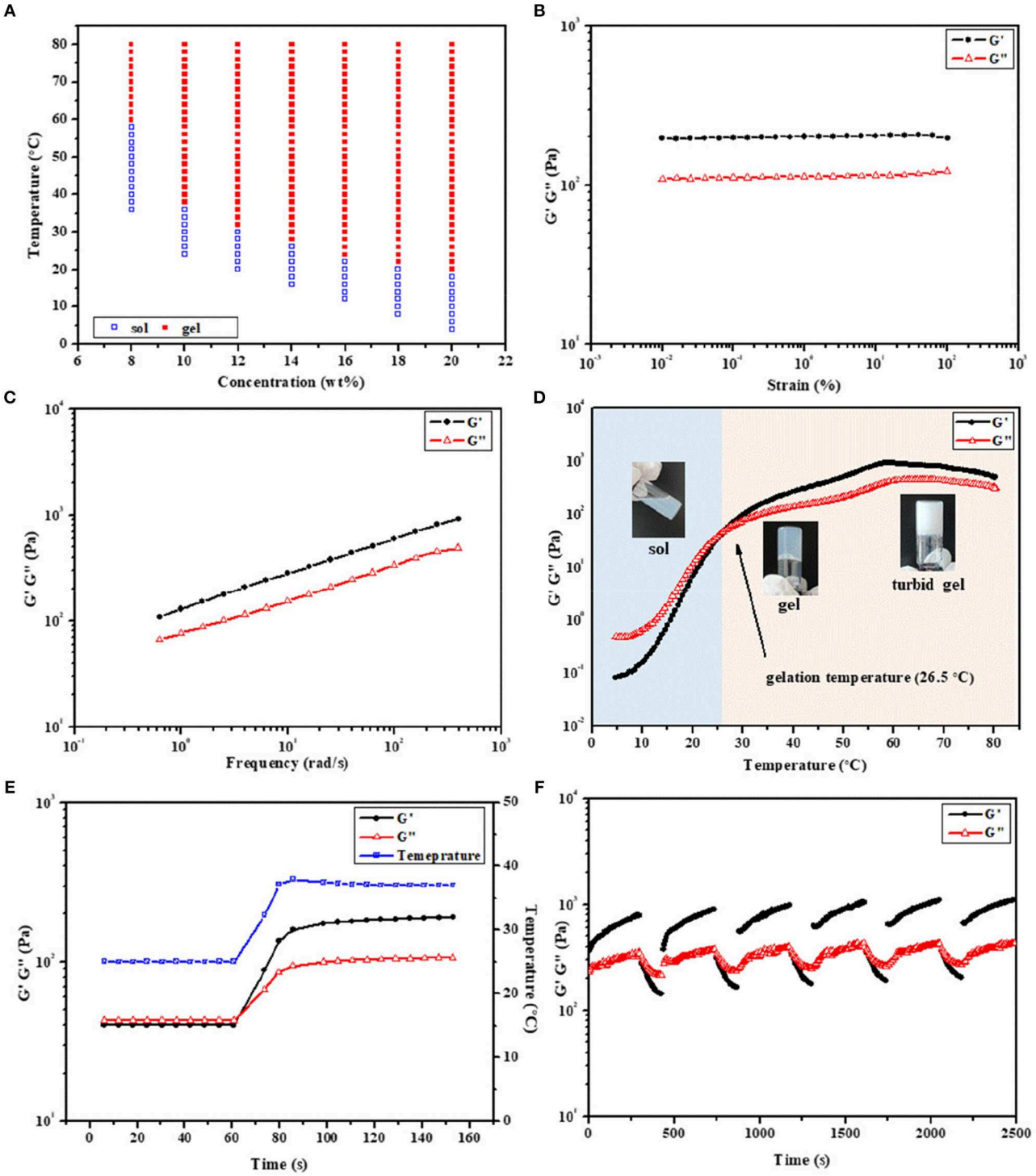

FIGURE 4 | (A) Phase diagrams of 2PDEP in aqueous solutions. Storage modulus (G') and loss modulus (G") of **(B)** amplitude sweep (0.01–100%, 1 Hz, 37°C), **(C)** frequency sweep (1%, 0.1–100 Hz, 37°C), **(D)** temperature sweep (1%, 1 Hz, 4–80°C) and **(E)** temperature ramp (1%, 1 Hz, 25 to 37°C) for 2PDEP aqueous solution (12 wt%) obtained from dynamic rheological analysis. **(F)** Self-healing cycle amplitude sweep (0.01 and 50%, 1 Hz, 37°C) for 8PDEP aqueous solution (16 wt%) obtained from dynamic rheological analysis.

many reported thermogelling systems resulted from the collapse of hydrogel networks, PDEP thermogels exhibit good stability at high temperature and demonstrated sol-gel-turbid gel transition (**Figure 4A**), which might be attributed to the strong association between hydrophobic PPDL and PPG segments and is supported by the thermal analysis results (Chan et al., 2018). Reverse phase transition were observed when the samples were cooled down from 80 to 4°C as well. Moreover, CGC values for 2PDEP, 5PDEP, and 8PDEP are around 7, 9, and 13.5 wt%, respectively, all lower than the CGC value for commercial Pluronic® F127 which is around 17 wt% on account that the incorporation of hydrophobic PPDL provides greater driving force for the copolymers to self-assemble into gels at certain concentrations (**Figure S3**). However, it also appears that the raise of PPDL content in the copolymers causes the CGC values to increase. The reason is probably because that the increasing amount of PPDL gives rise to high viscosity of the copolymer solutions and impede segmental motions in the process of self-assembly, and thus increase inhomogeneity and defects in the networks, which are not firm enough to be regarded as gels for low concentration groups (Barshtein et al., 1995).

The rheological behaviors of PDEP thermogels were measured to investigate their thermo-responsiveness. Amplitude sweep between the strain range of 0.01–100% was conducted at 37°C first to determine the linear viscoelastic regime. The storage modulus (G') and loss modulus (G") for 2PDEP aqueous solution with the concentration at 12 wt% are almost constant at all test strain, in which G' is much greater than G" and suggests the copolymer solution behaves a solid-like property at 37°C (**Figure 4B**). When the applied strain are higher above 100%, both G' and G" decline rapidly and a reversal of their relative position is observed at strain of around 180%, indicating the deformation of the thermogels (**Figure S6A**). Similar changes of G' and G" with increasing strain were observed for 5PDEP and 8PDEP (**Figures S4A, S5A**). Frequency sweep was also conducted between the frequency range of 0.1–100 Hz at 37°C and the results show positive dependence of G' and G" on oscillation frequency, where the copolymer solution is at gel state all the time and become stronger and stronger (**Figure 4C**, **Figures S4B, S5B**). This tendency could be explained by the time-temperature superposition principle for the viscoelastic behavior of polymers. Given that the intramolecular associations in thermogels would be strengthened and raise the value of both G' and G" at high temperature, which are supported by the result of temperature sweep (**Figure 4D**, **Figures S4C, S5C**), the increase of frequency is equivalent to the increase of temperature within certain range and therefore brings out the concomitant rise of G' and G". The thermogelling transition of the copolymer solutions was verified by consecutive temperature sweeps between 4 and 80°C. With temperature varying from low to high, the G' and G" of the copolymer solutions keep increasing, resulting in a transition from liquid-like property to solid-like property. Gelation temperature for 2PDEP copolymers at the concentration 12 wt% is determined by the crossover of G' and G" curves. As the copolymer solution at this point actually presents a semi-solid state which is not yet firm, it is justified for the gelation temperature obtained from rheological studies (26.5°C) to be a bit lower than the value obtained from tube inverting method (32°C). Besides, it's noteworthy that PDEP thermogels demonstrate fast sol-gel transition in a time frame of less than second upon the change of temperature (**Figure 4E**, **Figures S4D, S5D**). As shown in **Figure 4E**, 2PDEP aqueous solution performs as liquid-like state (G'<G") at 25°C and immediately converts to stable solid-like state (G'>G") as the temperature was raised to 37°C, the fast responsiveness of which makes it advantageous in biomedical application such as minimally invasive *in situ* delivery system.

The self-healing properties of the thermogels were also evaluated by dynamic rheological analysis. Though the

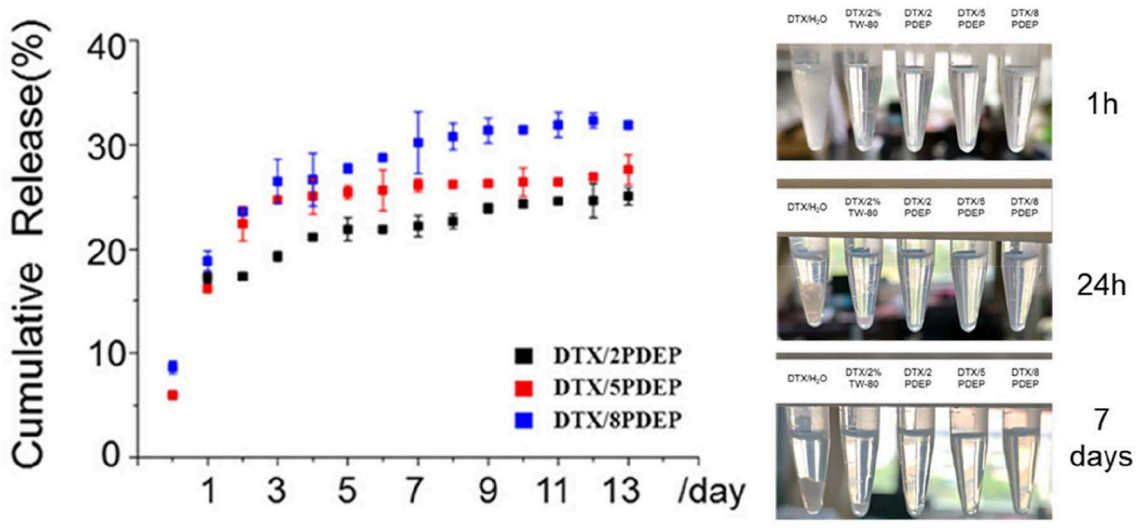

FIGURE 5 | *In vitro* drug release profile of DTX released from PDEP micelle-hydrogel system.

non-covalent interactions in the thermogels are strong enough for the formation of a gel, they were actually weak for the network when the gel is exposed to external force which is possible to break then. Thus, the ability of the materials to self-heal to original gel structure by the same physical interactions when the external stress is removed is practical in applications (Karim and Loh, 2015). As shown in **Figure 4F**, the thermogels formed from 8PDEP present rapid sol-gel transition and regular changing profile of G' and G" with the strain alternately varying between

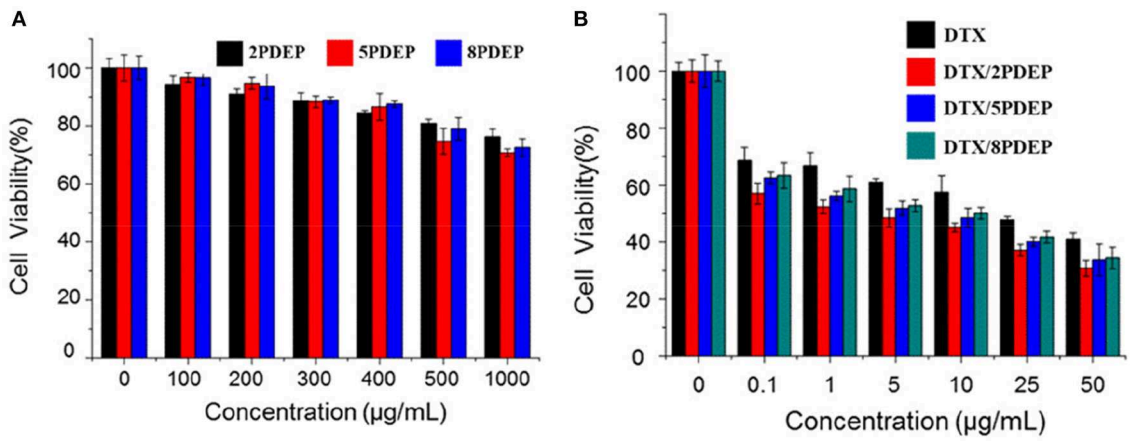

FIGURE 6 | Cytotoxicity of different drug forms for HepG2 cells. **(A)** Different PDEP micelle forms; **(B)** different DTX drug forms.

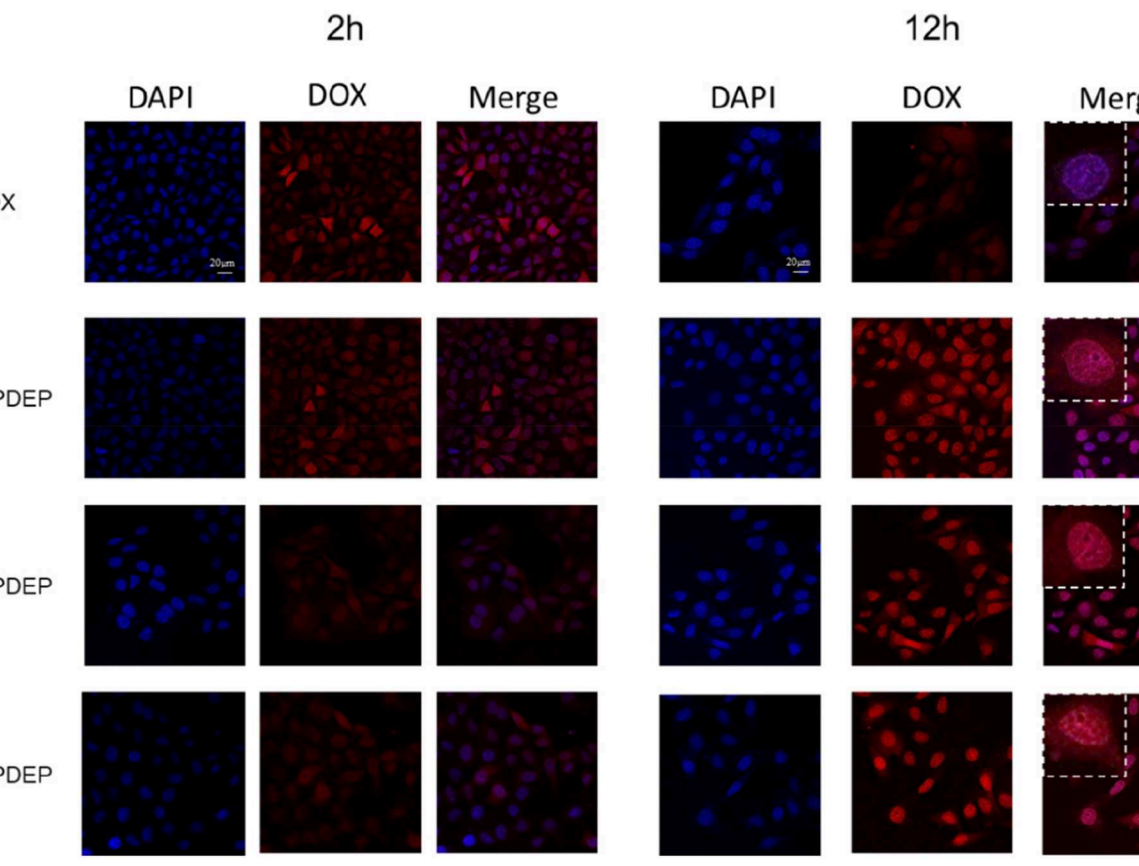

FIGURE 7 | Confocal images of HepG2 cells incubated with DOX (1 μg·mL^{-1}) and PDEP micelles (5 μg·mL^{-1}) loaded with DOX (1 μg·mL^{-1}) after 2 or 12 h.

0.01 and 50%, and are able to recover original strength gradually after being damaged by high strain. Similar phenomena are observed in the thermogels of 2PDEP and 5PDEP (**Figures S6B,C**), offering them prolonged lifetime as biomaterials *in vivo*.

DTX Release From PDEP Thermogels *in vitro*

Some chemotherapeutic drugs with good anticancer effect are often limited in clinical use due to their poor water-solubility. Improving the water solubility and stability of some hydrophobic drugs is of great significance for improving their anti-tumor effects. As is apparent from **Figure 5**, PDEP-wrapped DTX can significantly increase the water solubility of the hydrophobic DTX drug. Compared with the commonly used surfactant Tween-80, DPEP loaded DTX showed more stability, and no obvious DTX precipitation was observed after 1 week at room temperature

In order to verify whether the micelle-hydrogel system loaded with DTX drugs could continuously and effectively release the drug, we conducted a 14 day *in vitro* release experiment, and the experimental results are shown in **Figure 5**. There is a burst release of DTX occurred in the first 5 days, and then the drug release from the three hydrogels tends to be stable. As can be seen from the figure, after 14 days of drug release, the maximum drug release of 2PDEP, 5PDEP, 8PDEP thermogels was 25, 27, and 32%, respectively. All three hydrogels were able to release the drug continuously and effectively, and the drug release profile was similar.

Cytotoxicity Analysis

The killing ability of PDEP micelles loaded with DTX drugs for liver cancer HepG2 cells was verified by using the classical

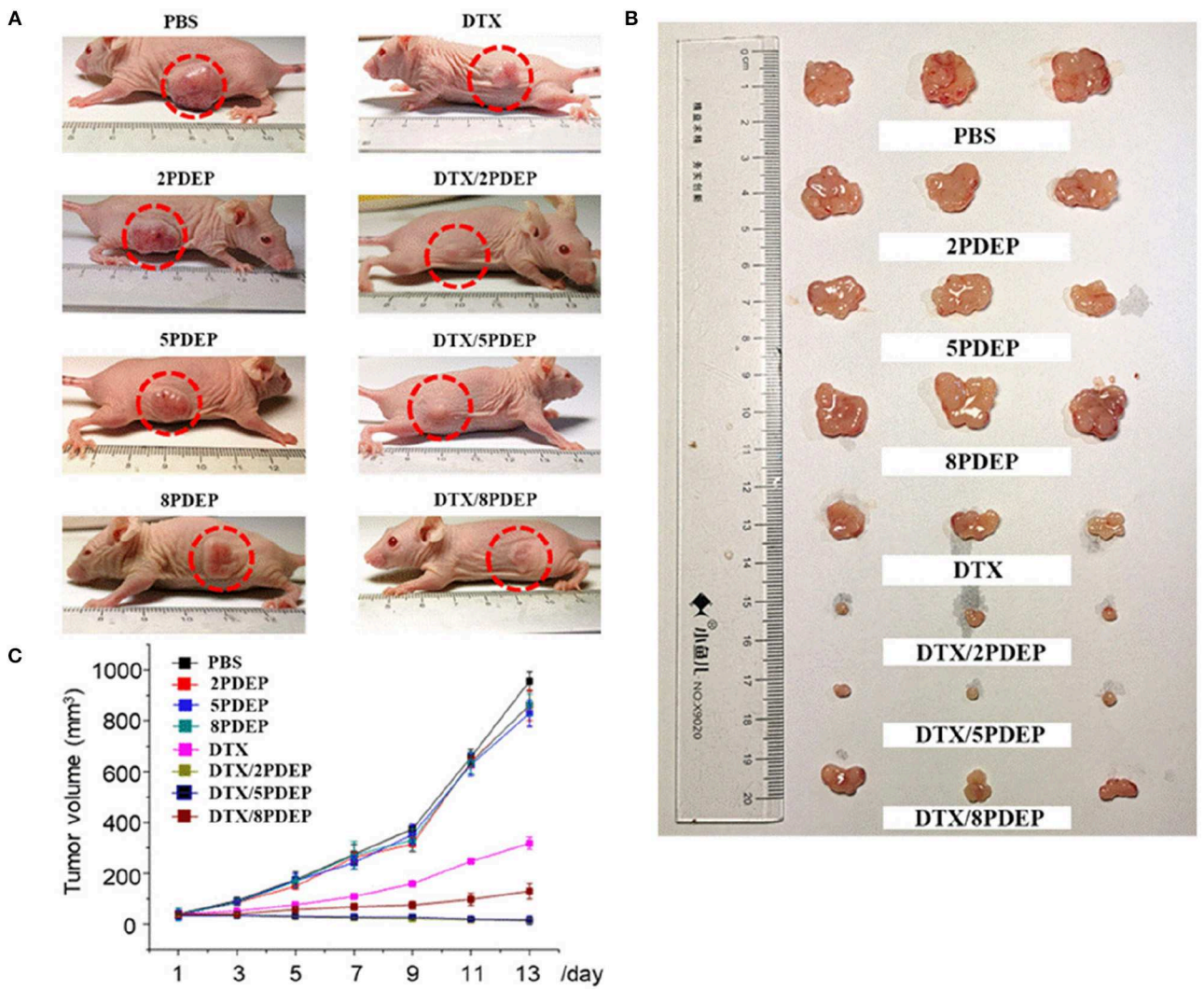

FIGURE 8 | The therapeutic effect of the DTX-loaded micelle-PDEP thermogel system on xenograft tumor mice established with HepG2 cells. **(A)** Tumor in the body of mice. **(B)**Tumor isolated from mouse. **(C)** Tumor volume size curve.

MTT method. From **Figure 6A**, it could be seen that when the concentration of the PDEP copolymers reaches 1 mg·mL^{-1}, the cell survival rate still has nearly 80% of cell survival. This shows that our material itself is not significantly toxic to cells. From **Figure 6B**, we can see that compared with individual DTX group, the killing ability of the drug against HepG2 cells in the DTX/PDEP group could be significantly improved. It might be because the formation of DTX/PDEP micelles could increase the solubility and stability of the drug and the amount of drug entering the tumor cell. Therefore, when the drug-loaded micelles are encapsulated into the PDEP thermogels, continuous drug delivery in the form of micelles and increasing amount of drug taken by tumor cells could be achieved, resulting in better anti-tumor effects.

Cell Uptake Analysis

To explore the ability of HepG2 cells to take in micelles, fluorescent DOX instead of DTX was used. **Figure 7** shows the confocal images of hepatoma cell HepG2 incubated with DOX/PDEP micelles. Red fluorescence represents the drug DOX and blue fluorescence represents the DAPI stained nuclei. It could be seen that at 2 h, the HepG2 cells of individual DOX group shows obvious red fluorescence while the red fluorescence in the DOX/PDEP group was dim. It might be because that

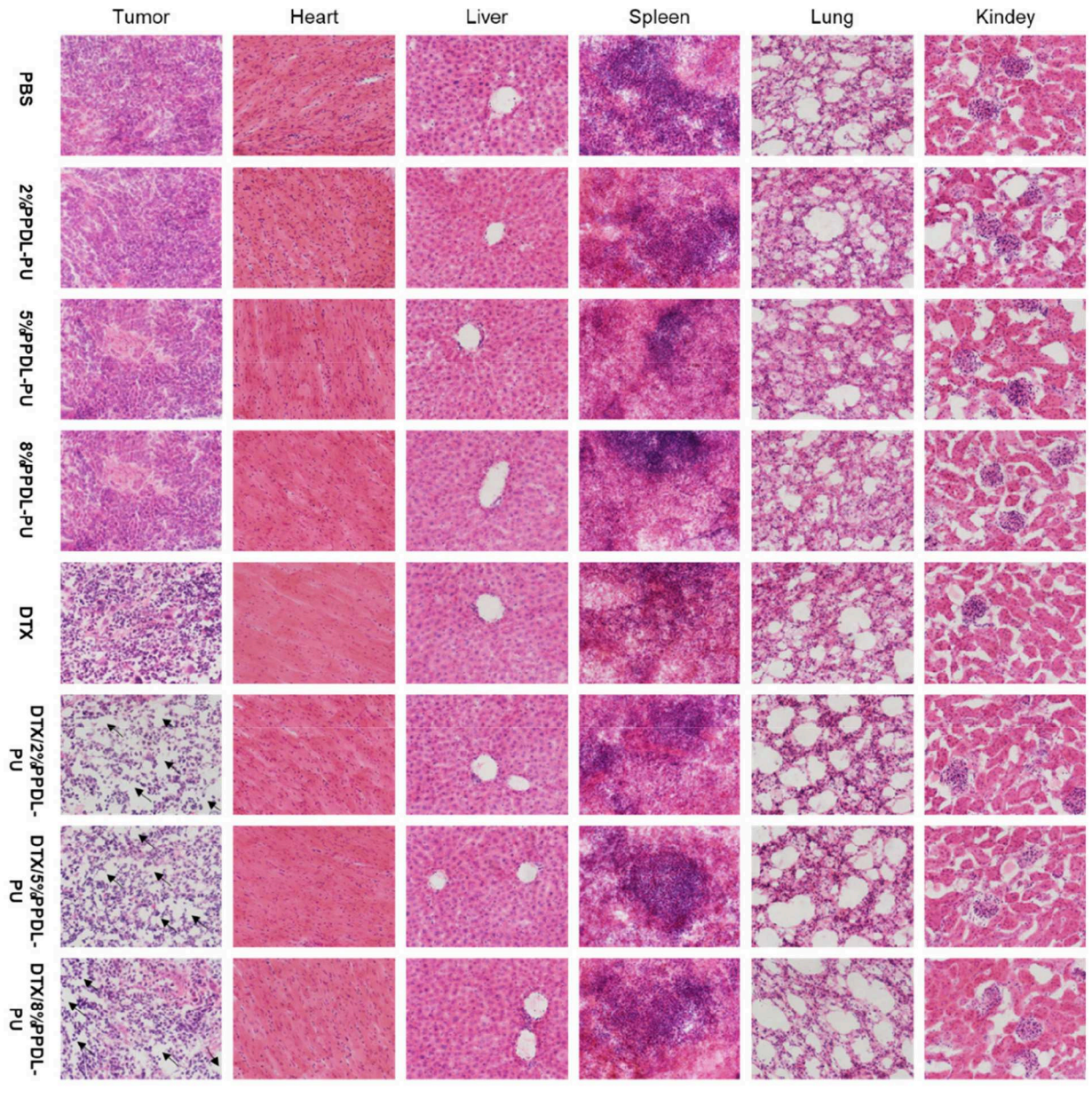

FIGURE 9 | HandE staining analysis of the effects of different drug forms on tumors and major organs (heart, liver, spleen, lung, and kidney).

individual drug enters the cell mainly through diffusion while the drug encapsulated in copolymer micelles enters the cell mainly through endocytosis. The rate of the former manner is faster and brings about stronger red fluorescence in early period. At 12 h, the intensity of red fluorescence for DOX/PDEP group is significantly stronger than that of the individual DOX group, but there is no significant difference among three groups of PDEP. This might be due to the fact that the amounts of DOX that is swallowed into the cells are more than the drugs that are diffused alone, and the material might be able to increase the stability of the drug within the cell. From the confocal images, we could see that the cells are able to ingest the material well, and the material could increase the amount and stability of the drug into the cells, which is potential to be a good drug delivery carrier.

Antitumor Effect *in vivo*

To explore the *in vivo* anti-tumor effects of DTX-loaded micelle encapsulated in PDEP thermogels, we established a subcutaneous HepG2 liver cancer xenograft model for exploration. In initial stage, intratumoral injection of DTX/PDEP thermogels were implemented. When the tumor size on the back of the mouse reached 40 mm^3, we started subcutaneous administration. The therapeutic effect after 14 day treatment is shown in **Figure 8**. It could be seen that the size of the tumor in PDEP alone group is close to that of controlled PBS group, and the final tumor size is about 900 mm^3, indicating that a single material does not have the effect of inhibiting the tumor. Compared to the DTX alone group whose final tumor size is about 300 mm^3, the DTX/PDEP group is able to significantly inhibit tumor growth. Among three copolymers, 2PDEP and 5PDEP work best and there is no significant difference between each them, both the final tumor size of which is about 15 mm^3. The final tumor size of the DTX/8PDEP group is about 120 mm^3, whose inhibition effect is relatively poor in comparison with other two copolymers. It might be because the rate of drug release in 8PDEP thermogels faster and imbalanced with the retention ability of drug in tissue, resulting in lesser release of the drug in later stage and thus poorer inhibition effect. As 2PDEP and 5PDEP thermogel systems could effectively achieve sustained drug release and effectively inhibit the development of HepG2 tumors, they are considered to have a good prospect in clinical application.

H&E Staining Analysis

To further explore the effects of different drug forms on tumor tissues and other tissues and organs, we analyzed sections of tumor tissues and major organs by H&E staining. From the results shown in **Figure 9**, we could see that the tumor tissue sections of the PDEP alone group did not differ significantly compared with the PBS controlled group, further verifying that the individual materials could not kill the tumor cells. In the drug-administered group, it is obvious that there is a large area of tumor cell apoptosis in the tumor tissue section, and the number of tumor cells was significantly reduced, especially for DTX/2PDEP and DTX/5PDEP group. As for other organs (heart, liver, spleen, lung, and kidney) sections, all the groups have no significant difference compared with the PBS controlled group, further indicating that the hydrogel has a good biosafety.

CONCLUSION

In this work, a series of multiblock poly(PPDL/PEG/PPG) urethane polymers were synthesized with good thermal stability and miscibility. The dilute PDEP copolymer aqueous solutions self-assembled into micelles with lower CMC values ($\sim 7 \times 10^{-4}$ g·mL^{-1}) compared to commercial Pluronic® F127, which shrank and aggregated at elevated temperatures and exhibited good reversibility as characterized by DLS. In certain concentration and temperature, the PDEP copolymer aqueous solutions could form thermogels and kept stable even at temperature as high as 80°C. The CGC values of PDEP copolymers were related to the composition of PPDL segment and all lower than that of commercial Pluronic® F127, among which 2PDEP copolymer gave the best gelation performance with CGC at 7 wt%. According to rheological results, the PDEP based thermogels presented fast response to temperature change and good self-healing properties after being broken by high strain. As for biocompatibility, individual PDEP copolymers displayed low toxicity both *in vitro* and *in vivo*. *In vitro* drug release studies showed continuous release of DTX from PDEP based thermogels for about 5 days with the cumulative amount up to 32%, and cell uptake studies demonstrated that the DOX loaded PDEP based micelles could increase the amount and stability of the drug entering the cells by endocytosis. Through *in vivo* anti-tumor effect studies, the growth of xenograft HepG2 tumor on mice was proved to be significantly inhibited by DTX loaded PDEP thermogel system, especially for 2DPEP and 5PDEP, while no damage were caused to other normal tissues. As all these results shown, the PDEP copolymers are promising to be a good drug delivery depot for chemotherapeutic applications.

DATA AVAILABILITY STATEMENT

The datasets generated for this study are available on request to the corresponding author.

ETHICS STATEMENT

All animal experiments were carried out in accordance with the Animal Care Guidelines of Xiamen University under Protocol Number: XMULAC20190033.

AUTHOR CONTRIBUTIONS

HS: gel synthesis and manuscript writing. HC: materials characterization and discussion. ZLu: mice model built and bio-experiments. LJ: rheology evaluation. XL: technical advisor for drug formulation and discussion. CH: rational design of material composition and structure-property relationship. ZLi: technical advisor to overview the project, manuscript planning, and revision.

SUPPLEMENTARY MATERIAL

The Supplementary Material for this article can be found online at: https://www.frontiersin.org/articles/10.3389/fchem.2019.00683/full#supplementary-material

REFERENCES

Alexandridis, P., Holzwarth, J. F., and Hatton, T. A. (1994). Micellization of poly (ethylene oxide)-poly (propylene oxide)-poly (ethylene oxide) triblock copolymers in aqueous solutions: thermodynamics of copolymer association. *Macromolecules* 27, 2414–2425. doi: 10.1021/ma00087a009

Amjad, M. W., Kesharwani, P., Amin, M. C. I. M., and Iyer, A. K. (2017). Recent advances in the design, development, and targeting mechanisms of polymeric micelles for delivery of siRNA in cancer therapy. *Prog. Polym. Sci.* 64, 154–181. doi: 10.1016/j.progpolymsci.2016.09.008

Araneda, E., Leiva, A., Gargallo, L., Hadjichristidis, N., Mondragon, I., and Radic, D. (2012). Crystallization behavior of PEO in blends of poly(ethylene oxide)/poly(2-vinyl pyridine)-b-(ethylene oxide) block copolymer. *Polym. Eng. Sci.* 52, 1128–1136. doi: 10.1002/pen.22183

Barshtein, G., Almagor, A., Yedgar, S., and Gavish, B. (1995). Inhomogeneity of viscous aqueous solutions. *Phys. Rev. E* 52, 555–557. doi: 10.1103/PhysRevE.52.555

Chan, B., Cheng, H., Liow, S., Dou, Q., Wu, Y.-L., Loh, X., et al. (2018). Poly (carbonate urethane)-based thermogels with enhanced drug release efficacy for chemotherapeutic applications. *Polymers* 10:89. doi: 10.3390/polym10010089

Chung, H. J., Lee, Y., and Park, T. G. (2008). Thermo-sensitive and biodegradable hydrogels based on stereocomplexed Pluronic multi-block copolymers for controlled protein delivery. *J. Control. Release* 127, 22–30. doi: 10.1016/j.jconrel.2007.12.008

Desai, P. R., Jain, N. J., Sharma, R. K., and Bahadur, P. (2001). Effect of additives on the micellization of PEO/PPO/PEO block copolymer F127 in aqueous solution. *Colloids Surf. A* 178, 57–69. doi: 10.1016/S0927-7757(00)00493-3

Eloy, J. O., Petrilli, R., Topan, J. F., Antonio, H. M. R., Barcellos, J. P. A., Chesca, D. L., et al. (2016). Co-loaded paclitaxel/rapamycin liposomes: development, characterization and *in vitro* and *in vivo* evaluation for breast cancer therapy. *Colloids Surf. B* 141, 74–82. doi: 10.1016/j.colsurfb.2016.01.032

Jiang, L., Luo, Z., Loh, X. J., Wu, Y.-L., and Li, Z. (2019). PHA-based thermogel as a controlled zero-order chemotherapeutic delivery system for the effective treatment of melanoma. *ACS Appl. Bio Mater.* 8, 83591–83600. doi: 10.1021/acsabm.9b00467

Jiang, Z. (2011). Lipase-catalyzed copolymerization of dialkyl carbonate with 1, 4-butanediol and ω-pentadecalactone: synthesis of poly (ω-pentadecalactone-co-butylene-co-carbonate). *Biomacromolecules* 12, 1912–1919. doi: 10.1021/bm2002522

Karim, A. A., and Loh, X. J. (2015). Design of a micellized α-cyclodextrin based supramolecular hydrogel system. *Soft Matter* 11, 5425–5434. doi: 10.1039/C5SM00665A

Kim, H. A., Lee, H. J., Hong, J. H., Moon, H. J., Ko, D. Y., and Jeong, B. (2017). α,ω-Diphenylalanine-end-capping of PEG-PPG-PEG polymers changes the micelle morphology and enhances stability of the thermogel. *Biomacromolecules* 18, 2214–2219. doi: 10.1021/acs.biomac.7b00626

Kratz, K., Voigt, U., Wagermaier, W., and Lendlein, A. (2009). Shape-memory properties of multiblock copolymers consisting of poly(ω-pentadecalactone) hard segments and crystallizable poly(ε-caprolactone) switching segments. *Mater. Res. Soc. Symp. Proc.* 1140, 17–22. doi: 10.1557/PROC-1140-HH03-01

Kuru, A., and Aksoy, S. A. (2014). Cellulose–PEG grafts from cotton waste in thermo-regulating textiles. *Text. Res. J.* 84, 337–346. doi: 10.1177/0040517513494251

Li, B., Chen, S.-C., Qiu, Z.-C., Yang, K.-K., Tang, S.-P., Yu, W., et al. (2008). Synthesis of poly(lactic acid-b-p-dioxanone)block copolymers from ring opening polymerization of p-dioxanone by poly(L-lacticacid) macroinitiators. *Polym. Bull.* 61, 139–146. doi: 10.1007/s00289-008-0939-1

Li, Z., Cheng, S., Li, S., Liu, Q., Xu, K., and Chen, G.-Q. (2008). Novel amphiphilic poly(ester-urethane)s based on poly[(R)-3-hydroxyalkanoate]: synthesis, biocompatibility and aggregation in aqueous solution. *Polym. Int.* 57, 887–894. doi: 10.1002/pi.2424

Li, Z., Liu, X., Chen, X., Chua, M. X., and Wu, Y.-L. (2017). Targeted delivery of Bcl-2 conversion gene by MPEG-PCL-PEI-FA cationic copolymer to combat therapeutic resistant cancer. *Mater. Sci. Eng. C* 76, 66–72. doi: 10.1016/j.msec.2017.02.163

Li, Z., Zhang, Z., Liu, K. L., Ni, X., and Li, J. (2012). Biodegradable hyperbranched amphiphilic polyurethane multiblock copolymers consisting of poly (propylene glycol), poly (ethylene glycol), and polycaprolactone as *in situ* thermogels. *Biomacromolecules* 13, 3977–3989. doi: 10.1021/bm3012506

Liow, S. S., Dou, Q., Kai, D., Karim, A. A., Zhang, K., Xu, F., et al. (2016). Thermogels: *in situ* gelling biomaterial. *ACS Biomater. Sci. Eng.* 2, 295–316. doi: 10.1021/acsbiomaterials.5b00515

Liu, Z., Liow, S. S., Lai, S. L., Alli-Shaik, A., Holder, G. E., Parikh, B. H., et al. (2019). Retinal-detachment repair and vitreous-like-body reformation via a thermogelling polymer endotamponade. *Nat. Biomed. Eng.* 3, 598–610. doi: 10.1038/s41551-019-0382-7

Loh, X. J., Goh, S. H., and Li, J. (2007). New biodegradable thermogelling copolymers having very low gelation concentrations. *Biomacromolecules* 8, 585–593. doi: 10.1021/bm0607933

Loh, X. J., Guerin, W., and Guillaume, S. M. (2012a). Sustained delivery of doxorubicin from thermogelling poly (PEG/PPG/PTMC urethane) s for effective eradication of cancer cells. *J. Mater. Chem.* 22, 21249–21256. doi: 10.1039/c2jm33777k

Loh, X. J., Tan, Y. X., Li, Z., Teo, L. S., Goh, S. H., and Li, J. (2008). Biodegradable thermogelling poly (ester urethane) s consisting of poly (lactic acid)–thermodynamics of micellization and hydrolytic degradation. *Biomaterials* 29, 2164–2172. doi: 10.1016/j.biomaterials.2008.01.016

Loh, X. J., Yee, B. J. H., and Chia, F. S. (2012b). Sustained delivery of paclitaxel using thermogelling poly(PEG/PPG/PCL urethane)s for enhanced toxicity against cancer cells. *J. Biomed. Mater. Res.* 100A, 2686–2694. doi: 10.1002/jbm.a.34198

MacDiarmid, J. A., Amaro-Mugridge, N. B., Madrid-Weiss, J., Sedliarou, I., Wetzel, S., Kochar,. K., et al. (2009). Sequential treatment of drug-resistant tumors with targeted minicells containing siRNA or a cytotoxic drug. *Nat. Biotechnol.* 27, 643–651. doi: 10.1038/nbt.1547

Martino, L., Scandola, M., and Jiang, Z. (2012). Enzymatic synthesis, thermal and crystalline properties of a poly (β-amino ester) and poly (lactone-co-β-amino ester) copolymers. *Polymer* 53, 1839–1848. doi: 10.1016/j.polymer.2012.03.005

McGlynn, K. A., Petrick, J. L., and London, W. T. (2015). Global epidemiology of hepatocellular carcinoma: an emphasis on demographic and regional variability. *Clin. Liver Dis.* 19, 223–238. doi: 10.1016/j.cld.2015.01.001

Moon, H. J., Park, M. H., Joo, M. K., and Jeong, B. (2012). Temperature-responsive compounds as *in situ* gelling biomedical materials. *Chem. Soc. Rev.* 41, 4860–4883. doi: 10.1039/c2cs35078e

Nakashima, K., and Bahadur, P. (2006). Aggregation of water-soluble block copolymers in aqueous solutions: recent trends. *Adv. Colloid Interface Sci.* 123–126, 75–96. doi: 10.1016/j.cis.2006.05.016

Norouzi, M., Nazari, B., and Miller, D. W. (2016). Injectable hydrogel-based drug delivery systems for local cancer therapy. *Drug Discov. Today* 21, 1835–1849. doi: 10.1016/j.drudis.2016.07.006

Perry, C. C., Sabir, T. S., Livingston, W. J., Milligan, J. R., Chen, Q., Maskiewicz, V., et al. (2011). Fluorescence of commercial Pluronic F127 samples: temperature-dependent micellization. *J. Colloid Interface Sci.* 354, 662–669. doi: 10.1016/j.jcis.2010.10.028

Pilate, F., Stoclet, G., Mincheva, R., Dubois, P., and Raquez, J.-M. (2018). Poly (ε-caprolactone) and poly (ω-pentadecalactone)-based networks with two-way shape-memory effect through [2+2] cycloaddition reactions. *Macromol. Chem. Phys.* 219:1700345. doi: 10.1002/macp.201700345

Qin, L., Sun, Y., Liu, P., Wang, Q., Han, B., and Duan, Y. (2013). F127/Calcium phosphate hybrid nanoparticles: a promising vector for improving siRNA delivery and gene silencing. *J. Biomater. Sci. Polym. Ed.* 24, 1757–1766. doi: 10.1080/09205063.2013.801702

Shinohara, K., Yamashita, M., Uchida, W., Okabe, C., Oshima, S., Sugino, M., et al. (2014). Preparation of polypseudorotaxanes composed of cyclodextrin and polymers in microspheres. *Chem. Pharm. Bull.* 62, 962–966. doi: 10.1248/cpb.c14-00313

Sun, T., Zhang, Y. S., Pang, B., Hyun, D. C., Yang, M., and Xia, Y. (2014). Engineered nanoparticles for drug delivery in cancer therapy. *Angew. Chem. Int. Ed.* 53, 12320–12364. doi: 10.1002/anie.201403036

Wang, C., Zheng, Y., Xie, Y., Qiao, K., Sun, Y., and Yue, L. (2015). Synthesis of bio-castor oil polyurethane flexible foams and the influence of biotic component on their performance. *J. Polym. Res.* 22:145. doi: 10.1007/s10965-015-0782-7

Wee, C. Y., Liow, S. S., Li, Z., Wu, Y.-L., and Loh, X. J. (2017). New poly[(R)-3-hydroxybutyrate-co-4-hydroxybutyrate] (P3HB4HB)-based thermogels. *Macromol. Chem. Phys.* 218:1700196. doi: 10.1002/macp.201700196

Wu, Y.-L., Chen, X., Wang, W., and Loh, X. J. (2016a). Engineering bioresponsive hydrogels toward healthcare applications. *Macromol. Chem. Phys.* 217, 175–188. doi: 10.1002/macp.201500172

Wu, Y.-L., Wang, H., Qiu, Y.-K., Liow, S. S., Li, Z., and Loh, X. J. (2016b). PHB-based gels as delivery agents of chemotherapeutics for the effective shrinkage of tumors. *Adv. Healthcare Mater.* 5, 2679–2685. doi: 10.1002/adhm.201600723

Wu, Y.-L., Wang, H., Qiu, Y.-K., and Loh, X. J. (2016c). PLA-based thermogel for the sustained delivery of chemotherapeutics in a mouse model of hepatocellular carcinoma. *RSC Adv.* 6, 44506–44513. doi: 10.1039/C6RA08022G

Xiao, Y., Pan, J., Wang, D., Heise, A., and Lang, M. (2018). Chemo-enzymatic synthesis of poly (4-piperidine lactone-b-ω-pentadecalactone) block copolymers as biomaterials with antibacterial properties. *Biomacromolecules* 19, 2673–2681. doi: 10.1021/acs.biomac.8b00296

Xing, R., Liu, K., Jiao, T., Zhang, N., Ma, K., Zhang, R., et al. (2016). An injectable self-assembling collagen–gold hybrid hydrogel for combinatorial antitumor photothermal/photodynamic therapy. *Adv. Mater.* 28, 3669–3676. doi: 10.1002/adma.201600284

Yang, D. P., Oo, M., Deen, G. R., Li, Z., and Loh, X. J. (2017). Nano-star-shaped polymers for drug delivery applications. *Macromol. Rapid Commun.* 38:1700410. doi: 10.1002/marc.201700410

Yang, S., You, G., Wang, Y., Chang, J., and Tsiang, R. C. (2017). "Preparation of block copolymer SBSIS having various polystyrene block lengths via anionic polymerization and the properties research," in *2017 International Conference on Applied System Innovation (ICASI)* (Sapporo), 1118–1121.

Yeo, J. C. C., Muiruri, J. K., Tan, B. H., Thitsartarn, W., Kong, J., Zhang, X., et al. (2018). Biodegradable PHB-Rubber copolymer toughened PLA green composites with ultrahigh extensibility. *ACS Sustain. Chem. Eng.* 6, 15517–15527. doi: 10.1021/acssuschemeng.8b03978

Yu, L., Zhang, Z., Zhang, H., and Ding, J. (2009). Mixing a sol and a precipitate of block copolymers with different block ratios leads to an injectable hydrogel. *Biomacromolecules* 10, 1547–1553. doi: 10.1021/bm900145g

Zheng, C., Gao, H., Yang, D.-P., Liu, M., Cheng, H., Wu, Y., et al. (2017). PCL-based thermo-gelling polymers for *in vivo* delivery of chemotherapeutics to tumors. *Mater. Sci. Eng. C* 74, 110–116. doi: 10.1016/j.msec.2017.02.005

Zhu, J.-L., Yu, S. W.-K., Chow, P. K.-H., Tong, Y. W., and Li, J. (2018). Controlling injectability and *in vivo* stability of thermogelling copolymers for delivery of yttrium-90 through intra-tumoral injection for potential brachytherapy. *Biomaterials* 180, 163–172. doi: 10.1016/j.biomaterials.2018.07.023

Conflict of Interest: The authors declare that the research was conducted in the absence of any commercial or financial relationships that could be construed as a potential conflict of interest.

frontiers in Chemistry

ORIGINAL RESEARCH
published: 18 October 2019
doi: 10.3389/fchem.2019.00677

Intra-articular Injection of Kartogenin-Incorporated Thermogel Enhancing Osteoarthritis Treatment

Shao-Jie Wang[1*†], *Ji-Zheng Qin*[1†], *Tong-En Zhang*[2] *and Chun Xia*[1*]

[1] Department of Joint Surgery and Sports Medicine, Xiamen University Zhongshan Hospital, Xiamen, China, [2] Medical School of Xiamen University, Xiamen, China

To provide a vehicle for sustained release of cartilage-protective agent for the potential application of osteoarthritis (OA) treatment, we developed a kartogenin (KGN)-incorporated thermogel for intra-articular injection. We fabricated a poly(lactide-co-glycolide)-block-poly(ethylene glycol)-block-poly(lactide-co-glycolide) (PLGA–PEG–PLGA) thermogel as a KGN carrier for IA injection. OA chondrocytes were cultured in thermogel with or with no KGN to investigate the effect of KGN thermogel on cartilage matrix. The *in vivo* effect of KGN thermogel on OA was examined in a rabbit OA model. The KGN thermogel showed a sustained *in vitro* release of KGN for 3 weeks. OA chondrocytes proliferated well both in thermogel and KGN thermogel. In addition, OA chondrocytes produced higher amount of [type 2 collagen (COL-2) and glycosaminoglycan (GAG)], as well as lower level of matrix metalloproteinase 13 (MMP-13) in KGN thermogel that those in thermogel with no addition of KGN. The gene analysis supported that KGN thermogel enhanced expression of hyaline-cartilage specific genes Col 2 and AGC, and inhibited the expression of MMP-13. Compared with intra-articular injection of saline or thermogel containing no KGN, KGN thermogel can enhance cartilage regeneration and inhibit joint inflammation of arthritic knees in a rabbit ACLT-induced OA model at 3 weeks after the injection. Therefore, the KGN-incorporated PLGA–PEG–PLGA thermogel may provide a novel treatment modality for OA treatment with IA injection.

Keywords: chondrocytes, osteoarthritis, cartilage regeneration, kartogenin (KGN), thermogel

OPEN ACCESS

Edited by:
Xing Wang,
Institute of Chemistry (CAS), China

Reviewed by:
Da Huang,
Fuzhou University, China
Zhenlong Liu,
Peking University Third Hospital, China

***Correspondence:**
Shao-Jie Wang
wangshaojie@xmu.edu.cn
Chun Xia
chunxia99@aliyun.com

†These authors have contributed equally to this work

Specialty section:
This article was submitted to Polymer Chemistry, a section of the journal Frontiers in Chemistry

Received: *22 August 2019*
Accepted: *30 September 2019*
Published: *18 October 2019*

Citation:
Wang S-J, Qin J-Z, Zhang T-E and Xia C (2019) Intra-articular Injection of Kartogenin-Incorporated Thermogel Enhancing Osteoarthritis Treatment. Front. Chem. 7:677. doi: 10.3389/fchem.2019.00677

INTRODUCTION

Osteoarthritis (OA) is a common degenerative joint pathology affecting 151 million people worldwide. Direct intra-articular injections of drugs are commonly used to improve the joint bioavailability while minimizing systemic complications. Recently a small molecule, kartogenin (KGN), has been reported to promote collagen synthesis (Johnson, 2012). Intra-articular injection of KGN has been reported to enhance cartilage regeneration (Kang et al., 2014; Mohan et al., 2016; Fan et al., 2018). However, KGN cannot provide long-term therapeutic effects due to fast clearance and short retention of KGN in joints, posing a disadvantage in its clinical application. In order to improve residence time of treatment agents in joints, researchers have employed hydrogels for drug delivery and drug control release (Seliktar, 2012).

Poly(lactide-co-glycolide)–poly(ethylene glycol)-poly(lactide-co-glycolide) (PLGA–PEG–PLGA) triblock copolymer has been used as a potential matrix of thermogel, and can dissolve in water at low temperature (e.g., 4°C), and the solution gels around body temperature (i.e., 37°C) (Yu et al., 2011; Li et al., 2012; Wang et al., 2016c, 2019; Zhang et al., 2019). Given the advantages of possessing and minimally invasive way of delivering bioactive molecules, in the current study we used PLGA–PEG–PLGA copolymer to fabricate thermogel incorporated with therapeutic concentration of KGN for intra-articular injection. KGN thermogel system was evaluated both *in vitro* and *in vivo* to examine the potential for OA treatment. We cultured chondrocytes pre-treated with IL-1β to mimic OA chondrocytes (Cui et al., 2016) in to investigate the effect of KGN thermogel on OA chondrocytes in terms of cartilage matrix production and degradation. Then the PLGA–PEG–PLGA thermogel with or without KGN was injected in to OA knees in rabbits to examine the effects of KGN thermogel on OA.

MATERIALS AND METHODS

PLGA–PEG–PLGA Thermogel Preparation

PLGA–PEG–PLGA triblock copolymers were purchased from (Daigang Co., Ltd., Jinan, Shandong, China). The copolymers were synthesized through the ring-opening polymerization (ROP) of L-LA and GA with PEG as a macroinitiator and Sn(Oct)2 as a catalyst as previously reported (Wang et al., 2016c). The Mns of PEG and PLGA were 1,500 and 1,400 g/mol, respectively. The molar ratio of L-LA and GA in PLGA segment is 75:25. PLGA–PEG–PLGA triblock copolymers was dissolved in PBS (pH 7.4) to obtain a 20 wt% gel solution, which was then kept at 4°C before being used in the following experiments. The sol—gel transition behavior of PLGA-PEG-PLGA thermogel was confirmed by incubation at 37°C for 15 min.

Preparation of KGN Thermogel

Ten milligrams of KGN (Selleck Chemicals, Shanghai, China) was dissolved in 0.6 ml dimethyl sulfoxide (DMSO) and then diluted with PBS (pH 7.4) to obtain 5 mM KGN working solutions. KGN thermogel was prepared by mixing 100 μl 5 mM KGN solution with 10 ml PLGA-PEG-PLGA gel solution to obtain KGN gel solution containing 50 μM KGN. PLGA-PEG-PLGA gel solution without KGN was used as control.

In vitro KGN Release

The *in vitro* sustained release of KGN from the KGN thermogel was determined by an ultra-micro UV spectrophotometer (Nanodrop 2000). Briefly, 1 mL of 20 wt% thermogel or KGN thermogel solution was placed in a vial of a 16 mm inner diameter for gelation at 37°C. Then 2 mL PBS was added on top of the gel. The supernatant was collected at set time intervals (0.0, 1.0, 3.0, 7.0, 11.0, 15.0, and 20.0 days). Another 2 ml PBS was then replaced. Serial concentrations of KGN in PBS solution were used as standards. The measurement was carried out with a detection wavelength of 277 nm. The amount of released KGN at each time point was calculated as percentage of the total KGN content of a 1 mL 20 wt% thermogel or KGN thermogel solution.

Isolation and Culture of Chondrocytes

Two-month-old adult New Zealand White rabbits weighing around 1.5 kg were sacrificed for isolation of chondrocytes as previously mentioned (Wang et al., 2016a). Primary chondrocytes were harvested from the cartilage of knees and shoulders. First, the minced cartilage was digested for 6 h in 10 mL of 0.2% w/v collagenase type 2 (Gibco BRL Co. Ltd.) solutions at 37°C. The resultant cell suspension was centrifuged and resuspended in low-glucose DMEM supplemented with 10% FBS (HyCloneTM, Thermo Scientific, Australia) and 1% penicillin and streptomycin. Isolated chondrocytes were cultured in monolayer cultures in a humidified incubator at 37°C, 5% CO_2, and 21% O_2. Passage 2 chondrocytes were utilized for subsequent experiment.

Chondrocytes Treated With IL-1β

Passage 2 adherent rabbit chondrocytes reaching 60–70% confluency was cultured with serum-starved medium (DMEM/F12 supplemented with 1% FBS) for 12 h, and then was treated with IL-1β (10 ng/ml) for 2 h for the following *in vitro* experiments.

Design of Rabbit Knee OA Model

This study was carried out in accordance with the Guide for the Care and Use of Laboratory Animals of the National Institutes of Health. The protocol was approved by the Committee on the Ethics of Animal Experiments of Xiamen University. The anterior cruciate ligament transection (ACLT) procedure was performed to induce knee OA model as previously reported (Liu et al., 2016). New Zealand white rabbits ($n = 24$, age 5 months, weight 2.5–3.0 kg) were then divided into two groups (sham and ACLT). After anesthesia and routine preparation, 18 rabbits were performed ACLT on the left knees and six rabbits were performed a sham surgery. At 3 weeks after ACLT, rabbits were randomly divided into three groups (six rabbits in each group) for intra-articular injection of saline, thermogel, or KGN thermogel. At 6 weeks after the sham surgery or 3 weeks after the intra-articular injection, the left knees in every group were harvested for histological analysis, and synovial fluid was collected for analysis of interleukin-1 (IL-6) and MMP-13, to evaluate the inflammation of knees.

In vitro Culture of IL-1β Treated Chondrocytes in KGN Thermogel

The cell suspension containing 5.0×10^5 IL-1β treated chondrocytes was mixed with 100.0 μL of thermogel or KGN thermogel solution at 4°C and then transferred into a 24-well plate. The mixed cells–copolymer solution was incubated at 37°C for 15 min for gelation and cell initial attachment. 2.0 mL of fresh DMEM supplemented with 10% (V/V) FBS (HyCloneTM, Thermo Scientific, Australia), and 1% penicillin and streptomycin (Invitrogen, Carlsbad, CA, USA) was added.

For cell proliferation assay and DNA content analysis, the cells-laden thermogel was cultured for 1 week in DMEM. The culture medium was changed every 2 days. The proliferation activity of cells was measured at day 1, 5, and 7 using a Cell Counting Kit-8 assay (CCK-8; Dojindo Laboratories,

Kumamoto, Japan) according to the manufacturers' instructions. Briefly, cell culture ($n = 3$) were gently rinsed with PBS and then submerged in a mixed solution of 10.0 μL of CCK-8 reagent with 90.0 μL of fresh medium at 37°C for 2 h. The absorbance readings at 450 nm were observed using a plate reader.

Biochemical Analysis

To reveal the effect of KGN thermogel on OA chondrocytes, we measured the matrix degradation enzyme (MMP-13), extracellular matrix component [type 2 collagen (COL-2) and glycosaminoglycan (GAG)] secreted from OA chondrocytes. Briefly, the specimens were digested in a pre-prepared papain solution containing 0.5 M EDTA, 0.05 M cysteine hydrochloride, and 1.0 mg/mL papain enzyme (Sigma, St. Louis, MO, USA) at 60°C for 12 h. The aliquots of the sample digestion were used for the measurements of DNA and GAG, as previously reported (Wang et al., 2016a). DNA content was measured using a fluorescence assay. Total glycosaminoglycan (GAG) content was determined using a 1,9-dimethylmethylene blue (DMMB; Sigma, St. Louis, MO, USA) dye-binding assay. The culture medium of IL-1β treated chondrocytes was collected after 3 weeks of culture in KGN thermogel. Supernatant was separated from insoluble residues by centrifugation at 12,000 rpm for 10 min. Rabbit MMP-13 and COL-2 ELISA Kits (Cloud-Clone, Corp., Houston, TX, USA) were used to measure the COL-2 and MMP-13 according to the manufacturer's instructions. GAG, COL-2, and MMP-13 concentrations were normalized to DNA content which was determined fluorometrically using Hoechst staining as previously described (Wang et al., 2016a).

Gene Expression Analyses

To evaluate the effect of KGN on OA chondrocytes, we measured the expressions of arthritis -related genes and cartilage-related genes. Gene expressions were detected by real-time polymerase chain reaction (RT-PCR) as previously reported (Wang et al., 2016a). At predesignated time points, samples ($n = 3$) were homogenized in Trizol Reagent (Invitrogen, Carlsbad, CA, USA) with a tissue grinder and RNA was extracted according to the manufacturer's instructions. Isolated RNA concentration was determined by an ND-2000 spectrophotometer (Nanodrop Technologies). One microgram of RNA from each sample was reverse transcribed into cDNA using the MMLV Reverse kit (Promega, Madison, WI, USA), and RT-PCR analysis was performed using ABI 7300 real-time PCR system (Applied Biosystems, Foster City, CA, USA) with SYBR Green PCR Master Mix (Toyobo, Osaka, Japan). The relative gene expression was expressed by fold difference which was calculated as $2^{\Delta\Delta CT}$. The relative expression changes in these target genes were quantified by normalizing their expression to that of housekeeping gene glyceraldehyde-3-phosphate dehydrogenase (GAPDH). PCR primers for: type 1 collagen (COL-1), type 2 collagen (COL-2), aggrecan (AGC), MMP-13, and GAPDH were listed in **Table 1**.

TABLE 1 | Primer sequences used for real-time PCR.

Gene	Forward primers (5′-3′)	Reverse primers (5′-3′)
COL-1	TGGCAAGAACGGAGATGACG	GCACCATCCAAACCACTGAA
COL-2	CCACGCTCAAGTCCCTCAAC	AGTCACCGCTCTTCCACTCG
AGC	CGTGGTCTGGACAGGTGCTA	GGTTGGGGTAGAGGTAGACG
MMP-13	TTGACCACTCCAAGGACCCAG	GAGGATGCAGACGCCAGAAGA
GAPDH	CCATCACCATCTTCCAGGAG	GATGATGACCCTTTTGGCTC

Col-1, type 1 collagen; Col-2, type 2 collagen; AGC, aggrecan; MMP-13, matrix metalloproteinase 13; GAPDH, glyceraldehyde-3-phosphate dehydrogenase.

Histological Analysis

After intra-articular injection for 3 weeks, each group of rabbits was euthanized with overdose of pentobarbital sodium. Distal femur was resected for histological evaluation. No joint infection occurred in all knees. To evaluate the inflammation of knee joints, synovial fluid was collected for analysis of interleukin-6 (IL-6) and MMP-13. After dissection and fixation, the samples were decalcified in 15% EDTA (pH 7.2 in PBS) with 5% paraformaldehyde at 4°C. The decalcified medial condyles were then trimmed, dehydrated in a graded ethanol series and embedded in paraffin. Sections were stained with H&E, TB (positive for proteoglycans) and immunohistochemical (IHC) staining (positive for COL-2). The protocols for detection of COL-2 were described in above sections. The histological sections were blindly reviewed for quantitative evaluation of the cartilage destruction using the Osteoarthritis Research Society International (OARSI) scoring system (Pritzker et al., 2006).

Statistical Analysis

All data were expressed as means ± standard deviation and represented at least three independent experiments. All data were analyzed using a two-way ANOVA test. $P < 0.05$ were considered significant. When ANOVA results were significant, *post-hoc* analysis was performed via Tukey's multiple comparison test. All analyses were carried out using GraphPad Prism version 6.0 for Windows (GraphPad Software, San Diego, CA).

RESULTS

In vitro Assessments of KGN Release

The PLGA–PEG–PLGA copolymer in PBS (20 wt%) with or without KGN showed stable gelation at 37°C. The sustainably release KGN *in vitro* from the KGN thermogel determined whether the functionalized thermogel can produce sufficiently chondrogenic effects (commonly used concentration is 100 nM−10 μM *in vitro* and 10 μM−100 μM *in vivo*). The KGN concentration in the 20 wt% polymer solution was about 50 μM. Therefore, the KGN thermogel showed an abrupt release (20%) of KGN at day 1 (10 μM), followed by a sustained release (about 3% per day) of KGN per day (1.5 μM /day), as shown in **Figure 1**.

Cell Viability and Proliferation

After culture in growth medium for 72 h, CCK assay showed that OA chondrocytes proliferated in both PLGA-PEG-PLGA thermogel and KGN thermogel showed an increased proliferation during 7 days of *in vitro* culture (**Figure 2A**). However, the number of OA chondrocytes in thermogel and

KGN thermogel on Day 7 did not differ significantly, compared to that on Day 1 ($p > 0.05$). Notably, the number of MSCs in KGN thermogel slightly surpassed that in the thermogel.

Extracellular Matrix Related Component Production

GAG and COL-2 content were detected to quantify cartilaginous matrix production by OA chondrocytes. Increased amount of GAG and COL-2 from OA chondrocytes were found after culture in thermogel or KGN thermogel for 14 days (**Figure 2B**). Significantly higher amount of GAG and COL-2 was detected in KGN thermogel than that in thermogel group ($p < 0.05$). On the other hand, increased secretion of MMP-13 was only found in thermogel, whereas minimal increase of MMP-13 was detected in KGN thermogel. These results showed that KGN enhanced the production of COL-2 and GAG and inhibited the production of MMP-13 from OA chondrocytes, suggesting that KGN played an anti-arthritic role in OA chondrocyte-laden thermogel.

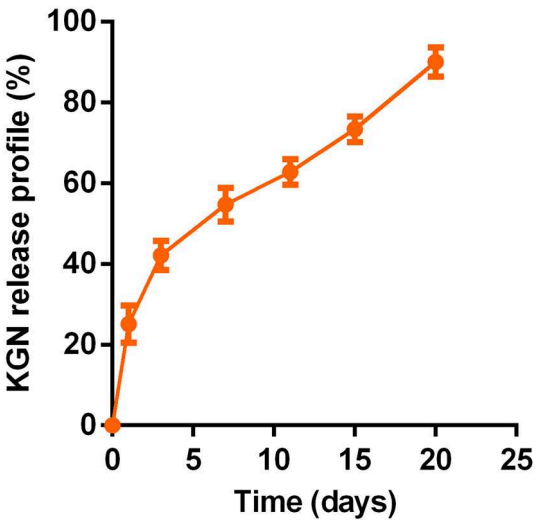

FIGURE 1 | *In vitro* sustained KGN release from KGN thermogel (20.0 wt%) in PBS (pH 7.4) at 37°C ($n = 3$).

Cartilage-Specific Gene Expression Analyses

To compare the chondro-protective capacity of KGN thermogel, we measured gene expressions of COL-1, COL-2, AGC, and MMP-13. Significant differences of gene expression were found between thermogel group and KGN thermogel group at both 14 and 21 days of *in vitro* culture (**Figure 3**). Greater upregulation of hyaline-cartilage specific genes COL-2 and AGC were detected in KGN thermogel system that that in thermogel with no KGN ($p < 0.05$). However, the expression of fibrocartilage-related marker COL-1 was similar between the two groups. In addition, the MMP-13 expression was reduced in KGN thermogel group suggesting KGN could inhibit matrix degradation.

In vivo Cartilage Regeneration

The histological staining showed that the OA model was successfully established in rabbit knees at 3 weeks after ACLT. Obvious OA changes of cartilage occurred at 6 weeks after ACLT in OA group, OA + Gel group, and OA + KGN gel group, with cartilage fibrillation, surface erosion, fissure, denudation, and deformation (**Figure 4**). Slight cartilage degeneration was observed in sham group with chondrocyte hypertrophy and clustering. Importantly, we noted a distinct chondroprotective effect of KGN thermogel in OA + KGN gel group which showed shallow vertical fissures of the superficial cartilage, localized proteoglycan depletion, and partial COL-2 loss in limited zones of the cartilage. In comparison, both OA and OA+ thermogel groups showed severe OA changes, with significant cartilage denudation and deformation, as well as marked proteoglycan and COL-2 depletion. These data suggested that IA injection of KGN showed an anti-inflammatory effect and promoted cartilage regeneration, as compared to IA injection of saline or thermogel.

OA knees treated with KGN thermogel injection demonstrated delayed cartilage degeneration and low level of articular inflammation, as indicated by IL-6 and MMP-13 content. In contrast, the IL-6 and MMP-13 levels

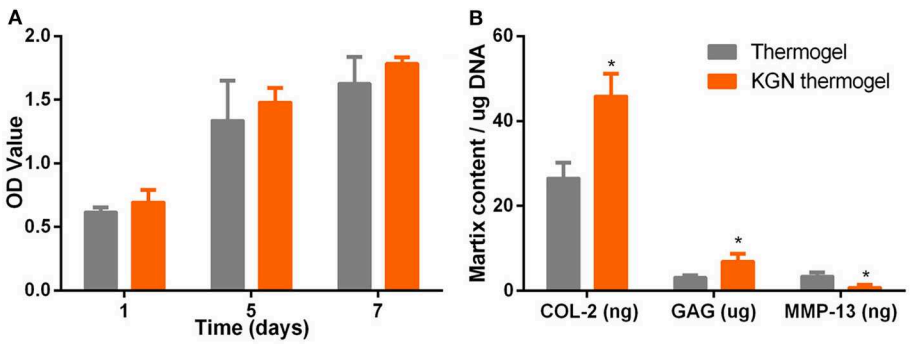

FIGURE 2 | *In vitro* cell proliferation and matrix component production. **(A)** CCK-8 assay showed that the proliferation of IL-1β treated chondrocytes in thermogel or KGN thermogel increased over time **(B)** GAG content was measured by DMMB assay, COL-2, and MMP-13 were determined by ELISA after IL-1β treated chondrocytes were cultured in thermogel or KGN thermogel for 2 weeks ($n = 3$, $^*P < 0.05$).

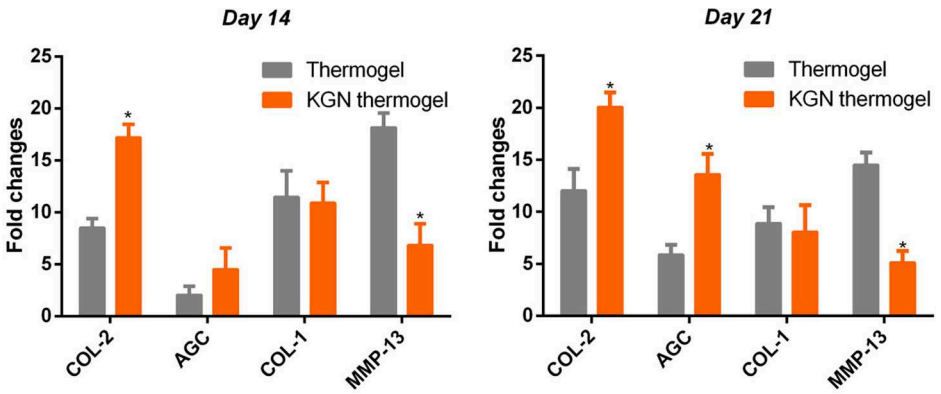

FIGURE 3 | Expression of cartilage-related genes of COL-2 and AGC, COL-1, and MMP-13 of OA chondrocytes within thermogel with or without KGN ($n = 3$; $^*p < 0.05$).

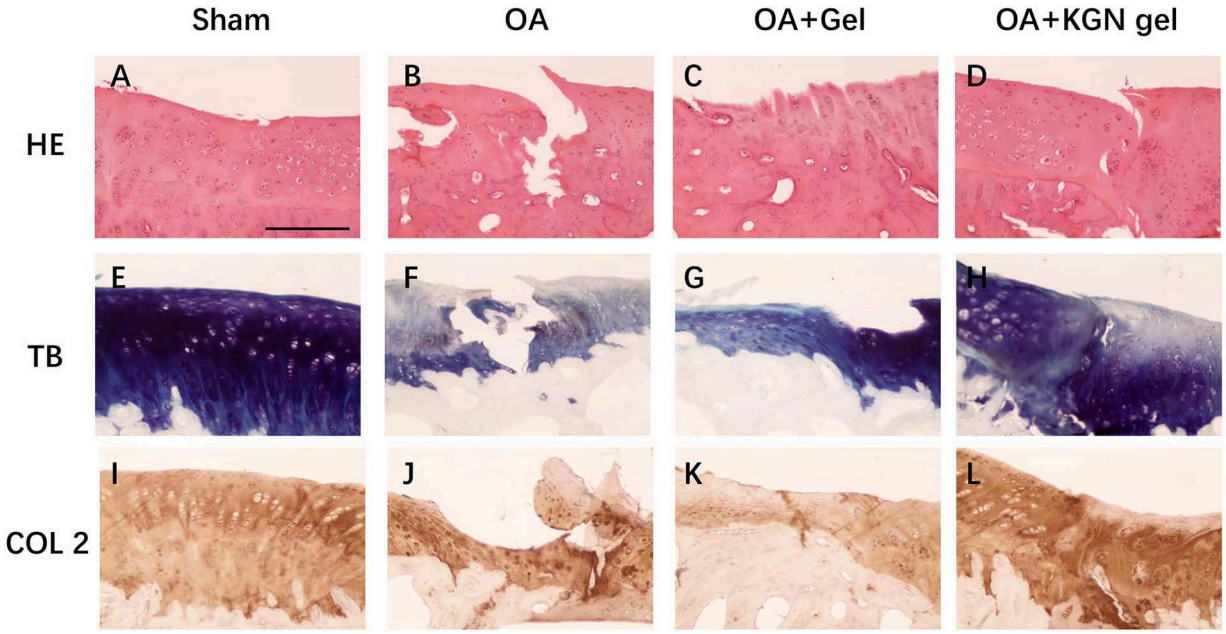

FIGURE 4 | Histological staining of OA knee treated with saline (OA), thermogel (OA + Gel), and KGN thermogel (OA + KGN gel) at 6 weeks after ACLT surgery. **(A–D)** H&E, **(E–H)** toluidine blue (TB), and **(I–L)** immunohistochemistry (IHC) COL-2 staining.

were significantly higher in OA and OA + Gel groups ($p < 0.01$; **Figure 5**).

The OARSI scores grade histopathology of OA based on extent of joint involvement and the depth of lesion (Pritzker et al., 2006). As shown in **Figure 6**, OARSI scores were significantly lower in sham group and OA + KGN group that those of OA and OA + Gel groups ($p < 0.001$). The OA group treated with saline IA injection displayed progressive cartilage degeneration with extensive and deep involvement of cartilage. The OARSI scores revealed no significant differences between OA gel group and OA group ($p > 0.05$). These data suggested ongoing arthritis and cartilage destruction in OA group and OA + Gel group, and subsided arthritis and regenerated cartilage in arthritic knees treated with KGN thermogel.

DISCUSSION

OA is characterized by extracellular matrix (ECM) degradation and cell loss. The main components of ECM in cartilage are proteoglycans and collagens, and the loss of AGC and COL-2 in ECM leads to cartilage degradation. Matrix metalloproteinases (MMPs), for example, MMP-13, have been shown to directly cleave collagens and aggrecan (Zhao et al., 2014).

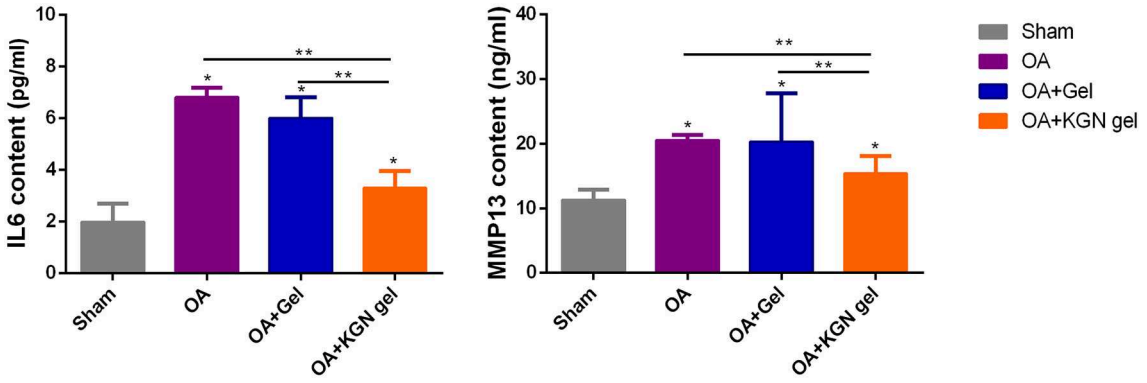

FIGURE 5 | ELISA method detecting IL-6 and MMP-13 content in synovial fluid of all groups at 6 weeks ($n = 8$, $^{*}p < 0.05$, $^{**}p < 0.01$).

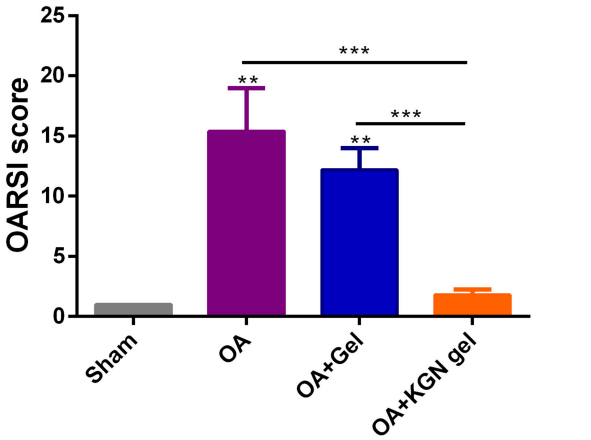

FIGURE 6 | OARSI scores were significantly lower in Sham group and OA + KGN gel group that those of OA and OA + Gel groups ($^{**}p < 0.01$, $^{***}p < 0.001$).

The close articular cavity allows the possibility of IA drug administration for OA patients. IA injection of drugs will avoid or minimize side effects of systematically administered drugs, such as toxicity and gastrointestinal complications (He et al., 2017). However, the low retention time limits the application of IA injection. Hydrogels are physically or chemically cross-linked three-dimensional polymers swollen in water that allows the controlled release of bioactive agents (Park et al., 2009) and possesses the capacity of maintaining chondrocyte phenotype (Chung and Burdick, 2008; Spiller et al., 2011; Liu et al., 2018). Among various hydrogels, the thermo-sensitive hydrogel from PLGA–PEG–PLGA copolymer has been especially attractive, as their spontaneous gelation under physiological conditions presents some advantages: minimal invasive wounds, efficiency of cell encapsulation and controlled release of bioactive molecules (Zhang et al., 2014, 2015; Li et al., 2016).

In the current work, the cartilage-protective molecule KGN was incorporated into the PLGA–PEG–PLGA thermogel with the capacity of sustained release of KGN for as long as 3 weeks. We used IL-1β treated rabbit chondrocytes to investigate the effect of KGN on OA chondrocytes. *In vitro* experiment showed that KGN thermogel was compatible with cell survival, however with no capacity to promote proliferation of OA chondrocytes. In addition, when cultured in KGN thermogel, OA chondrocytes produced higher amount of GAG and COL-2 than those in thermogel without addition of KGN. These data are consistent with others which showed that KGN promoted cartilage regeneration and induced chondrogenic differentiation of mesenchymal stem cells (Kang et al., 2014, 2016; Wang et al., 2016b; Fan et al., 2018; Han et al., 2019). In addition, the level of MMP-13 produced by OA chondrocytes in KGN thermogel was much less compared to that in thermogel. This is consistent to the increased amount of COL-2 and GAG, which can be directly degraded by MMP-13. Therefore, KGN thermogel system have showed biocompatibility and cartilage-protectiveness. The gene analysis was in line with the above ELISA results, as KGN thermogel group enhanced expression of hyaline-cartilage specific genes COL-2 and AGC, and inhibited the expression of MMP-13. This result is again supported by other researchers (Wang et al., 2015; He et al., 2017; Patel et al., 2019).

To confirmed the feasibility of using KGN thermogel for the treatment of OA, we established knee OA model using ACLT procedure. The OA knees treated with KGN thermogel yielded significantly greater cartilage regeneration and less joint inflammation, as suggested by histological staining, OARSI score and synovial fluid analysis of inflammatory cytokines. These *in vivo* data strongly indicated that KGN played an anti-arthritic and chondro-protective role in arthritis.

Some limitations remain in the present study. Firstly, the current study is only a preliminary study for the effect of KGN on the early stage OA. However, more time points for IA injection at different OA stages will add more clarification for the effect of KGN on OA treatment. Secondly, the potential molecular mechanism regarding the effect of KGN on OA was not revealed in the current study. Further studies about KGN in anti-inflammation or redifferentiation of OA chondrocytes should be needed in the future.

In summary, we have shown that KGN thermogel can release KGN both *in vitro* and *in vitro*. IA injection of KGN thermogel can enhance cartilage regeneration and inhibit joint inflammation in OA knees in a rabbit model. KGN thermogel protects the cartilage by promoting OA chondrocytes to produce COL-2 and GAG, while reducing the secretion of MMP-13.

DATA AVAILABILITY STATEMENT

The raw data supporting the conclusions of this manuscript will be made available by the authors, without undue reservation, to any qualified researcher.

ETHICS STATEMENT

The animal study was reviewed and approved by Committee on the Ethics of Animal Experiments of the University of Xiamen.

AUTHOR CONTRIBUTIONS

S-JW and J-ZQ: conception and design, collection and assembly of data, analysis and interpretation of data, and drafting of the manuscript. T-EZ: assistance in analysis and interpretation of data. CX and S-JW: conception and design, critical revision of the manuscript, and final approval of the manuscript.

FUNDING

This work was supported by the National Natural Science Foundation of China (81572189) and Joint Funding of Fujian Science and Technology Department (2015J01525).

ACKNOWLEDGMENTS

The authors thank Dr. Yang Zhou (Ph.D. student of Medical School of Xiamen University) who provided a lot of help and assistance in the current study.

REFERENCES

Chung, C., and Burdick, J. A. (2008). Engineering cartilage tissue. *Adv. Drug Deliv. Rev.* 60, 243–262. doi: 10.1016/j.addr.2007.08.027

Cui, X., Wang, S., Cai, H., Lin, Y., Zheng, X., Zhang, B., et al. (2016). Overexpression of microRNA-634 suppresses survival and matrix synthesis of human osteoarthritis chondrocytes by targeting PIK3R1. *Sci. Rep.* 6:23117. doi: 10.1038/srep23117

Fan, W., Li, J., Yuan, L., Chen, J., Wang, Z., Wang, Y., et al. (2018). Intra-articular injection of kartogenin-conjugated polyurethane nanoparticles attenuates the progression of osteoarthritis. *Drug Deliv.* 25, 1004–1012. doi: 10.1080/10717544.2018.1461279

Han, Y., Li, X., Zhang, Y., Han, Y., Chang, F., and Ding, J. (2019). Mesenchymal stem cells for regenerative medicine. *Cells* 8:886. doi: 10.3390/cells8080886

He, Z., Wang, B., Hu, C., and Zhao, J. (2017). An overview of hydrogel-based intra-articular drug delivery for the treatment of osteoarthritis. *Colloids Surf. B Biointerfaces* 154, 33–39. doi: 10.1016/j.colsurfb.2017.03.003

Johnson, K. (2012). A stem cell–based approach to cartilage repair. *Science* 336, 717–721 doi: 10.1126/science.1215157

Kang, M. L., Kim, J. E., and Im, G. I. (2016). Thermoresponsive nanospheres with independent dual drug release profiles for the treatment of osteoarthritis. *Acta Biomater.* 39, 65–78. doi: 10.1016/j.actbio.2016.05.005

Kang, M. L., Ko, J. Y., Kim, J. E., and Im, G. I. (2014). Intra-articular delivery of kartogenin-conjugated chitosan nano/microparticles for cartilage regeneration. *Biomaterials* 35, 9984–9994. doi: 10.1016/j.biomaterials.2014.08.042

Li, X., Ding, J., Zhang, Z., Yang, M., Yu, J., Wang, J., et al. (2016). Kartogenin-incorporated thermogel supports stem cells for significant cartilage regeneration. *ACS Appl. Mater. Interfaces* 8, 5148–5159. doi: 10.1021/acsami.5b12212

Li, Y., Rodrigues, J., and Tomas, H. (2012). Injectable and biodegradable hydrogels: gelation, biodegradation and biomedical applications. *Chem. Soc. Rev.* 41, 2193–2221. doi: 10.1039/C1CS15203C

Liu, H., Cheng, Y., Chen, J., Chang, F., Wang, J., Ding, J., et al. (2018). Component effect of stem cell-loaded thermosensitive polypeptide hydrogels on cartilage repair. *Acta Biomater.* 73, 103–111. doi: 10.1016/j.actbio.2018.04.035

Liu, Z., Hu, X., Man, Z., Zhang, J., Jiang, Y., and Ao, Y. (2016). A novel rabbit model of early osteoarthritis exhibits gradual cartilage degeneration after medial collateral ligament transection outside the joint capsule. *Sci. Rep.* 6:34423. doi: 10.1038/srep34423

Mohan, G., Magnitsky, S., Melkus, G., Subburaj, K., Kazakia, G., Burghardt, A. J., et al. (2016). Kartogenin treatment prevented joint degeneration in a rodent model of osteoarthritis: a pilot study. *J. Orthop. Res.* 34, 1780–1789. doi: 10.1002/jor.23197

Park, H., Guo, X., Temenoff, J.S., Tabata, Y., Caplan, A. I., Kasper, F. K., et al. (2009). Effect of swelling ratio of injectable hydrogel composites on chondrogenic differentiation of encapsulated rabbit marrow mesenchymal stem cells *in vitro*. *Biomacromolecules* 10, 541–546. doi: 10.1021/bm801197m

Patel, J. M., Saleh, K. S., Burdick, J. A., and Mauck, R. L. (2019). Bioactive factors for cartilage repair and regeneration: improving delivery, retention, and activity. *Acta Biomater.* 93, 222–238. doi: 10.1016/j.actbio.2019.01.061

Pritzker, K. P., Gay, S., Jimenez, S. A., Ostergaard, K., Pelletier, J. P., Revell, P. A., et al. (2006). Osteoarthritis cartilage histopathology: grading and staging. *Osteoarthr. Cartil.* 14, 13–29. doi: 10.1016/j.joca.2005.07.014

Seliktar, D. (2012). Designing cell-compatible hydrogels for biomedical applications. *Science* 336, 1124–1128. doi: 10.1126/science.1214804

Spiller, K. L., Maher, S. A., and Lowman, A. M. (2011). Hydrogels for the repair of articular cartilage defects. *Tissue Eng. Part B Rev.* 17, 281–299. doi: 10.1089/ten.teb.2011.0077

Wang, C., Feng, N., Chang, F., Wang, J., Yuan, B., Cheng, Y., et al. (2019). Injectable cholesterol-enhanced stereocomplex polylactide thermogel loading chondrocytes for optimized cartilage regeneration. *Adv. Healthc. Mater.* 8:e1900312. doi: 10.1002/adhm.201900312

Wang, S. J., Jiang, D., Zhang, Z. Z., Huang, A. B., Qi, Y. S., Wang, H. J., et al. (2016a). Chondrogenic potential of peripheral blood derived mesenchymal stem cells seeded on demineralized cancellous bone scaffolds. *Sci. Rep.* 6:36400. doi: 10.1038/srep36400

Wang, S. J., Yin, M. H., Jiang, D., Zhang, Z. Z., Qi, Y. S., Wang, H. J., et al. (2016b). The chondrogenic potential of progenitor cells derived from peripheral blood: a systematic review. *Stem Cells Dev.* 25, 1195–1207. doi: 10.1089/scd.2016.0055

Wang, S. J., Zhang, Z. Z., Jiang, D., Qi, Y. S., Wang, H. J., Zhang, J. Y., et al. (2016c). Thermogel-coated poly(ε-caprolactone) composite scaffold for enhanced cartilage tissue engineering. *Polymers* 8:200. doi: 10.3390/polym8050200

Wang, Y., Zhu, G., Li, N., Song, J., Wang, L., and Shi, X. (2015). Small molecules and their controlled release that induce the osteogenic/chondrogenic commitment of stem cells. *Biotechnol. Adv.* 33, 1626–1640. doi: 10.1016/j.biotechadv.2015.08.005

Yu, L., Zhang, Z., and Ding, J. (2011). Influence of LA and GA sequence in the PLGA block on the properties of thermogelling PLGA-PEG-PLGA block copolymers. *Biomacromolecules* 12, 1290–1297. doi: 10.1021/bm101572j

Zhang, Y., Yu, J., Ren, K., Zuo, J., Ding, J., and Chen, X. (2019). Thermosensitive hydrogels as scaffolds for cartilage tissue engineering. *Biomacromolecules* 20, 1478–1492. doi: 10.1021/acs.biomac.9b00043

Zhang, Y. B., Ding, J. X., Sun, D. K., Sun, H., Zhuang, X. L., Chang, F., et al. (2015). Thermogel-mediated sustained drug delivery for *in situ* malignancy chemotherapy. *Mater. Sci. Eng. C Mater. Biol. Appl.* 49, 262–268. doi: 10.1016/j.msec.2015.01.026

Zhang, Y. B., Ding, J. X., Xu, W. G., Wu, J., Chang, F., Zhuang, X. L., et al. (2014). Biodegradable thermogel as culture matrix of bone marrow mesenchymal stem cells for potential cartilage tissue engineering. *Chin. J. Polym. Sci.* 32, 1590–1601. doi: 10.1007/s10118-014-1551-5

Zhao, H., Zhang, T., Xia, C., Shi, L., Wang, S., Zheng, X., et al. (2014). Berberine ameliorates cartilage degeneration in interleukin-1β-stimulated rat chondrocytes and in a rat model of osteoarthritis via Akt signalling. *J. Cell. Mol. Med.* 18, 283–292. doi: 10.1111/jcmm.12186

Conflict of Interest: The authors declare that the research was conducted in the absence of any commercial or financial relationships that could be construed as a potential conflict of interest.

frontiers in Chemistry

ORIGINAL RESEARCH
published: 01 November 2019
doi: 10.3389/fchem.2019.00745

Low-Molecular-Weight Heparin-Functionalized Chitosan-Chondroitin Sulfate Hydrogels for Controlled Release of TGF-β3 and *in vitro* Neocartilage Formation

You-Rong Chen[1†], Zhu-Xing Zhou[1†], Ji-Ying Zhang[1], Fu-Zhen Yuan[1], Bing-Bing Xu[1], Jian Guan[1], Chao Han[1,2], Dong Jiang[1], Yan-Yu Yang[3,4] and Jia-Kuo Yu[1*]*

[1] Knee Surgery Department of the Institute of Sports Medicine, Peking University Third Hospital, Beijing, China, [2] School of Clinical Medicine, Weifang Medical University, Weifang, China, [3] Beijing National Laboratory for Molecular Sciences, State Key Laboratory of Polymer Physics & Chemistry, Institute of Chemistry, Chinese Academy of Sciences, Beijing, China, [4] College of Materials Science and Engineering, Zhengzhou University, Zhengzhou, China

Repair of hyaline cartilage remains a huge challenge in clinic because of the avascular and aneural characteristics and the paucity of endogenous repair cells. Recently, tissue engineering technique, possessing unique capacity of repairing large tissue defects, avoiding donor complications and two-stage invasive surgical procedures, has been developed a promising therapeutic strategy for cartilage injury. In this study, we incorporated low-molecular-weight heparin (LMWH) into carboxymethyl chitosan-oxidized chondroitin sulfate (CMC-OCS) hydrogel for loading transforming growth factor-β3 (TGF-β3) as matrix of peripheral blood mesenchymal stem cells (PB-MSCs) to construct tissue-engineered cartilage. Meanwhile, three control hydrogels with or without LMWH and/or TGF-β3 were also prepared. The gelling time, microstructures, mechanical properties, degradation rate, cytotoxicity, and the release of TGF-β3 of different hydrogels were investigated. *In vitro* experiments evaluated the tri-lineage differentiation potential of PB-MSCs, combined with the proliferation, distribution, viability, morphology, and chondrogenic differentiation. Compared with non-LMWH-hydrogels, LMWH-hydrogels (LMWH-CMC-OCS-TGF-β3) have shorter gelling time, higher mechanical strength, slower degradation rate and more stable and lasting release of TGF-β3. After two weeks of culture *in vitro*, expression of cartilage-specific genes collagen type-2 (COL-2) and aggrecan (AGC), and secretion of glycosaminoglycan (GAG), and COL-2 proteins in LMWH-CMC-OCS-TGF-β3 group were significantly higher than those in other groups. COL-2 immunofluorescence staining showed that the proportion of COL-2 positive cells and immunofluorescence intensity in LMWH-CMC-OCS-TGF-β3 hydrogel were significantly higher than those in other groups. The LMWH-CMC-OCS-TGF-β3 hydrogel

OPEN ACCESS

Edited by:
Clemens Kilian Weiss, Fachhochschule Bingen, Germany

Reviewed by:
Guoqing Pan, Jiangsu University, China
Jianxun Ding, Changchun Institute of Applied Chemistry (CAS), China
Nonappa, Aalto University, Finland
Caiyan Zhao, Brigham and Women's Hospital, Harvard Medical School, United States
Hao Hu, Qingdao University, China

***Correspondence:**
Jia-Kuo Yu
yujiakuo@126.com
Yan-Yu Yang
yyyang@iccas.ac.cn

[†] These authors have contributed equally to this work

Specialty section:
This article was submitted to Polymer Chemistry, a section of the journal Frontiers in Chemistry

Received: *19 August 2019*
Accepted: *17 October 2019*
Published: *01 November 2019*

Citation:
Chen Y-R, Zhou Z-X, Zhang J-Y, Yuan F-Z, Xu B-B, Guan J, Han C, Jiang D, Yang Y-Y and Yu J-K (2019) Low-Molecular-Weight Heparin-Functionalized Chitosan-Chondroitin Sulfate Hydrogels for Controlled Release of TGF-β3 and in vitro Neocartilage Formation. Front. Chem. 7:745. doi: 10.3389/fchem.2019.00745

can slowly release TGF-β3 in a long term, and meanwhile the hydrogel can provide a biocompatible microenvironment for the growth and chondrogenic differentiation of PB-MSCs. Thus, LMWH functionalized CMC-OCS hydrogels proposed in this work will be beneficial for constructing functional scaffolds for tissue-engineered cartilage.

Keywords: low-molecular-weight heparin, hydrogel, controlled release, peripheral blood mesenchymal stem cell, tissue-engineered cartilage

INTRODUCTION

Cartilage injury has brought about an increasing social and economic burden as a common joint disease (Everhart et al., 2019). On account of its avascular characteristics and lack of endogenous repair cells, articular cartilage has a limited regenerative and self-healing ability (Armiento et al., 2018). Currently, traditional clinical methods included the osteochondral transplantation, bone marrow stimulation and autologous chondrocyte transplantation, but they still could not achieve the satisfactory therapeutic effect (Redondo et al., 2018). Fortunately, tissue engineering technology has provided a promising therapeutic strategy for cartilage injury (Liaw et al., 2018; Zylinska et al., 2018; Ding et al., 2019). By means of the three elements of tissue engineering methods (biological scaffolds, growth factors, and seed cells), tissue-engineering cartilage possesses unique capacity to repair large tissue defects, avoid donor complications and two-stage invasive surgical procedures and has a wide range of scaffold materials and seed cells sources (Andriolo et al., 2017; Sadlik et al., 2017; Kwon et al., 2019).

For development of desirable tissue engineering program, it is urgent to prepare the functionally specific biomaterials that mimic the components of natural extracellular matrix of cartilage for biomedical applications (Stuckensen et al., 2018). As a typical biological scaffold, hydrogel has been widely utilized on account of their highly hydrated three-dimensional cross-linked soft-wet materials with good biocompatibility (Pan et al., 2013; Liu and Hsu, 2018; Hu et al., 2019). As for construction of tissue-engineered cartilage, hydrogel can provide a suitable microenvironment for cartilage differentiation, and cartilage-specific extracellular matrix (ECM) regeneration (Wang et al., 2019; Zhang Y. et al., 2019). Heparin is a kind of highly sulfated anionic glycosaminoglycan existing in extracellular matrix, which can bind electropositive protein and growth factors into stable complexes by electrostatic interaction to repair and regenerate various tissues (Sun et al., 2018; Thones et al., 2019). Heparin-functionalized hydrogel scaffold can protect proteins or growth factors from degradation and maintain their biological activity *in vivo*, meanwhile the electrostatic interaction can effectively avoid burst release and realize the sustained release of proteins or growth factors (Kim I. et al., 2018; Kim S. et al., 2018). Compared with unfractionated heparin (UFH), low-molecular-weight heparin (LMWH) has superiority on the long half-life, less bleeding side effects and no need for laboratory monitoring (Ali-Hassan-Sayegh et al., 2016; Robertson and Jones, 2017). Therefore, LMWH-functionalized hydrogel scaffold may be a kind of suitable and promising materials for generating tissue-engineered cartilage.

Incorporation and controlled release of bioactive factor is a universal strategy to promote tissue repair and regeneration (Li X. et al., 2016; Qian et al., 2017). During the process of cartilage repair and regeneration, transforming growth factor-β3 (TGF-β3), as one of the relatively newer isoforms of TGF-β, can effectively promote the differentiation of mesenchymal stem cells (MSCs) into cartilage cell and induce the expression of extracellular matrix of cartilage by regulating the metabolism of articular cartilage and multifunctional proteins in a time- and concentration-dependent manner (Crecente-Campo et al., 2017; Wang et al., 2017). TGF-β3 can inhibit the activity of inflammatory mediators such as IL-1, MMPs, and TNF-α, and meanwhile reduce the body's immune response (Yanagawa et al., 2016; Frangogiannis, 2017). In addition, TGF-β3 plays a vital role in the growth and reconstruction of cartilage in both *vitro* and *vivo*, which has been proved by many previous reports (Yang et al., 2017; Deng et al., 2019). MSCs are multipotent precursor cells with multidirectional differentiation, self-renewal and low immunogenicity, which are widely used as seed cells for cartilage repair and regeneration (Liu H. et al., 2018; Han et al., 2019). Compared to frequently-used bone marrow mesenchymal stem cells (BM-MSCs), peripheral blood mesenchymal stem cells (PB-MSCs) possess distinct advantages, for example more minimally invasive, less complications (Wang et al., 2016a). Our previous studies proved that PB-MSCs had similar biological characteristics to BM-MSCs and even better cartilage differentiation tendency in each of monolayer culture and three-dimensional condition (Fu et al., 2011; Wang et al., 2016a). Therefore, PB-MSCs are one better kind of seed cells for repair and regeneration of bone and cartilage *in vivo* (Fu et al., 2014). In this work, we prepared a low-molecular-weight heparin-functionalized chitosan-chondroitin sulfate hydrogel, which could load TGF-β3 as matrix of PB-MSCs to construct tissue-engineered cartilage (**Figure 1**). The hydrogel scaffold can be capable of mimicking the biochemical composition of cartilage tissue and providing a bionic environment for seed cells; in this case, the TGF-β3 can be controlled released from the hydrogel in about one month and effectively promote differentiation into cartilage of PB-MSCs. This study will open a new venue for fabricating tissue scaffolds materials and investigating the mechanism/behavior of cartilage differentiation from PB-MSCs.

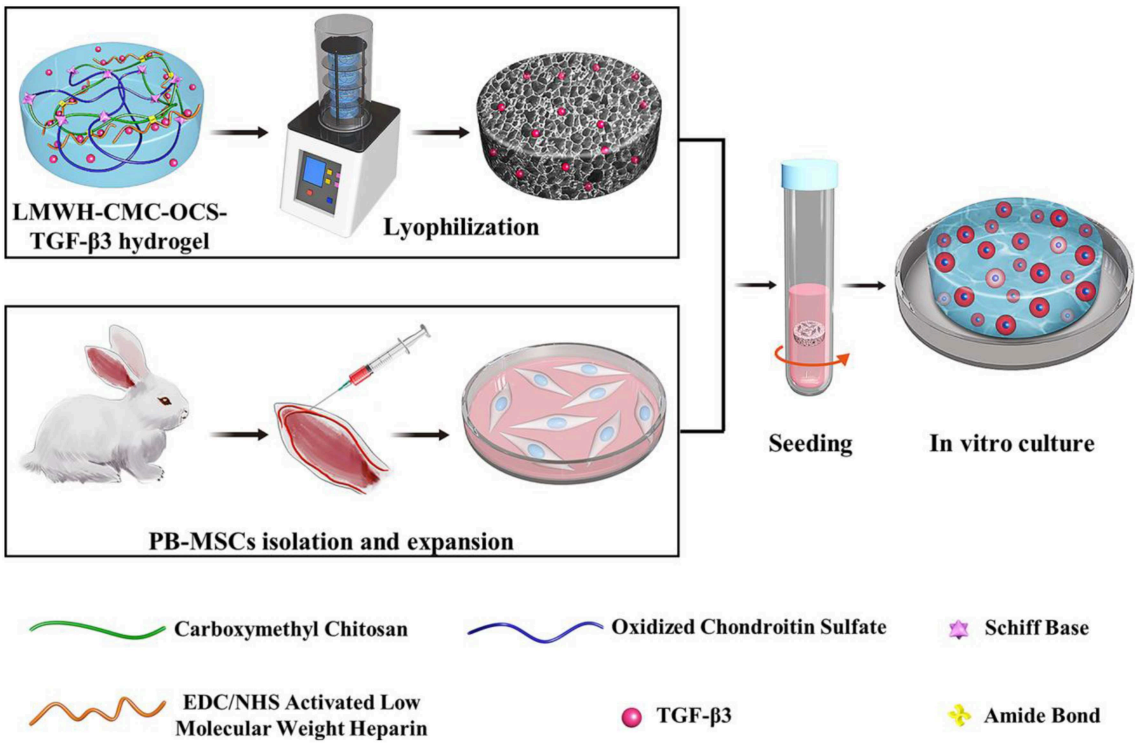

FIGURE 1 | Schematic illustration of LMWH-CMC-OCS-TGF-β3 hydrogel as matrix of PBMSCs for constructing tissue-engineered cartilage *in vitro*.

MATERIALS AND METHODS

Materials

Chondroitin sulfate (CS, *M*n = 19.9 kDa) was provided by Xingyuan Chemical Reagent Co., Henan. Carboxymethyl chitosan (viscosity of 10 ∼ 80 mPa·s, carboxylation degree of 80%) and low-molecular-weight heparin (LMWH, *M*n = 5,600–6,400 Da) were obtained from Dalian Meilun Biotechnology Co., Ltd. Dalian, China. Sodium periodate, 1-ethyl-3-(dimethylaminopropyl) carbodiimide hydrochloride (EDC) and N-hydroxysuccinimide (NHS) were purchased from Sinopharm Chemical Reagent Co., Ltd. Shanghai, China. Recombinant Human TGF-β3 was obtained from PeproTech, Inc. USA. TGF-β3 ELISA kit was purchased from Cloud-Clone Corp, China.

Preparation of Oxidized Chondroitin Sulfate (OCS) and EDC/NHS-activated LMWH

Five gram of CS was reacted with 3.5 g of $NaIO_4$ in 100 mL of distilled water in dark for 6 h, and then OCS was separated by adding 200 mL alcohol to the mixture and stirring for another 15 min (Fan et al., 2017). LMWH solution was prepared at a concentration of 1 mg/mL in PBS (0.01 M, pH 7.4), and carboxylic acid groups of LMWH (LMWH-COOH) were activated using NHS groups at a molar ratio of 10:10:1 (EDC: NHS: LMWH-COOH). The reaction was allowed to proceed for 12 h at 37°C with a pH value of 5.7 (Elahi et al., 2014; Liu Z. et al., 2018). The OCS and EDC/NHS activated LMWH were dialysis against the distilled water for 72 h and further lyophilized to obtain a purified material.

Preparation of Hydrogels

Solutions of CMC (30 mg/mL) and OCS (100 mg/mL) were mixed with each other (volume ratio = 4: 1) in room temperature to obtain the CMC-OCS hydrogel. To prepare CMC-OCS-TGF-β3, LMWH-CMC-OCS and LMWH-CMC-OCS-TGF-β3 hydrogels, EDC/NHS-activated LMWH, and/or TGF-β3 were added to the OCS solution before mixing with CMC solution. EDC/NHS-activated LMWH and/or TGF-β3 were added within hydrogels at concentrations of 1.5 mg/mL and/or 250 ng/mL, respectively. The loading contents of TGF-β3 in hydrogels of CMC-OCS-TGF-β3 and LMWH-CMC-OCS-TGF-β3 were 5.68 and 5.49 ng/mg, respectively. The gelation time of hydrogel was obtained by the vial tilting method (Bu et al., 2016) and rheological measurements (time sweep experiment).

Fourier Transform Infrared Spectra

Hydrogels were lyophilized in freeze dryer at −80°C for 48 h. The film samples of CS, OCS, CMC, LMWH, activated LMWH, LMWH-CMC, CMC-OCS hydrogels, and LMWH-CMC-OCS hydrogels were prepared by the technique of potassium bromide tableting. TENSOR-27 spectrometer (Bruker) was used to obtain the Fourier transform infrared (FTIR) spectra of samples with the method of previous reported (Bu et al., 2017).

Scanning Electron Microscopy

A JSM-7900F scanning electron microscope (SEM, Hitachi, Japan) was used to observe the microstructure of the hydrogels. Briefly, the freeze-dried hydrogels were sliced and bonded to the sample stage with conductive resin, and then coated with a layer of gold and obtain the SEM images at 3 kV acceleration voltage. The pore size of hydrogels was measured with the help of Image-pro® Plus 6.0 (Media Cybernetics, Inc., Rockville, USA) (Yang et al., 2018b).

Porosity Determination

The method of liquid displacement was used to determine the porosities of freeze-dried hydrogels. First, samples with regular form were calculated and weighed the initial volume and weight (V_0 and W_0). Second, samples hydrogels saturated with absolute ethyl alcohol were weighted again (W_1). The equation as below was used to calculate the porosities of four hydrogels (Qin et al., 2018):

$$\text{Porosity}\ (\%) = [(W_1 - W_0)/(V_0 \times \rho)] \times 100\%$$

ρ represents the density of absolute ethyl alcohol.

Rheological Measurements

Thermo Haake Rheometer with a cone-parallel plate geometry (d = 35 mm) was used to measure the gelation time and shear modulus of four hydrogels. Time sweeps experiments were performed with a constant strain of 0.05% and oscillatory frequency of 1 rad/s. The samples in solution state (0.5 mL) were placed between two plates and the gap was set at 0.5 mm. Frequency sweep experiment were performed with a constant strain of 0.05% in the frequency range of 0.1–10 rad s^{-1}. The hydrogels (d = 35 mm, h = 3.5 mm) were placed between two plates and tested at a gap of 3 mm (Wu et al., 2010; Wang L. et al., 2016).

Compressive Testing

The mechanical properties of hydrogels were calculated with a universal material testing machine of Instron 3365 (Instron Co., USA). Samples were prepared (diameter 15 mm and height 7.5 mm) and compressive testing was carried out with a rate of 3 mm/min. The fracture strain, fracture compressive stress and compressive elastic modulus were calculated based on the stress-strain curve. Every kind of hydrogels was tested three times (Yang et al., 2016).

Swelling Properties

The swelling properties of hydrogels were measured according to the methods reported in previous literature (Bu et al., 2016). We prepared the dried hydrogel samples (20 mg) and recorded the initial weight (W_d), and then placed samples in 50 mL of PBS (pH 7.4) at 37°C. The samples were weighed again (W_s) after incubation for certain time (0.25, 0.5, 1, 2, 4, 6, 8, 12, 16, 24, 48, 72, 96, 120, 144, and 168 h). The calculational equation of swelling ratio was used as below:

$$\text{Swelling ratio}\ (\%) = (W_s - W_d)/W_d \times 100\%$$

Degradation *in vitro*

The weight loss of samples in PBS solution during 21 days were recorded to describe the degradation behaviors of hydrogels. We recorded the initial weight of lyophilized samples (W_0), and incubated them in PBS solution at 37°C. After incubating for certain time (1, 4, 7, 14, and 21 days), the samples were lyophilized and weighed again (W_t). The degradation ratio can be obtained by the following equation:

$$\text{Degradation ratio}\ (\%) = (W_0 - W_t)/W_0 \times 100\%$$

TGF-β3 Release Experiments

The lyophilized samples (4.4 mg, $n = 5$) were placed in PBS solution (pH 7.4, 1 mL) at 37°C under the continuous agitation to obtain the release behavior of TGF-β3. After incubation for certain time (1, 4, 7, 10, 14, and 21 days), we withdrawn the PBS solution with released TGF-β3 and added same volume of fresh PBS to maintain the total volume of 1 mL. The released amounts of TGF-β3 was quantified with sandwich enzyme-linked immunosorbent assay (ELISA) using a Human TGF-β3 ELISA Kits (Cloud-Clone, Corp., Houston, TX, USA) (Ariyati et al., 2019).

Isolation and Culture of PB-MSCs

The Animal Care and Use Committee of Peking University Third Hospital approved all of the protocols of animal experiments which were implemented follow the Guide for the Care and Use of Laboratory Animals. Peripheral blood (PB, 20 mL) was isolated from the central auricular arteries of New Zealand White rabbits after mobilizing with granulocyte colony stimulating factor (G-CSF, Qilu Pharmaceutical Co. Ltd.) and AMD3100 (MedChemExpress LLC., USA). Peripheral blood mononuclear cells (MNCs) were collected by using the method of density gradient centrifugation, and cultured in medium of α-MEM with 15% fetal bovine serum, 100 U/mL penicillin and 100 U/mL streptomycin. Culture medium was replaced every 3 days until the confluence of primary PB-MSCs reached around 90%, and then subculture was carried out at ratio of 1:3. PB-MSCs at passage 3 [PB-MSCs (P3)] were used for subsequent experiments (Fu et al., 2011).

Tri-lineage Differentiation Potential

Multilineage differentiation potential of PB-MSCs was assessed with the method of tri-lineage differentiations. Osteogenic medium, adipogenic induction and maintenance medium, and chondrogenic medium (Cyagen Biosciences Inc., Suzhou, China), following the manufacturer's instructions, were used for osteogenesis, adipogenesis, and chondrogenesis of PB-MSCs, respectively. The deposition of calcium nodules, accumulation of lipid vacuoles in cells, and cartilage-specific aggregating proteoglycans were detected with the methods of Alizarin red staining, Oil red O staining, and Alcian blue staining (Fu et al., 2011).

Cytotoxicity Studies of Hydrogels

Cell Counting Kit-8 assay (CCK-8, Dojindo Laboratories, Japan) was applied to evaluate the cytotoxicity of hydrogel by culturing

PB-MSCs with the extracting liquid of hydrogels. Rabbit PB-MSCs at passage 3 were seeded into 96-well microplates (2×10^3 cells/100 μL/well), and then 10 μL of hydrogel extracting liquid or PBS was added into cell medium and further incubated for predetermined time. After incubation for 12, 24, and 48 h, we removed the original culture medium and added fresh culture medium (100 μL) with CCK-8 reagent (10 μL). A microplate reader (Thermo, USA) was used to obtain the optical density (OD) value of 450 nm after incubating for another 1 h. The equation as below was used to calculate the cell viability:

$$\text{Cell viability} = [(\text{As} - \text{Ab})/(\text{Ac} - \text{Ab})] \times 100\%$$

Where the As, Ac, Ab are the optical density (OD) of hydrogels for the extracts group, control group and blank group. It was considered to be cytotoxic if cell viability was <70% after incubation with hydrogel extracting liquid (Bu et al., 2017).

Cell Seeding and Cell-Scaffold Construct Culture

Fifty microliter of PB-MSCs suspension (1 × 107 cells/mL) was carefully seeded on freeze-dried hydrogel (diameter of 6 mm and thickness of 2 mm) with the method of centrifugation as we previously reported (Zhang Z. et al., 2015). The cell-hydrogel composites were incubated for 1 h to facilitate cell adhesion, and then 2 mL fresh chondrogenic differentiation medium (removal of TGF-β3 components, Cyagen Biosciences Inc., Suzhou, China) was added for further culture. Culture medium was replaced every 3 days until cell-hydrogel composites were used in subsequent experiments.

Cell Distribution on Scaffolds

LIVE/DEAD Viability/Cytotoxicity Kit assay (Invitrogen, CA, USA) was used to visualize the cell survival and distribution on hydrogels. After culturing for 7 days, the cell-hydrogel composites were washed with PBS solution to remove culture medium, and immersed in reagents of calcein AM (2 mM) and ethidium homodimer-1 (4 mM) for 1 h at 37°C. Live (green) and dead (red) cells was detected by using a confocal microscopy with excitation wavelength of 568 and 488 nm. Imaris software 7.4.2 (Bitplane, Oxford) was used to create three-dimensional rendering in order to observe and analyze the distribution of PB-MSCs on hydrogels.

Cell Proliferation on Hydrogels

Cell proliferation on hydrogels was assessed by using the method of CCK-8 assay. After incubation for 1, 3, 5, and 7 days, we removed the original culture medium, and added fresh culture medium (100 μL) with CCK-8 reagent (10 μL). A microplate reader (Thermo, USA) was used to obtain the optical density (OD) value of 450 nm after incubating for another 2 h. The cell proliferation curves of each groups obtained by normalizing the OD value at each point against the average value of the first day.

Analysis of Cartilage-Specific and Hypertrophic Genes Expression

After incubation for 7 and 14 days, cell-hydrogel composites were removed from culture medium and washed with PBS. TRIZOL reagent (Invitrogen, Carlsbad, CA, USA) and RevertAid First Strand cDNA Synthesis Kit (K1622, Thermo Scientific, Carlsbad, CA, USA), following the manufacturer's instructions, were used to extract total RNA and reverse-transcribe isolated RNA, respectively. According to the conditions reported in previous literature (Zhang Z. Z. et al., 2019), quantitative Real-time polymerase chain reaction (RT-PCR) analysis was performed to detect the expression of cartilage-specific marker gene (COL-2 and aggrecan, AGC) and hypertrophic marker gene (collagen type-10, COL-10) by using an ABI 7300 real-time PCR system (Applied Biosystems, Foster City, CA, USA) with SYBR® Select Master Mix (4472908, Thermo Scientific, Carlsbad, CA, USA). The value of relative expression in these target genes were plotted as $2^{-\Delta\Delta CT}$ with the method of previous reported (Zhang Z. Z. et al., 2019). The PCR primers are listed in **Table S1**.

Quantification of DNA, Collagen Type-2 (COL-2), and Glycosaminoglycan (GAG) Content

Hoechst33258 staining and fluorometric assay was performed to measure the DNA content of cell-hydrogel composites. After culturing for 1, 7, and 14 days, the cell-hydrogel composites were weighed and then digested in a prepared papain solution (Sigma, St. Louis, Missouri, USA) at 60°C for 24 h to obtained aliquots of the sample digestion. Aliquots of the sample digestion (10 μL) were mixed with Hoechst33258 working solution (2 μg/mL, 100 μL) and incubated at 37°C for 1 h. A microplate reader (Thermo, USA) was used to detect the fluorescent intensities with excitation wavelength of 360 nm and emission wavelength of 460 nm. A standard curve of calf thymus DNA (Sigma, St. Louis, Missouri, USA) was used to normalize the content of DNA.

High efficiency RIPA tissue/cell lysis solution (R0010, Solarbio Science & Technology Co., Ltd., Beijing, China) was used to obtain total proteins of the cell-hydrogel constructs. Rabbit COL-2 ELISA Kits (Cloud-Clone, Corp., Houston, TX, USA) and Rabbit GAGs ELISA kit (BlueGene Biotech., Shanghai, China) were applied to measure the COL-2 content according to the manufacture protocol, and the contents of COL-2 and GAG were normalized to DNA content.

Immunofluorescent Staining of COL-2

Immunofluorescent staining was performed to visualize the secretion of COL-2 in cell-hydrogel composites after culturing for 14 days. First, cell-hydrogel composites were washed with PBS to remove culture medium and fixed with 4% paraformaldehyde. Then, 10% bovine serum albumin (BSA), mouse anti-COL-2 primary antibody (CP18, Merck KGaA, Darmstadt, Germany), Alexa Fluor® 594 goat anti-mouse IgG antibodies (ZF-0513, ZSGB-BIO Co., Ltd., Beijing, China) and DAPI (Sigma, St. Louis, Missouri, USA) were used successively to incubate composites, and the immunofluorescence images were obtained by using confocal microscopy. The fluorescent intensity of COL-2 and proportion of COL-2 positive cells were calculated as previously reported (Wang et al., 2016a; Zhang Z. Z. et al., 2019).

Cell Morphology on Scaffolds

Cytoskeleton staining was performed, and confocal microscopy was used to observe the morphology of PB-MSCs in hydrogels

at day 7. After removal of culture medium of scaffolds and fixing with paraformaldehyde, rhodamine phalloidin (100 nM; Cytoskeleton Inc., Denver, USA) and DAPI working solution (1 μg/mL, Sigma-Aldrich, Inc., USA) stained the cytoskeleton (30 min) and nuclei (5 min) at 37°C, respectively (Wang et al., 2016a).

Statistical Analyses

All statistical data were expressed as mean ± standard deviation (*SD*). One-way analysis of variance (ANOVA) was used to distinguish the differences among groups after testing for homogeneity of variances, $P < 0.05$ was considered statistically significant. When the results of ANOVA results were significantly different, the Least Significant Difference test (LSD-t) was performed. All analyses were carried out using SPSS 25.0 software (SPSS Inc., Armonk, USA).

RESULTS AND DISCUSSION

Synthesis of Hydrogel Scaffolds

The chemical structures of CMC, CS, OCS, CMC-OCS, LMWH, EDC/NHS activated LMWH and the schematic diagram of

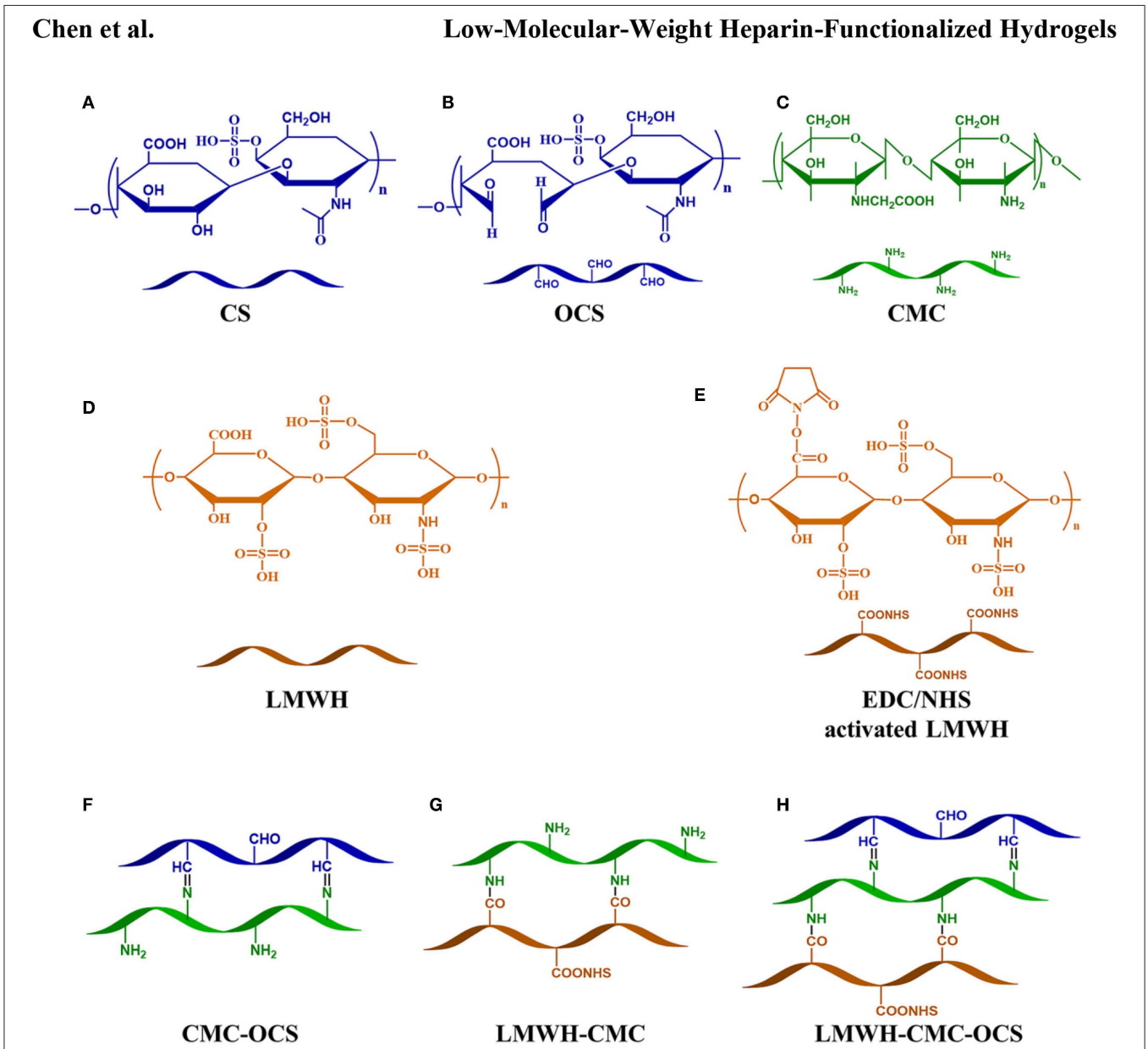

FIGURE 2 | Chemical structures of CS **(A)**, OCS **(B)**, CMC **(C)**, LMWH **(D)**, EDC/NHS activated LMWH **(E)** and schematic diagram of various cross-linked reaction in hydrogels **(F–H)**.

various cross-linked reaction in hydrogels were illustrated in **Figure 2**. OCS was obtained by oxidizing the hydroxyl groups of CS into aldehyde groups using sodium periodate. Also, the carboxylic acid groups (-COOH) of LMWH were activated by reacting with EDC/NHS to obtain activated ester group (-COONHS). The CMC-OCS hydrogel was prepared by simply mixing and the crosslinking network was formed by Schiff base reaction. Moreover, LMWH-OCS-CMC hydrogel was obtained by incorporating the activated LMWH into OCS-CMC hydrogel, wherein the NHS groups of LMWH can chemically linked with amino groups of CMC. In addition, TGF-β3 were *in-situ* encapsulated into CMC-OCS and LMWH-OCS-CMC composites to obtain CMC-OCS-TGF-β3 and LMWH-CMC-OCS-TGF-β3 hydrogels.

FTIR Spectra of Polysaccharide Derivatives and Cross-Linked Hydrogels

The chemical compositions and structures of polysaccharide derivatives and cross-linked hydrogels were testified by the FTIR in **Figure 3**. On account of the similar composition of CS and LMWH, they almost exhibited the same characteristic peaks. For example, the peak at 1253.2 cm^{-1} corresponded to S=O stretching vibrations was a characteristic absorption peak of CS and LMWH samples. The peak at 1316.2 cm^{-1} belonged to epoxide ring stretching vibrations was used as a characteristic absorption peak of CMC sample. OCS showed an absorption signal at 1727.6 cm^{-1} corresponded to the aldehyde groups (Fan et al., 2017). By comparing with LMWH, the spectrum of EDC/NHS activated LMWH exhibited a new absorption signal at 1732.8 cm^{-1}, which was attributed to the stretching vibrations of C=O of NHS groups (Elahi et al., 2014). For the CMC-OCS hydrogel sample, the coexistence of characteristic absorption peaks of CMC at 1316.2 cm^{-1} and OCS at 1253.2 cm^{-1} and the disappearance of the peak at 1727.6 cm^{-1} revealed that hydrogel cross-linked through Schiff base reaction between CMC and OCS. For the LMWH-CMC sample, the generated characteristic absorption peaks of CMC (1316.2 cm^{-1}), LMWH (1253.2 cm^{-1}) and the disappeared peak at 1732.8 cm^{-1} demonstrated that EDC/NHS activated LMWH was involved by the formation of amide bonds. The spectra of CMC-OCS, LMWH-CMC, LMWH-CMC-OCS samples were very similar, displaying a absorption signals at 1608.2 cm^{-1} which corresponded to the amide I band (Elahi et al., 2014).

Morphological Observation of Hydrogels Scaffolds

The CMC, OCS, activated LMWH and TGF-β3 were easily soluble in water and evenly mixed to form a viscous solution. After the extruding and injecting through a conventionally medical syringe, the hydrogels could be generated after several minutes with the colorless and transparence, presenting the injectable property which might be suitable for minimally invasive surgery (Li T. et al., 2018; Chen et al., 2019). After the sufficient cross-linking reaction overnight, the hydrogels were removed from vials and exhibited a clear, slightly brown color as shown in **Figures 4A–C**. Morphologies of hydrogels

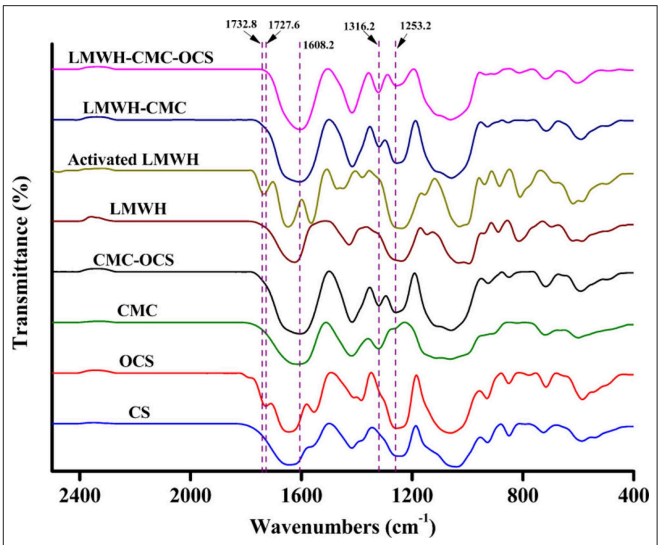

FIGURE 3 | FTIR spectra of polysaccharide derivatives (CS, OCS, CMC, LMWH, and EDC/NHS activated LMWH) and cross-linked CMC-OCS, LMWH-CMC, and LMWH-CMC-OCS hydrogels.

were observed in SEM images in **Figure 4D**, four hydrogels possessed homogeneous porous and interconnected structures. The average pore sizes of CMC-OCS and CMC-OCS-TGF-β3 hydrogels were 31.75 ± 0.91 and 31.58 ± 0.83 μm respectively. After the addition of EDC/NHS activated LMWH, the average pore sizes were decreased to 29.29 ± 0.98 μm (LMWH-CMC-OCS) and 29.49 ± 0.83 μm (LMWH-CMC-OCS-TGF-β3), which may be ascribed to improvement of solid content and crosslinking degree (**Figure 4E**). Porosities of hydrogels were measured by method of liquid displacement. The porosities of the CMC-OCS, CMC-OCS-TGF-β3, LMWH-CMC-OCS and LMWH-CMC-OCS-TGF-β3 were 86.30 ± 5.16, 87.63 ± 5.03, 79.31 ± 2.80, and 79.21 ± 4.56%, respectively (**Figure 4F**). The average pore sizes ($n = 3$) and porosities ($n = 5$) of LMWH-CMC-OCS and LMWH-CMC-OCS-TGF-β3 groups were lower than CMC-OCS and CMC-OCS-TGF-β3 groups, with significant difference ($^*P < 0.05$). The gelation time of hydrogel was obtained by the vial tilting method in **Figure 4G** (Bu et al., 2016). The gelation time of CMC-OCS and CMC-OCS-TGF-β3 was 269.11 ± 18.07 and 271.71 ± 10.27 s, respectively. No statistical difference was found between the two groups ($n = 5$, $P > 0.05$). Upon adding the EDC/NHS activated LMWH, the gelation time decrease to 224.24 ± 17.80 and 223.98 ± 14.13 s for LMWH-CMC-OCS and LMWH-CMC-OCS-TGF-β3 hydrogels, respectively. The gelling rate is obviously faster than groups of CMC-OCS and CMC-OCS-TGF-β3 ($n = 5$, $^*P < 0.05$). The gelation time of hydrogels was also determined by the method of rheological measurements. **Figure S1** showed that storage modulus G′ of samples increased with time and exceeded dissipative modulus G″, the intersection of G′ and G indicated a gel point. Compared to CMC-OCS and CMC-OCS-TGF-β3 hydrogels, a shorter gelation time was observed in the hydrogels of LMWH-CMC-OCS and LMWH-CMC-OCS-TGF-β3. The faster gelation time was attributed to the much

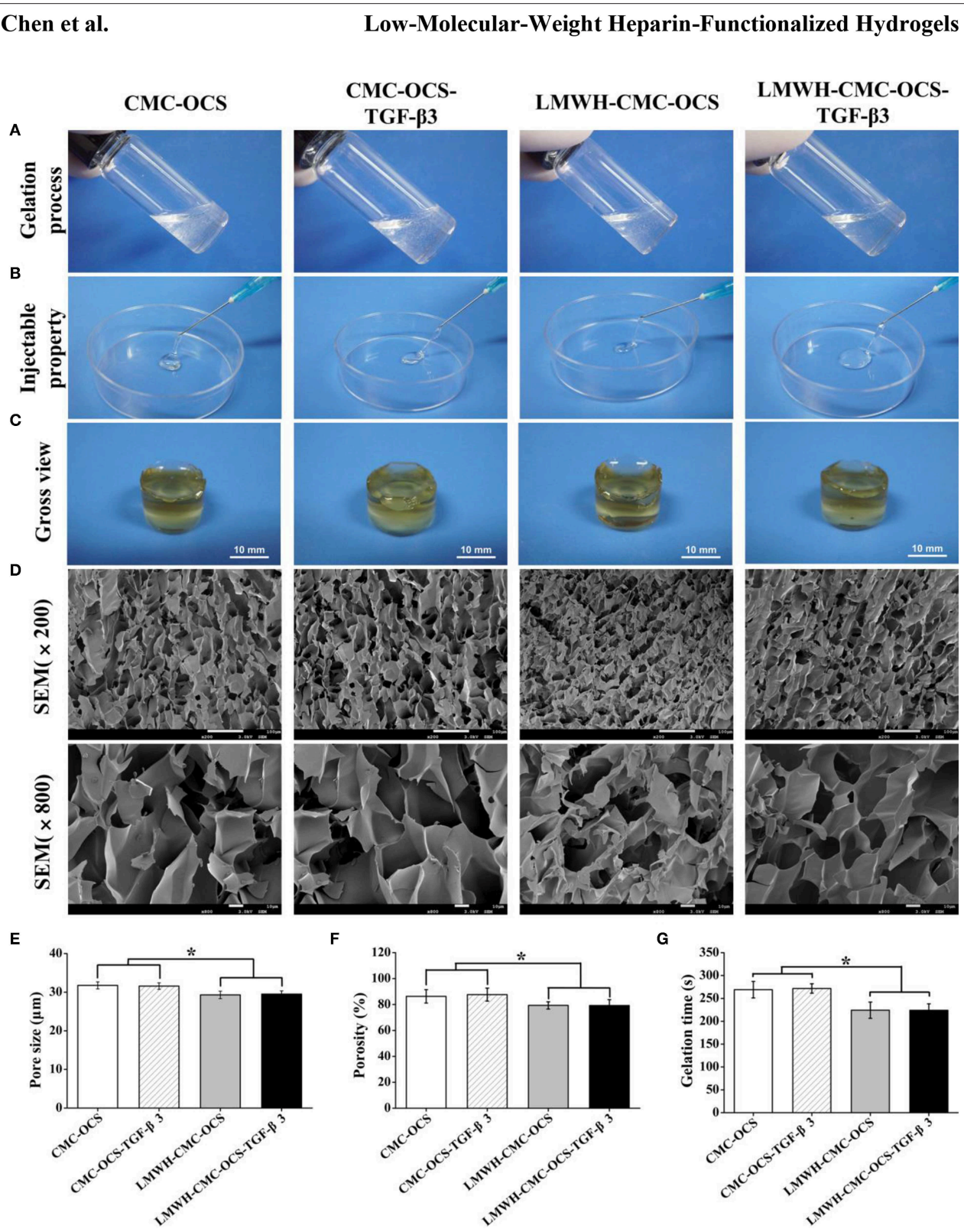

FIGURE 4 | (A) Morphologies of hydrogels before gelation. **(B)** The extrusion of four hydrogels from medical syringes to show injectable properties. **(C)** Photographs of gross view. **(D)** Scanning electron micrographs of hydrogels illustrating the porous and interconnected microstructure. **(E)** The average pore sizes of four hydrogels ($n = 3$, $^*P < 0.05$). **(F)** The porosities of four hydrogels ($n = 5$, $^*P < 0.05$). **(G)** Gelation time of four hydrogels ($n = 5$, $^*P < 0.05$).

more reactive groups and the higher crosslinking degree in the gelation system.

Mechanical Properties

Compressive performances of hydrogels were shown in **Figures 5A–C**. The fracture compressive stresses of CMC-OCS, CMC-OCS-TGF-β3, LMWH-CMC-OCS, and LMWH-CMC-OCS-TGF-β3 hydrogels were 76.44 ± 11.49, 75.23 ± 9.19, 102.41 ± 3.94, and 100.41 ± 6.34 kPa, respectively. The compressive modulus of these hydrogels were 3.80 ± 0.23, 3.93 ± 0.43, 7.61 ± 0.53, and 7.62 ± 0.80 kPa, respectively. There were no statistical differences of the fracture strain (79-83%) among four hydrogels ($n = 3$, $P > 0.05$). The higher compressive properties of LMWH-CMC-OCS and LMWH-CMC-OCS-TGF-β3 hydrogels was due to the denser crosslinking structure and higher solid content compared to CMC-OCS and CMC-OCS-TGF-β3 hydrogels ($n = 3$, $^*P < 0.05$). Oscillatory frequency sweeps experiments were also performed to confirm the mechanical properties of hydrogels (**Figure S2**). Storage modulus G′ of all hydrogels was higher than dissipative modulus G″, and showed a frequency-independent characteristic. A higher storage modulus G′ was observed in the hydrogels of LMWH-CMC-OCS and LMWH-CMC-OCS-TGF-β3 compared with hydrogels of CMC-OCS and CMC-OCS-TGF-β3, and LMWH-CMC-OCS and LMWH-CMC-OCS-TGF-β3 hydrogels might be more suitable for cartilage repair and regeneration since they were closer to the mechanical strength of native cartilage (Wang et al., 2016b).

Swelling Property of Hydrogels

The curves of swelling ratio of four hydrogels were illustrated in **Figure 5D**. All of four hydrogels could reach the swelling equilibrium after incubating at PBS for 72 h. Compared with CMC-OCS and CMC-OCS-TGF-β3 hydrogels, the LMWH-CMC-OCS, and LMWH-CMC-OCS-TGF-β3 hydrogels showed higher swelling ratio (3,100 and 2,600%) and basically maintained their stable swelling behaviors even after 96 h in water, resulting from the higher crosslinking degree of hydrogels. Due to the slight degradation of CMC-OCS and CMC-OCS-TGF-β3 hydrogels after 96 h, the swelling ratio curves displayed a decline trend.

Degradation Behavior *in vitro*

The degradation behavior of hydrogels was observed in PBS at 37°C. As shown in **Figure 5E**, the incorporation of LMWH in hydrogels increased their cross-linked density and enhanced the internal structural compactness, therefore the hydrogels containing LMWH showed a slower degradation rate than the hydrogels without LMWH. after incubation for 21 days, the degradation ratio of LMWH-CMC-OCS and LMWH-CMC-OCS-TGF-β3 hydrogels (56.30 ± 3.09 and 55.91 ± 1.40%) was lower than that of CMC-OCS and CMC-OCS-TGF-β3 (60.21 ±

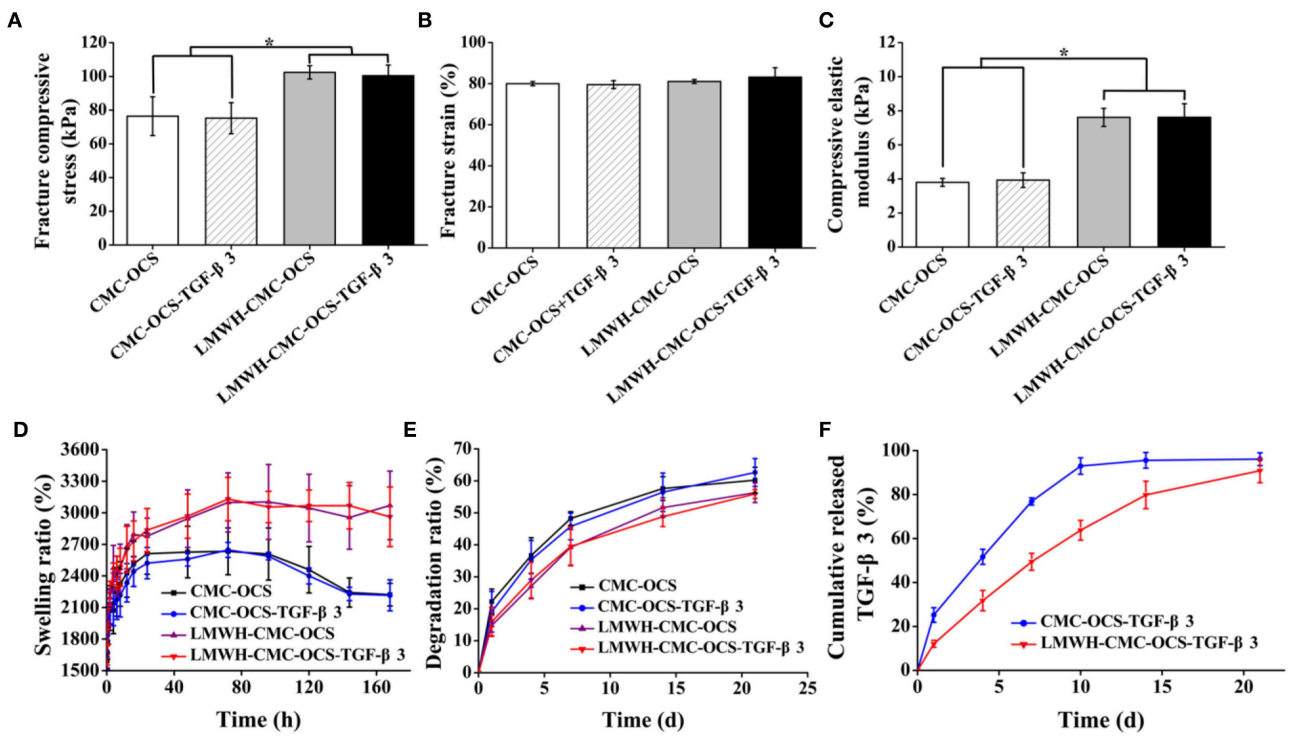

FIGURE 5 | (A) Fracture compressive stress ($n = 3$, $^*P < 0.05$), **(B)** fracture strain ($n = 3$, $P > 0.05$), and **(C)** compressive elastic modulus ($n = 3$, $^*P < 0.05$) obtained by unconfined compressive mechanical tests. **(D)** Swelling kinetics of hydrogels in PBS at each time point ($n = 5$). **(E)** *In vitro* degradation of hydrogels in PBS at each time point ($n = 5$). **(F)** Cumulative release of TGF-β3 from CMC-OCS-TGF-β3 and LMWH-CMC-OCS-TGF-β3 hydrogels after incubation for 1, 4, 7, 10, 14, and 21 days ($n = 5$).

4.04 and 62.62 ± 4.36%). The addition of TGF-β3 into hydrogel had negligible effect on the physical properties of hydrogels. The incorporation of EDC/NHS activated LMWH was beneficial to maintain the structural stability of hydrogel scaffolds and had a significant influence on degradation rate and release rate for a long period of time. Structurally stable hydrogels would facilitate cell adhesion, proliferation and extracellular matrix production *in vitro* (Wang et al., 2019).

Release of Growth Factors

The release behavior of TGF-β3 was determined by ELISA assay. **Figure 5F** showed that the release ratio of TGF-β3 from the CMC-OCS hydrogel was quicker than that of functionalized LMWH-CMC-OCS hydrogel. The release ratio of TGF-β3 from CMC-OCS and LMWH-CMC-OCS hydrogel achieve 92.97 ± 3.73 and 63.75 ± 4.50% after 10 days with a sustainable release plateau. The reason was mainly attributed to that the heparin can

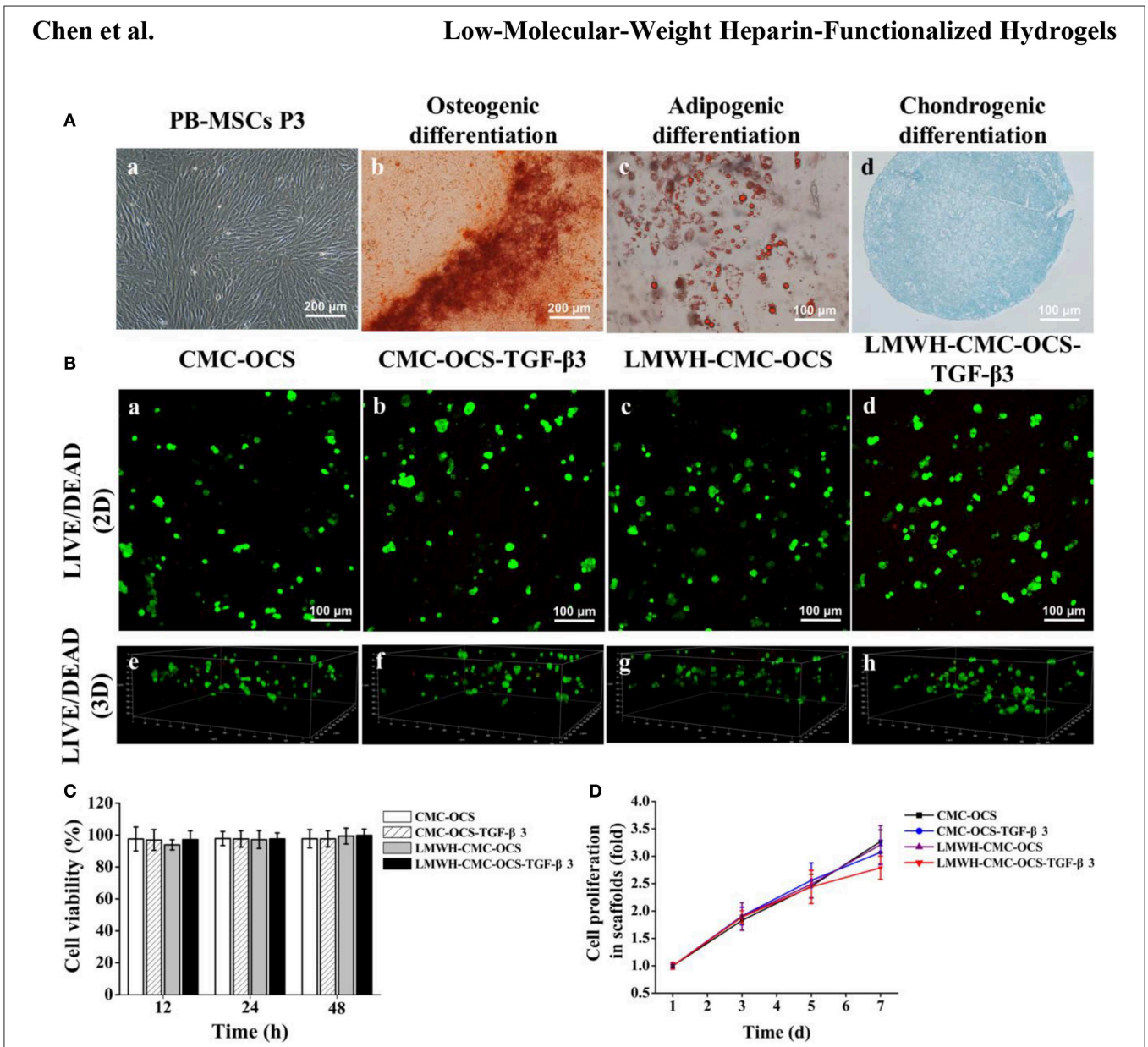

FIGURE 6 | (A) The morphological characteristics and multilineage differentiation potential of PB-MSCs. a. PB-MSCs showed a typical spindle shape at passage 3 *in vitro* (×100). b. Osteogenic differentiation was assessed by Alizarin red staining. c. Adipogenic differentiation was detected by Oil Red O staining. d. Chondrogenic differentiation was confirmed by Alcian Blue staining. **(B)** LIVE/DEAD staining of PB-MSCs on various hydrogels. a–d. Cell viability of four groups in hydrogels was demonstrated by using Live/Dead staining after 7 days of culture *in vitro*. Green represented live cells and red represented dead cells. e–h. 3D renderings of PB-MSCs to show distribution of live and dead cells in hydrogels after 7 days of culture. **(C)** Detection of cytotoxicity of hydrogels using CCK-8 assay ($n = 5$, $P > 0.05$). **(D)** CCK-8 assay detected the cell proliferation of four groups over time, the cell proliferation curves of each groups obtained by normalizing the OD value at each point against the average value of the first day.

combine with growth factors (TGF-β3) to form stable complex through electrostatic interaction; in this case, LMWH-CMC-OCS hydrogel displayed a much lower release rate of TGF-β3. In addition, the dense structures and the slow degradation rate of LMWH-CMC-OCS hydrogel may also contribute to the slow continued release behavior with the 90.85 ± 5.48% after 3 weeks. These results confirmed that LMWH incorporated in hydrogel had enough effect on controlling the release of TGF-β3, and that would effectively promote the chondrogenic differentiation of MSCs and induce the expression of cartilage extracellular matrix since TGF-β3 regulated the metabolism of articular cartilage and multifunctional proteins in a time-and concentration-dependent manner (Wang et al., 2017). Therefore, the physicochemical property of hydrogels demonstrated that the LMWH-CMC-OCS hydrogels had shorter gelling time, higher mechanical strength, smaller porosity, higher and more stable swelling ratio, slower degradation rate and lower release rate of growth factors, compared with CMC-OCS hydrogels.

Isolation, Culture, and Identification of PB-MSCs

A number of PB-MSCs clusters began to appear after the culture of initial 12–14 days, and then transformed into typical spindle morphology. After incubation for 21 days, these primary cells achieved the confluence about 80–90%. PB-MSCs exhibited a relative homogeneity at passage 3 (**Figure 6A**-a).

Multilineage differentiation potential of PB-MSCs was identified with the method of tri-lineage differentiations.

Alizarin red staining was used to detect the deposition of calcium nodules to confirm osteogenic differentiation after 14 days (**Figure 6A**-b).

Oil red O staining showed the accumulation of lipid vacuoles in cells at 21 days, which suggested adipogenic differentiation of PB-MSCs. (**Figure 6A**-c). A spherical pellet formed under the condition of micromass culture at 3 days. Alcian blue staining detected cartilage-specific aggregating proteoglycans and determined the chondrogenic differentiation potential of PB-MSCs after incubation for 21 days (**Figure 6A**-d).

An increasing number of literatures reported that the peripheral blood was a potential alternative source of MSCs and recognized as a similar potential for the proliferation and chondrogenic differentiation as BM-MSCs both *in vitro* and *in vivo* (Fu et al., 2014; Wang et al., 2016a). Based on this, we isolated PB-MSCs with the methods reported above. The PB-MSCs adhered to the bottom of plastic culture dishes and displayed a typical spindle morphology, and differentiated into the

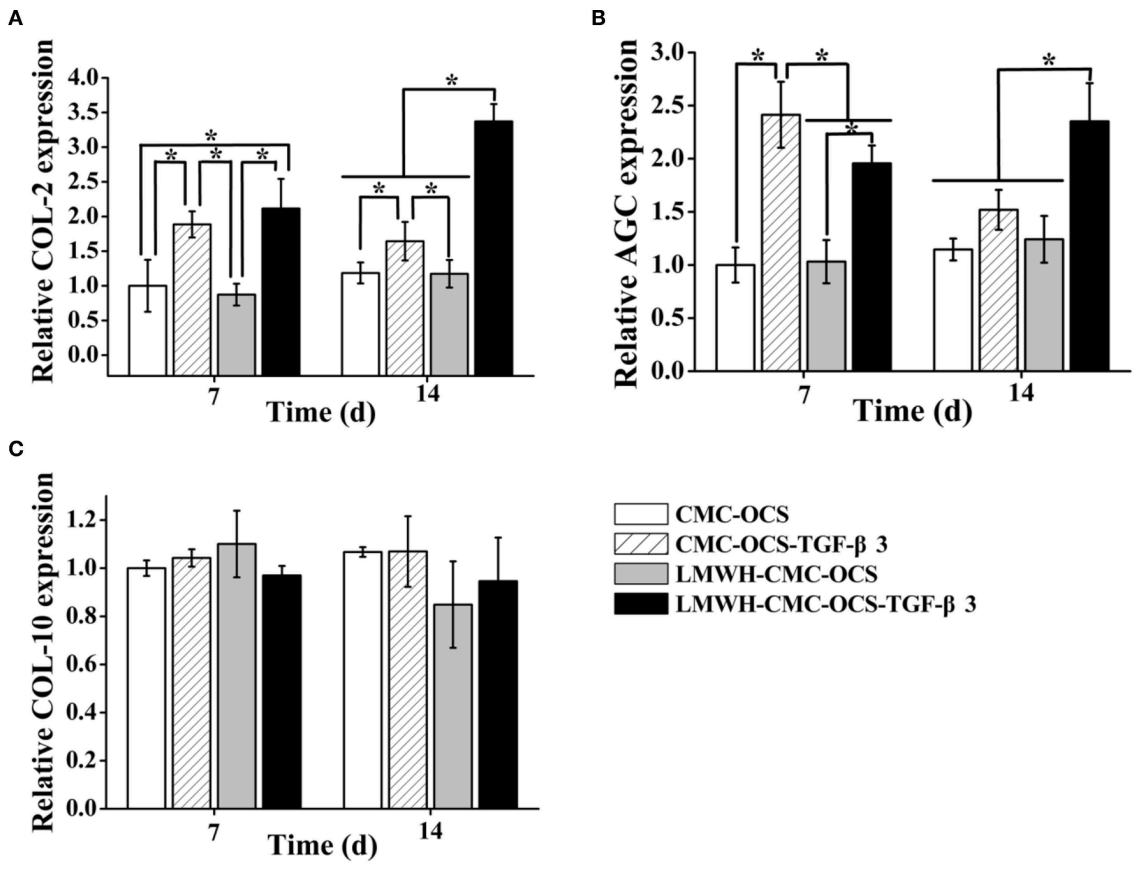

FIGURE 7 | (A) Expression of cartilage-specific genes COL-2 and **(B)** AGC ($n = 3$, $^*P < 0.05$). **(C)** Expression of hypertrophic gene COL-10.

osteoblasts, adipocytes and chondroblasts in appropriate conditions *in vitro*.

LIVE/DEAD Staining of PB-MSCs on Hydrogel Scaffolds

After 7 days of culture in growth medium, LIVE/DEAD Viability Kit assay showed that majority of seeded cells survived in the scaffolds with few dead cells, further confirming the low toxicity of four biocompatible hydrogels (**Figure 6B**,a–d). Three-dimensional rendering of the cell-scaffolds composites showed that PB-MSCs were evenly distributed on the surface and inside of the hydrogel (**Figure 6B**,e–h) with the method of centrifugal seeding which could significantly improve the distribution and proliferation of MSCs on scaffolds (Zhang Z. et al., 2015).

Cytotoxicity of Hydrogel Scaffolds

To detect the cytotoxicity of hydrogels, PB-MSCs were cultured in medium containing extracting liquid of four hydrogels for 12, 24, and 48 h. As shown in **Figure 6C**, the CCK-8 assay demonstrated that the cell viability could remain over 93%, indicating good biocompatibility of all of the four hydrogels. No statistical differences were found among the four groups ($n = 5$, $P > 0.05$).

CCK-8 Assay

The CCK-8 assay demonstrated the proliferation of PB-MSCs on four hydrogels during the first week (**Figure 6D**). There was no statistical difference among the four groups at day 1, 3, and 5 ($n = 5$, $P > 0.05$). However, compared to CMC-OCS and LMWH-CMC-OCS groups, PB-MSCs cultured on CMC-OCS-TGF-β3 and LMWH-CMC-OCS-TGF-β3 hydrogels showed slower proliferation rate at day 7 ($n = 5$, $^*P < 0.05$). It has been reported that the proliferation rate of chondrocytes is slower than that of mesenchymal stem cells (Yang et al., 2018a). Therefore, we concluded that the stronger chondrogenic differentiation of PB-MSCs with these two groups could result in the slower proliferation of PB-MSCs.

Analysis of Cartilage-Specific and Hypertrophic Genes Expression

We analyzed the expression of cartilage-specific genes COL-2 and AGC, and hypertrophic gene COL-10 (**Figure 7**). LMWH-CMC-OCS-TGF-β3 showed the highest expression of COL-2 among the four groups at day 7 and 14 ($n = 3$, $^*P < 0.05$). The expression of COL-2 in CMC-OCS-TGF-β3 hydrogel was lower than LMWHH-CMC-OCS-TGF-β3 hydrogel at any time

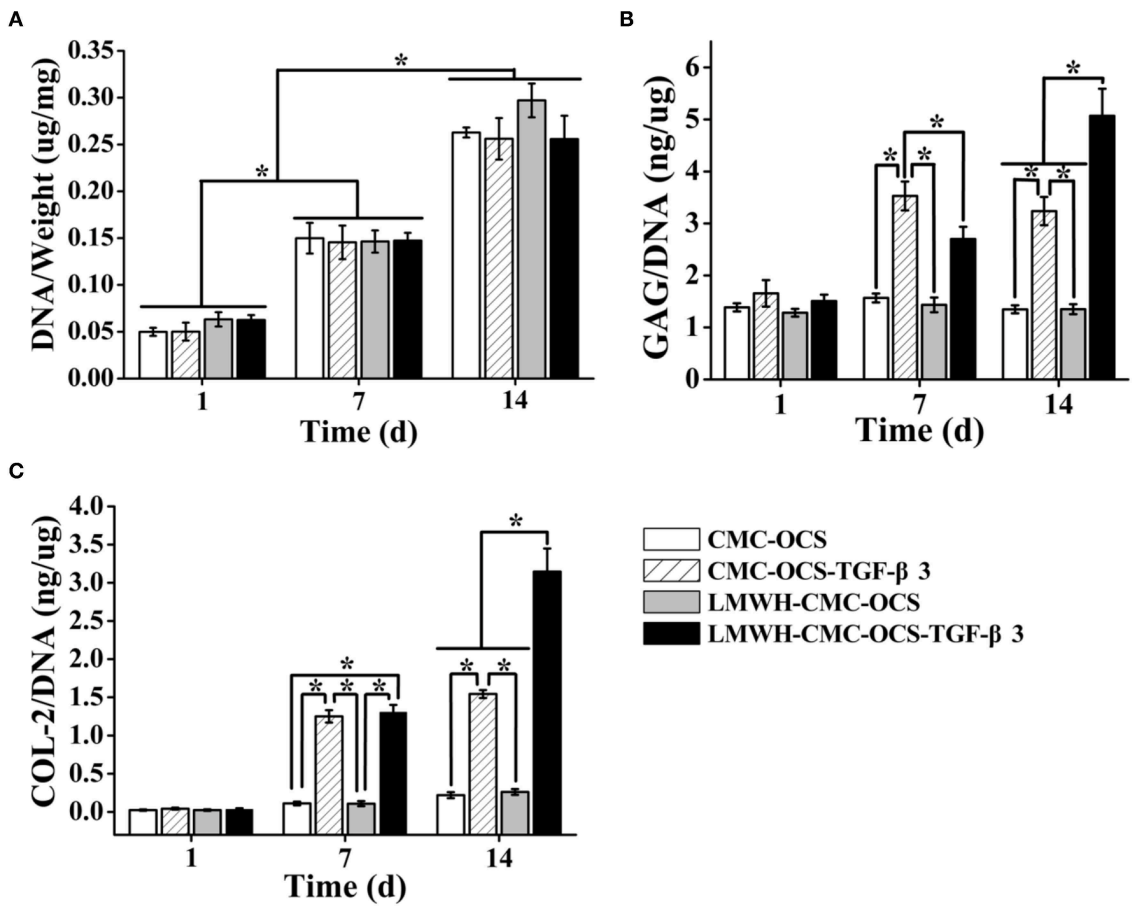

FIGURE 8 | (A) DNA contents of four cell-hydrogel composites increased over time ($n = 3$, $^*P < 0.05$). **(B)** GAG and **(C)** COL-2 deposition on four hydrogels by PB-MSCs at different time points ($n = 3$, $^*P < 0.05$).

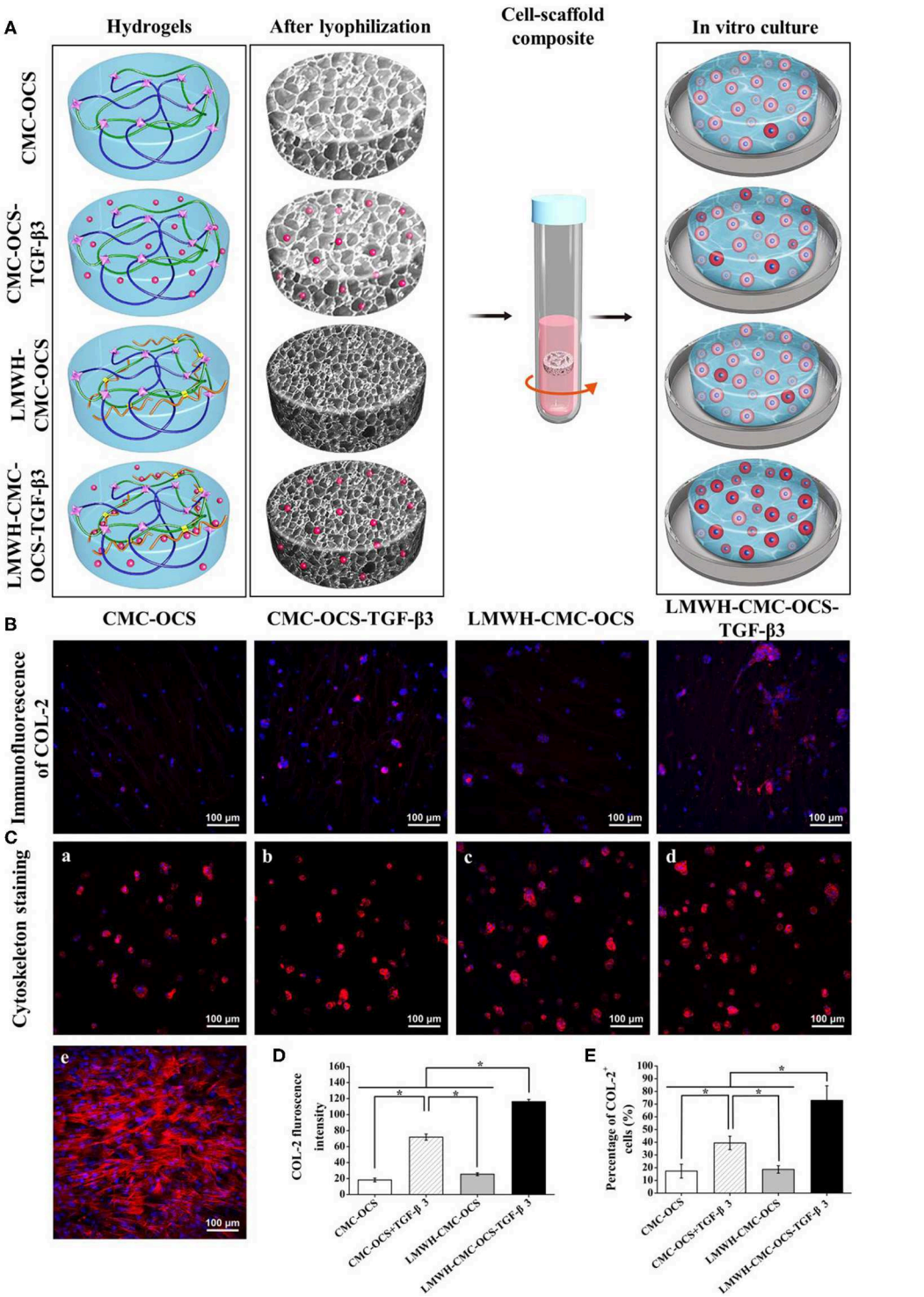

FIGURE 9 | (A) Diagrams of four hydrogels before and after freeze-drying, and seeding with PB-MSCs for *in vitro* culture. The redder the cytoplasm represented the higher the degree of chondrogenic differentiation of PB-MSCs in hydrogels. **(B)** Immunoflurorescent staining visualized the production of COL-2 in the PB-MSCs-hydrogel composites after 14 days of *in vitro* culture. **(C)** Cytoskeleton staining revealing morphology of PB-MSCs on hydrogels (a–d) and in culture dish (e) after 7 days of culture. (Red, cytoskeleton; blue, nuclei). **(D)** LMWH-CMC-OCS-TGF-β3 group showed the highest fluorescence intensity of COL-2 ($n = 3$, $^*P < 0.05$) and **(E)** the highest percentage of COL-2 positive cells ($n = 5$, $^*P < 0.05$) among the four groups.

points, although more TGF-β3 released at day 7. We believed that LMWH in hydrogels can protect TGF-β3 from degradation and maintain their biological activity, which might explain the results of the expression of COL-2. AGC expression in the group of CMC-OCS-TGF-β3 peaked at day 7 ($n = 3$, $^*P < 0.05$), but decreased at 14 days. However, the expression of AGC in the hydrogel of LMWH-CMC-OCS-TGF-β3 up-regulated continuously as time extends, and reached its highest expression at day 14 that was obviously higher than the other three hydrogels at any time points ($n = 3$, $^*P < 0.05$). No significant differences of the expression of hypertrophic gene COL-10 was found among the four groups ($n = 3$, $P > 0.05$), and it suggested that four hydrogels could support cell growth and effectively inhibit cell aging.

Extracellular Matrix Deposition on Hydrogels

The DNA contents continued to increase over time during 2 weeks of culture (**Figure 8A**). The average DNA contents in groups of LMWH-CMC-OCS and LMWH-CMC-OCS-TGF-β3 groups were higher than CMC-OCS and CMC-OCS-TGF-β3 groups at day 1, which was due to the better structural stability and cell adhesion on the LMWH-functionalized hydrogels compared to non-LMWH-functionalized hydrogels. The LMWH-CMC-OCS showed highest average DNA contents at 2 weeks, but no statistical difference was found among four groups ($n = 3$, $P > 0.05$). The contents of GAG and COL-2 in four hydrogels were quantitatively evaluated through ELISA analysis (**Figures 8B,C**). GAG synthesis in the group of CMC-OCS-TGF-β3 peaked at day 7 ($n = 3$, $^*P < 0.05$), but decreased at day 14. Content of GAG and COL-2 in the hydrogel of LMWH-CMC-OCS-TGF-β3 increased continuously as time extends, and reached its highest amount at day 14 that was obviously higher than the other three hydrogels at any time points ($n = 3$, $^*P < 0.05$). The COL-2 content in the CMC-OCS and LMWH-CMC-OCS groups increased slowly, but the GAG secretion almost remained unchanged.

Immunofluorescent Staining of COL-2 and Cell Morphology on Scaffolds

The production of COL-2 protein in cell-hydrogel composites were detected through the immunofluorescent staining after culturing for 2 weeks as shown in **Figures 9A,B**. COL-2 expression in LMWH-CMC-OCS-TGF-β3 group was stronger than that in the other three groups. In terms of the fluorescence intensity of COL-2 (**Figure 9D**) and the percentage of COL-2 positive cells (**Figure 9E**), the LMWH-CMC-OCS-TGF-β3 group showed highest intensity among the four groups ($n = 3$, $^*P < 0.05$). These results of COL-2 immunofluorescence detection were similar to those of ELISA analysis. This is related to the excessive release of TGF-β3 in the early stage and the lack of growth factor in the later stage in the CMC-OCS-TGF-β3 group. Therefore, the long-term slow release of TGF-β3 is more conducive to the expression of cartilage-specific genes and the secretion of extracellular matrix in PB-MSCs, which can be explained by the concentration and time dependence of TGF-β3 on mesenchymal stem cells, and many studies have demonstrated that TGF-β3 stimulate chondrogenesis of mesenchymal stem cells through intracellular pathways involving small mothers against decapentaplegic proteins (Smads) (Chen et al., 2016). As for CMC-OCS scaffold, about 17% of PB-MSCs were positive cells of COL-2 after culturing *in vitro* for 14 days, and COL-2 content also increased as time extended, indicating that CMC-OCS hydrogel could partly promote chondrogenic differentiation of PB-MSCs. The chondroitin sulfate in hydrogels probably contribute to the proliferation and chondrogenic differentiation of seed cells and the synthesis of extracellular matrix (Meghdadi et al., 2019).

Cytoskeleton staining was used to show the morphology of PB-MSCs in four hydrogel scaffolds after culturing for 7 days. PB-MSCs shifted from a spindle-like morphology in the 2D dish (**Figure 9C**-e) to a similar rounded chondrocyte-like shape in 3D hydrogel scaffolds (**Figure 9C**,a–d), fully demonstrating the significant effects of CMC-OCS, CMC-OCS-TGF-β3, LMWH-CMC-OCS, and LMWH-CMC-OCS-TGF-β3 hydrogel scaffolds on inducing the chondrogenic differentiation of PB-MSCs.

Although we have constructed a new tissue engineering cartilage scheme with CMC-OCS hydrogel, LMWH controlled-release TGF-β3 and PB-MSCs, there are still some limitations in this study. First, the optimal concentration of LMWH in hydrogel was not further explored. It has been reported that the release rate of growth factor can be regulated by the concentration of heparin in hydrogel. Second, this study was a preliminary research focused on the applicability *in vitro*, the future studies will be conducted on *in vivo*.

CONCLUSION

In summary, the LMWH functionalized CMC-OCS hydrogels were facilely prepared through Schiff base and amidation reactions at physiological temperature as biological scaffolds. The hydrogels had highly interconnected porous microstructure with appropriate swelling ratio and degradation ratio, which could favor the ingrowth and proliferation of living cells, as well as water convection. The presence of EDC/NHS activated LMWH within the hydrogel can not only improve the crosslinking degree and enhance the stability of scaffolds in PBS, but also the LMWH can complex the TGF-β3 and realize the long-term controlled release of TGF-β3 by means of electrostatic interaction. *In vitro* experiments proved that PB-MSCs had good tri-lineage differentiation potential and can be used as a suitable seed cell in tissue-engineered cartilage. Live/Dead staining, CCK-8 and extracellular matrix deposition assay displayed that the LMWH-CMC-OCS-TGF-β3 hydrogels had no obvious cytotoxicity and can provide a biocompatible microenvironment for PB-MSCs to growth, chondrogenic differentiation and ECM production. As a new kind of construction strategy for tissue-engineered cartilage, the future studies conducted on *in vivo* are worthy for cartilage repair and regeneration.

DATA AVAILABILITY STATEMENT

All datasets generated for this study are included in the article/**Supplementary Material**.

ETHICS STATEMENT

The animal study was reviewed and approved by Animal Care and Use Committee of Peking University Third Hospital.

AUTHOR CONTRIBUTIONS

J-KY and Y-YY conceived and designed the study. Y-RC and Z-XZ carried out the experiments, analyzed the data, and drafted the article. J-YZ, F-ZY, and B-BX edited and proofread the manuscript. JG, CH, and DJ provided oversight for this study.

FUNDING

This work was supported by the National Natural Science Foundation of China (Grant Nos. 51773004, 81630056, 51920105006, 51803188, 31670982) and National Key Research and Development Program (Grant No. 2016YFC1100704).

SUPPLEMENTARY MATERIAL

The Supplementary Material for this article can be found online at: https://www.frontiersin.org/articles/10.3389/fchem.2019.00745/full#supplementary-material

REFERENCES

Ali-Hassan-Sayegh, S., Mirhosseini, S. J., Shahidzadeh, A., Mahdavi, P., Tahernejad, M., Haddad, F., et al. (2016). Administration of low molecular weight and unfractionated heparin during percutaneous coronary intervention. *Indian Heart J.* 68, 213–224. doi: 10.1016/j.ihj.2016.01.014

Andriolo, L., Merli, G., Filardo, G., Marcacci, M., and Kon, E. (2017). Failure of autologous chondrocyte implantation. *Sports Med. Arthrosc. Rev.* 25, 10–18. doi: 10.1097/JSA.0000000000000137

Ariyati, N., Kusworini, K., Nurdiana, N., and Wirohadidjojo, Y. W. (2019). Low degree hyaluronic acid crosslinking inducing the release of TGF-B1 in conditioned medium of wharton's jelly-derived stem cells. *Open Access Maced. J. Med. Sci.* 7, 1572–1575. doi: 10.3889/oamjms.2019.307

Armiento, A. R., Stoddart, M. J., Alini, M., and Eglin, D. (2018). Biomaterials for articular cartilage tissue engineering: learning from biology. *Acta Biomater.* 65, 1–20. doi: 10.1016/j.actbio.2017.11.021

Bu, Y., Shen, H., Yang, F., Yang, Y., Wang, X., and Wu, D. (2017). Construction of tough, in situ forming double-network hydrogels with good biocompatibility. *ACS Appl. Mater. Inter.* 9, 2205–2212. doi: 10.1021/acsami.6b15364

Bu, Y., Zhang, L., Liu, J., Zhang, L., Li, T., Shen, H., et al. (2016). Synthesis and properties of hemostatic and bacteria-responsive in situ hydrogels for emergency treatment in critical situations. *ACS Appl. Mater. Inter.* 8, 12674–12683. doi: 10.1021/acsami.6b03235

Chen, H., Cheng, R., Zhao, X., Zhang, Y., Tam, A., Yan, Y., et al. (2019). An injectable self-healing coordinative hydrogel with antibacterial and angiogenic properties for diabetic skin wound repair. *NPG Asia Mater.* 11:3. doi: 10.1038/s41427-018-0103-9

Chen, J., Wang, Y., Chen, C., Lian, C., Zhou, T., Gao, B., et al. (2016). Exogenous heparan sulfate enhances the TGF-β3-induced chondrogenesis in human mesenchymal stem cells by activating TGF-β/smad signaling. *Stem Cells Int.* 2016, 1–10. doi: 10.1155/2016/1520136

Crecente-Campo, J., Borrajo, E., Vidal, A., and Garcia-Fuentes, M. (2017). New scaffolds encapsulating TGF-β3/BMP-7 combinations driving strong chondrogenic differentiation. *Eur. J. Pharm. Biopharm.* 114, 69–78. doi: 10.1016/j.ejpb.2016.12.021

Deng, Y., Sun, A. X., Overholt, K. J., Yu, G. Z., Fritch, M. R., Alexander, P. G., et al. (2019). Enhancing chondrogenesis and mechanical strength retention in physiologically relevant hydrogels with incorporation of hyaluronic acid and direct loading of TGF-β. *Acta Biomater.* 83, 167–176. doi: 10.1016/j.actbio.2018.11.022

Ding, J., Zhang, J., Li, J., Li, D., Xiao, C., Xiao, H., et al. (2019). Electrospun polymer biomaterials. *Prog. Polym. Sci.* 90, 1–34. doi: 10.1016/j.progpolymsci.2019.01.002

Elahi, M., Guan, G., Wang, L., and King, M. (2014). Influence of layer-by-layer polyelectrolyte deposition and EDC/NHS activated heparin immobilization onto silk fibroin fabric. *Materials* 7, 2956–2977. doi: 10.3390/ma7042956

Everhart, J. S., Campbell, A. B., Abouljoud, M. M., Kirven, J. C., and Flanigan, D. C. (2019). Cost-efficacy of knee cartilage defect treatments in the United States. *Am. J. Sports Med.* doi: 10.1177/0363546519834557. [Epub ahead of print].

Fan, M., Ma, Y., Tan, H., Jia, Y., Zou, S., Guo, S., et al. (2017). Covalent and injectable chitosan-chondroitin sulfate hydrogels embedded with chitosan microspheres for drug delivery and tissue engineering. *Mater. Sci. Eng. C Mater. Biol. Appl.* 71, 67–74. doi: 10.1016/j.msec.2016.09.068

Frangogiannis, N. G. (2017). The role of transforming growth factor (TGF)-β in the infarcted myocardium. *J. Thor. Dis.* 9, S52–S63. doi: 10.21037/jtd.2016.11.19

Fu, W., Zhou, C., and Yu, J. (2014). A new source of mesenchymal stem cells for articular cartilage repair. *Am. J. Sports Med.* 42, 592–601. doi: 10.1177/0363546513512778

Fu, W. L., Jia, Z. Q., Wang, W. P., Zhang, J. Y., Fu, X., Duan, X. N., et al. (2011). Proliferation and apoptosis property of mesenchymal stem cells derived from peripheral blood under the culture conditions of hypoxia and serum deprivation. *Chin. Med. J.* 124, 3959–3967. doi: 10.3760/cma.j.issn.0366-6999.2011.23.022

Han, Y., Li, X., Zhang, Y., Han, Y., Chang, F., and Ding, J. (2019). Mesenchymal stem cells for regenerative medicine. *Cells* 8:886. doi: 10.3390/cells8080886

Hu, X., Gao, Z., Tan, H., Wang, H., Mao, X., and Pang, J. (2019). An injectable hyaluronic acid-based composite hydrogel by DA click chemistry with ph sensitive nanoparticle for biomedical application. *Front. Chem.* 7:477. doi: 10.3389/fchem.2019.00477

Kim, I., Lee, S. S., Bae, S., Lee, H., and Hwang, N. S. (2018). Heparin functionalized injectable cryogel with rapid shape-recovery property for neovascularization. *Biomacromolecules* 19, 2257–2269. doi: 10.1021/acs.biomac.8b00331

Kim, S., Cui, Z., Kim, P. J., Jung, L. Y., and Lee, M. (2018). Design of hydrogels to stabilize and enhance bone morphogenetic protein activity by heparin mimetics. *Acta Biomater.* 72, 45–54. doi: 10.1016/j.actbio.2018.03.034

Kwon, H., Brown, W. E., Lee, C. A., Wang, D., Paschos, N., Hu, J. C., et al. (2019). Surgical and tissue engineering strategies for articular cartilage and meniscus repair. *Nat. Rev. Rheumatol.* 15, 550–570. doi: 10.1038/s41584-019-0255-1

Li, T., Song, X., Weng, C., Wang, X., Sun, L., Gong, X., et al. (2018). Self-crosslinking and injectable chondroitin sulfate/pullulan hydrogel for cartilage tissue engineering. *Appl. Mater. Today* 10, 173–183. doi: 10.1016/j.apmt.2017.12.002

Li, X., Ding, J., Zhang, Z., Yang, M., Yu, J., Wang, J., et al. (2016). Kartogenin-incorporated thermogel supports stem cells for significant cartilage regeneration. *ACS Appl. Mater. Interf.* 8, 5148–5159. doi: 10.1021/acsami.5b12212

Liaw, C. Y., Ji, S., and Guvendiren, M. (2018). Engineering 3D hydrogels for personalized *in vitro* human tissue models. *Adv. Healthc. Mater.* 7:1701165. doi: 10.1002/adhm.201701165

Liu, H., Cheng, Y., Chen, J., Chang, F., Wang, J., Ding, J., et al. (2018). Component effect of stem cell-loaded thermosensitive polypeptide hydrogels on cartilage repair. *Acta Biomater.* 73, 103–111. doi: 10.1016/j.actbio.2018.04.035

Liu, Y., and Hsu, S. (2018). Synthesis and biomedical applications of self-healing hydrogels. *Front. Chem.* 6:499. doi: 10.3389/fchem.2018.00449

Liu, Z., Li, G., Zheng, Z., Li, Y., Han, Y., Kaplan, D. L., et al. (2018). Silk fibroin-based woven endovascular prosthesis with heparin surface modification. *J. Mater. Sci.* 29:46. doi: 10.1007/s10856-018-6055-3

Meghdadi, M., Pezeshki-Modaress, M., Irani, S., Atyabi, S. M., and Zandi, M. (2019). Chondroitin sulfate immobilized PCL nanofibers enhance chondrogenic differentiation of mesenchymal stem cells. *Int. J. Biol. Macromol.* 136, 616–624. doi: 10.1016/j.ijbiomac.2019.06.061

Pan, G., Guo, Q., Ma, Y., Yang, H., and Li, B. (2013). Thermo-responsive hydrogel layers imprinted with RGDS peptide: a system for harvesting cell sheets. *Angew. Chem. Int. Ed.* 52, 6907–6911. doi: 10.1002/anie.201300733

Qian, Y., Han, Q., Chen, W., Song, J., Zhao, X., Ouyang, Y., et al. (2017). Platelet-rich plasma derived growth factors contribute to stem cell differentiation in musculoskeletal regeneration. *Front. Chem.* 5:89. doi: 10.3389/fchem.2017.00089

Qin, H., Wang, J., Wang, T., Gao, X., Wan, Q., and Pei, X. (2018). Preparation and characterization of chitosan/β-glycerophosphate thermal-sensitive hydrogel reinforced by graphene oxide. *Front. Chem.* 6:565. doi: 10.3389/fchem.2018.00565

Redondo, M. L., Naveen, N. B., Liu, J. N., Tauro, T. M., Southworth, T. M., and Cole, B. J. (2018). Preservation of knee articular cartilage. *Sports Med. Arthrosc. Rev.* 26, e23–e30. doi: 10.1097/JSA.0000000000000226

Robertson, L., and Jones, L. E. (2017). Fixed dose subcutaneous low molecular weight heparins versus adjusted dose unfractionated heparin for the initial treatment of venous thromboembolism. *Cochr. Database Syst. Rev.* 2:CD001100. doi: 10.1002/14651858.CD001100.pub4

Sadlik, B., Gobbi, A., Puszkarz, M., Klon, W., and Whyte, G. P. (2017). Biologic inlay osteochondral reconstruction: arthroscopic one-step osteochondral lesion repair in the knee using morselized bone grafting and hyaluronic acid-based scaffold embedded with bone marrow aspirate concentrate. *Arthrosc. Tech.* 6, e383–e389. doi: 10.1016/j.eats.2016.10.023

Stuckensen, K., Schwab, A., Knauer, M., Muinos-Lopez, E., Ehlicke, F., Reboredo, J., et al. (2018). Tissue mimicry in morphology and composition promotes hierarchical matrix remodeling of invading stem cells in osteochondral and meniscus scaffolds. *Adv. Mater.* 30:e1706754. doi: 10.1002/adma.201706754

Sun, T., Liu, M., Yao, S., Ji, Y., Shi, L., Tang, K., et al. (2018). Guided osteoporotic bone regeneration with composite scaffolds of mineralized ECM/heparin membrane loaded with BMP2-related peptide. *Volume* 13, 791–804. doi: 10.2147/IJN.S152698

Thones, S., Rother, S., Wippold, T., Blaszkiewicz, J., Balamurugan, K., Moeller, S., et al. (2019). Hyaluronan/collagen hydrogels containing sulfated hyaluronan improve wound healing by sustained release of heparin-binding EGF-like growth factor. *Acta Biomater.* 86, 135–147. doi: 10.1016/j.actbio.2019.01.029

Wang, C., Feng, N., Chang, F., Wang, J., Yuan, B., Cheng, Y., et al. (2019). Injectable cholesterol-enhanced stereocomplex polylactide thermogel loading chondrocytes for optimized cartilage regeneration. *Adv. Healthc. Mater.* 8:e1900312. doi: 10.1002/adhm.201900312

Wang, J., Sun, B., Tian, L., He, X., Gao, Q., Wu, T., et al. (2017). Evaluation of the potential of rhTGF- β3 encapsulated P(LLA-CL)/collagen nanofibers for tracheal cartilage regeneration using mesenchymal stems cells derived from Wharton's jelly of human umbilical cord. *Mater. Sci. Eng. C* 70, 637–645. doi: 10.1016/j.msec.2016.09.044

Wang, L., Li, L., Wang, X., Huang, D., Yang, F., Shen, H., et al. (2016). UV-triggered thiol–disulfide exchange reaction towards tailored biodegradable hydrogels. *Polym. Chem.-UK* 7, 1429–1438. doi: 10.1039/C5PY01925G

Wang, S. J., Jiang, D., Zhang, Z. Z., Huang, A. B., Qi, Y. S., Wang, H. J., et al. (2016a). Chondrogenic potential of peripheral blood derived mesenchymal stem cells seeded on demineralized cancellous bone scaffolds. *Sci. Rep.* 6:36400. doi: 10.1038/srep36400

Wang, S. J., Zhang, Z. Z., Jiang, D., Qi, Y. S., Wang, H. J., Zhang, J. Y., et al. (2016b). Thermogel-coated poly(epsilon-Caprolactone) composite scaffold for enhanced cartilage tissue engineering. *Polymers* 8:200. doi: 10.3390/polym8050200

Wu, D., Loh, X. J., Wu, Y., Lay, C. L., and Liu, Y. (2010). 'Living' controlledin situ gelling systems: thiol–disulfide exchange method toward tailor-made biodegradable hydrogels. *J. Am. Chem. Soc.* 132, 15140–15143. doi: 10.1021/ja106639c

Yanagawa, Y., Hiraide, S., and Iizuka, K. (2016). Isoform-specific regulation of transforming growth factor-β mRNA expression in macrophages in response to adrenoceptor stimulation. *Microbiol. Immunol.*. 60, 56–63. doi: 10.1111/1348-0421.12344

Yang, Q., Teng, B., Wang, L., Li, K., Xu, C., Ma, X., et al. (2017). Silk fibroin/cartilage extracellular matrix scaffolds with sequential delivery of TGF-β3 for chondrogenic differentiation of adipose-derived stem cells. *Volume* 12, 6721–6733. doi: 10.2147/IJN.S141888

Yang, Y., Lin, H., Shen, H., Wang, B., Lei, G., and Tuan, R. S. (2018a). Mesenchymal stem cell-derived extracellular matrix enhances chondrogenic phenotype of and cartilage formation by encapsulated chondrocytes *in vitro* and *in vivo*. *Acta Biomater.* 69, 71–82. doi: 10.1016/j.actbio.2017.12.043

Yang, Y., Wang, X., Yang, F., Shen, H., and Wu, D. (2016). A universal soaking strategy to convert composite hydrogels into extremely tough and rapidly recoverable double-network hydrogels. *Adv. Mater.* 28, 7178–7184. doi: 10.1002/adma.201601742

Yang, Y., Wang, X., Yang, F., Wang, L., and Wu, D. (2018b). Highly elastic and ultratough hybrid ionic-covalent hydrogels with tunable structures and mechanics. *Adv. Mater.* 30:1707071. doi: 10.1002/adma.201707071

Zhang, Y., Yu, J., Ren, K., Zuo, J., Ding, J., and Chen, X. (2019). Thermosensitive hydrogels as scaffolds for cartilage tissue engineering. *Biomacromolecules* 20, 1478–1492. doi: 10.1021/acs.biomac.9b00043

Zhang, Z., Jiang, D., Wang, S., Qi, Y., Zhang, J., and Yu, J. (2015). Potential of centrifugal seeding method in improving cells distribution and proliferation on demineralized cancellous bone scaffolds for tissue-engineered meniscus. *ACS Appl. Mater. Inter.* 7, 15294–15302. doi: 10.1021/acsami.5b03129

Zhang, Z. Z., Chen, Y. R., Wang, S. J., Zhao, F., Wang, X. G., Yang, F., et al. (2019). Orchestrated biomechanical, structural, and biochemical stimuli for engineering anisotropic meniscus. *Sci. Transl. Med.* 11:eaao0750. doi: 10.1126/scitranslmed.aao0750

Zylinska, B., Silmanowicz, P., Sobczynska-Rak, A., Jarosz, Ł., and Szponder, T. (2018). Treatment of articular cartilage defects: focus on tissue engineering. *In vivo* 32, 1289–1300. doi: 10.21873/invivo.11379

Conflict of Interest: The authors declare that the research was conducted in the absence of any commercial or financial relationships that could be construed as a potential conflict of interest.

frontiers in Chemistry

ORIGINAL RESEARCH
published: 08 November 2019
doi: 10.3389/fchem.2019.00769

Fabrication of Customized Nanogel Carriers From a UV-Triggered Dynamic Self-Assembly Strategy

Wuren Bao[1], *Jieran Lyu*[2,3], *Chunlin Li*[4], *Jifeng Zhang*[5], *Tunan Sun*[4], *Xing Wang*[3,6]*, *Jin Zhou*[4]* and *Dawei Li*[4]*

[1] School of Nursing, Inner Mongolia University for Nationalities, Tongliao, China, [2] Clinical Medicine Academy of Shandong First Medical University, Tai'an, China, [3] Beijing National Laboratory for Molecular Sciences, State Key Laboratory of Polymer Physics and Chemistry, Institute of Chemistry, Chinese Academy of Sciences, Beijing, China, [4] The 8th Medical Center of Chinese PLA General Hospital, Beijing, China, [5] Department of Orthopedic Surgery, Tongliao City Hospital, Tongliao, China, [6] University of Chinese Academy of Sciences, Beijing, China

OPEN ACCESS

Edited by:
Clemens Kilian Weiss,
Fachhochschule Bingen, Germany

Reviewed by:
Xiaoyun Qin,
Zhengzhou University of Light Industry, China
Xuyu Tan,
Massachusetts Institute of Technology, United States

***Correspondence:**
Xing Wang
wangxing@iccas.ac.cn
Jin Zhou
huoshan1975@sina.com
Dawei Li
ldw309@126.com

Specialty section:
This article was submitted to Polymer Chemistry, a section of the journal Frontiers in Chemistry

Received: 04 August 2019
Accepted: 24 October 2019
Published: 08 November 2019

Citation:
Bao W, Lyu J, Li C, Zhang J, Sun T, Wang X, Zhou J and Li D (2019) Fabrication of Customized Nanogel Carriers From a UV-Triggered Dynamic Self-Assembly Strategy. Front. Chem. 7:769. doi: 10.3389/fchem.2019.00769

Recent advances in self-assembled nanogel carriers have allowed precise design of hierarchical structures by a low-cost solution-phase approach. Typically, photochemical strategy on the tailor of morphology and dimension has emerged as a powerful tool, because light-trigger has exceptional advantages of an instant "on/off" function and spatiotemporal precision at arbitrary time. Herein, we report a tunable manipulation of sequentially morphological transition via a "living" thiol-disulfide exchange reaction from a UV-tailored hierarchical self-assembly strategy. By varying the irradiation time, the photochemical method can easily fabricate and guide a series of attractively architectural evolution in dilute aqueous solutions, by which the improving hydrophobicity and sensitive redox-responsiveness endowed these disulfide-linked nanoparticles with remarkable capacities of abundant encapsulation, effective separation, and controlled release of hydrophobic cargoes. Notably, once the exchange reaction is suspended at any point of time by removing the UV lamp, these active sites within the nanogel carriers are instantaneous deactivated and the correspondingly structural transformations are also not conducted any more. However, if the stable inert sites are reactivated as needed by turning on the UV light, the interrupting morphology evolution can continue its previous steps, which may provide a simple and novel approach to fabricating the desired self-assemblies in solutions. With regard to this advanced functionality, various nanogel carriers with customizable structures and properties have been yielded and screened for cancer therapy. Thus, this "living" controlled self-assembled method to program morphology evolution *in situ* is a universal strategy that will pave novel pathways for creating sequential shape-shifting and size-growing nanostructures and constructing uniform nanoscopic functional entities for advanced bio-applications.

Keywords: nanogel, morphology evolution, UV-trigger, redox-responsive, drug carrier

INTRODUCTION

Hydrogel particles (microgels and nanogels), composed of a series of microsized or nanosized cross-linking networks, own the high water contents, satisfying structural stability and desirable mechanical property, which has great potentials in applications of biosensing and drug delivery (Stefik et al., 2015; Palivan et al., 2016). Although frequently used methodologies have been reported to prepare hydrogel particles by the polymer polymerization, self-assembly, template-assisted nanofabrication, and microfluidic techniques, the precise and successive fabrication of microgels/nanogels is still challenging because of the difficult design and complex process for tailoring the structures and properties.

The solution self-assembly of nanogels offers an efficient and bottom-up approach on creating various well-defined nanoparticles with significant fields of drug delivery, nanoreactors, photonic detectors, etc. (Lee et al., 2016; Yang et al., 2018). Fabrication of shape-shifting and size-growing architectures appears as an important approach on improving the nanoscience and nanotechnology, because a number of functional nanogel carriers are directly determined by their shapes and sizes. Various approaches on generation of uniform morphologies and desire dimensions are always relied on the fine control of special architectures (chemical composition, geometry, hydrophobic/hydrophilic ratio, surface chemistry, and flexibility), external environments (pH, temperature, light, stress, photon, ultrasound, and ionic strength), and selective cosolvent mixtures (Gröschel et al., 2013; Newkome and Moorefield, 2015; Tan et al., 2015; Hunt et al., 2016; Mason et al., 2016; Zhang et al., 2018). Whereas, these methods are still difficult to delicately manipulate the self-assembled system and veritably observe all kinds of solution-assemblies or pre-assemblies because of the complexity in precise control of intrinsic properties (hydrophobic/hydrophilic ratio, architecture, rigidity, size, etc.) for amphiphiles at any moment once trigging the self-assembly system at the beginning, and hence the simple management of *in-situ* morphology evolution with an instant "on/off" function to tailor the solution-assemblies at arbitrary time is of the utmost importance. Therefore, it is urgent and important to develop some manipulative reactions to regulate the self-assembly systems with a vital criteria that the self-assembly behaviors could be controllably activated, terminated, and interrupted at any time, and should also be reinitiated by trigger of the external stimuli whenever needed. Although the pH-triggered "living" morphology evolution and controlled hydrogels are well-researched based on a thiol-disulfide exchange reaction in our previous works (Wu et al., 2010; Zhang et al., 2012; Wang et al., 2013, 2018a), consequences of harsh pH environments on the modulation of thiol-disulfide exchange reaction and the corresponding self-assembled nanogels are typically overlooked for the biomedical applications.

Alternatively, a photochemical reaction is a powerful tool to modulate the thiol-disulfide reaction, which possess unique advantages like remote trigger, variable light intensity, smart on-off function and spatiotemporal precision, realizing the real-time control over the whole photochemical process. Inspired from this intriguing concept, we demonstrate a "living" controlled

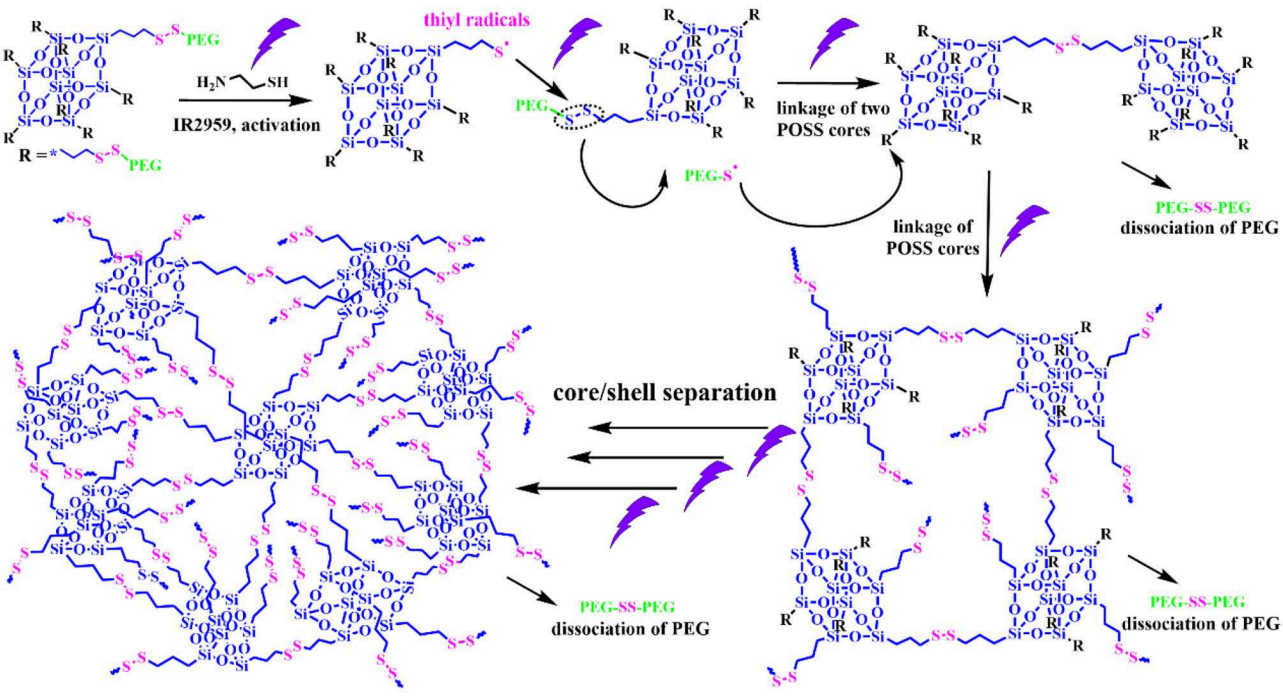

SCHEME 1 | Schematic representation of controlled thiol-disulfide exchange reaction via a UV switcher.

strategy on successful regulation of the self-assembled evolution *in situ* by manipulating UV switcher to turn on/off thiol-disulfide exchange reaction for an amphiphilic POSS-$(SS\text{-}PEG)_8$ polymer in dilute aqueous solutions. **Scheme 1** illustrated the possible mechanism of UV-triggered thiol-disulfide exchange that can cause the spontaneous dissociation of PEG shells and linkage of POSS cores along with the continuous reaction progress; in this case, the hydrophobic territory was gradually enlarged and topological architecture was continuously evolved. Thus, we found that the rational control of UV trigger and thiol-disulfide reaction time could easily adjust the hydrophobic/hydrophilic ratios and topological structures, thus generating time-dependent morphology transition and size growth during the continuous exchange reaction. Notably, this self-assembled evolution behavior can be interrupted at any time by turning off the UV light and restarted by turning on the irradiation. The rigid POSS backbone and its strong aggregation ability endow the POSS-containing hybrid polymers with hierarchically self-assembly behaviors in selective solvents, presenting the multifarious morphologies and *in situ* assembling process (Zhang and Muller, 2013; Li et al., 2015; Ni et al., 2015; Wang et al., 2015, 2016, 2018b; Dong et al., 2016; Qian et al., 2019). More importantly, unlike previously reported shape-shifting organic nanostructures by tediously adjusting conditions, the morphology conversion in this "living" controlled system, relied on the stimuli-responsive "on/off" reaction, was tunable, continuous, and diversified, by which high-throughput synthesis and fabrication of polymeric colloids are well-realized for biomedical applications. Thus, it is worth carrying out the scientific studies to systemically understand the fundamental principles governing the slow-growth and morphology transition of nanostructures based on such inherent advantages and facile strategies.

MATERIALS AND METHODS

Materials

POSS-$(SS\text{-}PEG)_8$ ($M_{n,PEG} = 750$ g/mol) was prepared according to the previous work (Wang et al., 2013), DMEM was purchased from Beijing BioDee Biotechnology Co. Ltd. Cell counting kit-8 was purchased from Beyotime Biotechnology. MCF-7 cell lines were purchased from the American type Culture Collection (ATCC, Rockville, MD). Other chemical reagents were commercially purchased and directly used without any further purifications.

Characterizations

Infrared spectrum was performed on an Excalibur Series FT-IR spectrometer (DIGILAB, Randolph, MA) by drop-casting sample films on the KBr plate. The polymeric compositions were determined by NMR spectra using a Bruker DRX-400 spectrometer with $CDCl_3$ as the solvent and tetramethylsilane (TMS) as the internal standard. Transmission electron microscopy (TEM) images were obtained on a JEM-2200FS microscope (JEOL, Japan). A 5 μL droplet of assembled solution was dropped onto a copper grid (300 mesh) coated with a carbon film, followed by drying at room temperature. Scanning electron microscopy (SEM) images were obtained at acceleration voltage of 5 kV on a JSM-6700F microscope (JEOL, Japan). The samples were sputter-coated with a thin layer of Pt for 90 s to make the samples conductive before testing.

Preparation of POSS-$(SS\text{-}PEG)_8$@TPE Aggregates

POSS-$(SS\text{-}PEG)_8$@TPE aggregates were self-assembled as follows: 5 mg of POSS-$(SS\text{-}PEG)_8$ polymers and 1 mg of TPE-CHO molecules were firstly dissolved in 1 mL of THF, then 4 mL of ultrapure water were added dropwise at the rate of 0.05 mL/min via a syringe pump. After addition of the IR2959 and cysteamine, the exchange reaction and self-assembly behavior were triggered by turning on/off the UV irradiation (365 nm, power density of 3 mW/cm^2) at a predetermined time.

Preparation of POSS-$(SS\text{-}PEG)_8$@DOX Aggregates

POSS-$(SS\text{-}PEG)_8$@DOX aggregates were self-assembled as follows: 5 mg of POSS-$(SS\text{-}PEG)_8$, a predetermined amount of DOX·HCl and 1.5 molar equiv of triethylamine were dissolved in 1 mL of DMF at room temperature for 2 h. Then 4 mL of ultrapure water were added dropwise at the rate of 0.05 mL/min via a syringe pump. The stable morphology can be facilely yielded by turning on/off the UV irradiation at a predetermined time, and the various dried DOX-loaded aggregates were finally obtained after dialyzing against deionized water for 24 h (MW cutoff, 4 kDa) to remove the unencapsulated DOX molecules and byproducts.

CCK-8 Assay

The cytotoxicity of POSS-$(SS\text{-}PEG)_8$ polymers and DOX-loaded aggregates (after exchange reaction under UV irradiation for 4 and 24 h, respectively) was investigated by CCK-8 assay. Specifically, MCF-7 cells were seeded onto a 96-well plate with a density of 1×10^4 cells per well in 180 μL of DMEM containing 10% fetal bovine serum (FBS) and incubated for 24 h (37°C, 5% CO_2). The medium was replaced by 90 μL of fresh DMEM medium and then 20 μL of samples with 2–10 mg/mL of the aggregate suspensions in PBS (pH 7.4) were added. After incubation for another 24 h, the culture media were removed from cell culture plates, and 100 μL of fresh culture media and 10 μL of CCK-8 kit solutions were immediately poured into and homogeneously mixed with another 4 h of incubation in a CO_2 incubator. Finally, 100 μL of self-assembled solutions were put into 96-well plate. The optical density of each well at 450 nm was read using a microplate reader. Cells cultured in DMEM medium containing 10% FBS (without exposure to polymers or aggregates) were used as controls.

RESULTS AND DISCUSSION

The precursor of POSS-$(SS\text{-}PEG)_8$ was yielded according to our previous work (Wang et al., 2013). IR spectrum give an intuitive observation with the shark peak of 2,887 cm^{-1} attributed to *C-H* stretching of CH_2 at PEG and strong signal of 1,115 cm^{-1} belonged to the Si-O-Si at POSS. ^1H NMR spectrum showed

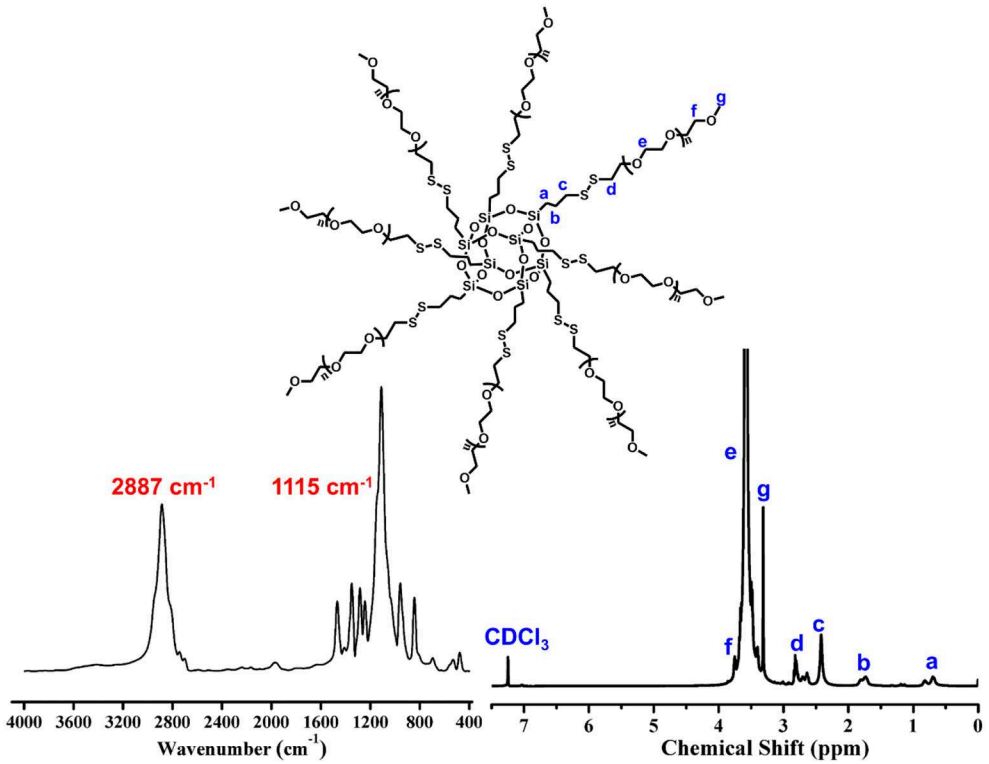

FIGURE 1 | FT-IR and ^{1}H NMR spectra of POSS-(SS-PEG)$_8$.

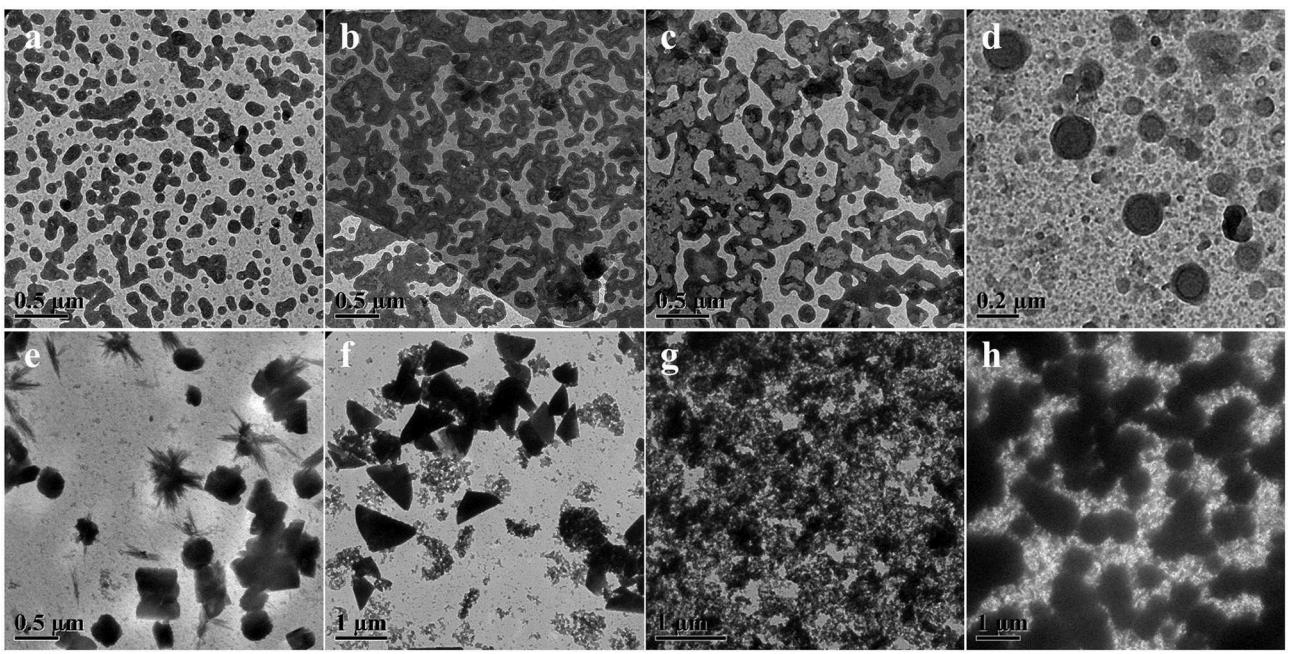

FIGURE 2 | TEM images showing morphology and size evolution with a concentration of 1 mg/mL aqueous media under UV irradiation at **(a)** 0.5, **(b)** 1, **(c)** 4, **(d)** 8, **(e)** 24, **(f)** 32, **(g)** 40, and **(h)** 48 h.

a preferable assignment of all characteristic peaks (**Figure 1**), demonstrating uniform disulfide-crosslinked core/shell structure with a POSS core and eight peripheral PEG shells.

As a representative dynamic bond, disulfide bond could undergo the thiol-disulfide exchange reaction with thiol groups by an anion-mediated or a radical-mediated mechanism under the alkali solutions or irradiation conditions (Xia et al., 2016). Compared to the harsh pH solution to tailor the exchange reactions, UV-triggered radical-mediated behaviors possessed remote manipulation, variable light intensity, smart on-off function and spatiotemporal precision capacities, which could easily achieve the real-time control over the whole photochemical process. Thus, we utilized the IR2959 as a photo-initiator to adjust the radical-centered disulfide exchange reaction by varying the irradiation time followed with concomitant changes in the morphology. On account of high-effective UV-triggered thiol-disulfide exchange reaction, 1 mg/mL concentration of POSS-$(SS\text{-}PEG)_8$ polymers was applied to reduce the thiol-disulfide exchange reaction without the gelation process in dilute solutions. As shown from **Figures 2a,b**, the emergence and growth of cylindrical micelles were observed under UV irradiation within 1 h. Shortly, the close-grained networks were generated because the UV-triggered multiple reactive sites were guided by the simultaneous multi-thiol-disulfide exchange reactions in **Figure 2c**. The existence of intermediates indicated the impossibly homogeneous exchange reaction and ongoing self-organization process (**Figure S1a**). The increase of fiber clusters in length and width proved the oriented morphology transformation toward the minimization of overall free energy of system during the self-assembly process, in which the strong POSS aggregation capacity to assemble into layered crystals may drive the chain-like structures to evolve into ellipsoids, so the oligomer micellar linkages and junctions could preferentially grow into the long and narrow cylinders at the lowest state of free energy. Then, the thick cylinder-linked networks were slowly dissociated and transferred into vesicles with distinct size gradient distribution (**Figure 2d** and **Figure S1b**). After the morphological fusion stage (**Figure S1c**), the shuttle-shaped sheets were born and grown up, as observed in **Figure S1d**. Prolonging the irradiation time for cluster fusion, some intermediates and rhombus-shaped nanosheets were inconceivably obtained in **Figure 2e** and **Figure S1e**. After UV irradiation for 24 h, the square sheets collapsed and gestated into the triangle-shaped plates in **Figure 2f** and **Figure S1f**. The formation of well-defined 2D nanosheets may ascribe to the ordered arrangement of rigid POSS-embedded macromolecules into layers driven by hydrophobic forces. In addition, the fractured segments may also be induced by the degradable nanoparticles under the long periods of irradiation, because the irradiation had more chances to break down the high-density disulfides; in this case, the thicker cluster aggregates could degrade into the shuttle-shaped sheets and other small chips. When the hydrophobic/hydrophilic ratio was substantially increased for a longer time, the morphology evolution come to an end, ultimately forming the silkworm particles with augmented dimension and density (**Figures 2g,h**, and **Figures S1g,h**). Overall, the morphology evolution *in situ* from cylindrical micelles to vesicles to clusters to various 2D nanosheets and finally to silkworm particles was well-programmed in sequence with the gradually increased dimensions based on ongoing UV-triggered exchange reaction and ever-changing self-assembled environments.

SEM images in **Figure 3A** gave additional evidence to testify this UV-controlled morphology evolution. UV-controlled self-assembled transition possessed instant a "on/off" function that can facilely obtain the desired shape and size with high stability in the aqueous solutions only by simple removal of the UV illumination within a predetermined time. **Figure 3B** vividly depicted the summary representation of morphology and size evolution, intuitively presenting this traceable morphological growth, fusion and transition. It was mentioned that although the size of nanogel is enlarged theoretically, the UV-triggered multiple reactive sites could lead to the simultaneous multi-thiol-disulfide exchange reaction, which may make the random thiol-disulfide exchange, poor-selective core/shell separation and ill-defined size evolution. In addition, UV irradiation could destroy the high-density disulfides incidentally so that the size variation was basically irregular though the morphological transition was well-performed thermodynamically in dilute aqueous solutions. More importantly, once the thiol-disulfide exchange reaction was suspended at any point of time by turning off the UV switcher, the thiyl radicals of self-assemblies were quickly deactivated into the thiols and no further exchange reaction and morphology evolution were conducted any more. However, these stable inert thiols could be reactivated whenever restarted the UV lamp, and the trapped morphology evolution could return back on its right track. For example, when the polymer solution was exposed to the UV irradiation in **Figure 4**, the short cylindrical micelles were formed around 1 h later. Once removing the irradiation, the inactivation of thiol-disulfide exchange could interrupt the morphology evolution and keep the cylinders for a long time. After turning on the UV irradiation, the reactivation of exchange reaction impelled the morphology transformation to reboot the following process as before. Similarly, stable triangle-shaped plates and other morphologies of nanogels could also be achieved by the suspension of the self-assembled evolution within a predetermined time. Mentioned that the interrupted nanogels could basically maintain their shapes and sizes for more than 3 days in mild environments, which provided a simple and universe approach to yield the conceivable self-assembled nanogels with customized structures and properties through manipulation of the UV switcher within the appointed irradiation time.

The thiol-disulfide exchange mechanism can be utilized to interpret the morphology evolution as a "living" controlled process as depicted in **Scheme 2**. For the disulfide-linked star-shaped POSS-$(SS\text{-}PEG)_8$ molecule, UV irradiation could active the thiyl radicals to attack the disulfide linkages within the polymer chains and trigger the exchange reaction in extramolecular disulfides or inner radical combinations, which resulted in the connection of two isolated polymers along with the escape of two well-soluble PEG chains that were regarded as good leaving groups in aqueous solutions. The driving force ascribed to the shifting of the equilibrium toward the stable cross-linked nanogels by the detachment of hydrophilic

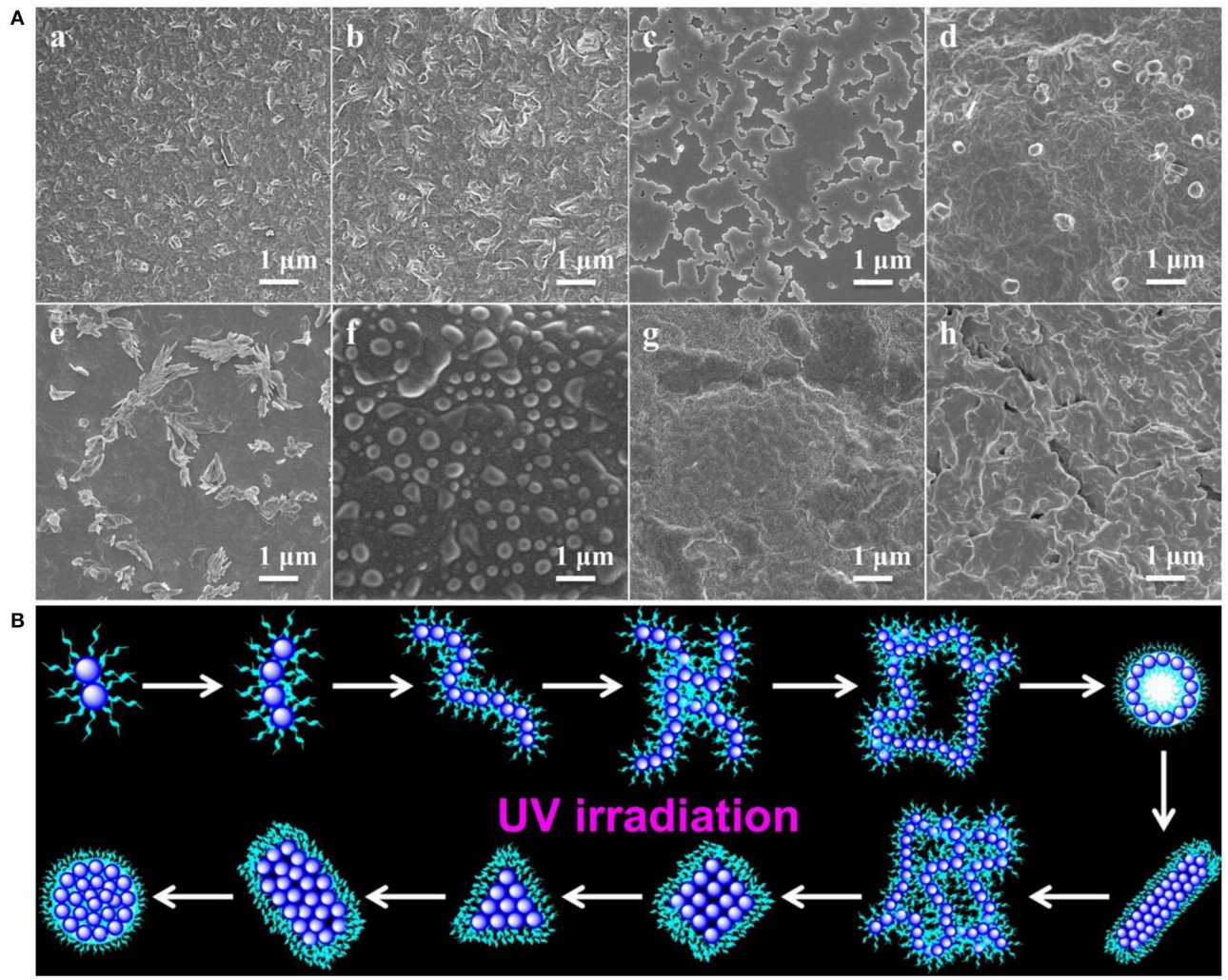

FIGURE 3 | (A) SEM images showing morphology and size evolution with a concentration of 1 mg/mL aqueous media under UV irradiation at (a) 1, (b) 2, (c) 4, (d) 8, (e) 12, (f) 24, (g) 36 and (h) 48 h; **(B)** Schematic representation of morphological evolution.

PEG shells. After a greater degree of thiol-disulfide exchange reactions, more and more crosslinking POSS cores rupturing of PEG segments were induced so as to sustainably decrease the star-shaped polymeric hydrophilicity and cause the regular morphological transition simultaneously. Notice that unlike the flexible hydrophobic polymers to tangle with each other, the POSS-linked cores were rigid and not easy to deformation to decline the free energy of system. So once the re-arrangement of hydrophilic and hydrophobic segments was launched, the repulsive force would compel the multi-architectonical rigid cores to keep spatial distance with adjacent giant POSS molecules, which inevitably enlarged their own hydrophobic spatial areas in spite of no alteration of the hydrophobic components. In other words, although the hydrophilic/hydrophobic ratios had not been changed severely in a period of time, the spatial conformational cores may produce great self-enhancement of hydrophobicity. Therefore, a slight variation of hydrophobic POSS contents and geometries was apt to result in a distinct morphology transition that was consistent with Yan's work (Jin et al., 2012). Besides, the unique POSS aggregation ability brought about the liable axial growth of assemblies, resulting in the emergence and growth of cylinders initially. However, longer UV irradiation may destroy the disulfide linkages so that the cluster nanostructures could dissociate into some kinds of shuttle-shaped sheets or small fragments. Therefore, under the synergistic effects of random thiol-disulfide exchange and photodegradation, many unusual and inconceivable morphology of nanogels came along successively like square, triangle-shaped, rhombus-shaped and silkworm nanoparticles. Based on the above analysis, we concluded that the effects of such unique self-assembly behaviors were mainly depended on below four key factors: ever-changing hydrophobic/hydrophilic ratio, rigid POSS-embedded topology, strong POSS aggregation ability and unpredictable degradation.

High loading efficiency and stimuli-responsive property of the nanogel carriers were two pivotal factors for creation

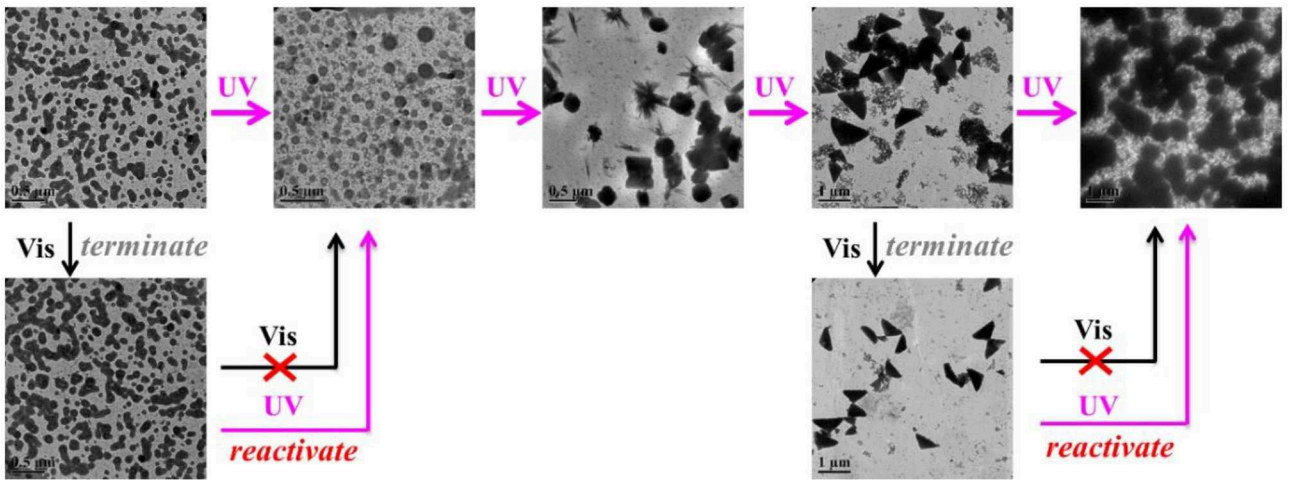

FIGURE 4 | TEM images of *in situ* morphology evolution with UV-responsive "on/off" reaction function.

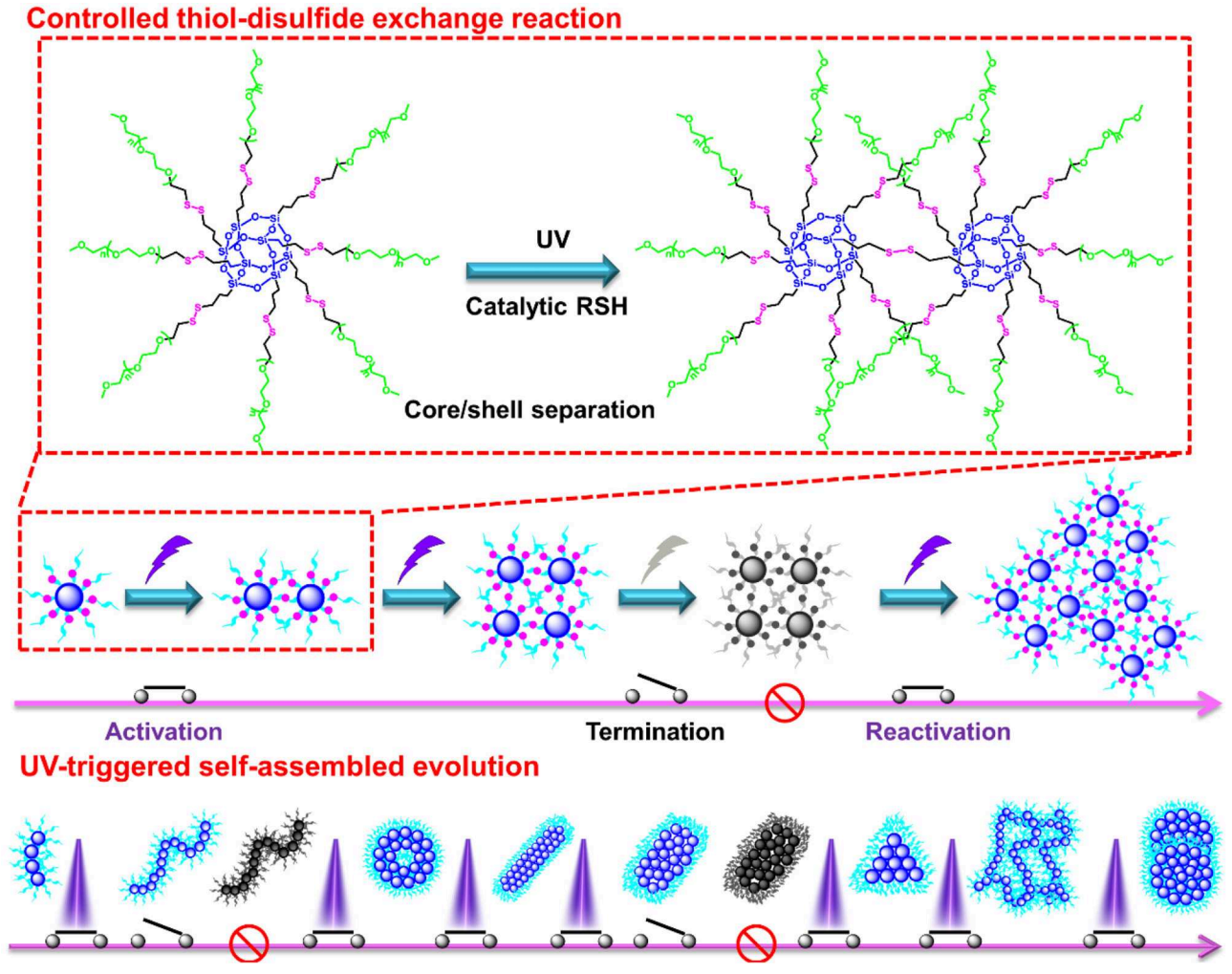

SCHEME 2 | Possible self-assembled mechanism of morphology evolution of nanogels by a UV-switched thiol-disulfide exchange reaction.

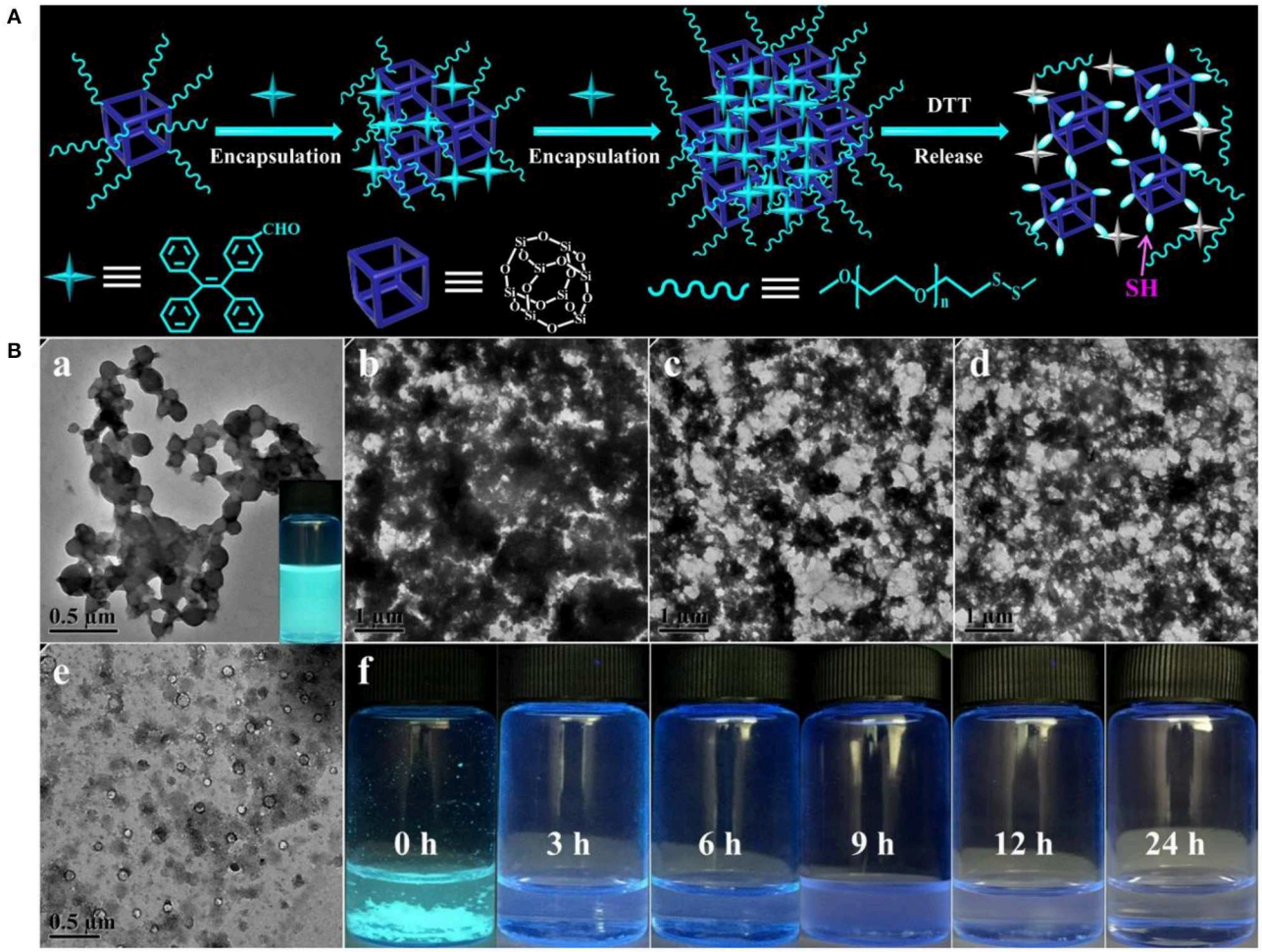

FIGURE 5 | (A) Schematic mechanism of the encapsulation, separation and release of TPE-CHO molecules in the process of self-assembled morphology evolution. **(B)** TPE-encapsulated aggregates in the THF/H_2O mixture containing 10 mM concentration of reductive DTT with the various soaking time.

of a robust biomedical platform in targeted drug delivery (Guan et al., 2016). On account of the thiol-disulfide exchange reaction that can induce the ever-improving hydrophobicity of the assemblies, TPE-CHO, as a hydrophobic AIE probe, was employed to quantitatively assess the encapsulation and separation efficiency, as schemed in **Figure 5A**. When the TPE-CHO molecules were added into the THF/H_2O mixture containing the POSS-$(SS\text{-}PEG)_8$ molecules, the solution emitted weak fluorescence due to that the TPE-CHO has not efficient capacity to achieve the critical aggregate state of AIE effects. Along with the activation and process of morphology evolution, more and more hydrophobic molecules were gradually encapsulated and aggregated into the self-assembled nanogels due to the strong hydrophobic interactions, leading to the enhancement of fluorescent intensity with obvious AIE attributes (**Figure 5B-a**). After incubation for more than 24 h, the hydrophobicity of aggregates was dramatically increased and thus the precipitates were slowly formed as observed in **Figure 5B-f**, which meant the full encapsulation of TPE-CHO molecules into the polymeric nanogels, exhibiting the excellent encapsulation ability for hydrophobic molecules. More importantly, these encapsulated hydrophobic molecules can be separated from the aggregates by resolution of precipitates into good solvents (THF or $CHCl_3$) and further recycled by precipitation and centrifugation methods.

The formation of nanogels was attributed to the POSS cores connected by built-up disulfide linkages; therefore, these self-assembled nanoparticles were biodegradable since disulphide bonds could be cleaved by dithiothreitol (DTT). Here, we further evaluated the degradation behavior of the eventually disulphide-linked nanogels in THF/H_2O mixture containing 10 mM of DTT. On account of the numerous disulfides throughout the backbone of self-assembled nanogels, high concentration of reductive DTT can quickly damage the disulfide bonds to thiol groups and lead to the rapid disruption of aggregates (**Figure 5B**). As the TPE-loaded aggregates were under high level of reductive solutions, TPE molecules escaped from the disulfide-linked assembled nanogels and the aggregates transferred into the

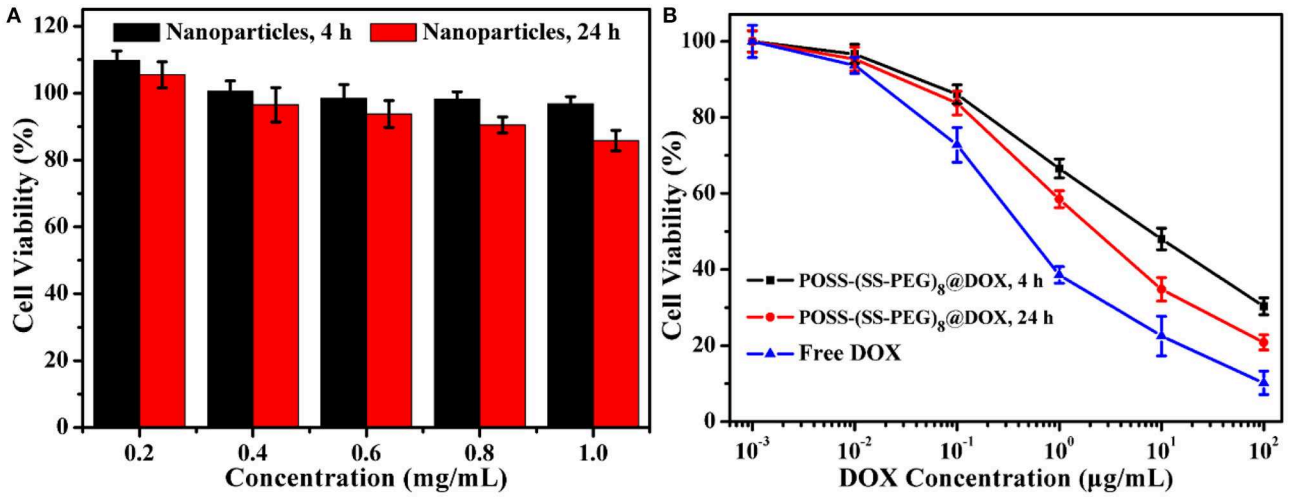

FIGURE 6 | (A) Cytotoxicity of two typical kinds of POSS-$(SS\text{-}PEG)_8$ nanoparticles (after exchange reaction under UV irradiation for 4 and 24 h) to MCF-7 cells following 24 h incubation ($n = 5$ per group). **(B)** Viability assessment of MCF-7 cells with POSS-$(SS\text{-}PEG)_8$@DOX aggregates (after exchange reaction under UV irradiation for 4 and 24 h) and free DOX as a function of DOX dosages. All the data were presented as the average ± standard deviation.

fiber clusters and small vesicles along with the bankrupt of AIE phenomenon, which was intuitively observed from the fluorescent solution (0 h) to turbid solution (3 h) and then to the clear solutions (24 h). Based on the above analysis, we found that although these new molecular constitutes were different from the previous amphiphiles, DTT-induced structural variation can still be understood as a disassembly-induced morphology and size evolution, after all, it triggered the disassembled morphology transition, which would be promising for developing advanced materials for sustained drug delivery system, diagnostic sensor, sensitive detector and opto-electronic transmission.

Similarly, the antitumor DOX drugs were also encapsulated into the nanogels. For example, to overcome the incompatible alkaline environments for living cells, we utilized the *in situ* light-triggered thiol-disulfide exchange reaction with irradiation time of 4 and 24 h. As the exchange reaction induced the continuous improvement of hydrophobic/hydrophilic ratio and variation of architectural topology, the drug loading efficiency could achieve 38.1 and 57.8%. Cytotoxicity of POSS-$(SS\text{-}PEG)_8$ nanogel carriers (exchange reaction for 4 and 24 h) was investigated by the MCF-7 cells following 24 h of incubation. These two groups exhibited low toxic to MCF-7 cells on account of their biodegradable behaviors with the exposure into high levels of reductive agents. **Figure 6A** showed that the cell viability was more than 87% even in a concentration of 1.0 mg/mL, presenting the good biocompatibility of nanoparticles. In addition, the viability was also evaluated with two typical POSS-$(SS\text{-}PEG)_8$@DOX aggregates (exchange reaction for 4 and 24 h) and free DOX as a function of DOX dosage using the MCF-7 cells. **Figure 6B** displayed that these DOX-loaded nanoparticles possessed high efficiency in cancer cell inhibition. In a low concentration, two DOX-loaded nanoparticles had a similar toxicity as free DOX, but a high concentration of self-assembled nanogel carriers had to be endocytosed to enter the MCF-7 cells, which made free DOX molecules rapider than DOX-loaded aggregates in the whole internalization process.

CONCLUSIONS

In conclusion, we reported a feasible manipulation strategy of self-assembled evolution of nanogels *in situ* using the "living" controlled thiol-disulfide exchange reaction and hierarchically self-assembly behaviors of amphiphilic POSS-$(SS\text{-}PEG)_8$ polymer. Careful tailoring UV-triggered exchange reaction, the optimal morphology and size evolutions were well-performed, exhibiting the unimolecular, spherical, cylindrical and worm-like micelles, vesicles, rhombus, triangle and square-shaped nanosheets, cluster fibers, hollow spheres and dense nanospheres as well as the gradually dimensional growth process, which ascribed to the sequentially increscent hydrophobic/hydrophilic ratio, variably rigid POSS-embedded topologies and specific POSS aggregation ability. Notably, this morphology and size evolution could be suspended and reactivated as needed at any point of time by simple removal of external UV switcher, and thus the desirable nanogels with various morphologies and sizes were easily gained with good long-term stability in dilute aqueous solutions. The improvement of hydrophobic/hydrophilic ratio endowed these variational assembled nanogels with excellent loading and separation capacities of hydrophobic molecular cargoes. Besides, a large number of disulfide bonds could be degraded under the highly reductive environments, by which the encapsulated molecules were quickly released and the aggregates performed a disassembly-induced morphology evolution. Based on this artificial process technologies, these screened redox-responsive colloidal nanogels have been enabled to fabrication of polymeric nanogel carriers in applications of cancer therapy. This intriguing "living" controlled assembled strategy on fabrication

of morphology and size evolution of nanogels is also applicable for other disulfides-linked amphiphilic polymers, which will provide a useful guidance for delicately spatiotemporal control over the artificial superstructures and desired properties of disulfide-crosslinked nanogel carriers. We believe that these simple and smart drug delivery systems could bring about a thorough understanding of complex dynamic process for the amphiphiles nanogels.

DATA AVAILABILITY STATEMENT

The datasets generated for this study are available on request to the corresponding author.

AUTHOR CONTRIBUTIONS

DL, XW, and JZho designed and initiated the research. WB and JL analyzed the data, wrote a draft of the manuscript and completed the biological security of polymeric micelles and DOX-loaded nanoparticles. WB and XW synthesized and characterized amphiphilic polymers. CL, JZha, and TS made important suggestions and helped revising the paper. All authors contributed to discussions on the results and to the finalization of the manuscript.

FUNDING

This research was funded by the Science Research Program of Inner Mongolia University for Nationalities (NMDYB17132), National Natural Science Foundation of China (NSFC, 21604093, 81972081, and 51973226) and the Beijing Novel Program (Z181100006218059).

SUPPLEMENTARY MATERIAL

The Supplementary Material for this article can be found online at: https://www.frontiersin.org/articles/10.3389/fchem.2019.00769/full#supplementary-material

REFERENCES

Dong, X. H., Ni, B., Huang, M., Hsu, C. H., Bai, R., Zhang, W. B., et al. (2016). Molecular-curvature-induced spontaneous formation of curved and concentric lamellae through nucleation. *Angew. Chem. Int. Ed*. 55, 2459–2463. doi: 10.1002/anie.201510524

Gröschel, A. H., Walther, A., Löbling, T. I., Schacher, F. H., Schmalz, H., and Müller, A. H. (2013). Guided hierarchical co-assembly of soft patchy nanoparticles. *Nature* 503, 247–251. doi: 10.1038/nature12610

Guan, M., Ge, J. C., Wu, J., Zhang, G., Chen, D., Zhang, W., et al. (2016). Fullerene/photosensitizer nanovesicles as highly efficient and clearable phototheranostics with enhanced tumor accumulation for cancer therapy. *Biomaterials* 103, 75–85. doi: 10.1016/j.biomaterials.2016.06.023

Hunt, S. T., Milina, M., Alba-Rubio, A. C., Hendon, C. H., Dumesic, J. A., and Román-Leshkov, Y. (2016). Self-assembly of noble metal monolayers on transition metal carbide nanoparticle catalysts. *Science* 352, 974–978. doi: 10.1126/science.aad8471

Jin, H. B., Huang, W., Zhu, X. Y., Zhou, Y. F., and Yan, D. Y. (2012). Biocompatible or biodegradable hyperbranched polymers: from self-assembly to cytomimetic applications. *Chem. Soc. Rev*. 41, 5986–5997. doi: 10.1039/c2cs35130g

Lee, H. B., Bae, C. W., Duy, L. T., Sohn, I. Y., Kim, D. I., Song, Y. J., et al. (2016). Mogul-patterned elastomeric substrate for stretchable electronics. *Adv. Mater*. 28, 3069–3077. doi: 10.1002/adma.201505218

Li, D. W., Niu, Y., Yang, Y., Wang, X., Yang, F., Shen, H., et al. (2015). Synthesis and self-assembly behavior of POSS-embedded hyperbranched polymers. *Chem. Commun*. 51, 8296–8299. doi: 10.1039/C5CC01338K

Mason, T. O., Michaels, T. C., Levin, A., Gazit, E., Dobson, C. M., Buell, A. K., et al. (2016). Synthesis of nonequilibrium supramolecular peptide polymers on a microfluidic platform. *J. Am. Chem. Soc*. 138, 9589–9596. doi: 10.1021/jacs.6b04136

Newkome, G. R., and Moorefield, C. N. (2015). From 1→3 dendritic designs to fractal supramacromolecular constructs: understanding the pathway to the Sierpinski gasket. *Chem. Soc. Rev*. 44, 3954–3967. doi: 10.1039/C4CS00234B

Ni, B., Huang, M., Chen, Z., Chen, Y., Hsu, C. H., Li, Y., et al. (2015). Pathway toward large two-dimensional hexagonally patterned colloidal nanosheets in solution. *J. Am. Chem. Soc*. 137, 1392–1395. doi: 10.1021/ja511694a

Palivan, C. G., Goers, R., Najer, A., Zhang, X., Car, A., and Meier, W. (2016). Bioinspired polymer vesicles and membranes for biological and medical applications. *Chem. Soc. Rev*. 45, 377–411. doi: 10.1039/C5CS00569H

Qian, Q. Y., Xu, J., Zhang, M. Z., He, J. L., and Ni, P. H. (2019). Versatile construction of single-tailed giant surfactants with hydrophobic poly(ε-caprolactone) tail and hydrophilic POSS head. *Polymers* 11:311. doi: 10.3390/polym11020311

Stefik, M., Guldin, S., Vignolini, S., Wiesner, U., and Steiner, U. (2015). Block copolymer self-assembly for nanophotonics. *Chem. Soc. Rev*. 44, 5076–5091. doi: 10.1039/C4CS00517A

Tan, K. W., Jung, B., Werner, J. G., Rhoades, E. R., Thompson, M. O., and Wiesner, U. (2015). Transient laser heating induced hierarchical porous structures from block copolymer–directed self-assembly. *Science* 349, 54–58. doi: 10.1126/science.aab0492

Wang, X., Gao, P., Yang, Y., Guo, H., and Wu, D. (2018a). Dynamic and programmable morphology and size evolution via a living hierarchical self-assembly strategy. *Nat. Commun*. 9:2772. doi: 10.1038/s41467-018-05142-3

Wang, X., Li, D., Yang, F., Shen, H., Li, Z. B., and Wu, D. C. (2013). Controlled cross-linking strategy: from hybrid hydrogels to nanoparticle macroscopic aggregates. *Polym. Chem*. 4, 4596–4600. doi: 10.1039/c3py00811h

Wang, X., Yang, Y., Zuo, Y., Yang, F., Shen, H., and Wu, D. (2016). Facile creation of FRET systems from a pH-responsive AIE fluorescent vesicle. *Chem. Commun*. 52, 5320–5323. doi: 10.1039/C6CC01706A

Wang, X., Yang, Y. Y., Fan, L. F., Yang, F., and Wu, D. C. (2018b). POSS-embedded supramolecular hyperbranched polymers constructed from a 1→ 7 branching monomer with controllable morphology transitions. *Sci. China Chem*. 61, 311–318. doi: 10.1007/s11426-017-9168-3

Wang, X., Yang, Y. Y., Gao, P. Y., Yang, F., Shen, H., Guo, H. X., et al. (2015). Synthesis, self-assembly and photoresponsive behavior of tadpole-shaped azobenzene polymers. *ACS Macro Lett*. 4, 1321–1326. doi: 10.1021/acsmacrolett.5b00698

Wu, D. C., Loh, X. J., Wu, Y. L., Lay, C. L., and Liu, Y. (2010). 'Living' controlled *in situ* gelling systems: thiol-disulfide exchange method towards tailor-made biodegradable hydrogels. *J. Am. Chem. Soc*. 132, 15140–15143. doi: 10.1021/ja106639c

Xia, D., Wei, P., Shi, B., and Huang, F. (2016). A pillar [6] arene-based [2] pseudorotaxane in solution and in the solid state and its photo-responsive self-assembly behavior in solution. *Chem. Commun*. 52, 513–516. doi: 10.1039/C5CC08038J

Yang, Y., Wang, X., Yang, F., Wang, L., and Wu, D. C. (2018). Highly elastic and ultratough hybrid ionic-covalent hydrogels with tunable structures and mechanics. *Adv. Mater*. 30:1707071. doi: 10.1002/adma.201707071

Zhang, J., Li, X., Li, Y., Wang, H., Ma, C., Wang, Y. Z., et al. (2018). Cross-linked nanohybrid polymer electrolytes with POSS cross-linker for solid-state lithium ion batteries. *Front. Chem.* 6:186. doi: 10.3389/fchem.2018.00186

Zhang, J., Yang, F., Shen, H., and Wu, D. C. (2012). Controlled formation of microgels/nanogels from a disulfide-linked core/shell hyperbranched polymer. *ACS Macro Lett*. 1, 1295–1299. doi: 10.1021/mz300489n

Zhang, W. A., and Muller, A. H. E. (2013). Architecture, self-assembly and properties of well-defined hybrid polymers based on polyhedral oligomeric silsequioxane (POSS). *Prog. Polym. Sci.* 38, 1121–1162. doi: 10.1016/j.progpolymsci.2013.03.002

Conflict of Interest: The authors declare that the research was conducted in the absence of any commercial or financial relationships that could be construed as a potential conflict of interest.

frontiers in Chemistry

REVIEW
published: 06 March 2020
doi: 10.3389/fchem.2020.00124

Recent Advances on Magnetic Sensitive Hydrogels in Tissue Engineering

Zhongyang Liu[1,2†], *Jianheng Liu*[1,2†], *Xiang Cui*[1,2†], *Xing Wang*[3*], *Licheng Zhang*[1,2*] and *Peifu Tang*[1,2*]

[1] Department of Orthopedics, Chinese PLA General Hospital, Beijing, China, [2] National Clinical Research Center for Orthopedics, Sports Medicine and Rehabilitation, Beijing, China, [3] Beijing National Laboratory for Molecular Sciences, Institute of Chemistry, Chinese Academy of Sciences, Beijing, China

Tissue engineering is a promising strategy for the repair and regeneration of damaged tissues or organs. Biomaterials are one of the most important components in tissue engineering. Recently, magnetic hydrogels, which are fabricated using iron oxide-based particles and different types of hydrogel matrices, are becoming more and more attractive in biomedical applications by taking advantage of their biocompatibility, controlled architectures, and smart response to magnetic field remotely. In this literature review, the aim is to summarize the current development of magnetically sensitive smart hydrogels in tissue engineering, which is of great importance but has not yet been comprehensively viewed.

Keywords: magnetic particle, magnetic hydrogel, magnetic field, tissue engineering, functional recovery

OPEN ACCESS

Edited by:
Clemens Kilian Weiss, Fachhochschule Bingen, Germany

Reviewed by:
Rocktotpal Konwarh, Addis Ababa Science and Technology University, Ethiopia
Vincenzo Guarino, Italian National Research Council, Italy
Emilio Isaac Alarcon, University of Ottawa, Canada

***Correspondence:**
Xing Wang
wangxing@iccas.ac.cn
Licheng Zhang
zhanglcheng218@126.com
Peifu Tang
pftang301@163.com

[†] *These authors have contributed equally to this work*

Specialty section:
This article was submitted to Polymer Chemistry, a section of the journal Frontiers in Chemistry

Received: *20 September 2019*
Accepted: *10 February 2020*
Published: *06 March 2020*

Citation:
Liu Z, Liu J, Cui X, Wang X, Zhang L and Tang P (2020) Recent Advances on Magnetic Sensitive Hydrogels in Tissue Engineering. Front. Chem. 8:124. doi: 10.3389/fchem.2020.00124

INTRODUCTION

Tissue engineering, a branch of regenerative medicine, refers to the application of supporting cells, material scaffolds, bioactive molecules, or their combinations to repair and reconstruct tissues and organs. Hydrogels have been shown to be one of the most applicable biomaterials in tissue engineering (Kabu et al., 2015; Madl et al., 2017, 2019; Deng et al., 2019) mainly attributed to their inner 3D network microstructures, moderate biocompatibility, and good water content feature, which are analogous with those of the natural tissue (Cui Z.K. et al., 2019; Zhu et al., 2019). Meanwhile, hydrogel-based drug delivery systems for numerous therapeutic agents, with high water content, low interfacial tension with biological fluids, and soft consistency, have been shown to be more stable, economical, and efficient in comparison with conventional delivery systems (Li and Mooney, 2016; Moore and Hartgerink, 2017; Cheng et al., 2019; Fan et al., 2019; Zheng et al., 2019). Considering the above advantages, hydrogels have been conducted into the biomedical application to provide a tunable three-dimensional scaffold for cell adhesion, migration, and/or differentiation, and they could also be designed as the platform for the controlled release of cytokines and drugs in tissue engineering and drug delivery (Huang et al., 2017; Jiang et al., 2017; Hsu et al., 2019; Wei et al., 2019; Zheng et al., 2019).

Hydrogel first appeared in a literature as early as in 1894 (Van Bemmelen, 1894); however, the "hydrogel" described at that time was not the same form of hydrogels used nowadays; it was a type of a colloidal gel made from inorganic salts. Later on, the term "hydrogel" was applied for describing a 3D network of hydrophilic native polymers and gums by physical or chemical crosslinking approaches, and its application heavily relied on water availability in the environment (Lee et al., 2013). The current generation of hydrogel in the biological field was first performed by

Wichterle and LÍm (1960), indicating that glycoldimethacrylate-based hydrophilic gels exhibited adjustable mechanical properties and water content. From then on, more and more hydrogels have been developed, and the smart hydrogels were then introduced in different fields of biological science, such as drug delivery, bioseparation, biosensor, and tissue engineering. Smart hydrogels are described as they respond directly to the changes of environmental conditions (Wichterle and LÍm, 1960), and numerous studies of smart hydrogels in the applications of nanotechnology, drug delivery, and tissue engineering have been put into effect in the last few decades (Li X. et al., 2019; Li Z. et al., 2019; Zhang Y. et al., 2019).

Recently, magnetically responsive hydrogel, as one kind of smart hydrogels, has been introduced into biomedical applications in improving the biological activities of cells, tissues, or organs. This is mainly attributed to its magnetic responsiveness to external magnetic field and obtaining functional structures to remotely regulate physical, biochemical, and mechanical properties of the milieu surrounding the cells, tissues, or organs (Abdeen et al., 2016; Antman-Passig and Shefi, 2016; Rodkate and Rutnakornpituk, 2016; Bannerman et al., 2017; Omidinia-Anarkoli et al., 2017; Xie et al., 2017; Silva et al., 2018; Tay et al., 2018; Wang et al., 2018; Bowser and Moore, 2019; Ceylan et al., 2019; Luo et al., 2019). Recent studies have represented that magnetic hydrogel could act as an excellent drug release and targeting system. For example, Gao et al. (2019) fabricated a magnetic hydrogel based on ferromagnetic vortex-domain iron oxide and suggested that this unique magnetic hydrogel could significantly suppress the local breast tumor recurrences. Manjua et al. (2019) developed magnetic responsive poly(vinyl alcohol) (PVA) hydrogels, which could be motivated by ON/OFF magnetic field and non-invasively regulated protein sorption and motility, indicating a promising application for tissue engineering, drug delivery, or biosensor system. Moreover, a composite magnetic hydrogel prepared by a combination of a self-healing chitosan/alginate hydrogel and magnetic gelatin microspheres could be used as a suitable platform for tissue engineering and drug delivery (Chen X. et al., 2019a). In comparison with magnetic hydrogels, various kinds of smart biomaterials (e.g., scaffolds, biofilms, other smart hydrogels), which are activated by external stimuli, such as light, pH, temperature, stress, or charge, have great potential in biomedical applications (Chen H. et al., 2019; Cui L. et al., 2019; Wu C. et al., 2019; Zhao et al., 2019; Yang et al., 2020). However, the long response time and less precisely controlled architectures of these stimuli-responsive smart biomaterials are the two main limitations.

Magnetic hydrogels are usually made of a matrix hydrogel and a magnetic component that was incorporated into the matrix. Recently, superparamagnetic and biocompatible iron oxide-based magnetic nanoparticles (MNPs) are most commonly incorporated into polymer matrices to prepare magnetically responsive hydrogels for their application in tissue engineering, such as γ-Fe_2O_3, Fe_3O_4, and cobalt ferrite nanoparticles ($CoFe_2O_4$) (Zhang and Song, 2016; Rose et al., 2017; Ceylan et al., 2019). Magnetite (Fe_3O_4) is a compound of two kinds of iron sites with 1/3 of Fe^{2+} and 2/3 of Fe^{3+}. The intervalence charge transfer between Fe^{2+} and Fe^{3+} induces absorption throughout the ultraviolet–visible spectral region and the infrared spectral region, which generates a black appearance in color (Barrow et al., 2017). Maghemite (γ-Fe_2O_3), with a brown-orange color pattern, is an oxidative product of magnetite (Fe_3O_4) when the temperature is below 200°C (Tang et al., 2003). In terms of $CoFe_2O_4$, previous studies have shown that the concentration of 20% was toxic, whereas at 10% the toxicity was insignificant. Moreover, 10% (w/w) of $CoFe_2O_4$ could maximize magnetic response because of numerous amounts of nanoparticles, developing biocompatible biomaterials (Goncalves et al., 2015; Brito-Pereira et al., 2018). For example, Hermenegildo et al. (2019) designed a novel $CoFe_2O_4$/Methacrylated Gellan Gum/poly(vinylidene fluoride) hydrogel, which created a promising microenvironment for tissue stimulation.

In this literature review, we aim to summarize the preparation methods and current development of magnetically sensitive smart hydrogels in tissue engineering, especially in bone, cartilage, and neural tissue engineering, which are of great importance but have not yet been comprehensively reviewed.

THE FABRICATION PROCESSING OF MAGNETIC HYDROGELS

Magnetic hydrogels are made of composite materials that possess biocompatibility, biodegradation, and magnetic responsiveness. The characteristics of magnetic hydrogels depend upon several issues, including the magnetic particles and the component of hydrogels used, the magnetic particles and hydrogels' concentration, and the size and uniformity of magnetic particles within the hydrogels. There are mainly three preparation methods of fabricating magnetic hydrogels: (**i**) blending method; (**ii**) *in situ* precipitation method; (**iii**) grafting-onto method (**Table 1**). The scheme for the main three syntheses of the magnetic hydrogels is shown in **Figure 1**.

The Blending Method

In the blending approach, magnetic particles, and hydrogels are fabricated separately. The magnetic particles are normally synthesized using a coprecipitation process. The resulting magnetic particles are then stored in an aqueous or oily liquid to prevent aggregation and oxidization. Finally, the solution of magnetic particles is mixed with the hydrogel solution for crosslinking, and the magnetic particles are encapsulated into the hydrogels. Tóth et al. (2015) modified the surface of MNPs (magnetite) with biocompatible chondroitin-sulfate-A (CSA) to develop CSA-coated MNPs. Then, CSA-coated MNPs were dispersed into hyaluronate (HyA) hydrogel to prepare the HyA-based magnetic hydrogel. It was found that the HyA-based magnetic hydrogel could be conducted in the treatment of osteoarthritis by the intra-articular injection approach. Shi et al. (2019) fabricated bisphosphonate (BP)-modified hyaluronic acid (HA)/Fe_3O_4 magnetic hydrogel. This novel magnetic hydrogel showed outstanding compatibility and slow degradation *in vivo* and held the expectation of safety in clinic usage.

TABLE 1 | The preparation methods of magnetic hydrogels and the parameters of magnetic field in representative references.

Method	Magnetic particles	Hydrogels	Magnetic particle concentration	Physiochemical properties	Magnetic field	References
Blending method	Fe_3O_4	Bisphosphonate-modified HA	2 w/v%	Proper rheology and fast heat-generation	Alternating magnetic field	Shi et al., 2019
	Fe_3O_4	Chitosan/PEG	0–40 wt%	Nanoheat	Alternating magnetic field	Cao et al., 2018
	Fe_3O_4	NIPAAM-MAA	2.5 mg/mL	Uniform distribution of particles	–	Namdari and Eatemadi, 2017
	Fe_2O_3	Poly(vinyl alcohol)/n-HAP	4 wt%	High water content and good elasticity	–	Huang J. et al., 2018
	Magnetite	Hyaluronate hydrogel	0.2, 2.0 g/L	Stable and homogeneous dispersion in 3 months	–	Tóth et al., 2015
	Magnetite	Collagen	0.5 mg/mL	Aligned collagen fibers and normal electrical activity	Magnet (255 G)	Antman-Passig and Shefi, 2016
	Dextran iron oxide composite particles (Micromod®)	Agarose	20 wt% (surface) 7 wt% (middle) 10 wt% (deep)	Gradients in compressive modulus	Rare earth NdFeB magnets (0.4, 0.5, or 0.75 T; E-Magnets®)	Brady et al., 2017
	Streptavidin-coated magnetic particles	Agarose/collagen	10 v/v%	Mimicking the native multilayered tissues	Magnet (2 mT)	Betsch et al., 2018
	Nano-HAP-coated γ-Fe_2O_3 nanoparticles (m-nHAP)	Poly(vinyl alcohol)	0–80 wt%	Linearly saturated magnetic strength and porous structures, homogenous dispersion of m-nHAP and improved compressive strength	–	Hou et al., 2013
	PEG-functionalized iron oxide (II, III) nanoparticles	PEG hydrogel (modified with factor XIIIa)	1 mg/mL	Smooth inner gel texture, slow relaxation kinetics, and high elastic modulus	Neodymium magnets (50 mT)	Filippi et al., 2019
	MNPs	Collagen	–	Bio-mimetic 3D structures	Static magnetic fields	Yuan et al., 2018
	MNPs	Poly(lactide-co-glycolide)	1, 5, and 10 wt%	Homogenous distribution of MNPs and linear structures	Standard cuvette Magnets (100–300 mT)	Omidinia-Anarkoli et al., 2017
	MNPs	Six-arm star-PEG-acrylate	0.0046 vol%	Unidirectional structures and high controlled properties	Magnets (100, 130, and 300 mT)	Rose et al., 2017
	MNPs	RGD peptides modified alginate	7 wt%	Fatigue resistance	Magnet (6,510 G, 1 Hz)	Cezar et al., 2016
	MNPs	GRGDSPC peptides/six-arm PEG-acrylate	400 μg/mL	Tailed properties	Magnet (150 mT)	Rose et al., 2018
In situ precipitation method	Fe_3O_4	Chitosan	0–15 wt%	Uniform distribution of MNPs and enhanced mechanical properties	Low frequency magnetic field (60 Hz)	Wang et al., 2018
	Polydopamine-chelated carbon nanotube-Fe_3O_4	Acrylamide	0–15 wt%	Directional conductive and mechanical properties	Low static magnetic field (30 mT)	Liu et al., 2019
	Dextran-coated Fe_3O_4	Bacterial cellulose	25–100 mM	Magnetization saturation (10 emu/g) and moderate Young's modulus (200–380 KPa)	Neodymium magnets (0.3 T)	Arias et al., 2018

(Continued)

TABLE 1 | Continued

Method	Magnetic particles	Hydrogels	Magnetic particle concentration	Physiochemical properties	Magnetic field	References
Grafting-onto method	$CoFe_2O_4$	Polyacrylamide	–	High stability and homogeneity	–	Messing et al., 2011
	Poly(vinyl alcohol) modified Fe_3O_4	Hybrid hydrogel (containing HA, collagen, and PEG)	4 wt%	Increased surface roughness and biodegradation	Magnet	Zhang et al., 2015
	3-(trimethoxysilyl)propyl methacrylate coated Fe_3O_4	Polyacrylamide	20–60% (with respect to the total weight of the hydrogels and water)	High mechanical properties and excellent underwater performance (polydimethylsiloxane coating)	–	Hu et al., 2019
	Carboxyl-coated Nanomag® superparamagnetic nanoparticles (Micromod®)	RGD-tripeptide; TREK1-antibody	–	–	Mica Biosystem bioreactor	Henstock et al., 2014
	Saline modified carbonyl iron particles	Polyacrylamide	–	Elastic hysteresis	Alternating magnetic field	Abdeen et al., 2016
	Glycosylated MNPs	Agarose	10^{11} glycosylated MNPs in 100 μL 1 wt% agarose hydrogel	MNPs-gradient magnetic hydrogel	Finite element magnetic modeling	Li et al., 2018
	Methacrylated chondroitin sulfate (MA-CS)-MNPs	MA-CS enriched with platelet lysate	200 and 400 μg/mL	Homogenous trabecular structures and high storage modulus	Oscillating magnet array system	Silva et al., 2018
	Kartogenin (KGN) grafted ultrasmall superparamagnetic iron oxide	Cellulose nanocrystal/dextran hydrogel	0.06–0.3 wt%	Good mechanical strength, long-term sustained KGN release, and stable MRI capabilities	–	Yang et al., 2019
	PEG-magnetic microparticles	Thiolated HA	–	Uniform distribution of MMPs and mimicking the native tissue ECM	Applied magnetic field (2 T)	Tay et al., 2018

The blending method has several advantages in the preparation of magnetic hydrogels. Firstly, magnetic particles (e.g., MNPs, micrometer-iron oxides) with homogenous size in hydrogels can be obtained by modifying the stirring speed, the concentration of the substances, and the fabrication period. Secondly, the preparation process is easy to be performed since the preparation and crosslinking of magnetic particles are conducted separately. However, there are also some limitations that could be addressed in the future, including the asymmetric distribution of magnetic particles within the hydrogels and the diffusion of magnetic particles when the magnetic hydrogels were submerged in a solution.

In situ Precipitation Method

In the process of the *in situ* precipitation, the network of the hydrogels acts as a chemically reactive substance, within which the iron ions from inorganic salts in hydrogels react with alkali solutions (e.g., $NH_3{\cdot}H_2O$, NaOH; Arias et al., 2018; Liu et al., 2019) to prepare the magnetic particles. In detail, the hydrogels are firstly prepared through polymerization, temperature change, or a crosslinking reaction. Then, magnetite precursors containing iron(III) and iron(II) at a molar ratio of 1:2 are added into the hydrogels to obtain a homogenous solution. Finally, the mixture is immersed in an alkali solution to induce the crystallization of magnetite. The magnetic particles are incorporated into the hydrogels according to the following hydrolytic reaction ($2\ Fe^{3+} + Fe^{2+} + OH- \rightarrow Fe_3O_4 + 4\ H_2O$). Wang et al. (2018) designed a magnetic chitosan hydrogel by adding MNPs via *in situ* synthesis during chitosan hydrogel formation. The resulting magnetic hydrogel showed a magnetic response and improved morphological and mechanical features, including the homogenous distribution of MNPs and excellent wettability. Moreover, the mechanical properties (such as the compression strength, the yield strength, and the probe displacement) of the magnetic hydrogel was enhanced with the rising concentration of MNPs from 0 to 15 wt%, which was attributed to the crosslinking role of MNPs in the process. Under low-frequency alternating magnetic field (LAMF) exposure, the magnetic hydrogel laden with drugs exhibited a pulsatile drug release profile. In addition, the *in situ* fabricated MNPs in the magnetic hydrogel had excellent biocompatibility and no acute toxicity on MG-63 cells (human osteosarcoma cell line). Liu et al. (2019) fabricated

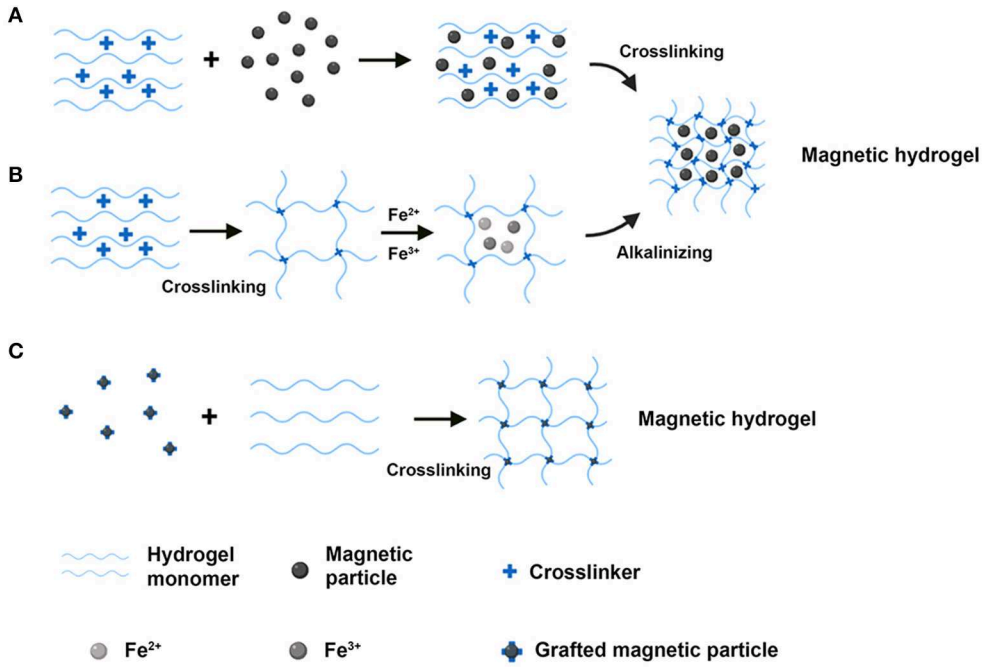

FIGURE 1 | The schematic diagram of the main three routes for the synthesis of the magnetic hydrogels. **(A)** The blending method. **(B)** The *in situ* precipitation method. **(C)** The grafting-onto method (Created with BioRender.com).

polydopamine (PDA)-chelated carbon nanotube (CNT)-Fe_3O_4 (PFeCNT) nanohybrids into the acrylamide hydrogel via an *in situ* precipitation method to generate the PFeCNT hydrogel. This magnetic hydrogel formed an anisotropic morphology under a low static magnetic field (SMF) (30 mT) and showed conductive and mechanical features. Interestingly, under external electrical stimulation, the myoblasts cultured on the magnetic hydrogel exhibited oriented outgrowth. Arias et al. (2018) designed a magnetic bacterial cellulose (MBC) hydrogel by an *in situ* synthesis approach that mixed the dextran-coated Fe_3O_4 nanoparticles with bacterial cellulose pellicles. The resulting MBC hydrogel could be activated with saturation magnetization and exhibited a moderate Young's modulus (200−380 kPa), which was appropriate for vascular tissue engineering. Under an external magnetic field (0.3 T) stimulation, the produced gradient magnetic fields resulted in higher cell retention for the magnetically activated MBC hydrogel.

With the *in situ* precipitation method, numerous kinds of inorganic substances could be applied in the fabrication of the hydrogel networks, with good dispersion in the hydrogel matrix. Moreover, the synthesized approach is straightforward and economical. However, this method is only appropriate for limited hydrogels that possess stable networks. This is because the alkali solution used in the process might destroy the hydrogel network and limit the application of cell encapsulation (Wang et al., 2009).

The Grafting-Onto Method

In the grafting-onto methodology, there are covalent bonds formed between the magnetic particles and the hydrogel network. In detail, several functional groups are grafted onto the surface of the magnetic particles, which act as micro- or nanocrosslinkers to generate covalent bonds with the hydrogel monomers. Hu et al. (2019) designed a magnetic hydrogel made from non-toxic polyacrylamide (PAAm) hydrogel and 3-(trimethoxysilyl)propyl methacrylate coated Fe_3O_4 via the grafting-onto approach. This novel magnetic hydrogel exhibited relatively high mechanical properties, including tensile strength and fracture toughness. In addition, polydimethylsiloxane (PDMS) was introduced to modify the surface of the magnetic hydrogel, and the resulting product exhibited excellent underwater performance. The PDMS-coated magnetic hydrogel kept stability even under fatigue loading, which highlighted significant potentials in the applications of artificial muscles. Messing et al. (2011) firstly fabricated methacrylic groups functionalized magnetic $CoFe_2O_4$ nanoparticles. Then the magnetic hydrogels were fabricated by adding this kind of magnetic nanoparticles into a polyacrylamide hydrogel network.

An advantage of the grafting-onto approach is that the covalent bonds are capable of encapsulating the magnetic particles within the hydrogels, which promote the stability of the magnetic hydrogel. However, the long fabrication time, the high-cost protocol, and the complicated fabrication process restrict its broader applications in the biomedical field.

APPLICATIONS IN BONE TISSUE ENGINEERING

The repair of large bone defects caused by traumas, infections, cancers, or other diseases is still a thorny clinical problem

(Herberg et al., 2019). Previous studies have shown that osteo-inductive growth factors played a significant role in bone regeneration (Cui L. et al., 2019; Ruehle et al., 2019) however, autologous bone graft remains the gold standard in the treatment of bone defects (Bouyer et al., 2016). Considering the donor site morbidity and limited source of the donor area, the development of bone tissue engineering biomaterials is becoming more and more attractive for researchers. Most endeavors have been applied for the evaluation of MNPs-incorporated hydrogels in bone repair. As hydroxyapatite (HAP) is one of the most important components in natural bone inorganic substances, exhibits excellent biocompatibility and osteo-conductivity, and plays a key role in biomineralization (Moncion et al., 2019; Zhou et al., 2019), the magnetic HAP composite hydrogel was designed. For example, nano-HAP coated γ-Fe_2O_3 nanoparticles (m-nHAP) were synthesized and then added into poly(vinyl alcohol) (PVA) solution to fabricate m-nHAP/PVA hydrogels. The PVA showed excellent biocompatibility, high mechanical properties, and slow biodegradation, which were crucial for its application (Iqbal et al., 2019; Venkataprasanna et al., 2019). The pore sizes of hydrogels rose gradually followed by the increased content of m-nHAP, which was accessible for nutrient exchange. Meanwhile, the adhesion and proliferation of human osteoblasts were dramatically promoted as the m-nHAP concentration increased (Hou et al., 2013). However, the magnetic field was not introduced in this study, which might be considered as a potential promoter in improving bone tissue regeneration using this magnetic hydrogel.

Cells, such as stem cells, neural cells, and osteoblasts, are an important component in tissue engineering (Cerqueira et al., 2018; He et al., 2018; Ahmad et al., 2019; Chen M. et al., 2019; Midgley et al., 2019); therefore, MNP labeled cells are becoming more and more available in magnetically bioinspired hydrogels. Henstock et al. (2014) first added TREK1-MNPs or Arg-Gly-Asp (RGD)-MNPs into human mesenchymal stem cells (hMSCs) to fabricate MNP labeled cells, which were then seeded into either collagen hydrogels or poly(D, L-lactide-coglycolide) (PLGA) encapsulating bone morphogenetic protein-2 (BMP-2)-releasing collagen hydrogels (as shown in **Figure 2A**). The RGD-binding sites of cell-surface mechanoreceptors (i.e., integrins) play an important role in transferring the external stimulus into the intracellular cytoskeleton (Cartmell et al., 2002). It was worth mentioning that hydrogels containing TREK1 or RGD-MNP labeled hMSCs showed significantly more mineralization than controls; moreover, hydrogels containing functionalized MNPs and BMP-2 had thicker and more numerous mineralized domains compared to those without BMP-2 (**Figures 2B–K**). In order to maintain the stem cell phenotype and multiple differentiation potential *ex vivo*, a magnetic cell levitation method was used to label the MSCs with MNPs and then fabricated multicellular spheroids, which were implanted into type I collagen to form a magnetic hydrogel. Biological analyses showed that the 3D spheroid hydrogel system retained the functionality of MSCs, maintained the expression of stem cell markers, produced hematopoietic factors, and decreased cell-cycle progression genes, which could be able to establish an attractive platform for osteogenesis and drug delivery (Lewis et al., 2017).

Critical size bone defects need adequate vascularization for reconstruction (Genova et al., 2016). Therefore, Filippi et al. (2019) designed cell-loading magnetic nanocomposite hydrogels by incorporation of human adipose tissue derived stromal vascular fraction (SVF) cells into polyethylene glycol (PEG)-MNPs-based PEG hydrogels, which were further examined to enhance the activity of alkaline phosphatase (ALP), to increase the expression of osteogenesis-related genes, and to improve the mineralized extracellular matrix (ECM) formation both *in vitro* and *in vivo*. The results suggested that magnetically actuated cell-laden hydrogels demonstrated more mineralization and faster vascularization in comparison with MNPs or SMF alone. In addition, the *in vitro* and *in vivo* tissue volume examinations showed that this magnetic hydrogel was biodegradable. Further studies are needed to investigate the effect of this construct in an orthotopic bone defect model and in combination with other hard supporting materials (e.g., HAP). Although a previous review has focused on the multifunction of magnetic HAP in nanomedicine application (Mondal et al., 2017), the characteristics involved in the magnetic PEG hydrogels should be tested comprehensively.

Previous studies have shown that the cell activity in the local milieu relies on the spatiotemporal regulation of biophysical and biochemical properties (Lukashev and Werb, 1998), and the ECM plays an important role in this process (Chantre et al., 2019; Ebata et al., 2019; Park et al., 2019; Zhang Z. et al., 2019). The introduction of the ECM into the preparation of hydrogels could mimic the microenvironment for cell behaviors, which is mainly attributed to predetermined hydrogel properties, such as the ultrastructure (Johnson et al., 2011, 2014), stiffness (Massensini et al., 2015; Ghuman et al., 2016), gelation kinetics (Medberry et al., 2013; Wu et al., 2015; Lin et al., 2018), etc. Therefore, the development of mimicked matrices is imperative for the regulation of ECM characteristics that control cellular biology. Abdeen et al. (2016) designed a magnetoactive hydrogel matrix fabricated by incorporating carbonyl iron particles into a polyacrylamide (PAAM) hydrogel, and the elasticity was modulated reversibly by alternating magnetic field from −1.0 to 1.0 T. It was worth mentioning that the storage modulus of the magnetic hydrogel had shown elastic hysteresis. A conditioned medium from MSCs seeded on magnetic hydrogels promoted the tube formation of functional vessels, which provides nutrients, oxygen, and ions for biomineralization (Qiu et al., 2020), suggesting enhanced secretion of proangiogenic factors from MSC loaded hydrogels. Runx2, the most common biomarker as the early osteogenesis, was significantly enhanced when MSCs were seeded on the magnetic hydrogel at day 10.

It is reported that the structural, compositional, and functional complexity of the native interface is present between bone and tendon (Phillips et al., 2008; Seidi et al., 2011), which is particularly mechanosensitive (Klein-Nulend et al., 2005; Chen et al., 2010). Therefore, a magnetic responsive hydrogel containing methacrylated chondroitin sulfate (MA-CS), platelet lysate (PL), and MNPs was fabricated. The preparation of MA-CS MNPs showed a superparamagnetic feature at room

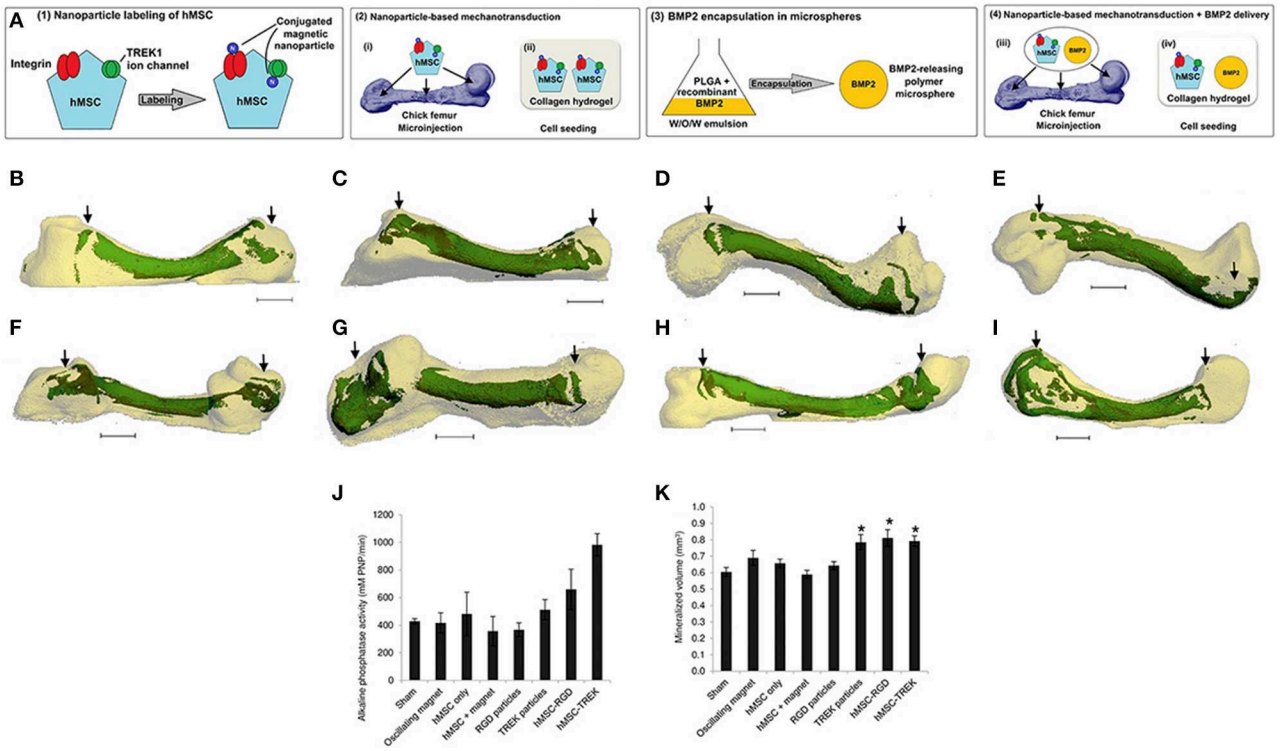

FIGURE 2 | The enhancement of hMSCs prelabeled with either RGD-modified or TREK-antibody-modified MNPs in hydrogel for biomineralization. **(A)** Schematic illustration of the experiment. (A1) The integrins or the TREK1 ion channel modified MNPs were used to label hMSCs. (A2) The MNP-labeled hMSCs were either transplanted into an *ex vivo* chick femur model (A2i) or incorporated into a hydrogel (A2ii). (A3) BMP-2-releasing PLGA microspheres were fabricated using an emulsion method. (A4) The combined effect of labeled cells and BMP-2-releasing hydrogels was studied. **(B–E)** Bone mineralization sites (green) within the cartilaginous chick fetal femur (white) were used to express the location and extent of mineralization. The experiments were conducted as follows: sham injection **(B)**, magnetic stimulation alone **(C)**, injection of hMSCs alone **(D)**, and injection of hMSCs followed by magnetic stimulation **(E)**. **(F,G)** The RGD tripeptide **(F)** or TREK-antibody **(G)** modified MNPs led to mineralization. **(H,I)** The injection of hMSCs prelabeled with either RGD-modified **(H)** or TREK-antibody-modified **(I)**. MNPs in femurs showed more alkaline phosphatase activity **(J)** and the greatest extent of mineralization **(K)**. $^*p < 0.05$. Scale bar = 1 mm [reproduced with permission from Henstock et al. (2014), Copyright 2014 John Wiley and Sons].

temperature and provided methacrylic groups for crosslinking to the hydrogel matrix. Human adipose-derived stem cells (hADSCs) or human tendon-derived cells (hTDCs) were encapsulated into hydrogels, and biological performance was evaluated. It was worth mentioning that the hydrogel possessed a gradient-like 3D structure with two interconnected layers (bone and tendon) and exhibited non-degradation without magnetic field during the testing period (20 days). Both hTDCs and hADSCs were viable within this construct. Interestingly, under magnetic field stimulation, the magnetic hydrogel showed degradation, and the cellular response of hADSCs on bone-mimicking units and hTDCs on tendon-mimicking units was modulated (Silva et al., 2018). Later on, a new gradient material was designed by incorporating continuous gradients of BMP-2 loaded glycosylated MNPs into agarose hydrogels with an external magnetic field via the grafting-onto method. Then hMSCs were included in this MNP-gradient magnetic hydrogel (schematic illustration is shown in **Figures 3A,B**). After a 28-day culture *in vitro*, the cumulative release of BMP-2 in hydrogels showed sustained diffusion-driven release kinetics (**Figure 3C**); osteogenic genes and chondrogenic genes were both significantly increased in comparison with those at day 0 (**Figures 3D,E**). Moreover, dense calcium-rich nodes (**Figure 3F**) and two distinct calcium phosphate types (HAP and β-tricalcium phosphate, β-TCP) (**Figure 3G**) were observed in the bone region of the hydrogel, suggesting that more mineralization could be produced in this new MNP-gradient hydrogel and providing a novel platform for osteochondral tissue engineering (Li et al., 2018). However, this work was performed *in vitro*, and the overall mechanical properties and the biodegradation rate of this magnetic hydrogel should be tested *in vivo* in the future.

In order to evaluate various osteoblastic functions such as collagen formation, cell adhesion, and osteocalcin production, MG-63 as an experimental model was conducted by Yuan et al. (2018). In this literature, a multifunctional biomimetic 3D magnetic hydrogel was fabricated by incorporating MG-63 cells and MNPs into native collagen hydrogels. In the presence of SMFs, the proliferation, ALP formation, and mineralization of MG-63 cells were significantly enhanced; moreover, the osteogenic related gene expression of *Runx2, BMP-2,* and *BMP-4*

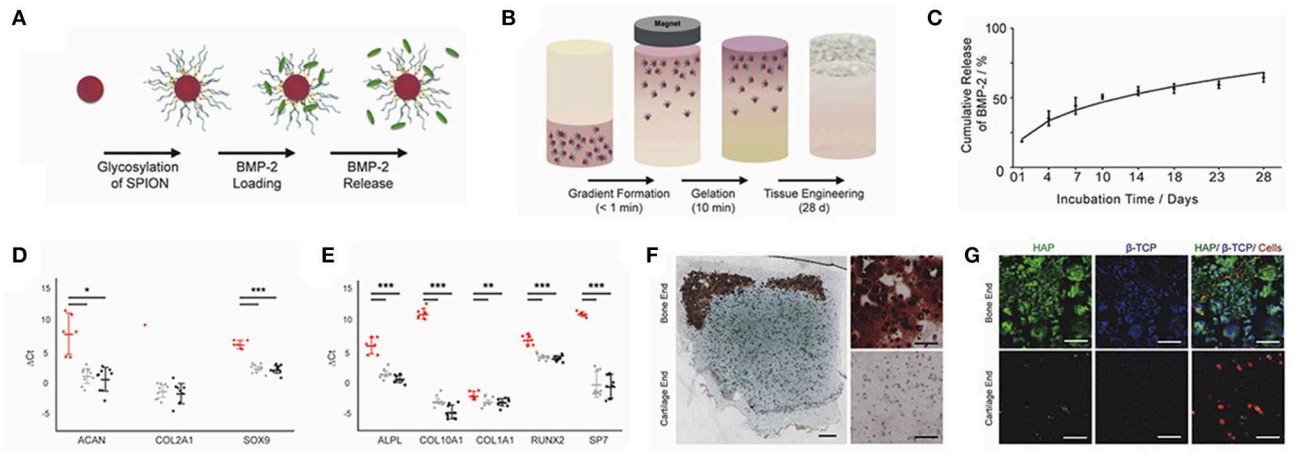

FIGURE 3 | The improvement of aligned glycosylated MNPs within an hMSC-laden agarose hydrogel in the osteochondral tissue engineering. **(A)** MNPs were incorporated into heparin to develop a glycosylated group. **(B)** Aligned glycosylated MNPs within an hMSC-laden agarose hydrogel was fabricated by an external magnetic field. **(C)** The release of BMP-2 from the magnetic agarose hydrogel was analyzed over 28 days. ΔCt values for the bone region (black), the cartilage region (gray), and a day 0 control (red) for genes associated with **(D)** cartilage formation and **(E)** bone formation (mean ± 95% confidence intervals, $N = 3$, $n = 3$ for 28 day constructs. $N = 3$, $n = 1$ for day 0 control; the *COL2A1* gene was only detected in one donor on day 0, but was detected for all 28-day samples). **(F)** Calcium nodules (red) stained by Alizarin Red S and sulfated glycosaminoglycan (blue) stained by Alcian Blue dying indicated mineralization at the bone end. **(G)** Roman microscopy of the cells (red), HAP (green), and β-TCP (blue) suggested mineralization at the bone end. Scale bar = 100 μm. $^{*}p < 0.05$, $^{**}p < 0.01$, and $^{***}p < 0.001$ [reproduced with permission from Li et al. (2018), Copyright 2018 Elsevier].

was also increased, indicating that this 3D magnetic hydrogel was a biocompatible platform for osteogenesis.

Due to the promotion of blood supply, regulation of bone metabolism, improvement of osteogenesis, and formation of new bone by appropriate temperature stimulation (Zanchetta and Bogado, 2001; Chen et al., 2013), appropriate hyperthermia on magnetic hydrogels highlights potential treatment for bone regeneration. Cao et al. (2018) designed a magnetic hydrogel containing MNPs and chitosan/PEG hydrogel, which showed excellent biocompatibility. It was worth mentioning that the cell viability of MSCs was decreased when the temperature was from 37 to 46°C; moreover, the MSCs could survive at below 46°C, and the growth and morphology had no significant changes. Intriguingly, when the temperature was at 43°C, the MSCs within magnetic hydrogel exhibited good cell viability and the highest ALP activity, which stands for the osteogenic differentiation capability. These findings indicate that magnetic hyperthermia hydrogel could be considered as a potential therapeutic strategy for bone regeneration after bone cancer excision.

APPLICATIONS IN CARTILAGE TISSUE ENGINEERING

Articular cartilage injury is one of the most usual types of orthopedic disease in the clinic and is challenging for surgeons because of the limitation of self-repair for articular cartilage. Recent endeavors of magnetic hydrogels have been developed to deal with the above issue. A previous study of magnetic hydrogels for potential cartilage tissue engineering was performed by Zhang et al. (2015). In this study, PVA modified Fe_3O_4 MNPs were first synthesized via the grafting-on method and then mixed with a hybrid hydrogel (MagGel) composed of HA, type II collagen, and PEG by mechanical dispersion. The *in vitro* degradation test showed that this MagGel lost structure integrity after 21 days' incubation at 37°C. It was worth mentioning that magnetic nanocomposite hydrogel showed similar microstructure and chemical components in comparison with natural hyaline cartilage and was able to support bone mesenchymal stem cells' (BMSCs) behavior *in vitro*, as shown in **Figure 4**. However, the combination of magnetic hydrogel and magnetic stimulation on cell functions was not evaluated, and the efficacy of magnetic hydrogels on cartilage tissue engineering *in vivo* should be further analyzed. Moreover, HA or chondroitin sulfate (CS), the two important biomolecules of polysaccharides, was used to modify the above-mentioned HAP/Fe_2O_3/PVA hydrogel and demonstrated the promotion of chondrocyte attachment and proliferation (Hou et al., 2015).

Later on, an advanced smart cell-embedded magnetic hydrogel was designed. The commercially available, biocompatible, and dextran-modified MNPs from Micromod® company were integrated into a tri-layered agarose scaffold to fabricate a ferrogel by using a blending method. The resulting magnetic hydrogel exhibited a depth-dependent mechanics and was capable of improving cell viability and sustaining the chondrocytes in culture upon magnetic stimulation (Brady et al., 2017). Furthermore, a multilayered mimicked tissue with mimetic architecture consisted of streptavidin-coated magnetic particles (diameter between 10 and 12 nm), agarose, and type I collagen was printed upon a magnetic field by using 3D bioprinting. The new magnetic hydrogel showed similar architecture to cartilage native tissues in comparison to a conventional, single-layered 3D matrix and expressed

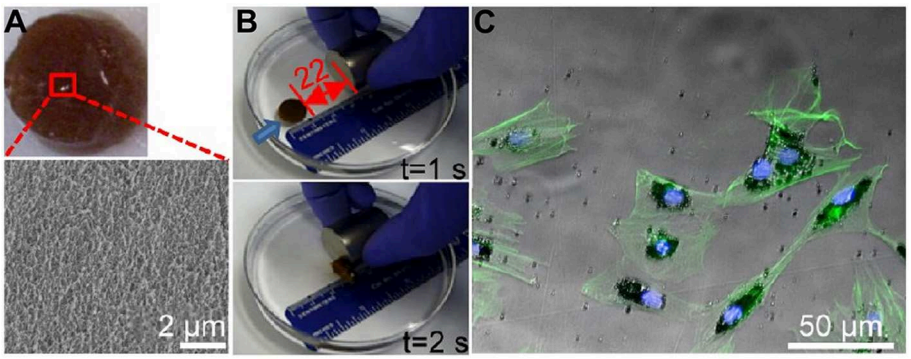

FIGURE 4 | The characteristics of the magnetic hydrogel. **(A)** General view of the magnetic hydrogel. The magnified image was obtained by a scanning electron microscope (SEM). **(B)** Magnetic responses of the magnetic hydrogel. Blue arrows suggested the hydrogel movement orientation before the next time point. **(C)** Representative images of F-actin (green) by fluorescence microscopy and magnetic nanoparticles (black) by light microscopy showed the endocytosis of MNPs by BMSCs [reproduced with permission from Zhang et al. (2015), Copyright 2015 American Chemical Society].

markedly more chondrocyte-related gene *in vitro* (Betsch et al., 2018). These novel magnetic hydrogels highlighted the potential application of location-specific cartilage replacement tissue, and further studies could be needed to assess the concentration of MNPs and the matrix, the intensity and type of magnetic fields, modification of MNPs with biological growth factors, and the repair efficacy of the damaged cartilage *in vivo*.

The stem cell therapy has been introduced into the treatment of cartilage injury (Toh et al., 2014; Hu et al., 2017); however, the chondrogenic differentiation of BMSCs requires the addition of an important cytokine. The currently available cytokines, such as transforming growth factor-β3 and BMP, have the limitation of short half-life time (Stowers et al., 2013) and less mineralization (Ren et al., 2016), respectively. Kartogenin (KGN) is a small molecule compound and is capable of inducing BMSC differentiation into chondrocytes (Xu et al., 2015). Therefore, KGN was grafted onto the surface of MNPs and then mixed with cellulose nanocrystal/dextran (CNC/Dex) hydrogel. The *in vitro* and *in vivo* experiments showed that KGN-MNPs incorporated hydrogel exhibited a long-term sustained release of KGN, recruited host cells, and induced chondrogenic differentiation of BMSCs, thus improving *in situ* cartilage regeneration (Yang et al., 2019).

Due to the high biocompatibility, strong toughness, and cell adhesive ability of nano-HAP, many kinds of literatures have reported that nano-HAP possessed effective repair capability for articular cartilage (Reddi et al., 2011; Zhou et al., 2015; Zhu et al., 2017). A magnetic nanocomposite hydrogel made of nano-HAP particles, Fe_2O_3 nanoparticles, and PVA in a ratio of 1:0.5:10 was fabricated by using the ultrasonic dispersion approach and then lyophilized by a freeze–thawing crosslinking process, as shown in **Figure 5A**. Thanks to the Fe_2O_3 nanoparticles within the hydrogel, the degradation experiment showed a relatively intermediate and slow mass loss rate. Moreover, the viability of BMSCs in the magnetic hydrogel had no significant change compared to BMSCs alone (**Figure 5B**), and the expression of chondrocyte-related genes was significantly stimulated, as shown in **Figure 5C** (Huang J. et al., 2018).

APPLICATIONS IN NEURAL TISSUE ENGINEERING

Neural tissue damages caused by either neurodegenerative diseases or high-energy trauma greatly affect the patients' quality of life worldwide. The mammalian neuronal cells show the limitation of regrowth performance and functional recovery, presenting a critical clinical challenge for surgeons (Yi et al., 2018; Zhang P.-X. et al., 2019). Most endeavors have been conducted to create a modified microenvironment for improving neural regeneration by supportive tissues and scaffolds. It has been reported that directly guiding the regenerated neurite outgrowth is able to promote neuronal regeneration and functional recovery (Huang L. et al., 2018; Shahriari et al., 2019). A hydrogel matrix containing MNPs and collagen hydrogel was designed, and then an external magnetic field was used to control the alignment of the collagen fibers remotely. After 7-day culture, neurons within a 3D aligned magnetic hydrogel complex exhibited good cell viability and more elongations and more directionality in comparison with those of without fiber alignment, indicating that 3D aligned magnetic hydrogels open up a promising possibility for directional neuronal regeneration (Antman-Passig and Shefi, 2016).

In order to rebuild the anisotropic architectures of the ECM, which support and instruct cells for neural regeneration, most aligned nanofibers with appropriate physical and biological properties have been tailored using electrospinning (Li et al., 2004; Corey et al., 2007; Ginestra, 2019; Hou et al., 2019; Idini et al., 2019; Hazeri et al., 2020). Omidinia-Anarkoli et al. (2017) developed a simple but effective strategy to create a novel "Anisogel" containing short, magnetically inspired poly(lactide-co-glycolide) (PLGA) fibers with evenly distributed elements by using a high-throughput electrospinning/micro-cutting approach, as shown in **Figures 6A–E**. Nerve cells attached well and extended unidirectionally within the "Anisogel" compared to that without fibers or oriented fibers, as shown in **Figures 6F–I**. Meanwhile, the neurons within the aligned magnetic hydrogel exhibited spontaneous electrical potential

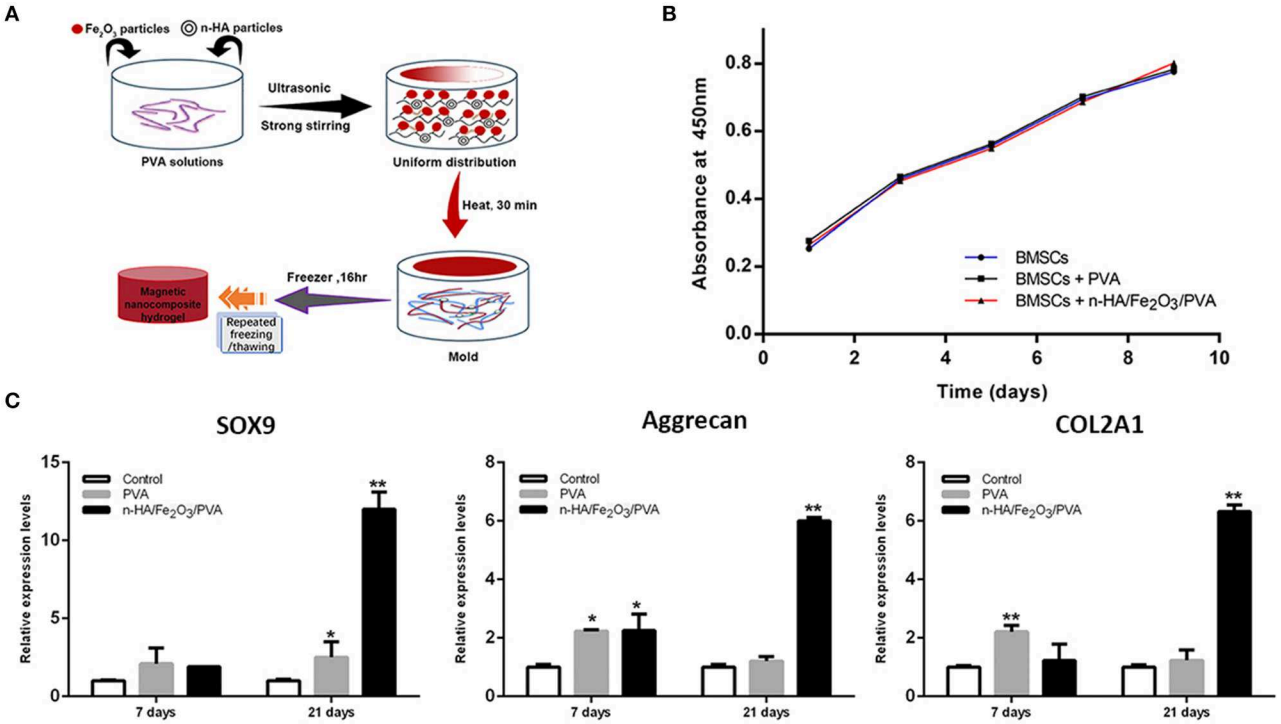

FIGURE 5 | The cell viability and the increased chondrogenesis-related genes in BMSCs within the magnetic hydrogel. **(A)** Schematic diagram of the fabrication of the magnetic hydrogel with nano-HAP particles, Fe_2O_3 nanoparticles, and PVA in a ratio of 1:0.5:10. **(B)** Cell viability of BMSCs alone, BMSCs inside PVA hydrogel, and BMSCs within magnetic hydrogel was analyzed by the CCK-8 experiment. **(C)** Chondrogenesis-related genes, such as *SOX9*, *Aggrecan*, and *COL2A1*, were analyzed by quantitative real-time polymerase chain reaction (PCR). Data were presented as means ± standard deviations. $^{**}p < 0.01$ and $^{*}p < 0.05$ vs. control (BMSCs cultured in medium) [reproduced with permission from Huang J. et al. (2018), Copyright 2018 American Chemical Society].

by triggering calcium signals, as shown in **Figures 6J,K**. Later on, magnetic responsive poly-L-lactic acid (PLLA) fibers were prepared by electrospinning and then injecting into a collagen or fibrinogen hydrogel solution. The resulting alignment of MNPs-PLLA fibers was obtained using an external magnetic field. This aligned electrospun fibers within hydrogels provided directional guidance to neurons, and the average length of neurites from dorsal root ganglions (DRGs) on magnetic fibers was significantly longer than those without MNP addition.

Due to the type, severity, and post-injury time of trauma, an injectable hydrogel matrix with minimal invasion and suitable elasticity for the regeneration of various damaged tissues has been developed (Yu and Ding, 2008; Macaya and Spector, 2012; Cheng et al., 2013; Li et al., 2014, 2015). Therefore, the rod-shaped MNP-incorporated microgels were formed, then dispersed in a biocompatible gel precursor, organized unidirectional alignments under a weak external magnetic field exposure, and finally developed a magnetoresponsive hydrogel "Anisogel." Primary DRGs inside the Anisogels with 3 vol% microgels revealed a clear difference in the orientation of neurite outgrowth in comparison with those random microgels. In addition, fibroblasts cultured on this Anisogel showed no significant difference in cytotoxicity compared with that cultured in a medium (Rose et al., 2017). These findings were performed *in vitro*; therefore, further studies are needed to be conducted *in vivo* to evaluate the efficacy of neurite regeneration and functional recovery *in vivo* by the injection of the magnetic hydrogel system.

Due to the similar biophysical and biochemical features of HA to the natural ECM of the spinal cord and brain (Bignami et al., 1993), a 3D magnetic HA hydrogel was synthesized by the magnetic microparticles, 4-arm-PEG-vinylsulfone, and thiolated HA. The resulting hydrogels had similar storage modulus as the spinal cord, and primary DRG neurons inside the magnetic hydrogels with magnetic fields showed healthy morphology, with no significant difference in cell viability compared to other groups. Interestingly, the calcium influx in DRG neurons was activated via mechanosensitive TRPV4 and $PIEZO_2$ channels under acute magnetic exposure, and the expression of $PIEZO_2$ was reduced when DRG neurons were stimulated by chronic magnetic exposure. This tailored magnetic biomaterial provided a general strategy for the regulation of different types of cells under remote magnetic stimulation (Tay et al., 2018). Moreover, a recent study has demonstrated that a biomimetic spinal cord structure was printed by a microscale continuous projection printing method (**Figure 7**), and this hydrogel loaded with neural progenitor cells was capable of promoting axon regeneration in a complete spinal cord injury model *in vivo* (Koffler et al., 2019), providing a promising strategy in the design of novel magnetic hydrogels in the neural tissue engineering.

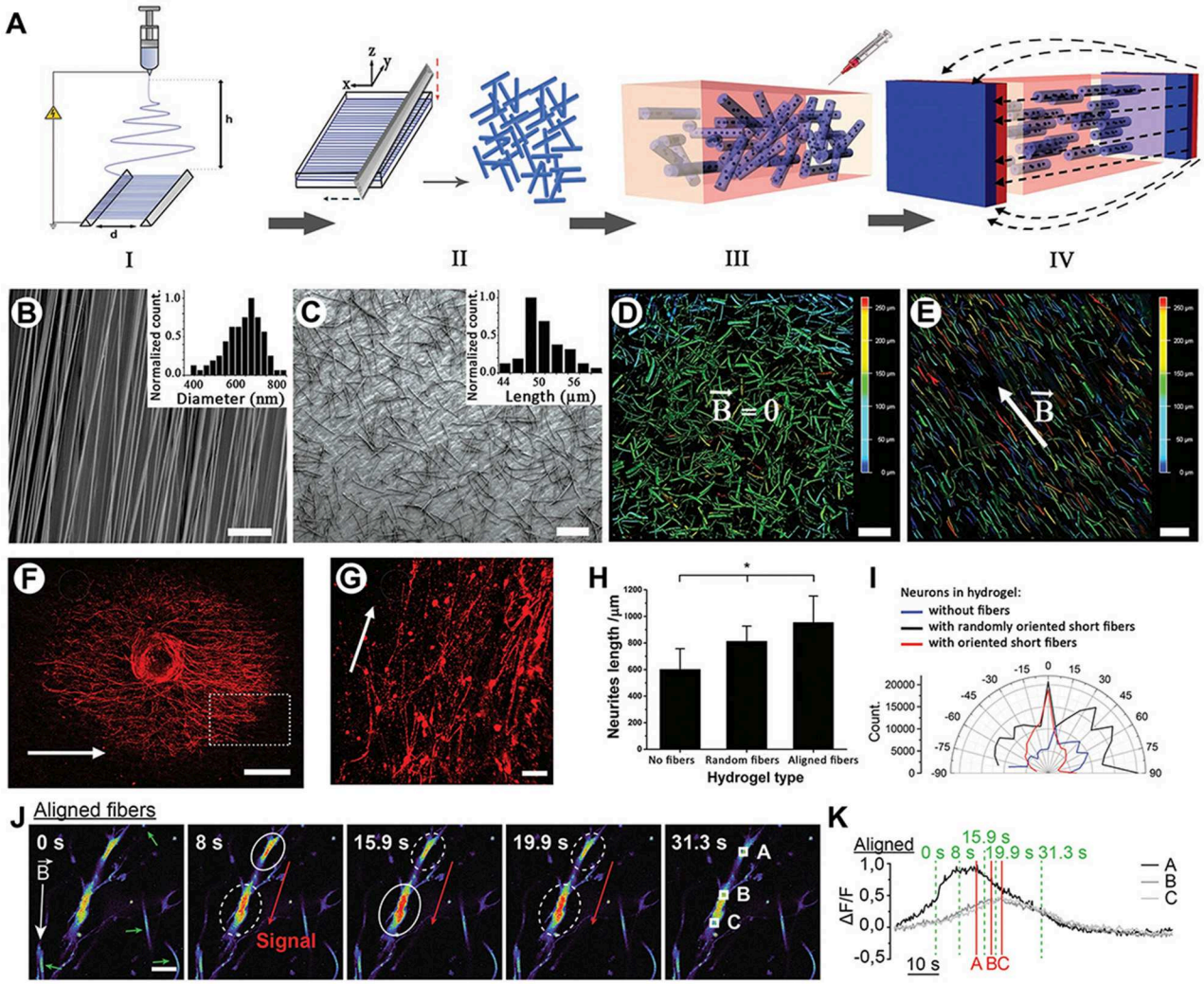

FIGURE 6 | The preparation of the Anisogels and its effect on DRG neurites. **(A)** Schematic illustration of the Anisogel preparation: step I, aligned fibers were electrospun on a parallel plate; step II, the resulting fibers were rinsed with distilled water to wash off redundant gels; step III, random short fibers were added into the hydrogel precursor; step IV, Anisogels were obtained by applying an external magnetic field. **(B)** Representative images of aligned PLGA fibers by SEM. Scale bar = 50 μm. **(C)** The average diameter of 50 μm in short fibers was observed by SEM. Scale bar = 50 μm. Representative images of magnetic fibers within hydrogels by a microscope without magnetic field exposure **(D)** and with 100 mT of magnetic field exposure **(E)**. Scale bars = 100 μm. **(F)** DRG extension in Anisogels. Scale bar = 500 μm. **(G)** A magnified image of DRG extension in Anisogels. Scale bar = 100 μm. **(H)** The length of neurite extensions was quantified. **(I)** The angular distribution of neurite extensions of single neuron. **(J)** Neurons were cultured within the aligned magnetic hydrogel. Red arrows indicated the calcium signal direction, while green arrows represented fibers. A solid circle indicated a maintained or increasing signal. **(K)** Normalized quantification of the calcium signals in the aligned magnetic hydrogel. *$p < 0.05$ [reproduced with permission from Omidinia-Anarkoli et al. (2017), Copyright 2017 John Wiley and Sons].

APPLICATIONS IN OTHER ORGANS

Besides the bone, cartilage, and nerve organs, magnetic hydrogels are also introduced into other organs, such as the heart, skin, and muscle, in order to evaluate the therapeutic potential. Namdari and Eatemadi (2017) designed a magnetic hydrogel by dissolving Fe_3O_4 and curcumin into the N-isopropylacrylamide-methacrylic acid (NIPAAM-MAA) hydrogel. The resulting magnetic hydrogel nanocomposite was able to reduce the doxorubicin-induced cardiac toxicity and hold the cardioprotective capability. Cezar et al. (2016) fabricated a ferrogel scaffold by using RGD peptides modified alginate and iron oxide. The magnetic ferrogel showed fatigue resistance and in combination with magnetic stimulation (6,510 Gauss, 5 min at 1 Hz every 12 h) could mechanically activate and promote severely injured muscle tissue regeneration. Rose et al. (2018) developed a magnetic hybrid hydrogel by blending the MNPs into the Gly-Arg-Gly-Asp-Ser-Pro-Cys (GRGDSPC) modified six-arm-PEG gel for fibroblast alignment, which is crucial for the wound healing.

INJECTABLE MAGNETIC HYDROGEL'S APPLICATION IN TISSUE ENGINEERING

Recently, the magnetic hydrogels as injectable systems have displayed great potential for tissue repair and magnetic

drug targeting. Various kinds of cells and molecules can be encapsulated homogeneously into the magnetic hydrogels and then targeted to the pathological sites with minimal invasiveness (Wu et al., 2018; Chen X. et al., 2019b; Shi et al., 2019; Wu H. et al., 2019; Xu et al., 2019). Several polymers, including ionic-response polymers (e.g., sodium alginate), natural biocompatible polymers (e.g., chitosan), and synthetic polymers (e.g., polyacrylic acid), conjugated with the magnetic particles have been used to fabricate the injectable hydrogels for therapeutic applications (Jalili et al., 2017; Hu et al., 2018; Amini-Fazl et al., 2019). These magnetic hydrogels could be guided to the diseased sites via external magnetic fields and exert a drug release influence there. Meanwhile, this kind of magnetic hydrogel is mainly targeted for the cancer therapy due to the hyperthermia effect under the applied magnetic field.

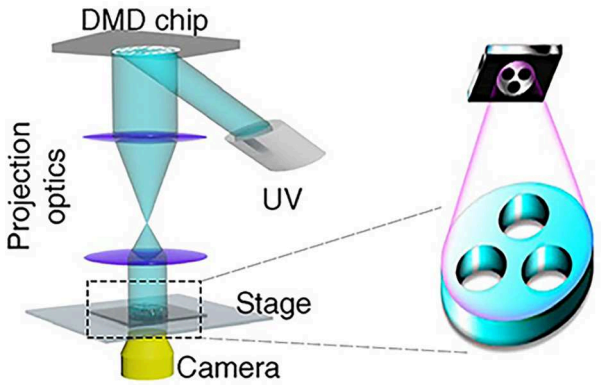

FIGURE 7 | Schematic diagram of 3D printing by a microscale continuous projection printing method [reproduced with permission from Koffler et al. (2019), Copyright 2019 Springer Nature].

THE METABOLISM OF MAGNETIC PARTICLES FROM THE MAGNETIC BIOMATERIALS

Although numerous studies have shown that magnetic biomaterials exhibited biocompatibility both *in vitro* and *in vivo*, the cytotoxicity and long-term fate of magnetic particles embedded within the magnetic hydrogels *in vivo* must be taken for consideration. No identical criteria have been made to evaluate this important issue of magnetic hydrogels since the fabrication process and physicochemical properties vary in many aspects. The Food and Drug Administration (FDA) in the United States had approved several MNPs in the clinical applications, such as the treatment of anemia caused by chronic kidney disease and the magnetic resonance imaging, and these MNPs could be removed quickly by the liver (Laconte et al., 2005; Ventola, 2017). The clearance of magnetic particles *in vivo* depends on the size of the particle. In detail, particles smaller than 5.5 nm could be removed quickly through the kidney (Sun et al., 2008), particles up to 200 nm could be sequestered by phagocytes of the spleen (Chen and Weiss, 1973), and particles larger than 5 μm could be cleared via the lymphatic system (Arruebo et al., 2007). In addition, magnetic fields have proven to control the anisotropic feature, constitution, and the degradation rate in the magnetic hydrogels (Huang J. et al., 2018; Silva et al., 2018). All these factors are crucial for the released amounts of magnetic particles from the magnetic constructs and the impact on organs. More efforts are needed to develop more controllable magnetic hydrogels for *in vivo* applications.

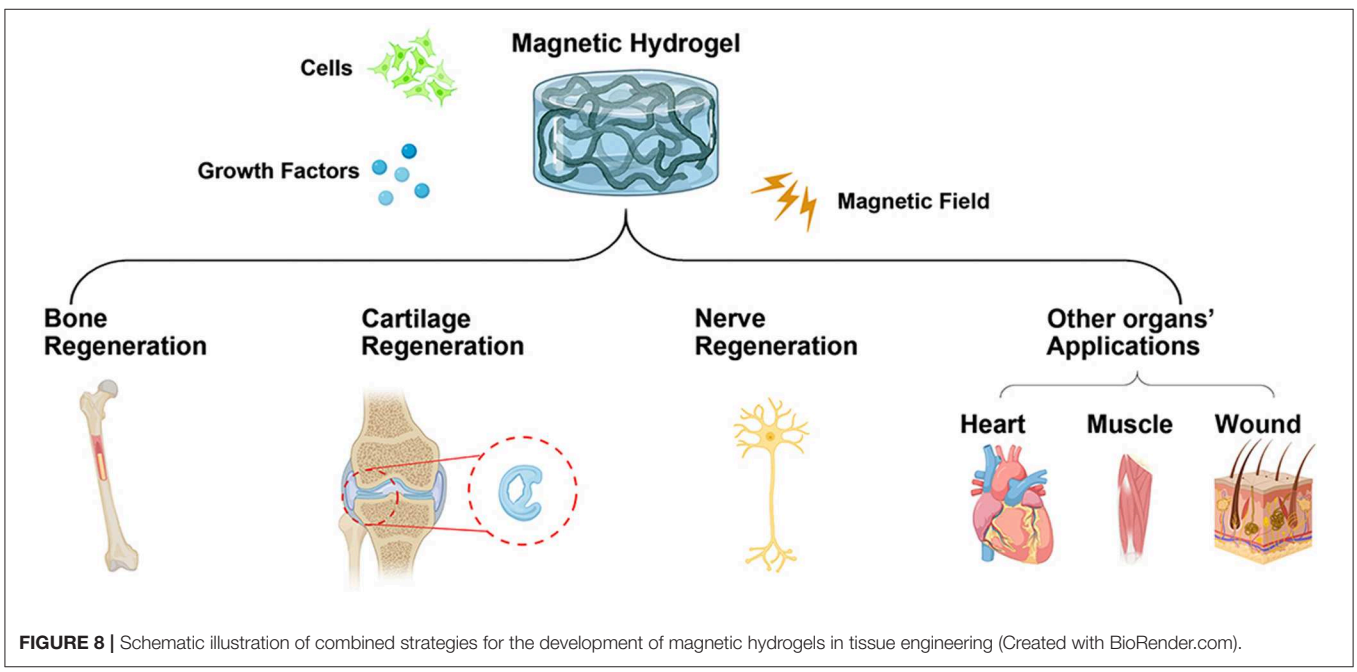

FIGURE 8 | Schematic illustration of combined strategies for the development of magnetic hydrogels in tissue engineering (Created with BioRender.com).

CONCLUSIONS AND PERSPECTIVES

The magnetically responsive smart hydrogels have emerged as an immensely potential biomaterial for developing bioaligned actuators. Benefiting from their intriguing features, including but not limited to quick response, mimetic native tissues, appealing mechanical properties, and biocompatibility, magnetic hydrogels have undergone unparalleled advances in biomedical fields, such as bone, cartilage, nerve, heart, muscle tissue engineering, and so on. However, the properties of magnetic particles, such as size, shape, composition, crystallinity, and so on, should be further modified in order to avoid overheating when cell-laden hydrogels are assembled. Meanwhile, the hydrogel matrices used in magnetic hydrogels need to be further evaluated by mimicking the native architectures of tissues and organs, which holds great potential for the preclinical treatment. Therefore, combined strategies should be developed to create more and more smart hydrogels in tissue engineering (**Figure 8**).

Future perspectives should focus on dealing with the existing difficulties. In addition, more attention should be taken into consideration in evaluating the magnetic hydrogels' pharmacokinetics/toxicokinetics, metabolism, biodegradation *in vivo*, and so on, which are of great significance in the applications of tissue engineering.

AUTHOR CONTRIBUTIONS

PT and ZL initiated the project. ZL, JL, XC, XW, LZ, and PT searched the data and wrote, revised, and completed the manuscript.

FUNDING

This literature was supported by the National Key Research and Development Program of China (2016YFC1102005), the National Defense Scientific and Technological Innovation Special Zone (18-163-12-ZT-003-016-01), the National Natural Science Foundation of China (81702121, 81702153, and 8170090601), the Military Medical Science and Technology Youth Development Program (19QNP052), the Scientific Research Project of Capital Health Development (2018-4-5014), the Subsidiary of PLA Major Project (AWS17J004), the Clinical Research Support Fund of PLA general hospital (2017FC-TSYS-2006), and the China Postdoctoral Science Foundation funded project (2017M613397 and 2019M664007).

REFERENCES

Abdeen, A. A., Lee, J., Bharadwaj, N. A., Ewoldt, R. H., and Kilian, K. A. (2016). Temporal modulation of stem cell activity using magnetoactive hydrogels. *Adv. Healthc. Mater.* 5, 2536–2544. doi: 10.1002/adhm.201600349

Ahmad, T., Byun, H., Lee, J., Madhurakat Perikamana, S. K., Shin, Y. M., Kim, E. M., et al. (2019). Stem cell spheroids incorporating fibers coated with adenosine and polydopamine as a modular building blocks for bone tissue engineering. *Biomaterials* 230:119652. doi: 10.1016/j.biomaterials.2019.119652

Amini-Fazl, M. S., Mohammadi, R., and Kheiri, K. (2019). 5Fluorouracil loaded chitosan/polyacrylic acid/Fe_3O_4 magnetic nanocomposite hydrogel as a potential anticancer drug delivery system. *Int. J. Biol. Macromol.* 132, 506–513. doi: 10.1016/j.ijbiomac.2019.04.005

Antman-Passig, M., and Shefi, O. (2016). Remote magnetic orientation of 3D collagen hydrogels for directed neuronal regeneration. *Nano Lett.* 16, 2567–2573. doi: 10.1021/acs.nanolett.6b00131

Arias, S. L., Shetty, A., Devorkin, J., and Allain, J. P. (2018). Magnetic targeting of smooth muscle cells *in vitro* using a magnetic bacterial cellulose to improve cell retention in tissue-engineering vascular grafts. *Acta Biomater.* 77, 172–181. doi: 10.1016/j.actbio.2018.07.013

Arruebo, M., Fernández-Pacheco, R., Ibarra, M. R., and Santamaría, J. (2007). Magnetic nanoparticles for drug delivery. *Nanotoday* 2, 22–32. doi: 10.1016/S1748-0132(07)70084-1

Bannerman, A. D., Li, X., and Wan, W. (2017). A 'degradable' poly(vinyl alcohol) iron oxide nanoparticle hydrogel. *Acta Biomater.* 58, 376–385. doi: 10.1016/j.actbio.2017.05.018

Barrow, M., Taylor, A., Fuentes-Caparros, A. M., Sharkey, J., Daniels, L. M., Mandal, P., et al. (2017). SPIONs for cell labelling and tracking using MRI: magnetite or maghemite? *Biomater. Sci.* 6, 101–106. doi: 10.1039/C7BM00515F

Betsch, M., Cristian, C., Lin, Y. Y., Blaeser, A., Schoneberg, J., Vogt, M., et al. (2018). Incorporating 4D into bioprinting: real-time magnetically directed collagen fiber alignment for generating complex multilayered tissues. *Adv. Healthc. Mater.* 7:e1800894. doi: 10.1002/adhm.201800894

Bignami, A., Hosley, M., and Dahl, D. (1993). Hyaluronic acid and hyaluronic acid-binding proteins in brain extracellular matrix. *Anat. Embryol.* 188, 419–433. doi: 10.1007/BF00190136

Bouyer, M., Guillot, R., Lavaud, J., Plettinx, C., Olivier, C., Curry, V., et al. (2016). Surface delivery of tunable doses of BMP-2 from an adaptable polymeric scaffold induces volumetric bone regeneration. *Biomaterials* 104, 168–181. doi: 10.1016/j.biomaterials.2016.06.001

Bowser, D., and Moore, M. J. (2019). Biofabrication of neural microphysiological systems using magnetic spheroid bioprinting. *Biofabrication*. doi: 10.1088/1758-5090/ab41b4

Brady, M. A., Talvard, L., Vella, A., and Ethier, C. R. (2017). Bio-inspired design of a magnetically active trilayered scaffold for cartilage tissue engineering. *J. Tissue Eng. Regen. Med.* 11, 1298–1302. doi: 10.1002/term.2106

Brito-Pereira, R., Correia, D. M., Ribeiro, C., Francesko, A., Etxebarria, I., Pérez-Álvarez, L., et al. (2018). Silk fibroin-magnetic hybrid composite electrospun fibers for tissue engineering applications. *Compos. Part B Eng.* 141, 70–75. doi: 10.1016/j.compositesb.2017.12.046

Cao, Z., Wang, D., Li, Y., Xie, W., Wang, X., Tao, L., et al. (2018). Effect of nanoheat stimulation mediated by magnetic nanocomposite hydrogel on the osteogenic differentiation of mesenchymal stem cells. *Sci. China Life Sci.* 61, 448–456. doi: 10.1007/s11427-017-9287-8

Cartmell, S. H., Dobson, J., Verschueren, S. B., and El Haj, A. J. (2002). Development of magnetic particle techniques for long-term culture of bone cells with intermittent mechanical activation. *IEEE Trans. Nanobioscience* 1, 92–97. doi: 10.1109/TNB.2002.806945

Cerqueira, S. R., Lee, Y. S., Cornelison, R. C., Mertz, M. W., Wachs, R. A., Schmidt, C. E., et al. (2018). Decellularized peripheral nerve supports schwann cell transplants and axon growth following spinal cord injury. *Biomaterials* 177, 176–185. doi: 10.1016/j.biomaterials.2018.05.049

Ceylan, H., Yasa, I. C., Yasa, O., Tabak, A. F., Giltinan, J., and Sitti, M. (2019). 3D-printed biodegradable microswimmer for theranostic cargo delivery and release. *ACS Nano* 13, 3353–3362. doi: 10.1021/acsnano.8b09233

Cezar, C. A., Roche, E. T., Vandenburgh, H. H., Duda, G. N., Walsh, C. J., and Mooney, D. J. (2016). Biologic-free mechanically induced muscle regeneration. *Proc. Natl. Acad. Sci. U.S.A.* 113, 1534–1539. doi: 10.1073/pnas.1517517113

Chantre, C. O., Gonzalez, G. M., Ahn, S., Cera, L., Campbell, P. H., Hoerstrup, S. P., et al. (2019). Porous biomimetic hyaluronic acid and extracellular matrix protein nanofiber scaffolds for accelerated cutaneous tissue repair. *ACS Appl. Mater. Interfaces* 11, 45498–45510. doi: 10.1021/acsami.9b17322

Chen, H., Qin, Z., Zhao, J., He, Y., Ren, E., Zhu, Y., et al. (2019). Cartilage-targeting and dual MMP-13/pH responsive theranostic nanoprobes for osteoarthritis imaging and precision therapy. *Biomaterials* 225:119520. doi: 10.1016/j.biomaterials.2019.119520

Chen, J., Shi, Z. D., Ji, X., Morales, J., Zhang, J., Kaur, N., et al. (2013). Enhanced osteogenesis of human mesenchymal stem cells by periodic heat shock in self-assembling peptide hydrogel. *Tissue Eng. Part A* 19, 716–728. doi: 10.1089/ten.tea.2012.0070

Chen, J. H., Liu, C., You, L., and Simmons, C. A. (2010). Boning up on wolff's law: mechanical regulation of the cells that make and maintain bone. *J. Biomech.* 43, 108–118. doi: 10.1016/j.jbiomech.2009.09.016

Chen, L. T., and Weiss, L. (1973). The role of the sinus wall in the passage of erythrocytes through the spleen. *Blood* 41, 529–537. doi: 10.1182/blood.V41.4.529.529

Chen, M., Reed, R. R., and Lane, A. P. (2019). Chronic inflammation directs an olfactory stem cell functional switch from neuroregeneration to immune defense. *Cell Stem Cell* 25, 501–513.e505. doi: 10.1016/j.stem.2019.08.011

Chen, X., Fan, M., Tan, H., Ren, B., Yuan, G., Jia, Y., et al. (2019a). Magnetic and self-healing chitosan-alginate hydrogel encapsulated gelatin microspheres via covalent cross-linking for drug delivery. *Mater. Sci. Eng. C Mater. Biol. Appl.* 101, 619–629. doi: 10.1016/j.msec.2019.04.012

Chen, X., Fan, M., Tan, H., Ren, B., Yuan, G., Jia, Y., et al. (2019b). Magnetic and self-healing chitosan-alginate hydrogel encapsulated gelatin microspheres via covalent cross-linking for drug delivery. *Mater. Sci. Eng. C Mater. Biol. Appl.* 101, 619–629.

Cheng, J., Amin, D., Latona, J., Heber-Katz, E., and Messersmith, P. B. (2019). Supramolecular polymer hydrogels for drug-induced tissue regeneration. *ACS Nano* 13, 5493–5501. doi: 10.1021/acsnano.9b00281

Cheng, T. Y., Chen, M. H., Chang, W. H., Huang, M. Y., and Wang, T. W. (2013). Neural stem cells encapsulated in a functionalized self-assembling peptide hydrogel for brain tissue engineering. *Biomaterials* 34, 2005–2016. doi: 10.1016/j.biomaterials.2012.11.043

Corey, J. M., Lin, D. Y., Mycek, K. B., Chen, Q., Samuel, S., Feldman, E. L., et al. (2007). Aligned electrospun nanofibers specify the direction of dorsal root ganglia neurite growth. *J. Biomed. Mater. Res. A* 83, 636–645. doi: 10.1002/jbm.a.31285

Cui, L., Zhang, J., Zou, J., Yang, X., Guo, H., Tian, H., et al. (2019). Electroactive composite scaffold with locally expressed osteoinductive factor for synergistic bone repair upon electrical stimulation. *Biomaterials* 230:119617. doi: 10.1016/j.biomaterials.2019.119617

Cui, Z. K., Kim, S., Baljon, J. J., Wu, B. M., Aghaloo, T., and Lee, M. (2019). Microporous methacrylated glycol chitosan-montmorillonite nanocomposite hydrogel for bone tissue engineering. *Nat. Commun.* 10:3523. doi: 10.1038/s41467-019-11511-3

Deng, X., Ren, Y., Hou, L., Liu, W., Jiang, T., and Jiang, H. (2019). Compound-droplet-pairs-filled hydrogel microfiber for electric-field-induced selective release. *Small* 15:e1903098. doi: 10.1002/smll.201903098

Ebata, H., Moriyama, K., Kuboki, T., and Kidoaki, S. (2019). General cellular durotaxis induced with cell-scale heterogeneity of matrix-elasticity. *Biomaterials* 230:119647. doi: 10.1016/j.biomaterials.2019.119647

Fan, C., Shi, J., Zhuang, Y., Zhang, L., Huang, L., Yang, W., et al. (2019). Myocardial-infarction-responsive smart hydrogels targeting matrix metalloproteinase for on-demand growth factor delivery. *Adv. Mater.* 31:e1902900. doi: 10.1002/adma.201902900

Filippi, M., Dasen, B., Guerrero, J., Garello, F., Isu, G., Born, G., et al. (2019). Magnetic nanocomposite hydrogels and static magnetic field stimulate the osteoblastic and vasculogenic profile of adipose-derived cells. *Biomaterials* 223:119468. doi: 10.1016/j.biomaterials.2019.119468

Gao, F., Xie, W., Miao, Y., Wang, D., Guo, Z., Ghosal, A., et al. (2019). Magnetic hydrogel with optimally adaptive functions for breast cancer recurrence prevention. *Adv. Healthc. Mater.* 8:1900203. doi: 10.1002/adhm.201900203

Genova, T., Munaron, L., Carossa, S., and Mussano, F. (2016). Overcoming physical constraints in bone engineering: 'the importance of being vascularized'. *J. Biomater. Appl.* 30, 940–951. doi: 10.1177/0885328215616749

Ghuman, H., Massensini, A. R., Donnelly, J., Kim, S. M., Medberry, C. J., Badylak, S. F., et al. (2016). ECM hydrogel for the treatment of stroke: characterization of the host cell infiltrate. *Biomaterials* 91, 166–181. doi: 10.1016/j.biomaterials.2016.03.014

Ginestra, P. (2019). Manufacturing of polycaprolactone - graphene fibers for nerve tissue engineering. *J. Mech. Behav. Biomed. Mater.* 100:103387. doi: 10.1016/j.jmbbm.2019.103387

Goncalves, R., Martins, P., Moya, X., Ghidini, M., Sencadas, V., Botelho, G., et al. (2015). Magnetoelectric CoFe2O4/polyvinylidene fluoride electrospun nanofibres. *Nanoscale* 7, 8058–8061. doi: 10.1039/C5NR00453E

Hazeri, Y., Irani, S., Zandi, M., and Pezeshki-Modaress, M. (2020). Polyvinyl alcohol/sulfated alginate nanofibers induced the neuronal differentiation of human bone marrow stem cells. *Int. J. Biol. Macromol.* 147, 946–953. doi: 10.1016/j.ijbiomac.2019.10.061

He, J., Sun, C., Gu, Z., Yang, Y., Gu, M., Xue, C., et al. (2018). Morphology, migration, and transcriptome analysis of schwann cell culture on butterfly wings with different surface architectures. *ACS Nano* 12, 9660–9668. doi: 10.1021/acsnano.8b00552

Henstock, J. R., Rotherham, M., Rashidi, H., Shakesheff, K. M., and El Haj, A. J. (2014). Remotely activated mechanotransduction via magnetic nanoparticles promotes mineralization synergistically with bone morphogenetic protein 2: applications for injectable cell therapy. *Stem Cells Transl. Med.* 3, 1363–1374. doi: 10.5966/sctm.2014-0017

Herberg, S., Mcdermott, A. M., Dang, P. N., Alt, D. S., Tang, R., Dawahare, J. H., et al. (2019). Combinatorial morphogenetic and mechanical cues to mimic bone development for defect repair. *Sci. Adv.* 5:eaax2476. doi: 10.1126/sciadv.aax2476

Hermenegildo, B., Ribeiro, C., Pérez-Álvarez, L., Vilas, J. L., Learmonth, D. A., Sousa, R. A., et al. (2019). Hydrogel-based magnetoelectric microenvironments for tissue stimulation. *Colloids Surf. B Biointerfaces* 181, 1041–1047. doi: 10.1016/j.colsurfb.2019.06.023

Hou, R., Nie, L., Du, G., Xiong, X., and Fu, J. (2015). Natural polysaccharides promote chondrocyte adhesion and proliferation on magnetic nanoparticle/PVA composite hydrogels. *Colloids Surf. B Biointerfaces* 132, 146–154. doi: 10.1016/j.colsurfb.2015.05.008

Hou, R., Zhang, G., Du, G., Zhan, D., Cong, Y., Cheng, Y., et al. (2013). Magnetic nanohydroxyapatite/PVA composite hydrogels for promoted osteoblast adhesion and proliferation. *Colloids Surf. B Biointerfaces* 103, 318–325. doi: 10.1016/j.colsurfb.2012.10.067

Hou, Y., Wang, X., Zhang, Z., Luo, J., Cai, Z., Wang, Y., et al. (2019). Repairing transected peripheral nerve using a biomimetic nerve guidance conduit containing intraluminal sponge fillers. *Adv. Healthc. Mater.* 8:e1900913. doi: 10.1002/adhm.201900913

Hsu, R. S., Chen, P. Y., Fang, J. H., Chen, Y. Y., Chang, C. W., Lu, Y. J., et al. (2019). Adaptable microporous hydrogels of propagating ngf-gradient by injectable building blocks for accelerated axonal outgrowth. *Adv. Sci.* 6:1900520. doi: 10.1002/advs.201900520

Hu, Q., Ding, B., Yan, X., Peng, L., Duan, J., Yang, S., et al. (2017). Polyethylene glycol modified PAMAM dendrimer delivery of kartogenin to induce chondrogenic differentiation of mesenchymal stem cells. *Nanomedicine* 13, 2189–2198. doi: 10.1016/j.nano.2017.05.011

Hu, X., Nian, G., Liang, X., Wu, L., Yin, T., Lu, H., et al. (2019). Adhesive tough magnetic hydrogels with high Fe3O4 content. *ACS Appl. Mater. Interfaces* 11, 10292–10300. doi: 10.1021/acsami.8b20937

Hu, X., Wang, Y., Zhang, L., Xu, M., Zhang, J., and Dong, W. (2018). Magnetic field-driven drug release from modified iron oxide-integrated polysaccharide hydrogel. *Int. J. Biol. Macromol.* 108, 558–567. doi: 10.1016/j.ijbiomac.2017.12.018

Huang, J., Liang, Y., Jia, Z., Chen, J., Duan, L., Liu, W., et al. (2018). Development of magnetic nanocomposite hydrogel with potential cartilage tissue engineering. *ACS Omega* 3, 6182–6189. doi: 10.1021/acsomega.8b00291

Huang, L., Zhu, L., Shi, X., Xia, B., Liu, Z., Zhu, S., et al. (2018). A compound scaffold with uniform longitudinally oriented guidance cues and a porous sheath promotes peripheral nerve regeneration *in vivo*. *Acta Biomater.* 68, 223–236. doi: 10.1016/j.actbio.2017.12.010

Huang, Q., Zou, Y., Arno, M. C., Chen, S., Wang, T., Gao, J., et al. (2017). Hydrogel scaffolds for differentiation of adipose-derived stem cells. *Chem. Soc. Rev.* 46, 6255–6275. doi: 10.1039/C6CS00052E

Idini, M., Wieringa, P., Rocchiccioli, S., Nieddu, G., Ucciferri, N., Formato, M., et al. (2019). Glycosaminoglycan functionalization of electrospun scaffolds enhances schwann cell activity. *Acta Biomater.* 96, 188–202. doi: 10.1016/j.actbio.2019.06.054

Iqbal, H., Khan, Z. U., Razzaq, A., Khan, N. U., Menaa, B., Khan, B. A., et al. (2019). Fabrication, physical characterizations and *in vitro* antibacterial activity of cefadroxil-loaded chitosan/poly(vinyl alcohol) nanofibers against *Staphylococcus aureus* clinical isolates. *Int. J. Biol. Macromol.* 144, 921–931. doi: 10.1016/j.ijbiomac.2019.09.169

Jalili, N. A., Jaiswal, M. K., Peak, C. W., Cross, L. M., and Gaharwar, A. K. (2017). Injectable nanoengineered stimuli-responsive hydrogels for on-demand and localized therapeutic delivery. *Nanoscale* 9, 15379–15389. doi: 10.1039/C7NR02327H

Jiang, B., Yang, J., Rahoui, N., Taloub, N., and Huang, Y. D. (2017). Functional polymer materials affecting cell attachment. *Adv. Colloid Interface Sci.* 250, 185–194. doi: 10.1016/j.cis.2017.09.002

Johnson, T. D., Dequach, J. A., Gaetani, R., Ungerleider, J., Elhag, D., Nigam, V., et al. (2014). Human versus porcine tissue sourcing for an injectable myocardial matrix hydrogel. *Biomater. Sci.* 2014:60283d. doi: 10.1039/C3BM60283D

Johnson, T. D., Lin, S. Y., and Christman, K. L. (2011). Tailoring material properties of a nanofibrous extracellular matrix derived hydrogel. *Nanotechnology* 22:494015. doi: 10.1088/0957-4484/22/49/494015

Kabu, S., Gao, Y., Kwon, B. K., and Labhasetwar, V. (2015). Drug delivery, cell-based therapies, and tissue engineering approaches for spinal cord injury. *J. Control. Release* 219, 141–154. doi: 10.1016/j.jconrel.2015.08.060

Klein-Nulend, J., Bacabac, R. G., and Mullender, M. G. (2005). Mechanobiology of bone tissue. *Pathol. Biol.* 53, 576–580. doi: 10.1016/j.patbio.2004.12.005

Koffler, J., Zhu, W., Qu, X., Platoshyn, O., Dulin, J. N., Brock, J., et al. (2019). Biomimetic 3D-printed scaffolds for spinal cord injury repair. *Nat. Med.* 25, 263–269. doi: 10.1038/s41591-018-0296-z

Laconte, L., Nitin, N., and Bao, G. (2005). Magnetic nanoparticle probes. *Mater. Today* 8, 32–38. doi: 10.1016/S1369-7021(05)00893-X

Lee, S. C., Kwon, I. K., and Park, K. (2013). Hydrogels for delivery of bioactive agents: a historical perspective. *Adv. Drug Deliv. Rev.* 65, 17–20. doi: 10.1016/j.addr.2012.07.015

Lewis, N. S., Lewis, E. E., Mullin, M., Wheadon, H., Dalby, M. J., and Berry, C. C. (2017). Magnetically levitated mesenchymal stem cell spheroids cultured with a collagen gel maintain phenotype and quiescence. *J. Tissue Eng.* 8:2041731417704428. doi: 10.1177/2041731417704428

Li, C., Armstrong, J. P., Pence, I. J., Kit-Anan, W., Puetzer, J. L., Correia Carreira, S., et al. (2018). Glycosylated superparamagnetic nanoparticle gradients for osteochondral tissue engineering. *Biomaterials* 176, 24–33. doi: 10.1016/j.biomaterials.2018.05.029

Li, D., Wang, Y., and Xia, Y. (2004). Electrospinning nanofibers as uniaxially aligned arrays and layer-by-layer stacked films. *Adv. Mater.* 16, 361–366. doi: 10.1002/adma.200306226

Li, J., and Mooney, D. J. (2016). Designing hydrogels for controlled drug delivery. *Nat. Rev. Mater.* 1:16071. doi: 10.1038/natrevmats.2016.71

Li, X., Wang, Y., Li, A., Ye, Y., Peng, S., Deng, M., et al. (2019). A novel pH- and salt-responsive N-succinyl-chitosan hydrogel via a one-step hydrothermal process. *Molecules* 24:E4211. doi: 10.3390/molecules24234211

Li, X., Zhou, J., Liu, Z., Chen, J., Lu, S., Sun, H., et al. (2014). A PNIPAAm-based thermosensitive hydrogel containing SWCNTs for stem cell transplantation in myocardial repair. *Biomaterials* 35, 5679–5688. doi: 10.1016/j.biomaterials.2014.03.067

Li, Y., Fang, X., and Jiang, T. (2015). Minimally traumatic alveolar ridge augmentation with a tunnel injectable thermo-sensitive alginate scaffold. *J. Appl. Oral Sci.* 23, 215–223. doi: 10.1590/1678-775720140348

Li, Z., Chen, H., Li, B., Xie, Y., Gong, X., Liu, X., et al. (2019). Photoresponsive luminescent polymeric hydrogels for reversible information encryption and decryption. *Adv. Sci.* 6:1901529. doi: 10.1002/advs.201901529

Lin, T., Liu, S., Chen, S., Qiu, S., Rao, Z., Liu, J., et al. (2018). Hydrogel derived from porcine decellularized nerve tissue as a promising biomaterial for repairing peripheral nerve defects. *Acta Biomater.* 73, 326–338. doi: 10.1016/j.actbio.2018.04.001

Liu, K., Han, L., Tang, P., Yang, K., Gan, D., Wang, X., et al. (2019). An anisotropic hydrogel based on mussel-inspired conductive ferrofluid composed of electromagnetic nanohybrids. *Nano Lett.* 19, 8343–8356. doi: 10.1021/acs.nanolett.9b00363

Lukashev, M. E., and Werb, Z. (1998). ECM signalling: orchestrating cell behaviour and misbehaviour. *Trends Cell Biol.* 8, 437–441. doi: 10.1016/S0962-8924(98)01362-2

Luo, Y., Wei, X., Wan, Y., Lin, X., Wang, Z., and Huang, P. (2019). 3D printing of hydrogel scaffolds for future application in photothermal therapy of breast cancer and tissue repair. *Acta Biomater.* 92, 37–47. doi: 10.1016/j.actbio.2019.05.039

Macaya, D., and Spector, M. (2012). Injectable hydrogel materials for spinal cord regeneration: a review. *Biomed. Mater.* 7:012001. doi: 10.1088/1748-6041/7/1/012001

Madl, C. M., Lesavage, B. L., Dewi, R. E., Dinh, C. B., Stowers, R. S., Khariton, M., et al. (2017). Maintenance of neural progenitor cell stemness in 3D hydrogels requires matrix remodelling. *Nat. Mater.* 16, 1233–1242. doi: 10.1038/nmat5020

Madl, C. M., Lesavage, B. L., Dewi, R. E., Lampe, K. J., and Heilshorn, S. C. (2019). Matrix remodeling enhances the differentiation capacity of neural progenitor cells in 3D hydrogels. *Adv. Sci.* 6:1801716. doi: 10.1002/advs.201801716

Manjua, A. C., Alves, V. D., Crespo, J. G., and Portugal, C. A. M. (2019). Magnetic responsive PVA hydrogels for remote modulation of protein sorption. *ACS Appl. Mater. Interfaces* 11, 21239–21249. doi: 10.1021/acsami.9b03146

Massensini, A. R., Ghuman, H., Saldin, L. T., Medberry, C. J., Keane, T. J., Nicholls, F. J., et al. (2015). Concentration-dependent rheological properties of ECM hydrogel for intracerebral delivery to a stroke cavity. *Acta Biomater.* 27, 116–130. doi: 10.1016/j.actbio.2015.08.040

Medberry, C. J., Crapo, P. M., Siu, B. F., Carruthers, C. A., Wolf, M. T., Nagarkar, S. P., et al. (2013). Hydrogels derived from central nervous system extracellular matrix. *Biomaterials* 34, 1033–1040. doi: 10.1016/j.biomaterials.2012.10.062

Messing, R., Frickel, N., Belkoura, L., Strey, R., Rahn, H., Odenbach, S., et al. (2011). Cobalt ferrite nanoparticles as multifunctional cross-linkers in PAAm ferrohydrogels. *Macromolecules* 44, 2990–2999. doi: 10.1021/ma102708b

Midgley, A. C., Wei, Y., Li, Z., Kong, D., and Zhao, Q. (2019). Nitric-oxide-releasing biomaterial regulation of the stem cell microenvironment in regenerative medicine. *Adv. Mater.* 32:e1805818. doi: 10.1002/adma.201805818

Moncion, A., Harmon, J. S., Li, Y., Natla, S., Farrell, E. C., Kripfgans, O. D., et al. (2019). Spatiotemporally-controlled transgene expression in hydroxyapatite-fibrin composite scaffolds using high intensity focused ultrasound. *Biomaterials* 194, 14–24. doi: 10.1016/j.biomaterials.2018.12.011

Mondal, S., Manivasagan, P., Bharathiraja, S., Santha Moorthy, M., Kim, H. H., Seo, H., et al. (2017). Magnetic hydroxyapatite: a promising multifunctional platform for nanomedicine application. *Int. J. Nanomedicine* 12, 8389–8410. doi: 10.2147/IJN.S147355

Moore, A. N., and Hartgerink, J. D. (2017). Self-assembling multidomain peptide nanofibers for delivery of bioactive molecules and tissue regeneration. *Acc. Chem. Res.* 50, 714–722. doi: 10.1021/acs.accounts.6b00553

Namdari, M., and Eatemadi, A. (2017). Cardioprotective effects of curcumin-loaded magnetic hydrogel nanocomposite (nanocurcumin) against doxorubicin-induced cardiac toxicity in rat cardiomyocyte cell lines. *Artif. Cells Nanomed. Biotechnol.* 45, 731–739. doi: 10.1080/21691401.2016.1261033

Omidinia-Anarkoli, A., Boesveld, S., Tuvshindorj, U., Rose, J. C., Haraszti, T., and De Laporte, L. (2017). An injectable hybrid hydrogel with oriented short fibers induces unidirectional growth of functional nerve cells. *Small.* 13:1702207. doi: 10.1002/smll.201702207

Park, D., Wershof, E., Boeing, S., Labernadie, A., Jenkins, R. P., George, S., et al. (2019). Extracellular matrix anisotropy is determined by TFAP2C-dependent regulation of cell collisions. *Nat. Mater.* 19, 227–238. doi: 10.1038/s41563-019-0504-3

Phillips, J. E., Burns, K. L., Le Doux, J. M., Guldberg, R. E., and García, A. J. (2008). Engineering graded tissue interfaces. 105, 12170–12175. doi: 10.1073/pnas.0801988105

Qiu, P., Li, M., Chen, K., Fang, B., Chen, P., Tang, Z., et al. (2020). Periosteal matrix-derived hydrogel promotes bone repair through an early immune regulation coupled with enhanced angio- and osteogenesis. *Biomaterials* 227:119552. doi: 10.1016/j.biomaterials.2019.119552

Reddi, A. H., Becerra, J., and Andrades, J. A. (2011). Nanomaterials and hydrogel scaffolds for articular cartilage regeneration. *Tissue Eng. Part B Rev.* 17, 301–305. doi: 10.1089/ten.teb.2011.0141

Ren, X., Weisgerber, D. W., Bischoff, D., Lewis, M. S., Reid, R. R., He, T.-C., et al. (2016). Nanoparticulate mineralized collagen scaffolds and BMP-9 induce a long-term bone cartilage construct in human mesenchymal stem cells. *Adv. Healthc. Mater.* 5, 1821–1830. doi: 10.1002/adhm.201600187

Rodkate, N., and Rutnakornpituk, M. (2016). Multi-responsive magnetic microsphere of poly(N-isopropylacrylamide)/carboxymethylchitosan hydrogel for drug controlled release. *Carbohydr. Polym.* 151, 251–259. doi: 10.1016/j.carbpol.2016.05.081

Rose, J. C., Cámara-Torres, M., Rahimi, K., Köhler, J., Möller, M., and De Laporte, L. (2017). Nerve cells decide to orient inside an injectable hydrogel with minimal structural guidance. *Nano Lett.* 17, 3782–3791. doi: 10.1021/acs.nanolett.7b01123

Rose, J. C., Gehlen, D. B., Haraszti, T., Kohler, J., Licht, C. J., and De Laporte, L. (2018). Biofunctionalized aligned microgels provide 3D cell guidance to mimic complex tissue matrices. *Biomaterials* 163, 128–141. doi: 10.1016/j.biomaterials.2018.02.001

Ruehle, M. A., Li, M. A., Cheng, A., Krishnan, L., Willett, N. J., and Guldberg, R. E. (2019). Decorin-supplemented collagen hydrogels for the co-delivery of bone morphogenetic protein-2 and microvascular fragments to a composite bone-muscle injury model with impaired vascularization. *Acta Biomater.* 93, 210–221. doi: 10.1016/j.actbio.2019.01.045

Seidi, A., Ramalingam, M., Elloumi-Hannachi, I., Ostrovidov, S., and Khademhosseini, A. (2011). Gradient biomaterials for soft-to-hard interface tissue engineering. *Acta Biomater.* 7, 1441–1451. doi: 10.1016/j.actbio.2011.01.011

Shahriari, D., Loke, G., Tafel, I., Park, S., Chiang, P. H., Fink, Y., et al. (2019). Scalable fabrication of porous microchannel nerve guidance scaffolds with complex geometries. *Adv. Mater.* 31:e1902021. doi: 10.1002/adma.201902021

Shi, L., Zeng, Y., Zhao, Y., Yang, B., Ossipov, D., Tai, C. W., et al. (2019). Biocompatible injectable magnetic hydrogel formed by dynamic coordination network. *ACS Appl. Mater. Interfaces*. 11, 46233–46240. doi: 10.1021/acsami.9b17627

Silva, E. D., Babo, P. S., Costa-Almeida, R., Domingues, R. M. A., Mendes, B. B., Paz, E., et al. (2018). Multifunctional magnetic-responsive hydrogels to engineer tendon-to-bone interface. *Nanomedicine* 14, 2375–2385. doi: 10.1016/j.nano.2017.06.002

Stowers, R. S., Drinnan, C. T., Chung, E., and Suggs, L. J. (2013). Mesenchymal stem cell response to TGF-β1 in both 2D and 3D environments. *Biomater. Sci.* 1, 860–869. doi: 10.1039/c3bm60057b

Sun, C., Lee, J. S., and Zhang, M. (2008). Magnetic nanoparticles in MR imaging and drug delivery. *Adv. Drug Deliv. Rev.* 60, 1252–1265. doi: 10.1016/j.addr.2008.03.018

Tang, J., Myers, M., Bosnick, K. A., and Brus, L. E. (2003). Magnetite Fe_3O_4 nanocrystals: spectroscopic observation of aqueous oxidation kinetics. *J. Phys. Chem. B* 107, 7501–7506. doi: 10.1021/jp027048e

Tay, A., Sohrabi, A., Poole, K., Seidlits, S., and Di Carlo, D. (2018). A 3D Magnetic hyaluronic acid hydrogel for magnetomechanical neuromodulation of primary dorsal root ganglion neurons. *Adv. Mater.* 10:e1800927. doi: 10.1002/adma.201800927

Toh, W. S., Foldager, C. B., Pei, M., and Hui, J. H. (2014). Advances in mesenchymal stem cell-based strategies for cartilage repair and regeneration. *Stem Cell Rev. Rep.* 10, 686–696. doi: 10.1007/s12015-014-9526-z

Tóth, I. Y., Veress, G., Szekeres, M., Illés, E., and Tombácz, E. (2015). Magnetic hyaluronate hydrogels: preparation and characterization. *J. Magn. Magn. Mater.* 380, 175–180. doi: 10.1016/j.jmmm.2014.10.139

Van Bemmelen, J. M. (1894). Das hydrogel und das krystallinische hydrat des kupferoxyds. *Zeitschrift für anorganische Chemie* 5, 466–483. doi: 10.1002/zaac.18940050156

Venkataprasanna, K. S., Prakash, J., Vignesh, S., Bharath, G., Venkatesan, M., Banat, F., et al. (2019). Fabrication of chitosan/PVA/GO/CuO patch for potential wound healing application. *Int. J. Biol. Macromol.* doi: 10.1016/j.ijbiomac.2019.10.029

Ventola, C. L. (2017). Progress in nanomedicine: approved and investigational nanodrugs. *P T.* 42, 742–755.

Wang, Y., Li, B., Xu, F., Han, Z., Wei, D., Jia, D., et al. (2018). Tough magnetic chitosan hydrogel nanocomposites for remotely stimulated drug release. *Biomacromolecules* 19, 3351–3360. doi: 10.1021/acs.biomac.8b00636

Wang, Y., Li, B., Zhou, Y., and Jia, D. (2009). *In situ* mineralization of magnetite nanoparticles in chitosan hydrogel. *Nanoscale Res. Lett.* 4, 1041–1046. doi: 10.1007/s11671-009-9355-1

Wei, Z., Volkova, E., Blatchley, M. R., and Gerecht, S. (2019). Hydrogel vehicles for sequential delivery of protein drugs to promote vascular regeneration. *Adv. Drug Deliv. Rev.* 149-150, 95–106 doi: 10.1016/j.addr.2019.08.005

Wichterle, O., and LÍm, D. (1960). Hydrophilic gels for biological use. *Nature* 185, 117–118. doi: 10.1038/185117a0

Wu, C., Huang, J., Chu, B., Deng, J., Zhang, Z., Tang, S., et al. (2019). Dynamic and hierarchically structured networks with tissue-like mechanical behavior. *ACS Nano* 13, 10727–10736. doi: 10.1021/acsnano.9b05436

Wu, H., Liu, L., Song, L., Ma, M., Gu, N., and Zhang, Y. (2019). Enhanced tumor synergistic therapy by injectable magnetic hydrogel mediated generation of hyperthermia and highly toxic reactive oxygen species. *ACS Nano* 13, 14013–14023. doi: 10.1021/acsnano.9b06134

Wu, H., Song, L., Chen, L., Zhang, W., Chen, Y., Zang, F., et al. (2018). Injectable magnetic supramolecular hydrogel with magnetocaloric liquid-conformal property prevents post-operative recurrence in a breast cancer model. *Acta Biomater.* 74, 302–311. doi: 10.1016/j.actbio.2018.04.052

Wu, J., Ding, Q., Dutta, A., Wang, Y., Huang, Y. H., Weng, H., et al. (2015). An injectable extracellular matrix derived hydrogel for meniscus repair and regeneration. *Acta Biomater.* 16, 49–59. doi: 10.1016/j.actbio.2015.01.027

Xie, W., Gao, Q., Guo, Z., Wang, D., Gao, F., Wang, X., et al. (2017). Injectable and self-healing thermosensitive magnetic hydrogel for asynchronous control release of doxorubicin and docetaxel to treat triple-negative breast cancer. *ACS Appl. Mater. Interfaces* 9, 33660–33673. doi: 10.1021/acsami.7b10699

Xu, X., Shi, D., Shen, Y., Xu, Z., Dai, J., Chen, D., et al. (2015). Full-thickness cartilage defects are repaired via a microfracture technique and intraarticular injection of the small-molecule compound kartogenin. *Arthritis Res. Ther.* 17, 20–20. doi: 10.1186/s13075-015-0537-1

Xu, Y., Patsis, P. A., Hauser, S., Voigt, D., Rothe, R., Gunther, M., et al. (2019). Cytocompatible, injectable, and electroconductive soft adhesives with hybrid covalent/noncovalent dynamic network. *Adv. Sci.* 6:1802077. doi: 10.1002/advs.201802077

Yang, W., Zhu, P., Huang, H., Zheng, Y., Liu, J., Feng, L., et al. (2019). Functionalization of novel theranostic hydrogels with kartogenin-grafted USPIO nanoparticles to enhance cartilage regeneration. *ACS Appl. Mater. Interfaces*. doi: 10.1021/acsami.9b12288

Yang, Y. N., Lu, K. Y., Wang, P., Ho, Y. C., Tsai, M. L., and Mi, F. L. (2020). Development of bacterial cellulose/chitin multi-nano fi bers based smart films containing natural active microspheres and nanoparticles formed *in situ*. *Carbohydr. Polym.* 228:115370. doi: 10.1016/j.carbpol.2019.115370

Yi, J., Jiang, N., Li, B., Yan, Q., Qiu, T., Swaminatha Iyer, K., et al. (2018). Painful terminal neuroma prevention by capping PRGD/PDLLA conduit in rat sciatic nerves. *Adv. Sci.* 5:1700876. doi: 10.1002/advs.201700876

Yu, L., and Ding, J. (2008). Injectable hydrogels as unique biomedical materials. *Chem. Soc. Rev.* 37, 1473–1481. doi: 10.1039/b713009k

Yuan, Z., Memarzadeh, K., Stephen, A. S., Allaker, R. P., Brown, R. A., and Huang, J. (2018). Development of a 3D collagen model for the *in vitro* evaluation of magnetic-assisted osteogenesis. *Sci. Rep.* 8:16270. doi: 10.1038/s41598-018-33455-2

Zanchetta, J. R., and Bogado, C. E. (2001). Raloxifene reverses bone loss in postmenopausal women with mild asymptomatic primary hyperparathyroidism. *J. Bone Miner. Res.* 16, 189–190. doi: 10.1359/jbmr.2001.16.1.189

Zhang, N., Lock, J., Sallee, A., and Liu, H. (2015). Magnetic nanocomposite hydrogel for potential cartilage tissue engineering: synthesis, characterization, and cytocompatibility with bone marrow derived mesenchymal stem cells. *ACS Appl. Mater. Interfaces* 7, 20987–20998. doi: 10.1021/acsami.5b06939

Zhang, P.-X., Han, N., Kou, Y.-H., Zhu, Q.-T., Liu, X.-L., Quan, D.-P., et al. (2019). Tissue engineering for the repair of peripheral nerve injury. *Neural Regen. Res.* 14, 51–58. doi: 10.4103/1673-5374.243701

Zhang, Y., Chen, K., Li, Y., Lan, J., Yan, B., Shi, L. Y., et al. (2019). High-strength, self-healable, temperature-sensitive, MXene-containing composite hydrogel as a smart compression sensor. *ACS Appl. Mater. Interfaces*. 11, 47350–47357. doi: 10.1021/acsami.9b16078

Zhang, Z., Qu, R., Fan, T., Ouyang, J., Lu, F., and Dai, J. (2019). Stepwise adipogenesis of decellularized cellular extracellular matrix regulates adipose tissue-derived stem cell migration and differentiation. *Stem Cells Int.* 2019:1845926. doi: 10.1155/2019/1845926

Zhang, Z. Q., and Song, S. C. (2016). Thermosensitive/superparamagnetic iron oxide nanoparticle-loaded nanocapsule hydrogels for multiple cancer hyperthermia. *Biomaterials* 106, 13–23. doi: 10.1016/j.biomaterials.2016.08.015

Zhao, X., Liu, Y., Shao, C., Nie, M., Huang, Q., Li, J., et al. (2019). Photoresponsive delivery microcarriers for tissue defects repair. *Adv Sci.* 6:1901280. doi: 10.1002/advs.201901280

Zheng, L., Li, C., Huang, X., Lin, X., Lin, W., Yang, F., et al. (2019). Thermosensitive hydrogels for sustained-release of sorafenib and selenium nanoparticles for localized synergistic chemoradiotherapy. *Biomaterials* 216:119220. doi: 10.1016/j.biomaterials.2019.05.031

Zhou, K., Yu, P., Shi, X., Ling, T., Zeng, W., Chen, A., et al. (2019). Hierarchically porous hydroxyapatite hybrid scaffold incorporated with reduced graphene oxide for rapid bone ingrowth and repair. *ACS Nano* 13, 9595–9606. doi: 10.1021/acsnano.9b04723

Zhou, T., Wu, J., Liu, J., Luo, Y., and Wan, Y. (2015). Fabrication and characterization of layered chitosan/silk fibroin/nano-hydroxyapatite scaffolds with designed composition and mechanical properties. *Biomed. Mater.* 10:045013. doi: 10.1088/1748-6041/10/4/045013

Zhu, W., Guo, D., Peng, L., Chen, Y. F., Cui, J., Xiong, J., et al. (2017). Repair of rabbit cartilage defect based on the fusion of rabbit bone marrow stromal cells and Nano-HA/PLLA composite material. *Artif. Cells Nanomed. Biotechnol.* 45, 115–119. doi: 10.3109/21691401.2016.1138482

Zhu, Y., Zhang, Q., Shi, X., and Han, D. (2019). Hierarchical hydrogel composite interfaces with robust mechanical properties for biomedical applications. *Adv. Mater.* 45:e1804950. doi: 10.1002/adma.201804950

Conflict of Interest: The authors declare that the research was conducted in the absence of any commercial or financial relationships that could be construed as a potential conflict of interest.

Advantages of publishing in Frontiers

OPEN ACCESS
Articles are free to read for greatest visibility and readership

FAST PUBLICATION
Around 90 days from submission to decision

HIGH QUALITY PEER-REVIEW
Rigorous, collaborative, and constructive peer-review

TRANSPARENT PEER-REVIEW
Editors and reviewers acknowledged by name on published articles

Frontiers
Avenue du Tribunal-Fédéral 34
1005 Lausanne | Switzerland

Visit us: www.frontiersin.org
Contact us: info@frontiersin.org | +41 21 510 17 00

REPRODUCIBILITY OF RESEARCH
Support open data and methods to enhance research reproducibility

DIGITAL PUBLISHING
Articles designed for optimal readership across devices

FOLLOW US
@frontiersin

IMPACT METRICS
Advanced article metrics track visibility across digital media

EXTENSIVE PROMOTION
Marketing and promotion of impactful research

LOOP RESEARCH NETWORK
Our network increases your article's readership